Department of Chemical Engineering

Faculty of Chemical Technologies and Sciences

University of Castilla-La Mancha

DEVELOPMENT OF NANOSTRUCTURED ELECTRODES BY MAGNETRON SPUTTERING FOR ANION EXCHANGE MEMBRANE WATER ELECTROLYSIS

Ester López Fernández

Thesis submitted in fulfilment of the requirements of the degree of Doctor (PhD) by the University of Castilla-La Mancha

Supervisors:

Dr. Antonio de Lucas Consuegra

Dr. Francisco Yubero Valencia

Ciudad Real, 2022

D. Antonio de Lucas Consuegra, Catedrático de Ingeniería Química de la Universidad de Castilla-La Mancha, y Francisco Yubero Valencia, Investigador Científico del Consejo Superior de Investigaciones Científicas,

Certifican que:

El presente trabajo de investigación titulado "Development of nanostructured electrodes by magnetron sputtering for anion exchange membrane water electrolysis" constituye la memoria que presenta Dña. Ester López Fernández para aspirar al grado de Doctor en Ingeniería Química y Ambiental por la Universidad de Castilla-La Mancha y que ha sido realizada en los laboratorios del Departamento de Ingeniería Química de la Universidad de Castilla-La Mancha bajo su dirección.

Y para que conste a efectos oportunos, firman el presente certificado.

Ciudad Real, 10 de noviembre de 2021.

D. Antonio de Lucas Consuegra   D. Francisco Yubero Valencia

Solo el propio doctorando sabrá, a su debido tiempo, como va a afrontar la realización de su tesis doctoral. Esto es algo que he aprendido a lo largo de estos cuatro años. En mi caso, puedo decir que he conseguido llevarla, la mayor parte del tiempo, de manera positiva y siempre con la sonrisa puesta. Pero esto no habría sido posible sin toda la gente que ha estado a mi lado durante todo este tiempo, y a la que quiero dedicar estas palabras. En primer lugar, agradezco el haber podido realizar este trabajo entre dos grupos de investigación distintos. Laboralmente he crecido muchísimo trabajando con perfiles y ambientes de trabajo tan diferentes, pero a modo personal, no puedo ser más afortunada. Aunque son muchos los altibajos de los últimos meses, y aunque a veces pienses que, si volvieses atrás, no elegirías este camino de nuevo, repetiría cada uno de los momentos de estrés, frustración o tristeza solo por compartir estos años con todos vosotros.

Gracias al Departamento de Ingeniería Química, por ayudarme a ser la persona que ahora soy. Gracias a todos los profesores del Departamento, por brindarnos su ayuda siempre que la hemos necesitado. Gracias también al grupo Nanotecnología en Superficies y Plasma, por hacerme sentir como en casa desde el primer día que pisé tierras andaluzas.

A mis directores, por todo el esfuerzo que han realizado para que este trabajo fuese fructífero. Antonio, tu gran dedicación ha hecho que llegase hasta aquí. A Paco, gracias por confiar en mí sin conocerme, y por hacerme pensar de manera más crítica.

A Agustín, por tus consejos, por transmitirnos a todos tu sabiduría y por la gran dedicación que has tenido en esta tesis. A Juan Pedro, por tus consejos y ayuda siempre que los he necesitado. A Jorge, porque cualquier complicación en el laboratorio se resolvía en tan solo cinco minutos gracias a ti. Gracias escuchar cada uno de mis "problemas". Después de hablar contigo todo parecía más fácil. Siempre he dicho que eres mi "hombro de lágrimas". Este trabajo también es vuestro.

A los "Mini-Nanos", quienes han hecho que adore ir a trabajar. A Jose, la persona más intensa que conozco. Siempre te estaré agradecida por ser mi primer amigo en Sevilla, pero también por esas tardes de música, por pasearme con el carrito de los residuos y por colgarme de cadenas. Confío en que algún día aprenderás a planchar y a bailar sevillanas. A Aurelio, ese gran doctor que dejó un vacío irreemplazable en el laboratorio. Gracias por enseñarme a entender (o más bien traducirme) el andaluz profundo. A Paula, por enseñarme los lugares remotos de la Sevilla profunda y a su gente, siempre tratándome como una más. Gracias por ayudarme en todo lo que he necesitado en cada momento y por tranquilizarme en mis muchos momentos de estrés. Ya lo sabes, siempre juntas. A Javi. Como sabes (y creo que todo el mundo que me conoce un poco lo ha notado), mi vida está llena de "Javis", pero conocería a infinitos más por encontrarme a alguien como tú. Gracias por escucharme y aconsejarme en cada uno de los pasos que he dado en mi vida desde el momento en el que te conocí. Jamás pensé que alguien, en tan poco tiempo, podría llegar a convertirse en un pilar tan fundamental para mí. Gracias por aguantarme en mis tardes "tontas" y por no salir corriendo cuando empezaba a reírme sola.

A todos los demás integrantes del grupo Nanotecnología en Superficies y Plasma. No voy a nombraros uno por uno, ya que podría escribir otra tesis de agradecimientos y anécdotas vividas con vosotros. Gracias por acogerme desde el primer día como una más, por hacerme sentir como en casa, y por brindarme vuestra ayuda y consejos siempre que los he necesitado. Tengo muy claro que no podría haber acabado en un grupo en el que me tratasen mejor que vosotros.

A Elena, por su sensatez y ayuda cuando la necesitas, y por enseñarnos la ciencia de forma tan bonita. A Sandra (Piña). Que bien nos entendimos nada más conocernos en aquel congreso en Salamanca. Gracias por cada conversación, y por acogerme en tu casa. A Encarna, sinónimo de inocencia y bondad. La que siempre está ahí para ayudarte, en cualquier momento o desde cualquier lugar. Tengo claro que llegarás muy lejos. Las croquetas de Casa Ricardo y las bicicletas siempre estarán aseguradas a nuestro lado. A Cristina.

Jamás podría haber imaginado que ir a comprar un traje de flamenca fuese a cambiar tanto mi vida. Solamente puedo darte las gracias, por cada uno de los momentos maravillosos que hemos vivido (y los que nos quedan por vivir) a partir de aquella tarde. Por cada noche de Vinilo (sí, tenía que aparecer en este libro, pues también es parte de esta tesis), cada viaje, cada mudanza, cada conversación. Mi casa siempre será tu casa.

A Rosalía, nunca podré agradecerte lo suficiente todas las risas que pasábamos en las comidas (incluso aquel día que me quedé sin albóndigas), ni el haberme presentado a Cristina. A Carmen, ojalá haber disfrutado más de ti, porque todos los momentos que hemos pasado juntas han sigo maravillosos. A Ale, con el que las mudanzas se convierten en cerveza, croquetas y guitarra.

A Estefanía y Sonia, mis "López". Siempre agradeceré tener este apellido para acabar juntas en esas prácticas. Estefanía, eres una de las personas más valientes que conozco. Siempre he admirado tu facilidad para irte a la otra punta del mundo sin dudar un segundo. Gracias por cada momento que hemos vivido. A Sonia, gracias por recorrer juntas cada etapa a partir de esas prácticas. Las dos sabemos el gran equipo que hacemos. Eres una de las personas más trabajadoras que conozco, y sé que la vida te lo va a recompensar. Gracias por estar ahí siempre que lo he necesitado.

A Estela, por lo bien que nos entendemos. Gracias por cada momento, tanto en Ciudad Real como, más inesperado para mí, en Sevilla. Ojalá poder tener muchas conversaciones profundas en terrazas contigo, que no salvarán el mundo, pero sí a nosotras mismas. Siempre tendrás un huequito en mi cuarto cuando lo necesites. No sé qué he hecho sin ti todos estos años. A Marina. Si pudiese definir una compañera de laboratorio perfecta y, mucho más importante, una amiga, daría tu nombre. Siempre has estado dispuesta a ayudarme en todo lo que he necesitado, sin necesidad de pedirlo. Gracias por escucharme a cualquier hora del día, por aguantarme mis días de risas y mis días de llantos, por tus bonitos abrazos. Nunca pierdas tu arte andaluz, pero sí el de encontrarte animalitos en el laboratorio. A Alberto, con el que siempre he

ido de la mano. Quién me iba a decir a mí que aquel "esparraguillo" que conocí en 1º de la ESO iba a ser mi compañero de instituto, grado, máster y tesis doctoral. Gracias por tu sabiduría y consejos (siempre podré decir que eres una de las personas más inteligentes que conozco), paciencia (que también has tenido mucha) y también por tus locuras (tengo alguna que otra para recordar). A Celia, mi 24/7, compañera de laboratorio, pádel, carnaval y amiga. Me has aguantado desde el primer día que llegaste al laboratorio, (casi) sin pensar nada raro de mí. Parece que hace una vida que te conozco con todo lo que hemos vivido juntas (y lo que nos queda). No sé qué hubiese hecho sin ti y tu gran ayuda, sobre todo en estos últimos meses. A Jesús, que sé que algún día empezará a hacer caso a los consejos que le doy. Sigue trabajando duro, la vida te lo recompensará. A Javi, que con su "pa ciencia" nos ha alegrado el día a día. Menos mal que has llegado al final de esta etapa, los dos sabemos que hubiese sido difícil acabarla de no ser así. A Ángel, que sabemos que se muere de envidia por no estar en el laboratorio "guay", pero también nos ha traído buenos ratos y cotilleos.

A Encarni, con quien compartí mi primer equipo de laboratorio, "Las Calce". Gracias por ser tan clara, sensata y hacer feliz a todo el mundo que está a tu alrededor. A Ana, gracias por enseñarme con toda tu paciencia toda mi base y por cada gran momento que pasamos tanto dentro como fuera del laboratorio.

A Juan, con quien también he compartido muchos años ya, por vivir más en nuestro laboratorio que en el tuyo, y ofrecer tu casa cuando más la necesitamos. A Fer y Pablo, por hacerme desconectar con cada tarde de pádel (aunque seáis unos "picaos") y con cada jueves.

Me gustaría también agradecer a la gente del laboratorio de Electroquímica, y a Conchi, por transmitirnos esa alegría y esas ganas de vivir. Ojalá más gente como tú.

Thanks to Catalytic and Electrochemical Process for Energy Applications group, at Dutch Institute for Fundamental Energy Research, for opening many doors of opportunities to me at its laboratories and for helping me in any way

A mis fontanarejeños, y en especial a Sergio. Por recargarme las pilas cada fin de semana. Por cada vez que no íbamos a ir a algún sitio y acabábamos llegando los primeros. Gracias por cada plan improvisado y por esos días en los que íbamos a tomarnos "una" cerveza y acababa pasando una jornada laboral. Sois los mejores. La ventanita del amor nunca morirá con vosotros. A Andrés, por estar ahí siempre dispuesto a ayudar o acercarnos a cualquier lugar para desconectar. A Patri, Prado y Javi, porque gracias a nuestro grupo, que por razones obvias no puede ser nombrado aquí, nos echamos muchas risas en ese dichoso encierro. Poder ir a las ovejas e incluso a la playa desde casa fue todo un lujo para mí.

A mi familia, en especial a mis padres, por su apoyo incondicional en cada decisión que he tomado. Por aceptar, sin avisar, que mi vida fuese un altibajo de emociones y de idas y venidas de un lugar para otro. A mi hermana, una de las personas más fuertes que conozco, la que siempre ha estado ahí, aguantando, sobre todo, mis días malos y aprovechando cada minuto de la vida. Todo lo que he conseguido es gracias a vosotros. A mis abuelos. Sé que nunca entenderéis muy bien lo que estoy haciendo, ni la razón por la que me tenía que ir de Ciudad Real largas temporadas, pero siempre me habéis recibido con la mayor de las alegrías y cariño. Como bien me decía mi abuelo José en esta etapa final: "no entiendo para que estudias tanto, si ya lo tendrás todo sabido". Para llegar hasta aquí, abuelo. Gracias por enseñarme que solo se vive una vez y que hay que disfrutar cada momento al máximo.

Y a ti, querido lector, por dedicar tiempo a la lectura de este libro.

"Nada en este mundo debe ser temido ...

sólo entendido."

Marie Curie.

CONTENTS

Resumen

El continuo incremento de la demanda energética y el carácter finito de las fuentes de energía tradicionales que emiten grandes cantidades de gases de efecto invernadero han contribuido a un cambio climático que solo puede salvarse con una rápida adopción de nuevas fuentes de energía que no dañen el medioambiente. Esta transformación energética requiere un cambio en la generación de electricidad, disminuyendo drásticamente el uso de combustibles fósiles y sustituyéndolos por fuentes de energía renovales como la energía solar o la eólica. Muchos países se han comprometido en los últimos años a alcanzar las "cero emisiones de CO_2" para el año 2050, sin embargo, nos queda mucho camino por recorrer hasta alcanzar ese ambicioso objetivo.

Aunque el hidrógeno es el elemento más abundante del planeta, no se encuentra en la naturaleza como fuente de energía, si no que funciona como vector energético pudiendo producirse mediante diferentes métodos de obtención y utilizando una gran variedad de fuentes de energía. Por otro lado, aunque la forma más simple de producir hidrógeno es mediante la electrólisis de agua, que además presenta la ventaja de no producir gases de efecto invernadero, actualmente la mayoría del hidrógeno (alrededor del 96 %) se genera mediante combustibles fósiles. En este contexto, esta tesis tiene como objetivo contribuir en el desarrollo de electrodos eficientes y económicos para su uso en electrolizadores de agua con membranas de intercambio aniónico para producir hidrógeno.

Para ello, esta tesis se enmarca en una colaboración entre el Laboratorio de Catálisis y Materiales de la Universidad de Castilla-La Mancha (UCLM) y el grupo de investigación Nanotecnología en Superficies y Plasma del Instituto de Ciencia de Materiales de Sevilla (ICMS), Centro Mixto Universidad de Sevilla - Consejo Superior de

Investigaciones Científicas (CSIC). Además, la doctoranda realizó una estancia de investigación de tres meses en el Dutch Institute for Fundamental Energy Research en Eindhoven (Países Bajos) y varias estancias cortas en el sincrotrón ALBA de Barcelona con el fin de completar los estudios con técnicas de caracterización.

El resumen de los resultados más relevantes de esta tesis se muestra a continuación:

En primer lugar, en el Capítulo 4 se demostró por primera vez en la bibliografía, la viabilidad de preparar electrodos para electrolizadores con membranas de intercambio aniónico mediante deposición física en fase vapor y, en particular, utilizando la técnica de preparación de películas delgadas basadas en pulverización catódica o *magnetron sputtering* en configuración de ángulo oblicuo (MS-OAD). Esta técnica, que trabaja a temperatura ambiente, permite la deposición de catalizadores nanoestructurados con bajo contenido metálico y un preciso control de la microestructura de los mismos directamente en la capa de difusión de gases. En particular, en el Capítulo 4 se realizó un estudio del efecto de la estequiometría y cristalización de óxidos de Co/Cu en la reacción de evolución de oxígeno y producción de hidrógeno. Este estudio se continuó en el Capítulo 5, donde se estudió la influencia de la carga de catalizador depositada en la capa de difusión de gases. Estos estudios se realizaron tanto en configuración de semicelda electroquímica como en configuración de celda de electrólisis completa. Así, junto con la exhaustiva caracterización llevada a cabo de los electrodos antes y después de su uso, se concluyó que los electrodos anódicos que proporcionaban un mayor rendimiento electroquímico eran electrodos amorfos con una proporción atómica de Co/Cu cercana a 1,8 y con una

cantidad de catalizador equivalente a una micra de espesor (0,4 mg cm^{-2}). Con estos electrodos, se obtuvieron densidades de corriente de 60 mA cm^{-2} a 2,0 V y 40 °C en configuración de celda de electrólisis.

En el Capítulo 6 se prepararon electrodos de níquel mediante la técnica de *magnetron sputtering* con diferentes estados de oxidación (metálicos, óxidos u oxihidróxidos). Esto fue posible gracias a la gran flexibilidad que ofrece la técnica de fabricación que, variando parámetros de proceso, permite la deposición de materiales con diferentes estados químicos sin modificar la microestructura. Se demostró que los catalizadores de níquel depositados mediante MS-OAD en estado metálico presentaban los mejores rendimientos en la reacción de evolución de oxígeno. Además, se determinaron las cantidades de catalizador óptimas de 1080 nm (0,78 mg cm^{-2}) en el ánodo y 540 nm en el cátodo, debido al balance entre el aumento de los sitios activos con el aumento de la carga de catalizador y su disminución cuando comienzan a producirse aglomeraciones. Con estos electrodos se obtuvieron alrededor de 45 mA cm^{-2} a 2,0 V y 40 °C en celda de electrólisis.

Teniendo en cuenta que en la bibliografía está reportado un efecto positivo en la reacción de evolución de oxígeno al añadir Fe a electrodos basados en Ni, el Capítulo 7 se basa en un estudio de electrodos de Ni-Fe variando la estequiometría. Al añadir Fe, se observó un desplazamiento del pico redox hacia valores de potenciales más positivos asociado con la formación de oxihidróxidos de Ni y Fe. Se observó que al aumentar la cantidad de Fe se mejoraba el rendimiento electroquímico del catalizador hasta unos resultados óptimos con una proporción atómica de Ni/Fe alrededor de 10. Los valores de actividad específica obtenidos en celda de electrólisis superaron incluso hasta en 10 veces los valores reportados por otros grupos de investigación, alcanzando valores de más de 1000 mA

5
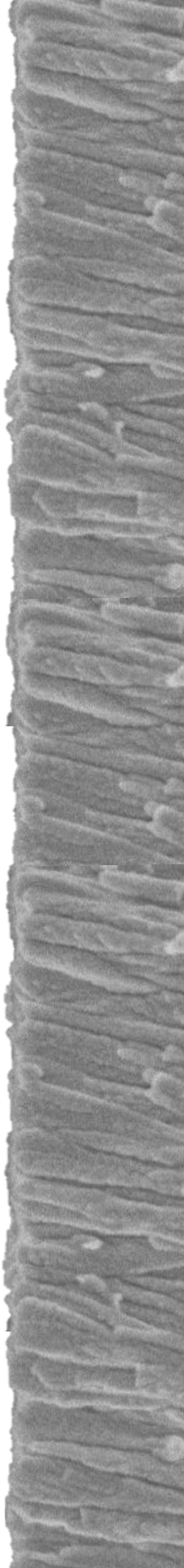
mg^{-1} a 40 °C (densidades de corriente alrededor de 400 mA cm^{-2}). Para este sistema se investigó también el efecto de añadir ionómero al electrodo, un punto crítico para la mayoría de los métodos de preparación tradicionales. En este capítulo se demostró que los electrodos sin ionómero presentaban los mejores resultados, simplificando su proceso de fabricación y reduciendo costes y problemas asociados a este compuesto.

Con el objetivo de continuar mejorando el sistema, en el Capítulo 8 se estudió la influencia del resto de elementos que componen un electrolizador. Se probaron diferentes capas de difusión de gases como papeles de carbón o aceros inoxidables, así como varias membranas de intercambio aniónico, y se optimizaron parámetros de operación. Con el uso de electrodos compuestos de una capa de catalizador de Ni-Fe con un *espesor equivalente* de 540 nm para el caso del electrodo anódico, y Ni con un *espesor equivalente* de 540 nm para el caso del electrodo catódico, ambas capas depositadas en un papel de fibras de acero inoxidable y una membrana comercial Sustainion® 37-50 como membrana de intercambio aniónico, se obtuvo una gran estabilidad durante 7 días, manteniendo la densidad de corriente constante a 400 mA cm^{-2}, con una degradación de apenas 0.05 % V h^{-1} utilizando 1.0 M KOH a una temperatura de 40 °C.

Por último, una de las limitaciones que presenta la electrólisis de agua son los relativamente altos sobrepotenciales necesarios para producir hidrógeno, lo que limita su comercialización. Para contribuir a minimizar este problema, en el Capítulo 9 se ha estudiado la viabilidad de usar electrodos basados en níquel fabricados mediante MS-OAD en un sistema de electrólisis híbrida de etanol-agua. Los menores requerimientos energéticos para producir hidrógeno se deben a que parte

de la energía la proporciona la propia molécula orgánica. Así, se demostró que, añadiendo etanol al electrolito básico, la reacción de oxidación de etanol comenzaba simultáneamente a la formación del oxihidróxido de níquel en el pico redox (en ausencia de reacción de evolución de oxígeno). Además, de forma inversa a la mejora observada al añadir Fe a los electrodos de Ni en la reacción de evolución de oxígeno, cuando añadimos Fe al electrodo de Ni, el rendimiento hacia la reacción de oxidación de etanol disminuye. Se observó una disminución del potencial requerido para alcanzar una cierta densidad de corriente al añadir etanol al sistema en comparación con electrolitos compuestos solamente por KOH. Por último, con la celda de electrólisis óptima y bajo unas condiciones de operación de 40 ºC, 1.0 M KOH y 1.5 M EtOH, se consiguió una reducción del consumo energético del 10 % (en kWh kg_{H2}^{-1}).

Summary

The continuous increase in the energy demand and the finite nature of traditional energy sources, emitting large amounts of greenhouse gases, have led to a global climate change that can only be solved with the fast adoption of new environmentally friendly energy sources. This energy transformation requires a change in electricity generation, drastically reducing the use of fossil fuels and replacing them by renewable energy sources as solar or wind energy. In recent years, many countries have committed to achieve zero CO_2 emissions by 2050. However, we still have a long road to go in order to reach this ambitious goal.

Hydrogen, as an element, is the most abundant in earth, but it is not found as an energy source, i.e., as molecular hydrogen, in nature. Molecular hydrogen is an energy vector that can be produced by different methods and using a wide variety of energy sources. On the other hand, even though the simplest way to produce hydrogen is by water splitting, a process without greenhouse gases emissions, currently most of molecular hydrogen (around 96 %) is generated by fossil fuels. In this context, this thesis work aims to contribute to develop efficient and cheap electrodes for use in water electrolyzers with anion exchange membranes to produce hydrogen.

The studies reported herein summarized a fruitful collaboration between the Laboratory of Catalysis and Materials of the University of Castilla-La Mancha (UCLM) and the research group Nanotechnology in Surfaces and Plasma of the Institute of Materials Science of Seville (ICMS), joint research center of University of Seville and the Spanish National Research Council (CSIC). In addition, a three-month research stay by the doctoral student at the Dutch Institute for Fundamental Energy Research in Eindhoven (Netherlands) and a couple of short stays at ALBA Synchrotron in Barcelona, complemented these studies.

The summary of the main results obtained in this thesis is as follows:

Chapter 4 demonstrates for the first time in the literature, that magnetron sputtering at oblique angle deposition (MS-OAD) configuration is a suitable technique to prepare catalyst electrodes for anion exchange membrane water electrolysis (AEMWE). This physical vapor deposition technique, that operates at room temperature, allows the deposition of controlled low amount of nanostructured catalysts directly on suitable gas diffusion layer (GDL). In particular, Chapter 4 shows a study of the effect of stoichiometry and crystallization of the Co/Cu mixed oxide towards oxygen evolution reaction (OER) and hydrogen production. The study of these mixed oxide catalysts is continued in Chapter 5, where it is mainly investigated how increasing catalyst loads deposited on a GDL affects the performance towards OER and hydrogen production. These studies are performed both in half-cell configuration and in membrane electrode assembly (MEA) cell configuration. Thus, together with the exhaustive physico-chemical characterization carried out for the electrodes before and after their use, it is concluded that the best electrochemical performance of these mixed oxide catalysts towards OER is achieved for amorphous catalyst layers with Co/Cu atomic ratio of about 1.8 and loads around 1000 nm *equivalent thickness* (0.4 mg cm^{-2}). The best reported performance was of 60 mA cm^{-2} at 2.0 V polarization voltage and 40 °C.

Chapter 6 shows a study of nickel-based catalyst electrodes prepared by magnetron sputtering deposition with different oxidation states (metallic, oxide and oxyhydroxide). This is possible thanks to the flexibility of the deposition technique that, upon variation of the process parameters, allows the deposition of materials with different chemistry and similar microstructure. It is found that nickel catalysts prepared by

means of MS-OAD as metallic present the best electrochemical performance towards OER. Besides, it is found that optimal catalyst loads for their implementation in a MEA are anode of 1080 nm (0.78 mg cm^{-2}) of *equivalent thickness* and 540 nm for the cathode, due to the balance between the increase of the active sites with the increase in catalyst loading and its decrease when agglomerations begin to occur. The best electrochemical performance obtained in this type of catalyst electrodes was of 45 mA cm^{-2} at 2.0 V polarization voltage and 40 $^{\circ}$C. This study is complemented by aging stability studies of the MEA.

Taking into account the positive effect towards OER that has been reported in the literature when adding Fe to Ni-based electrodes, Chapter 7 includes a study on Ni-Fe bimetallic electrodes with varying stoichiometry. It is found that, upon Fe incorporation into the nickel metallic structure, a shift of the redox peak towards more positive potential values associated with the formation of Ni and Fe oxyhydroxides takes place. We systematically obtain that the incorporation of iron to the nickel network improves the catalyst electrochemical performance with best results with a Ni/Fe atomic ratio about 10. The specific activity values obtained in the electrolysis cell exceeded those reported by other research groups by up to a factor ten, reaching values of more than 1000 mA mg^{-1} at 40 $^{\circ}$C (current densities around 400 mA cm^{-2}). For this system, it is also investigated the effect of the addition of the ionomer to the electrodes, a critical point for the most of traditional preparation methods. We find that ionomer-free Ni/Fe electrodes have better performance than equivalent electrodes where typical ionomer are incorporated. This result simplifies the electrode manufacturing process and may reduce costs and minimize problems associated with this compound.

Chapter 8 reports the influence of the rest of the elements of the electrolyzer. Different gas diffusion layers as carbon or stainless-steel papers and several anion exchange membranes, as well as operation conditions, were optimized. With the use of electrodes composed of a layer of Ni-Fe catalyst with an *equivalent thickness* of 540 nm as anodic electrode, and Ni with an *equivalent thickness* of 540 nm as cathodic electrode, both layers deposited in a stainless-steel fiber papers, and using a commercial Sustainion® 37-50 membrane as anion exchange membrane, a great stability was achieved for 7 days, maintaining the constant current density at 400 mA cm^{-2}, with a degradation of only 0.05 % V h^{-1} using 1.0 M KOH at a temperature of 40 °C.

Finally, Chapter 9 deals with the relatively high polarization potentials required to produce hydrogen, which limit its commercialization. To contribute to minimize this problem, the feasibility of using nickel-based electrodes manufactured by MS-OAD in an ethanol-water hybrid electrolysis system was explored. The lower energy requirement to produce hydrogen in this hybrid electrolysis is because the organic molecule provides part of it. It is found that once ethanol is added as fuel to the basic electrolyte, the ethanol oxidation reaction starts simultaneously to the initial formation of Ni oxyhydroxide (in absence of oxygen evolution). In addition, it was shown that, contrary to the improvement in the activity of adding Fe towards the OER, adding Fe to the Ni electrode leds to a decrease in the activity towards the ethanol oxidation reaction (EOR). A decrease in the potential required to reach a value of current density is observed when ethanol is added to the system compared to KOH-only electrolytes. Finally, with the optimal electrolysis cell and under operating conditions of 40 °C, 1.0 M KOH and 1.5 M EtOH,

a reduction in energy consumption of 10 % (in kWh kg_{H2}^{-1}) to produce hydrogen was achieved.

Chapter 1

Introduction
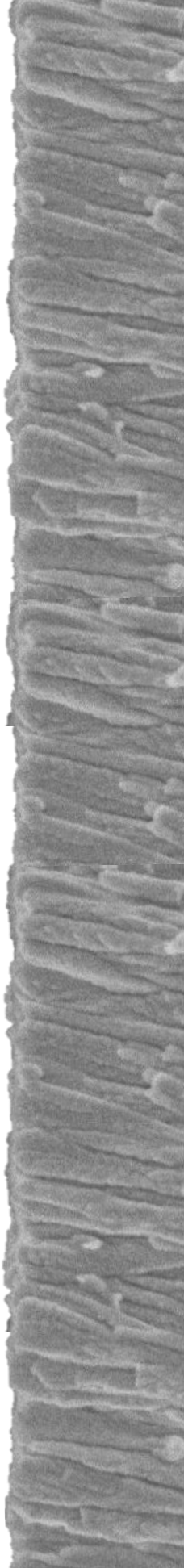
1.1. Green hydrogen as energy vector

While 2020 will be remembered for COVID-19, it has also been an important year in terms of the growth of hydrogen technology. The climate change and rise of the global energy demand have led to an increase in the number of countries that intend to reach net-zero CO_2 emission by 2050 to limit global temperature rise to 1.5 °C (International Renewable Energy Agency, 2021). For this purpose, many countries have announced the development of hydrogen technology strategies. Hydrogen is not an energy source found isolated in nature, but represents a suitable energy vector to guarantee engine operation, electricity production and heat supplies in domestic, transport and industrial sectors [1–3]. Nevertheless, not all types of hydrogen production are sustainable, environmentally friendly or zero-emissions. Only the hydrogen produced using renewable energy sources is considered as *green* hydrogen to achieve these requirements.

Currently, the global demand for hydrogen is around 70 Mt_{H_2} per year (International Energy Agency) from which most production relies on the steam-methane (or other hydrocarbons) reforming. This procedure is responsible for emitting a minimum of 7 kg of CO_2 per kg of H_2, an unmanageable figure in the quest for an effective reduction of carbon dioxide emissions [4,5]. For this reason, alternative hydrogen production processes using environmentally friendly routes with no waste emissions to the atmosphere constitute an urgent and unavoidable requirement.

Hydrogen presents advantages as the high energy density (140 MJ kg^{-1}) compared to other conventional fuels (50 MJ kg^{-1}), its easy conversion directly into electrical energy by fuel cells or the ease of producing it through a wide variety of sources and methods [6]. Nevertheless, *green* hydrogen production costs between twice and three

times more than *blue* hydrogen production (International Renewable
Energy Agency, 2021). There are two critical points to reduce the cost of
the hydrogen production, the cost of the renewable energy and the cost
of the electrolyzer. In addition, the main disadvantage of the hydrogen is
its volumetric density (0.08376 kg m^{-3} at room conditions), complicating
its transport and storage.

As it can be observed in **Figure 1.1**, Europe's energy hydrogen demand
is increasing from currently less than 2 % to an estimated demand of 24
% by 2050 to fuel transport vehicles, to supply heat and power for
buildings, or for the industry energy, between others (report Fuel Cell
and Hydrogen 2 Joint Undertaking, 2019).
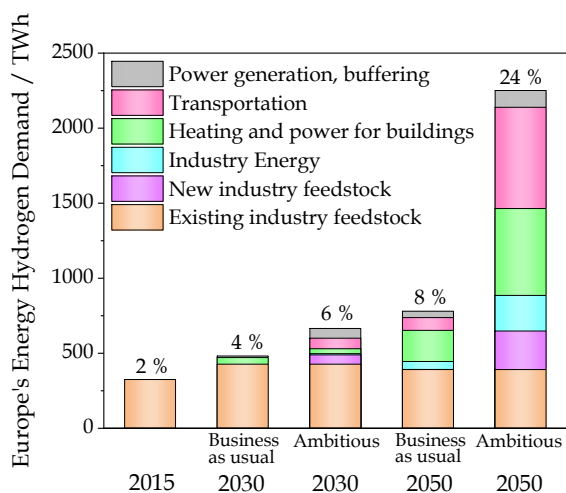
Figure 1.1. *Energy hydrogen demand of Europe through years. Adapted from [report Fuel Cell and Hydrogen 2 Joint Undertaking, 2019].*

1.2.   Low temperature water electrolysis as green hydrogen production method

The simplest pathway to produce hydrogen is the water splitting. However, due to its relative high energy demand, currently other production methods such as thermochemical conversions of fossil fuels or biological processes are mostly used. Nevertheless, in recent years, the generalized interest in water electrolysis has fostered a growing activity in the basic scientific aspects of the technology, as revealed by the increasing number of published papers in this topic (shown **Figure 1.2**, from Scopus source).
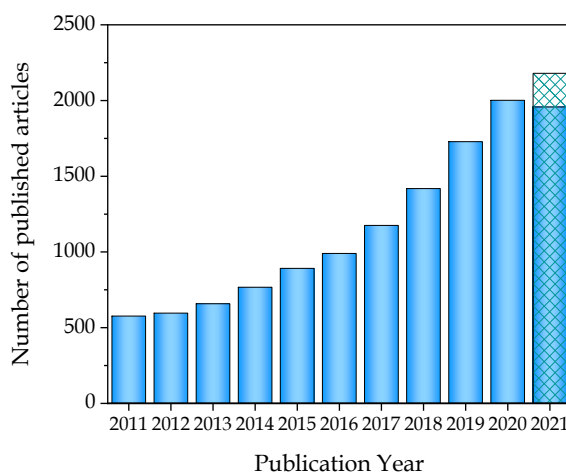
Figure 1.2. *Trend of published articles in this topic of water electrolysis in the last 10 years (Scopus source, 23/10/2021).*

Water electrolyzers can operate at high or low temperatures. Solid Oxide Electrolyzer Cells (SOEC) operate at high temperatures (500-800 ºC), while three major technologies for water electrolyzers operate at low temperatures (40-90 ºC): Alkaline Water Electrolysis (AWE), Proton

Exchange Membrane Water Electrolysis (PEMWE) and Anion Exchange
Membrane Water Electrolysis (AEMWE) [7,8].

A series of cell schemes utilized for three kinds of low temperature
water electrolysis, AWE, PEMWE, and AEMWE, can be observed in
Figure 1.3. Their most relevant features are summarised below.
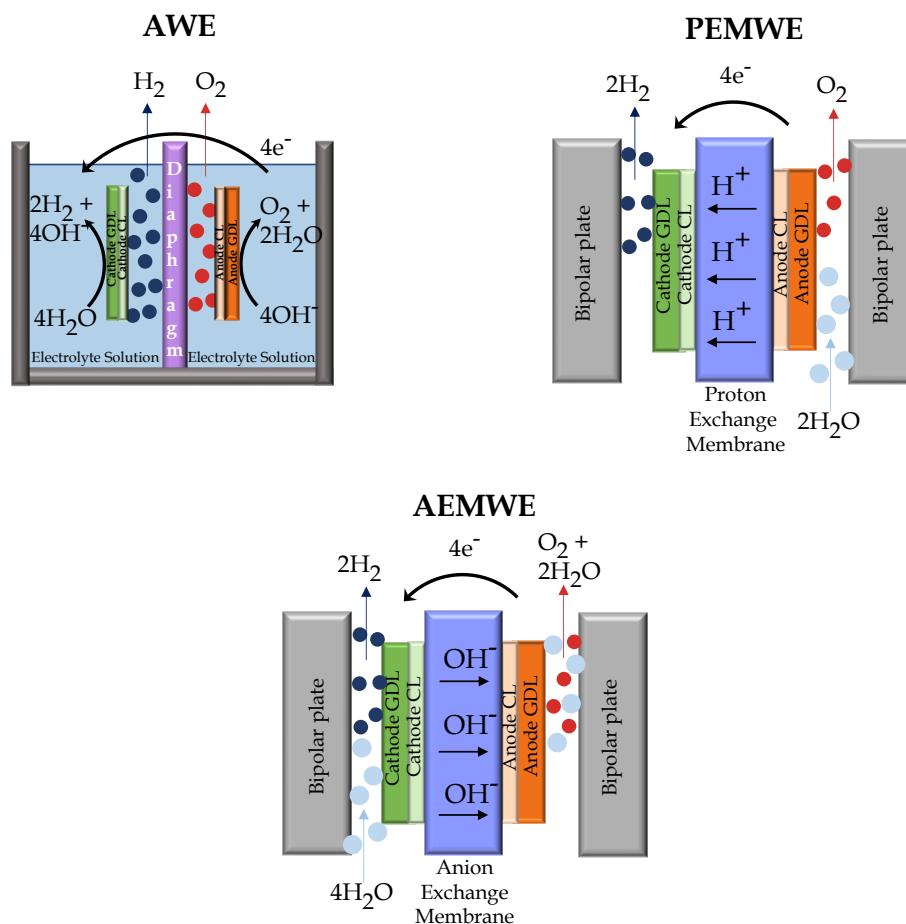
Figure 1.3. Schemes of typical cell configurations of low temperature water electrolyzers.

1.2.1.   <u>Alkaline water electrolysis (AWE)</u>

Alkaline water electrolysis is the most traditional water electrolysis technology. It runs at low temperatures (60-80 °C), commonly with KOH aqueous solutions at very high concentrations (20-40 % KOH) as liquid electrolyte [9–11]. AWE cells basically consist of two separate chambers. The cells incorporate a diaphragm, which is permeable to water and to hydroxide ions and serves to separate the anodic and cathodic chambers, where suitable anode and cathode are located. Unfortunately, the diaphragms do not completely prevent the cross-over of the gases neither that some oxygen arrives to the cathode where it can combine with hydrogen to form water. This results in a decrease of the overall cell efficiency and may cause safety related issues [11].

The AWE technology is compatible with non-noble metal catalyst electrodes [12]. Transition metals based catalysts incorporating cobalt and nickel are the most used compositions for anodic and cathodic electrodes, respectively [10]. The main problem of these systems relates to the high sensitivity of the KOH electrolyte to ambient CO_2 and the subsequent production of K_2CO_3. The resulting decrease in the amount of hydroxyl ions lowers the ionic conductivity, while the precipitation of K_2CO_3 produces the clogging of the pores of the anode gas diffusion layer and a reduction of the ion transfer through the diaphragm [10,13,14], both effects jeopardising the hydrogen yield production.

1.2.2.   <u>Proton exchange membrane water electrolysis (PEMWE)</u>

In the proton exchange membrane water electrolysis cells, proton conductor polymeric membranes (perfluorosulfonic acid membranes),

acting as a solid electrolyte are used to separate anode and cathode [11]. Cells run at low temperatures (25-80 $^{\circ}$C) [11] and use titanium bipolar plates that are compatible with the existing corrosive operation conditions [8].

PEMWE provides interesting advantages vs. AWE. For example, it renders high current densities, a fast response under intermittent electrical energy supply and a compact system design enabled by the absence of liquid electrolyte [15,16]. Besides, the gases cross-over problem through diaphragms in alkaline electrolysis is significantly reduced in PEMWE [9]. Also, this technology offers the possibility of using a high pressure H_2 stream in the cathode compartment, while operating at atmospheric pressure in the anode chamber [9–11]. However, its high cost is a clear drawback of this type of cells. Firstly, because it uses expensive noble metals such as Ir, Ru or Pt as catalyst for anode and cathode. A high cost is also a concern that affects the solid electrolyte membrane. For this purpose, Nafion™ proton exchange ionic membranes are commonly used. These membranes comply with the requirements of a great ionic H^+ conductivity and an extraordinary high chemical, thermal and mechanical stability [17], though at expenses of a high cost. Other related limitation is the high polarization voltage that has to be applied to the anode (~2.0 V) to achieve an efficient working regime [6,11].

1.2.3. Anion exchange membrane water electrolysis (AEMWE)

Anion exchange membrane water electrolysis is a relatively new technology that aims at combining the advantages of AWE and PEMWE, overcoming some of their limitations [18]. This technology has been scarcely investigated so far (the words "anion exchange membrane water

electrolysis" typed in Scopus render around 62 references (23/10/2021), with ~75 % of them published since 2019).

The AEMWE cells work in weak alkaline media, typically in low concentrations of KOH (usually below 10 %), or other alkaline solutions such as 1 % K_2CO_3 or even distilled water [19], thus under less corrosive environment than AWE. Weak alkaline operation conditions of the AEMWE cells are compatible with cheap electrode materials, mostly based on Ni and Co, similar catalysts than in traditional AWE. They also enable the use of membranes cheaper than those incorporated in PEMWE cells [8,19,20]. These anion exchange membranes (AEMs) are polymeric membranes that replace the traditional AWE diaphragm circumventing the gas cross-over between the anodic and cathodic chambers [11]. In addition, the use of distilled water or low concentrated alkaline solutions significantly reduces the problems associated with the K_2CO_3 formation, already mentioned as a crucial limitation by the traditional AWE cell configurations [10,19,21,22]. Other advantages associated with the AEMWE technology are the compact character of the cells and the low temperatures (25-80 $^{\circ}$C) of operation [23]. For all these reasons, AEMWE technology has emerged as a promising alternative complying with the conditions of a low cost of the integrated components and a straightforward operation.

The advantages mentioned above have led some authors to focus their attention on this technology in recent years.

1.3. Hybrid alcohol-water electrolysis

The oxygen evolution reaction (OER) at the anode of AEMWE is the bottleneck of the whole electrolysis process due to its high overpotential [24,25]. This leads to a high energy demand to produce hydrogen, handicapping its commercialization. To minimise this limitation, hybrid alcohol-water electrolysis has emerged in recent years, taking the advantages associated to the more favourable kinetics for the oxidation reaction of organic molecules [24]. There are several reactions as alcohol, urea, amine, or hydrazine oxidations, among others, adequate to replace the OER and decrease the energy required to produce hydrogen [26].

With the addition of organic molecules to the electrolyte solutions, the operation voltage required for the electrolysis process is reduced and valuable products in the anode, completely separated from the pure hydrogen stream produced at the cathode, are obtained [24]. The lack of oxygen production increases the security of water electrolysis system and allows to work without membrane.

Among alcohol oxidation reactions, ethanol electrolysis has been proposed as a promising method to produce hydrogen with lower power demands, since the organic molecule provides part of the energy required for electrolysis [27]. Ethanol is easy to produce [24], has low toxicity and high availability [28]. It can be produced by fermentation of biomass, without changes in the natural balance of carbon dioxide in the atmosphere [29]. A scheme of a hybrid ethanol-water electrolysis cell can be observed in **Figure 1.4**.

Conventionally, precious metals such as Pt or Pd are used as ethanol oxidation reaction (EOR) catalysts [30–32]. However, their high cost limits their use for practical applications. For this reason, some authors have

tested alternatives as Ni-based catalysts in alkaline medium for ethanol-water electrolysis obtaining a high reduction in the operation voltage compared to pure water electrolysis [24,28]. In addition, other organic molecules as benzyl alcohol [33] have also been tested in 1.0 M KOH solution using Mo-Ni alloy nanoparticles as catalyst obtaining a high reduction in the potential for hybrid water electrolysis compared to pure water electrolysis.
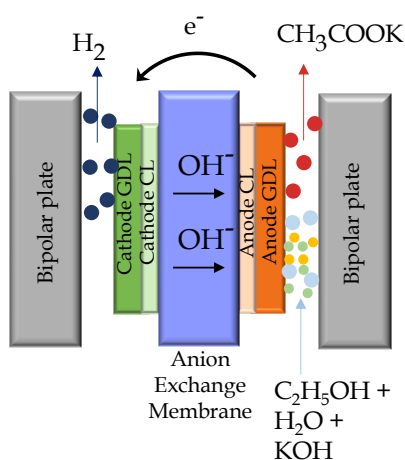
Figure 1.4. *Scheme of a typical hybrid ethanol-water AEM electrolyzer.*

1.4. Basis of anion exchange membrane water electrolysis cell and electrochemical reactions

A conventional single AEMWE cell consists of two bipolar flow field plates, two Teflon gaskets and the membrane electrode assembly (MEA). The bipolar plates should be corrosion resistant and have high electrical conductivity. Typical materials for the bipolar plates immersed in the alkaline environment cell are titanium [34,35], nickel [36,37] or graphite [38,39]; although nickel is particularly recommended [40]. A fluidic

circuit is engraved on the plates to guarantee an even liquid electrolyte flow through the electrodes. Besides their function to prevent gas and electrolyte leakage, the Teflon gaskets are used for electrical isolation between the two bipolar plates. The components of the MEA are described in detail below.

In the AEMWE, hydrogen and oxygen are produced from water using an external power supply. The overall process consists of two half-cell reactions, the hydrogen evolution reaction (HER) and the oxygen evolution reaction (OER), that take place at cathode and anode, respectively. They can be described as [10]:

HER (cathode): $4H_2O + 4e^- \rightarrow 2H_2 + 4OH^-$ $E_0 = -0.828$ V   (1.1)

OER (anode): $4OH^- \rightarrow O_2 + 2H_2O + 4e^-$ $E_0 = +0.401$ V   (1.2)

Overall reaction: $2H_2O \rightarrow 2H_2 + O_2$ $E_0 = +1.230$ V   (1.3)
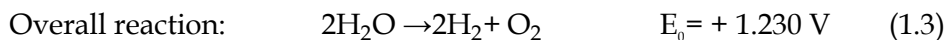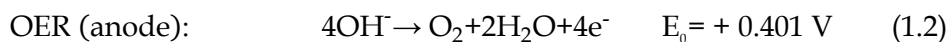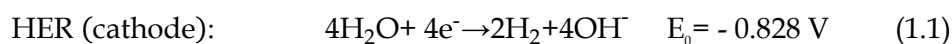
Water is fed to the cathodic compartment where it becomes reduced with electrons to produce hydrogen and OH⁻ ions (HER) (**Eq. (1.1)**). The OH⁻ ions pass through the membrane to the anode, where they become oxidized producing oxygen and water (OER) (**Eq. (1.2)**). The overall process is the splitting of water molecules into hydrogen and oxygen molecules as detailed in the overall reaction (**Eq. (1.3)**).

1.5. Membrane electrode assembly components

The membrane electrode assembly is the active element in the AEMWE. It is formed by an anion exchange membrane sandwiched between the anode and cathode electrodes. The electrodes mainly consist

of specific catalyst/ionomer coated electrically conductive macroporous gas diffusion layers.

1.5.1.   <u>Anion exchange membrane (AEM)</u>

The anion exchange membrane is a key component of the cell [10,41]. Its main function is the transport of hydroxyl ions from cathode to anode. It also acts as a barrier for the gases and other subproducts of the electrocatalytic reactions [11]. It consists of a polymer backbone functionalized with anion exchange groups, such as quaternary ammonium salts [42,43]. Its main requirements are a high ionic conductivity [22], a high mechanical and thermal stability, gas tightness [44,45] as well as stable long-lasting operation [11]. Besides, a low cost is an implicit condition to bear in mind for industrial applications.

Most commonly used commercial membranes in AEMWE are Fumasep® FAA-3, Sustainion® 37-50, Tokuyama A201, Aemion™, and Orion™1 membranes [44]. They are supplied in their bromide (Br⁻) or chloride (Cl⁻) forms, so they have to be pre-treated to replace these ions by hydroxide (OH⁻) groups before their incorporation in AEMWE cells. This is generally achieved by immersion in NaOH or KOH solutions for, at least, 24-48 h [46–49].

1.5.2.   <u>Gas diffusion layer (GDL)</u>

The AEMWE electrodes mainly consist of an active catalyst phase deposited or distributed on a macroporous support or gas diffusion layer. The catalyst can be coated onto the substrate (Catalyst-coated substrate,

CCS) or directly onto the membrane (Catalyst-coated membrane, CCM). The role of the GDL, besides supporting the catalyst phase in CCS is to allow electronic conductivity between catalysts sites and the bipolar plates, to polarise the catalyst loads to activate the OER and HER reactions, and to provide a removal path for the gaseous products [11] of the hydrogen and oxygen evolution reactions.

GDL supports made of carbon papers or cloths [38,50,51], Ti papers [49,52], stainless steel (SS) felt [45,53,54] or Ni foam [55,56] have been used for the anode. Ni or Ti metals show a high thermodynamic stability when acting as anodic GDL in alkaline medium. SS substrates generally passivize at anodic potentials in an alkaline environment, thus ensuring their stability [11]. On the other hand, long-term use of carbon paper anodic GDL may have some limitations due stability problems associated with that OH^- ions are excellent nucleophilic intermediates and accelerate the carbon degradation [57]. On the cathode side, carbon paper [51,56,58], Ni [59,60], or SS [55] foams are often used as GDL supports.

1.5.3. Catalyst materials

Currently, the most widely catalysts used for AEMWE are transition metals such as Co, Ni or Fe. This choice is supported by their electrochemical stability, low cost and easy accessibility [61,62]. In particular, non-PGM (non-platinum group metal) commercial catalysts Acta 3030 ($CuCoO_x$) and Acta 4030 ($Ni/CeO_2-La_2O_3/C$), for OER and HER, respectively, are extensively used [10]. Their incorporation in the cells releases the most common limitation of PEM electrolyzers, i.e., the high cost of the Pt or IrO_2 based catalysts [6]. Many authors are currently developing suitable electrodes for AEMWE; however, these have been

rarely scaled-up to complete cells. Below it is made a survey of the AEMWE catalysts most recently reported in the literature.

OER catalysts

Due to the limiting characteristics of the OER in water electrolysers, most studies related to AEMWE catalysts focus on the optimization of the anodic catalyst. Among the most promising non-noble catalysts, Ni and Ni-alloys, Co mixed oxides or graphene have demonstrated a high stability and activity towards this reaction [10]. Thus, in recent studies it has been demonstrated that the addition of Fe to Ni catalysts decreases the overpotential and increases the overall reaction performance [63]. The incorporation of Cu in the Co_3O_4 spinel structure has demonstrated the same effect, decreasing the onset potential of the OER [64]. Similar results have also been reported for other Co based catalyst incorporating Li, Ni or Cu [65].

HER catalysts

Today, $CuCoO_x$, nickel, Ni-alloys and graphene are extensively used as HER catalysts [10]. Some authors [66] have investigated the HER activity improvement of nickel after adding a serie of transition metals such as Fe, Cr and Ti. Several works have also addressed the need of reducing the cost of the whole electrolyzer, following the effect of the amount of catalyst at the cathode while varying other process variables in order to increase the system performance.

1.5.4. Ionomers

Traditional preparation methods of AEMWE electrodes using catalytic inks often involve the addition of polymeric organic ionomer binder

molecules to increase the cell performance [23,51]. The ionomer function is to increase the number of ion transport pathways between the catalyst layer and the anion exchange membrane. It is done thanks to its charged functional groups, that facilitate the exchange of water and OH^- anions at the catalyst surface [19,51]. However, ionomers can be also disadvantageous if, through electrostatic/covalent interactions, their charged groups occupy some catalytic active sites, leading to an increase in the HER and OER potentials [51]. Ionomers may also undergo aging chemical degradation, resulting in a deterioration of the effective catalyst-ionomer interface with operation time and, therefore, the decrease of electrochemically active surface area of the electrode [67].

Most MEA preparation methods use ionomers either applied directly on the GDL or AEM surfaces or incorporated to the catalytic inks used to prepare the electrodes [19,23,51,68].

For AEMWE cells, there is no standard ionomer as in the case of Nafion® for PEMWE [69–72]. Polysulfone (PSF) is very popular because it presents high thermal and chemical stability and low cost [73,74]. Other traditional ionomers are quaternary ammonia polysulfone (XQAPS) [75], Fumion FAA-3, from FumaTech company [49], Aemion™ supplied by Ionomr Innovations Inc. [76], I_2 from Acta Spa [19] or AS-4 from Tokuyama Corporation [74]. The proportion between ionomer and catalyst load at the electrodes is often optimized to obtain the best electrocatalytic performance of the electrolyzer (often an optimized proportion around 20 % ionomer/catalyst ratio is obtained) [19,23,77].

1.6.   Preparation methods for catalyst coated gas diffusion layer for anion exchange membrane cells

Among other requirements, electrode catalysts should present high electrochemical activity and stability, be cheap and have a secure supply.

From an electrode manufacturing point of view, critical points to consider include a precise control over catalyst microstructure, composition, and chemical state as well as its integration within the conducting GDL substrates. For industrial exploitation, to reduce the cost related to the catalyst load in the electrodes, it should be gifted of high specific activity towards the key reactions. Therefore, it is not only required to make a good choice of catalysts composition, but also to optimize the integration of the catalyst within the electrode, the MEA and the complete cell.

This makes important not only to choose the best formulation of the material catalyst for the specific anode and cathode reaction, or to use the most appropriate ionomer type and load, but also to select the best processing procedure for the integration of the catalyst material within the cell.

Most common methods to fabricate catalysts for low temperature water electrolyzers consist of traditional wet routes: co-precipitation, hydrothermal methods, or sol-gel. Common steps involve the preparation of the precursor solutions, the precipitation process itself, washings, filtrations, dryings or calcinations. In addition, in some cases, it is required a preliminary milling step to produce an initial fine catalyst powder.

After a catalyst powder has been obtained, a catalyst ink/slurry is prepared that, in a subsequent step, is sprayed or painted onto the GDL support [20,78]. Drawbacks of these wet routes are the use of solvents, the release of unwanted wastes potentially dangerous for the environment [79], and the large number of processing steps that make difficult to scale up the procedure and limit the reproducibility of the catalyst reactivity.

In the last years, alternative catalyst coated GDL electrode fabrication methods have been used to solve the aforementioned problems associated to the traditional wet fabrication routes. These include electrodeposition processes and other dry methods of film deposition such as chemical vapor deposition (CVD), atomic layer deposition (ALD), ion beam sputtering deposition (IBSD), or magnetron sputtering (MS) deposition.

1.6.1. <u>Traditional wet routes</u>

Co-precipitation method

One of the most widely used methods to fabricate catalysts for AEMWE is the co-precipitation technique. By this method, salts are dissolved and mixed to induce the nucleation and growth of a solid precursor incorporating the active metal phase. After precipitation, some washing steps are applied to remove residual components that may cause particle sintering and undesired agglomerations. Then, after filtering and drying, a powder is obtained. This powder is often annealed or calcined to get the desired crystalline catalyst phase and eventually grinded. Following this procedure large amount of small catalyst particles can be prepared [80]. The final catalyst powder is used to prepare a catalyst

slurry or ink that is deposited onto the macroporous gas diffusion layer supports, usually by ink spraying or ink painting.

Hydrothermal method

Hydrothermal method is another useful technique to obtain nanostructured catalysts. Crystal growth is carried out in an equipment consisting of a steel pressure vessel acting as autoclave [81]. This technique involves the use of a solvent and various precursors and provides an efficient way to control the size and structure of the synthetized nanoparticles [82]. Main advantage of this method is that direct crystallization of catalyst particles is achieved at low temperatures.

Sol-gel method

Due to its versatility, sol-gel methods are widely used to prepare catalysts with different compositions, homogeneity and structure [83]. Sol-gel catalysts are formed through kinetically controlled reactions starting from molecular precursors of the components integrated in the final materials catalyst [84].

1.6.2.   Thin film deposition routes

Electrodeposition method

Electrodeposition is other widely used fabrication technique of catalysts for water electrolysis. It is an electrochemical technique that combines electric charge induced diffusion and chemical transformation by redox reactions at the anode and cathode [85]. The deposition of the catalyst on the desired substrate (in this case, on a suitable GDL) is carried out applying a direct current to the electrodes immersed in an electrolyte

solution. This electrolyte solution contains cations of the metal that, under the applied electrical field, move to the electrode and are deposited in metal form [86]. By this technique the metal catalyst becomes deposited only at conductive sites of the electrode support [87]. Adjusting process parameters (composition of the electrolyte, applied voltage, geometrical aspects within the electrodeposition cell, temperature, etc.), this procedure renders films with different nanostructures and compositions. It also has the capacity to fabricate one-dimensional nanostructures such as nanorods, nanowires, nanotubes, nanosheets, flower-like nanostructures, etc [85]. Electrodeposition is a fast and low-cost process [88] that combined with other synthesis procedures has been applied to prepare highly performance and outstanding catalysts [89–91].

Chemical vapor deposition (CVD)

CVD is a dry method where a catalyst thin film becomes deposited on the substrate by its exposure to one or more volatile precursors [92]. In CVD, a thermally induced chemical reaction takes place between a mixture of precursor gases on the surface of the substrate material. The chemical decomposition and/or reaction of specific gaseous precursors gives rise to a solid coating layer [93]. CVD is a very versatile deposition technique that allows synthesis of monocrystalline, polycrystalline and amorphous phases [93].

CVD presents some disadvantages as the requirement of an additional step for the fabrication of the catalyst coated GDL or the fact that it does not permit an easy control over the film stoichiometry. In addition, CVD generally requires high temperatures at which some nanostructures may be unstable [92,94–96]. It is also noteworthy that the fabrication of some transition metals containing coatings via CVD may involve the use of

precursors whose decomposition generates toxic or hazardous substances [79].

Atomic layer deposition (ALD)

ALD is a variant of the CVD where gas precursors are introduced in a reaction chamber to form a thin film through chemical surface reactions. In ALD, the precursors are sequentially pulsed into a deposition chamber to avoid reactions in the gas phase. The successive self-terminated surface reactions of the reagents cause the growth of the desired material composition with an excellent conformity and uniformity of film thickness [97].

As disadvantages, ALD method produces homogenous and compact layers [98,99] where the availability of active sites at the surface, a requirement for an optimum electrochemical performance for water electrolysis, is small due to the lack of porosity. For practical applications though, a question to bear in mind is that the ALD method is strongly dependent on the design of the deposition reactor [97], thus adding issues regarding reproducibility and scalability.

Ion beam sputtering deposition (IBSD)

IBSD is a thin film deposition technique that utilizes an external ion source to cover the substrates with the material sputtered from selected targets. This technique has only been used in a few AEMWE studies probably because it gives rise to dense coatings that are less suitable for their use as electrodes for water electrolysis [100].

1.6.3. Magnetron sputtering (MS) deposition

Magnetron sputtering is a physical vapour deposition technology involving a low-pressure plasma (typically in the range 10^{-3} to 10^{-2} mbar), which is generated and confined to a space containing the target material to be deposited. The surface of the target is eroded by high-energy ion bombardment (typically argon ions) within the plasma, and the liberated atoms travel through the vacuum environment and deposit onto a nearby substrate to form a thin film.

This technique operates at room temperature, is highly reproducible and can be easily scaled-up for large area manufacturing at industrial level [101,102]. MS is an easy-to-use, safe technique, and due to its dry character, it does not generate wastes potentially detrimental for the environment [79,103]. In addition, MS provides a strict control of composition and load of the deposits.

Using this one-step preparation technique, it is possible to prepare a large variety of chemical compounds. The simplest configuration of the magnetron sputtering technique corresponds to the deposition of simple metal films. For this, an inert and easily ionizable gas is used in the plasma discharge, usually Ar [104,105] (see **Figure 1.5 a)**). This configuration can be also used to deposit metal alloys from a single-target with the desired composition [106]. In addition, it is possible to deposit alloys by co-sputtering using more than one target [107] (see **Figure 1.5 b)**).

Furthermore, an interesting option offered by MS is working with process mixtures of reactive gases, the reactive magnetron sputtering configuration. In this way, thin films of materials of a variable stoichiometry may be deposited, composed of atoms of the target (usually

a metal) and the reactive gas. One of the classic applications of the reactive magnetron sputtering technique is to obtain thin films of oxides [39] or nitrides [108] from metal targets and Ar/O_2 or Ar/N_2 mixtures, respectively.
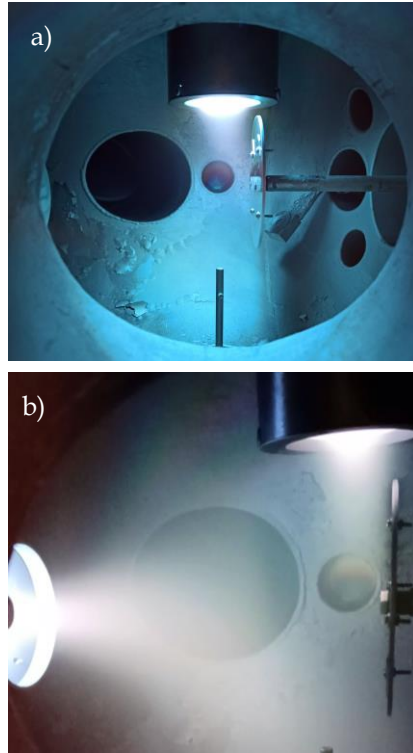
Figure 1.5. *Magnetron Sputtering technique: a) using one target, b) as co-sputtering using two targets.*

Furthermore, magnetron sputtering technique allows the control over the microstructure of the deposited materials varying the process pressure and the deposition geometry, i.e., the angle of the particle flux with respect to the surface normal of the substrate. This later configuration is known as magnetron sputtering at oblique angle deposition (MS-OAD) [101] (see **Figure 1.6**).

It is well known that MS-OAD technique induces the growth of mesoporous films mainly consisting of nanocolumns separated by large voids when deposition on flat substrates (mean roughness in the range of few nm or below) [102,109]. This nanocolumnar microstructure stems from the shadowing effects taking place during the deposition process [110–112].
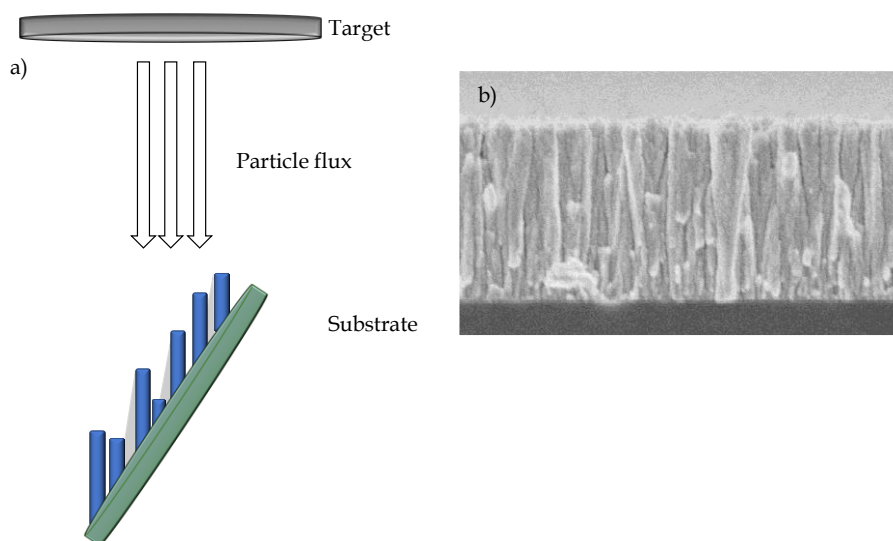
Figure 1.6. a) Scheme of magnetron sputtering technique in an oblique angle deposition configuration, b) Ni-Fe thin film prepared by MS-OAD.

MS is a one-step method, that could greatly simplify the manufacture of catalyst electrodes [114,115]. Using MS-OAD, the obtained catalyst coated GDL electrodes are gifted of high specific electrocatalytic activity for water electrolysis. In addition, it has been demonstrated the high reproducibility and stability of the electrodes fabricated by this technique [50,58]. Other advantages are the good adhesion of films to the substrates,

a high deposition rate that permits a short manufacturing time for the electrodes or the possibility to sputter any metal, alloy or other components varying the gas plasma composition [116]. An additional advantage in terms of costs is the possibility to fabricate catalyst electrodes at room temperature, decreasing the fabrication cost [50].

Despite of the great advantages offered by MS-OAD technique, to the best of our knowledge, it was never used before this thesis work to the manufacture catalyst electrodes for AEMWE cells. Thus, MS-OAD has been used through this doctoral thesis to grow catalyst electrodes, made of various metals and oxides under different preparation conditions, in order to demonstrate its feasibility for the manufacture of high-performance electrodes for water electrolyzer cells.

Finally, **Figure 1.7** shows a summary of advantages of various catalyst deposition processes intended for its implementation in AEMWE cells.

Co-Precipitation	Hydrothermal
✔ Small particles formed ✔ Simple catalyst preparation ✔ Energy efficient ✔ Does not involve use of organic solvent	✔ Low temperature ✔ Size control ✔ Structure control ✔ Low-cost synthesis

Sol-Gel	Electrodeposition
✔ Composition control ✔ Homogeneity ✔ Structure control ✔ Low-cost synthesis	✔ Composition control ✔ Structure control ✔ Low-cost and fast-response time ✔ Low amount of catalyst

CVD	ALD
✔ Composition control ✔ Structure control ✔ Good reproducibility ✔ Good adhesion	✔ Conformity and uniformity of films ✔ Low amount of catalyst ✔ Simple catalyst preparation ✔ Higher flexibility

IBSD	MS
✔ Composition control ✔ Low amount of catalyst ✔ Highly scalable ✔ Simple catalyst preparation	✔ Composition, structure and chemical state control ✔ One-step and high deposition rates ✔ Low amount of catalyst and high porosity ✔ Highly reproducible and scalable

Figure 1.7. *Summary of the main advantages of the catalyst deposition processes regarding their implementation in AEMWE.*

1.7. Current status of anion exchange membrane water electrolysis cell performance results

Finally, to compare the AEMWE performance using different catalyst formulations and preparation methods, **Table 1.1** gathers a series of examples from literature and those reported in this doctoral thesis work. The table includes data such as the components of the MEA, the catalyst fabrication procedure, the operating conditions, and the current density obtained at a particular voltage. In addition, due to the importance to decrease the catalyst cost, this table also includes an assessment of the anodic specific activity. It is remarkable that although the absolute activity achieved with catalyst electrodes reported in this doctoral thesis

is lower than that reported by other authors with similar catalyst composition, the catalyst electrodes reported here are the most efficient in terms of specific activity. For example, specific activities well above 100 mA mg^{-1} [39,58] were obtained for cobalt-cupper mixed oxides anodic catalysts reported in Chapters 4 and 5, values that outperform those of cells reported by other authors operated under similar conditions with catalysts of the same composition but prepared by other methods [19,49,117,118]. This is also clearly evidenced with Ni-Fe electrodes reported in Chapter 7 with the specific activity significantly higher than that reported for other Ni-based electrodes (maximum current per catalyst load of 1086 mA mg^{-1} in the former and 322 mA mg^{-1} [119] in the latter case, under similar operation conditions). Note that the specific activity achieved by the Ni-Fe catalyst anodes reported in Chapter 7, is even superior to that reported by iridium electrodes (438 mA mg^{-1} [120]). Emphasize that these results are achieved with nickel catalyst cathodes (also prepared by MS-OAD) while Pt is usually used in other works.

Table 1.1. *A review of some of the most relevant studies of AEMWE. Performance obtained under 1.0 M KOH at 2.0 V.*

Anode	Cathode	Membrane	Fabrication method	Catalyst load (mg cm^{-2}) Anode	Catalyst load (mg cm^{-2}) Cathode	Current density (mA cm^{-2})	Specific activity* (mA mg^{-1})	T (°C)	Ref.
NiCoO$_x$Fe	Pt	FAA-3	Hydrothermal	3	3	370	123	50	[49]
Co$_3$O$_4$	Pt	FAA-3	Hydrothermal	3	3	220	73	50	[49]
IrO$_x$	Pt	FAA-3	Hydrothermal	3	3	150	50	50	[49]
Ni$_{90}$Fe$_{10}$/CeO$_2$	Pt	FAA-3PE-30	Chemical Reduction	6	1	1930	322	50	[119]
NiCo$_2$O$_4$	NiFe$_2$O$_4$	Self-preparation	Co-precipitation	2.5	2.5	165	66	45	[121]
NiMn$_2$O$_4$	Pt	FAA-3-50	Oxalate	3	0.5	380	127	50	[68]
IrO$_2$	Pt	FAA-3-50	Commercial catalyst	4	0.4	1750	438	70	[23]
Cu$_{0.72}$Co$_{2.28}$O$_4$	Pt	Fumasep-30	Co-precipitation	10	1	1000	100	35	[117]
CuCoO$_x$	Ni/(CeO$_2$-La$_2$O$_3$)/C	A-201	Commercial catalyst	30	7.4	650	22	60	[19]
CuCo$_2$O$_4$	Pt	X-37-50 Grade T	Hydrothermal	23	1	1400	61	45	[118]
IrO$_2$	Cu-Co-P	Sustainion 37	Electrodeposition	3.13	-	1400	447	50	[120]
Fe$_2$P$_2$S$_6$	Fe$_2$P$_2$S$_6$	YAB	Hydrothermal + CVD	2	2	580	290	50	[122]
Ni	Ni	FAA-3-50	MS	0.78	0.38	42	54	40	**[50]
Ni	Ni	FAA-3-50	MS	0.38	0.17	31	82	40	**[50]
Cu$_x$Co$_y$O$_z$	Ni	FAA-3-50	MS	0.18	0.76	46	256	40	**[39]
Cu$_x$Co$_y$O$_z$	Ni	FAA-3-50	MS	0.4	0.38	60	150	40	**[58]
Ni-Fe	Ni	FAA-3-50	MS	0.35	0.38	380	1086	40	**

*per amount of anodic catalyst.

**This doctoral thesis.

1.8. References

[1] P.E. Dodds, I. Staffell, A.D. Hawkes, F. Li, P. Grünewald, W. McDowall, P. Ekins, Hydrogen and fuel cell technologies for heating: A review, Int. J. Hydrogen Energy. 40 (2015) 2065–2083. /https://doi.org/10.1016/j.ijhydene.2014.11.059.

[2] S. Singh, S. Jain, V. PS, A.K. Tiwari, M.R. Nouni, J.K. Pandey, S. Goel, Hydrogen: A sustainable fuel for future of the transport sector, Renew. Sustain. Energy Rev. 51 (2015) 623–633. https://doi.org/10.1016/j.rser.2015.06.040.

[3] J.M. Thomas, P.P. Edwards, P.J. Dobson, G.P. Owen, Decarbonising energy: The developing international activity in hydrogen technologies and fuel cells, J. Energy Chem. 51 (2020) 405–415. https://doi.org/10.1016/j.jechem.2020.03.087.

[4] A. Bassani, D. Previtali, C. Pirola, G. Bozzano, S. Colombo, F. Manenti, Mitigating carbon dioxide impact of industrial steam methane reformers by acid gas to syngas technology: Technical and environmental feasibility, J. Sustain. Dev. Energy, Water Environ. Syst. 8 (2020) 71–87. https://doi.org/10.13044/j.sdewes.d7.0258.

[5] R. Soltani, M.A. Rosen, I. Dincer, Assessment of CO_2 capture options from various points in steam methane reforming for hydrogen production, Int. J. Hydrogen Energy. 39 (2014) 20266–20275. https://doi.org/10.1016/j.ijhydene.2014.09.161.

[6] S. Shiva Kumar, V. Himabindu, Hydrogen production by PEM water electrolysis – A review, Mater. Sci. Energy Technol. 2 (2019) 442–454. https://doi.org/10.1016/j.mset.2019.03.002.

[7] J.P. Hughes, J. Clipsham, H. Chavushoglu, S.J. Rowley-Neale, C.E. Banks, Polymer electrolyte electrolysis: A review of the activity and stability of non-precious metal hydrogen evolution reaction and oxygen evolution reaction catalysts, Renew. Sustain. Energy Rev. 139 (2021) 110709. https://doi.org/10.1016/j.rser.2021.110709.

[8] B. Motealleh, Z. Liu, R.I. Masel, J.P. Sculley, Z. Richard Ni, L. Meroueh, Next-generation anion exchange membrane water electrolyzers operating for commercially relevant lifetimes, Int. J. Hydrogen Energy. 46 (2021) 3379–3386. https://doi.org/10.1016/j.ijhydene.2020.10.244.

[9] J. Chi, H. Yu, Water electrolysis based on renewable energy for hydrogen

production, Chinese J. Catal. 39 (2018) 390–394. https://doi.org/10.1016/S1872-2067(17)62949-8.

[10] I. Vincent, D. Bessarabov, Low cost hydrogen production by anion exchange membrane electrolysis: A review, Renew. Sustain. Energy Rev. 81 (2018) 1690–1704. https://doi.org/10.1016/j.rser.2017.05.258.

[11] H.A. Miller, K. Bouzek, J. Hnat, S. Loos, C.I. Bernäcker, T. Weißgärber, L. Röntzsch, J. Meier-Haack, Green hydrogen from anion exchange membrane water electrolysis: A review of recent developments in critical materials and operating conditions, Sustain. Energy Fuels. 4 (2020) 2114–2133. https://doi.org/10.1039/c9se01240k.

[12] M.K. Cho, A. Lim, S.Y. Lee, H.-J. Kim, S.J. Yoo, Y.-E. Sung, H.S. Park, J.H. Jang, A review on membranes and catalysts for anion exchange membrane water electrolysis single cells, J. Electrochem. Sci. Technol. 8 (2017) 183–196. https://doi.org/10.5229/JECST.2017.8.3.183.

[13] E. Gülzow, M. Schulze, Long-term operation of AFC electrodes with CO2 containing gases, J. Power Sources. 127 (2004) 243–251. https://doi.org/10.1016/j.jpowsour.2003.09.020.

[14] D. Li, E.J. Park, W. Zhu, Q. Shi, Y. Zhou, H. Tian, Y. Lin, A. Serov, B. Zulevi, E.D. Baca, C. Fujimoto, H.T. Chung, Y.S. Kim, Highly quaternized polystyrene ionomers for high performance anion exchange membrane water electrolysers, Nat. Energy. 5 (2020) 378–385. https://doi.org/10.1038/s41560-020-0577-x.

[15] A. Rodríguez-Gómez, F. Dorado, A. de Lucas-Consuegra, A.R. de la Osa, Influence of the GDL and assembly mode of a PEM cell on the ethanol revalorization into chemicals, Chem. Eng. J. 402 (2020) 125298. https://doi.org/10.1016/j.cej.2020.125298.

[16] D.M.F. Santos, C.A.C. Sequeira, J.L. Figueiredo, Hydrogen production by alkaline water electrolysis, Quim. Nova. 36 (2013) 1176–1193. https://doi.org/10.1590/S0100-40422013000800017.

[17] H. Ito, T. Maeda, A. Nakano, H. Takenaka, Properties of Nafion membranes under PEM water electrolysis conditions, Int. J. Hydrogen Energy. 36 (2011) 10527–10540. https://doi.org/10.1016/j.ijhydene.2011.05.127.

[18] M. David, C. Ocampo-Martínez, R. Sánchez-Peña, Advances in alkaline water electrolyzers: A review, J. Energy Storage. 23 (2019) 392–403.

https://doi.org/10.1016/j.est.2019.03.001.

[19] I. Vincent, A. Kruger, D. Bessarabov, Development of efficient membrane electrode assembly for low cost hydrogen production by anion exchange membrane electrolysis, Int. J. Hydrogen Energy. 42 (2017) 10752–10761. https://doi.org/10.1016/j.ijhydene.2017.03.069.

[20] A.Y. Faid, A.O. Barnett, F. Seland, S. Sunde, NiCu mixed metal oxide catalyst for alkaline hydrogen evolution in anion exchange membrane water electrolysis, Electrochim. Acta. 371 (2021) 137837. https://doi.org/10.1016/j.electacta.2021.137837.

[21] J. Parrondo, C.G. Arges, M. Niedzwiecki, E.B. Anderson, K.E. Ayers, V. Ramani, Degradation of anion exchange membranes used for hydrogen production by ultrapure water electrolysis, RSC Adv. 4 (2014) 9875–9879. https://doi.org/10.1039/C3RA46630B.

[22] K. Ayers, N. Danilovic, R. Ouimet, M. Carmo, B. Pivovar, M. Bornstein, Perspectives on low-temperature electrolysis and potential for renewable hydrogen at scale, Annu. Rev. Chem. Biomol. Eng. 10 (2019) 219–239. https://doi.org/10.1146/annurev-chembioeng-060718-030241.

[23] J.E. Park, S.Y. Kang, S.-H. Oh, J.K. Kim, M.S. Lim, C.-Y. Ahn, Y.-H. Cho, Y.-E. Sung, High-performance anion-exchange membrane water electrolysis, Electrochim. Acta. 295 (2019) 99–106. https://doi.org/10.1016/j.electacta.2018.10.143.

[24] S. Sheng, Y. Song, L. Sha, K. Ye, K. Zhu, Y. Gao, J. Yan, G. Wang, D. Cao, Simultaneous hydrogen evolution and ethanol oxidation in alkaline medium via a self-supported bifunctional electrocatalyst of Ni-Fe phosphide/Ni foam, Appl. Surf. Sci. 561 (2021) 150080. https://doi.org/10.1016/j.apsusc.2021.150080.

[25] W. Zhu, T. Zhang, Y. Zhang, Z. Yue, Y. Li, R. Wang, Y. Ji, X. Sun, J. Wang, A practical-oriented NiFe-based water-oxidation catalyst enabled by ambient redox and hydrolysis Co-precipitation strategy, Appl. Catal. B Environ. 244 (2018). https://doi.org/10.1016/j.apcatb.2018.12.021.

[26] L. Du, Y. Sun, B. You, Hybrid water electrolysis: Replacing oxygen evolution reaction for energy-efficient hydrogen production and beyond, Mater. Reports Energy. 1 (2021) 100004. https://doi.org/10.1016/j.matre.2020.12.001.

[27] A. Caravaca, F.M. Sapountzi, A. de Lucas-Consuegra, C. Molina-Mora, F.

Dorado, J.L. Valverde, Electrochemical reforming of ethanol–water solutions for pure H_2 production in a PEM electrolysis cell, Int. J. Hydrogen Energy. 37 (2012) 9504–9513. https://doi.org/10.1016/j.ijhydene.2012.03.062.

[28]   W. Wang, Y.-B. Zhu, Q. Wen, Y. Wang, J. Xia, C. Li, M.-W. Chen, Y. Liu, H. Li, H.-A. Wu, T. Zhai, Modulation of molecular spatial distribution and chemisorption with perforated nanosheets for ethanol electro-oxidation, Adv. Mater. 31 (2019) 1900528. https://doi.org/10.1002/adma.201900528.

[29]   J. Zhan, M. Cai, C. Zhang, C. Wang, Synthesis of mesoporous $NiCo_2O_4$ fibers and their electrocatalytic activity on direct oxidation of ethanol in alkaline media, Electrochim. Acta. 154 (2015) 70–76. https://doi.org/10.1016/j.electacta.2014.12.078.

[30]   G. Yang, Q. Zhang, H. Yu, F. Peng, Platinum-based ternary catalysts for the electrooxidation of ethanol, Particuology. 58 (2021) 169–186. https://doi.org/10.1016/j.partic.2021.01.007.

[31]   R. Rizo, S. Pérez-Rodríguez, G. García, Well-defined platinum surfaces for the ethanol oxidation reaction, ChemElectroChem. 6 (2019) 4725–4738. https://doi.org/10.1002/celc.201900600.

[32]   Z.X. Liang, T.S. Zhao, J.B. Xu, L.D. Zhu, Mechanism study of the ethanol oxidation reaction on palladium in alkaline media, Electrochim. Acta. 54 (2009) 2203–2208. https://doi.org/10.1016/j.electacta.2008.10.034.

[33]   X. Cui, M. Chen, R. Xiong, J. Sun, X. Liu, B. Geng, Ultrastable and efficient H2 production via membrane-free hybrid water electrolysis over a bifunctional catalyst of hierarchical Mo–Ni alloy nanoparticles, J. Mater. Chem. A. 7 (2019) 16501–16507. https://doi.org/10.1039/C9TA03924D.

[34]   H. Ito, N. Kawaguchi, S. Someya, T. Munakata, N. Miyazaki, M. Ishida, A. Nakano, Experimental investigation of electrolytic solution for anion exchange membrane water electrolysis, Int. J. Hydrogen Energy. 43 (2018) 17030–17039. https://doi.org/10.1016/j.ijhydene.2018.07.143.

[35]   A. Lim, H. Kim, D. Henkensmeier, S. [Jong Yoo], J. [Young Kim], S. [Young Lee], Y.-E. Sung, J.H. Jang, H.S. Park, A study on electrode fabrication and operation variables affecting the performance of anion exchange membrane water electrolysis, J. Ind. Eng. Chem. 76 (2019) 410–418. https://doi.org/10.1016/j.jiec.2019.04.007.

[36]   J. Hnát, R. Kodým, K. Denk, M. Paidar, J. Žitka, K. Bouzek, Design of a zero-gap laboratory-scale polymer electrolyte membrane alkaline water electrolysis stack, Chemie Ing. Tech. 91 (2019) 821–832. https://doi.org/10.1002/cite.201800185.

[37]   N. V Kuleshov, V.N. Kuleshov, S.A. Dovbysh, S.A. Grigoriev, S. V Kurochkin, P. Millet, Development and performances of a 0.5 kW high-pressure alkaline water electrolyser, Int. J. Hydrogen Energy. 44 (2019) 29441–29449. https://doi.org/10.1016/j.ijhydene.2019.05.044.

[38]   S.H. Ahn, S.J. Yoo, H.-J. Kim, D. Henkensmeier, S.W. Nam, S.-K. Kim, J.H. Jang, Anion exchange membrane water electrolyzer with an ultra-low loading of Pt-decorated Ni electrocatalyst, Appl. Catal. B Environ. 180 (2016) 674–679. https://doi.org/10.1016/j.apcatb.2015.07.020.

[39]   E. López-Fernández, J. Gil-Rostra, J.P. Espinós, A.R. González-Elipe, F. Yubero, A. de Lucas-Consuegra, $Cu_xCo_{3-x}O_4$ ultra-thin film as efficient anodic catalysts for anion exchange membrane water electrolysers, J. Power Sources. 415 (2019) 136–144. https://doi.org/10.1016/j.jpowsour.2019.01.056.

[40]   R. Phillips, C. Dunnill, Zero gap alkaline electrolysis cell designs for renewable energy storage as hydrogen gas, RSC Adv. 6 (2016) 100643–100651. https://doi.org/10.1039/C6RA22242K.

[41]   G.A. Lindquist, Q. Xu, S.Z. Oener, S.W. Boettcher, Membrane electrolyzers for impure-water splitting, Joule. 4 (2020) 2549–2561. https://doi.org/10.1016/j.joule.2020.09.020.

[42]   T.H. Pham, J.S. Olsson, P. Jannasch, Poly(arylene alkylene)s with pendant N-spirocyclic quaternary ammonium cations for anion exchange membranes, J. Mater. Chem. A. 6 (2018) 16537–16547. https://doi.org/10.1039/C8TA04699A.

[43]   J.S. Olsson, T.H. Pham, P. Jannasch, Poly(arylene piperidinium) hydroxide ion exchange membranes: synthesis, alkaline stability, and conductivity, Adv. Funct. Mater. 28 (2018) 1702758. https://doi.org/10.1002/adfm.201702758.

[44]   D. Henkensmeier, M. Najibah, C. Harms, J. Žitka, J. Hnát, K. Bouzek, Overview: State-of-the art commercial membranes for anion exchange membrane water electrolysis, J. Electrochem. Energy Convers. Storage. 18 (2020). https://doi.org/10.1115/1.4047963.

[45]   Z. Liu, S.D. Sajjad, Y. Gao, H. Yang, J.J. Kaczur, R.I. Masel, The effect of
         membrane on an alkaline water electrolyzer, Int. J. Hydrogen Energy. 42
         (2017) 29661–29665. https://doi.org/10.1016/j.ijhydene.2017.10.050.

[46]   S.C. Price, X. Ren, A.M. Savage, F.L. Beyer, Synthesis and characterization
         of   anion-exchange   membranes   based   on   hydrogenated
         poly(norbornene),   Polym.   Chem.   8   (2017)   5708–5717.
         https://doi.org/10.1039/C7PY01084B.

[47]   V.M. Truong, N.B. Duong, H. Yang, Comparison of carbon supports in
         anion   exchange   membrane   fuel   cells,   Mater.   13   (2020).
         https://doi.org/10.3390/ma13235370.

[48]   F. Razmjooei, R. Reißner, A.S. Gago, A. Arisai, Highly active binder free
         plasma sprayed non-noble metal electrodes for anion exchange
         membrane electrolysis at different reduced KOH concentrations, ECS
         Trans. (2019) 689–702. https://doi.org/10.1149/09208.0689ecst.

[49]   D. Xu, M.B. Stevens, M.R. Cosby, S.Z. Oener, A.M. Smith, L.J. Enman, K.E.
         Ayers, C.B. Capuano, J.N. Renner, N. Danilovic, Y. Li, H. Wang, Q.
         Zhang, S.W. Boettcher, Earth-abundant oxygen electrocatalysts for
         alkaline anion-exchange-membrane water electrolysis: effects of catalyst
         conductivity and comparison with performance in three-electrode cells,
         ACS Catal. 9 (2019) 7–15. https://doi.org/10.1021/acscatal.8b04001.

[50]   E. López-Fernández, J. Gil-Rostra, J.P. Espinós, A.R. González-Elipe, A.
         de Lucas Consuegra, F. Yubero, Chemistry and electrocatalytic activity of
         nanostructured nickel electrodes for water electrolysis, ACS Catal. 10
         (2020) 6159–6170. https://doi.org/10.1021/acscatal.0c00856.

[51]   A.Y. Faid, L. Xie, A.O. Barnett, F. Seland, D. Kirk, S. Sunde, Effect of anion
         exchange ionomer content on electrode performance in AEM water
         electrolysis, Int. J. Hydrogen Energy. 45 (2020) 28272–28284.
         https://doi.org/10.1016/j.ijhydene.2020.07.202.

[52]   A. Marinkas, I. Struźyńska-Piron, Y. Lee, A. Lim, H.S. Park, J.H. Jang, H.-
         J. Kim, J. Kim, A. Maljusch, O. Conradi, D. Henkensmeier, Anion-
         conductive   membranes   based   on   2-mesityl-benzimidazolium
         functionalised poly(2,6-dimethyl-1,4-phenylene oxide) and their use in
         alkaline water electrolysis, Polymer (Guildf). 145 (2018) 242–251.
         https://doi.org/10.1016/j.polymer.2018.05.008.

[53]   Q. Xu, S.Z. Oener, G. Lindquist, H. Jiang, C. Li, S.W. Boettcher, Integrated
         reference electrodes in anion-exchange-membrane electrolyzers: impact

of stainless-steel gas-diffusion layers and internal mechanical pressure, ACS Energy Lett. 6 (2021) 305–312. https://doi.org/10.1021/acsenergylett.0c02338.

[54] Z. Liu, S. Sajjad, Y. Gao, J. Kaczur, R. I.Masel, An alkaline water electrolyzer with sustainion™ membranes: 1 A/cm² at 1.9V with base metal catalysts, ECS Trans. 77 (2017) 71–73. https://doi.org/10.1149/07709.0071ecst.

[55] L. Xiao, S. Zhang, J. Pan, C. Yang, M. He, L. Zhuang, J. Lu, First implementation of alkaline polymer electrolyte water electrolysis working only with pure water, Energy Environ. Sci. 5 (2012) 7869–7871. https://doi.org/10.1039/C2EE22146B.

[56] I. Vincent, Hydrogen production by water electrolysis with an ultrathin anion-exchange membrane (AEM), Int. J. Electrochem. Sci. 13 (2018) 11347–11358. https://doi.org/10.20964/2018.12.84.

[57] X. Wu, K. Scott, F. Xie, N. Alford, A reversible water electrolyser with porous PTFE based OH⁻ conductive membrane as energy storage cells, J. Power Sources. 246 (2014) 225–231. https://doi.org/10.1016/j.jpowsour.2013.07.081.

[58] E. López-Fernández, J. Gil-Rostra, C. Escudero, I.J. Villar-García, F. Yubero, A. de Lucas Consuegra, A.R. González-Elipe, Active sites and optimization of mixed copper-cobalt oxide anodes for anion exchange membrane water electrolysis, J. Power Sources. (2020). https://doi.org/10.1016/j.jpowsour.2020.229217.

[59] M. Bhavanari, K.-R. Lee, C.-J. Tseng, I.-H. Tang, H.-H. Chen, CuFe electrocatalyst for hydrogen evolution reaction in alkaline electrolysis, Int. J. Hydrogen Energy. (2021). https://doi.org/10.1016/j.ijhydene.2021.01.227.

[60] S. Seetharaman, R. Balaji, K. Ramya, K.S. Dhathathreyan, M. Velan, Graphene oxide modified non-noble metal electrode for alkaline anion exchange membrane water electrolyzers, Int. J. Hydrogen Energy. 38 (2013) 14934–14942. https://doi.org/10.1016/j.ijhydene.2013.09.033.

[61] R. Gao, D. Yan, Recent Development of Ni/Fe-based micro/nanostructures toward photo/electrochemical water oxidation, Adv. Energy Mater. 10 (2020) 1900954. https://doi.org/10.1002/aenm.201900954.

[62]   H. Li, L. Chen, P. Jin, H. Lv, H. Fu, C. Fan, S. Peng, G. Wang, J. Hou, F. Yu, Y. Shi, Synthesis of $Co_{2-x}Ni_xO_2$ (0 < x < 1.0) hexagonal nanostructures as efficient bifunctional electrocatalysts for overall water splitting, Dalt. Trans. 49 (2020) 6587–6595. https://doi.org/10.1039/D0DT00925C.

[63]   Y. Cheng, S.P. Jiang, Advances in electrocatalysts for oxygen evolution reaction of water electrolysis-from metal oxides to carbon nanotubes, Prog. Nat. Sci. Mater. Int. 25 (2015) 545–553. https://doi.org/10.1016/j.pnsc.2015.11.008.

[64]   X. Wu, K. Scott, $Cu_xCo_{3-x}O_4$ (0 ≤ x < 1) nanoparticles for oxygen evolution in high performance alkaline exchange membrane water electrolysers, J. Mater. Chem. 21 (2011) 12344–12351. https://doi.org/10.1039/c1jm11312g.

[65]   I. Nikolov, R. Darkaoui, E. Zhecheva, R. Stoyanova, N. Dimitrov, T. Vitanov, Electrocatalytic activity of spinel related cobaltites $M_xCo_{3-x}O_4$ (M = Li, Ni, Cu) in the oxygen evolution reaction, J. Electroanal. Chem. 429 (1997) 157–168. https://doi.org/10.1016/S0022-0728(96)05013-9.

[66]   J. Kim, H. Jung, S.-M. Jung, J. Hwang, D.Y. Kim, N. Lee, K.-S. Kim, H. Kwon, Y.-T. Kim, J.W. Han, J.K. Kim, Tailoring binding abilities by incorporating oxophilic rransition metals on 3D nanostructured Ni arrays for accelerated alkaline hydrogen evolution reaction, J. Am. Chem. Soc. 143 (2021) 1399–1408. https://doi.org/10.1021/jacs.0c10661.

[67]   B.G. Pollet, A.A. Franco, H. Su, H. Liang, S. Pasupathi, 1 - Proton exchange membrane fuel cells, Woodhead Publ. Ser. Energy, Woodhead Publishing, Oxford, (2016) 3–56. https://doi.org/10.1016/B978-1-78242-363-8.00001-3.

[68]   A. Carbone, S.C. Zignani, I. Gatto, S. Trocino, A.S. Aricò, Assessment of the FAA3-50 polymer electrolyte in combination with a $NiMn_2O_4$ anode catalyst for anion exchange membrane water electrolysis, Int. J. Hydrogen Energy. 45 (2020) 9285–9292. https://doi.org/10.1016/j.ijhydene.2020.01.150.

[69]   W. Xu, K. Scott, The effects of ionomer content on PEM water electrolyser membrane electrode assembly performance, Int. J. Hydrogen Energy. 35 (2010) 12029–12037. https://doi.org/10.1016/j.ijhydene.2010.08.055.

[70]   P. Holzapfel, M. Bühler, C. Van Pham, F. Hegge, T. Böhm, D. McLaughlin, M. Breitwieser, S. Thiele, Directly coated membrane electrode assemblies for proton exchange membrane water electrolysis, Electrochem.

Commun. 110 (2020) 106640. https://doi.org/10.1016/j.elecom.2019.106640.

[71] G.G. Gagliardi, A. Ibrahim, D. Borello, A. El-Kharouf, Composite polymers development and application for polymer electrolyte membrane technologies—a review, Mol. 25 (2020). https://doi.org/10.3390/molecules25071712.

[72] M. Yasutake, D. Kawachino, Z. Noda, J. Matsuda, S.M. Lyth, K. Ito, A. Hayashi, K. Sasaki, Catalyst-integrated gas diffusion electrodes for polymer electrolyte membrane water electrolysis: porous titanium sheets with nanostructured TiO_2 surfaces decorated with Ir electrocatalysts, J. Electrochem. Soc. 167 (2020) 124523. https://doi.org/10.1149/1945-7111/abb37d.

[73] L. Zeng, T. Zhao, High-performance alkaline ionomer for alkaline exchange membrane fuel cells, Electrochem. Commun. 34 (2013) 278–281. https://doi.org/10.1016/j.elecom.2013.07.015.

[74] N. Chen, Y.M. Lee, Anion exchange polyelectrolytes for membranes and ionomers, Prog. Polym. Sci. 113 (2021) 101345. https://doi.org/10.1016/j.progpolymsci.2020.101345.

[75] Q. Hu, G. Li, J. Pan, L. Tan, J. Lu, L. Zhuang, Alkaline polymer electrolyte fuel cell with Ni-based anode and Co-based cathode, Int. J. Hydrogen Energy. 38 (2013) 16264–16268. https://doi.org/10.1016/j.ijhydene.2013.09.125.

[76] P. Fortin, T. Khoza, X. Cao, S.Y. Martinsen, A. Oyarce Barnett, S. Holdcroft, High-performance alkaline water electrolysis using Aemion™ anion exchange membranes, J. Power Sources. 451 (2020) 227814. https://doi.org/10.1016/j.jpowsour.2020.227814.

[77] M. Carmo, G. Doubek, R.C. Sekol, M. Linardi, A.D. Taylor, Development and electrochemical studies of membrane electrode assemblies for polymer electrolyte alkaline fuel cells using FAA membrane and ionomer, J. Power Sources. 230 (2013) 169–175. https://doi.org/10.1016/j.jpowsour.2012.12.015.

[78] A.Y. Faid, A.O. Barnett, F. Seland, S. Sunde, Highly active nickel-based catalyst for hydrogen evolution in anion exchange membrane electrolysis, Catalysts. 8 (2018). https://doi.org/10.3390/catal8120614.

[79]   J. Liang, Q. Liu, T. Li, Y. Luo, S. Lu, X. Shi, F. Zhang, A.M. Asiri, X. Sun,
        Magnetron sputtering enabled sustainable synthesis of nanomaterials for
        energy electrocatalysis, Green Chem. 23 (2021) 2834–2867.
        https://doi.org/10.1039/D0GC03994B.

[80]   P. Munnik, P.E. de Jongh, K.P. de Jong, Recent developments in the
        synthesis of supported catalysts, Chem. Rev. 115 (2015) 6687–6718.
        https://doi.org/10.1021/cr500486u.

[81]   B.P. Kafle, Chapter 6 - Introduction to nanomaterials and application of
        UV–Visible spectroscopy for their characterization, in: B.P.B.T.-C.A. and
        M.C. by S. Kafle (Ed.), Elsevier, 2020: pp. 147–198.
        https://doi.org/10.1016/B978-0-12-814866-2.00006-3.

[82]   A. Das, A.K. Ganguli, Design of diverse nanostructures by hydrothermal
        and microemulsion routes for electrochemical water splitting, RSC Adv.
        8 (2018) 25065–25078. https://doi.org/10.1039/C8RA04133D.

[83]   M.A. Cauqui, J.M. Rodríguez-Izquierdo, Application of the sol-gel
        methods to catalyst preparation, J. Non. Cryst. Solids. 147–148 (1992) 724–
        738. https://doi.org/10.1016/S0022-3093(05)80707-0.

[84]   U. Schubert, Chemistry and fundamentals of the sol–gel process, Sol-Gel
        Handb. (2015) 1–28. https://doi.org/10.1002/9783527670819.ch01.

[85]   R. Li, Y. Li, P. Yang, D. Wang, H. Xu, B. Wang, F. Meng, J. Zhang, M. An,
        Electrodeposition: Synthesis of advanced transition metal-based catalyst
        for hydrogen production via electrolysis of water, J. Energy Chem. 57
        (2021) 547–566. https://doi.org/10.1016/j.jechem.2020.08.040.

[86]   N.U. Saidin, K.K. Ying, N.I. Khuan, Electrodeposition: principles,
        applications and methods, NTC 2011 Nucl. Tech. Conv. (2011), Malaysia,
        2011. http://inis.iaea.org/search/search.aspx?orig_q=RN:44122714.

[87]   R.P. Ramasamy, Fuel cells - proton exchange membrane fuel cells,
        membrane–electrode assemblies, Encyclopedia of Electrochemical Power
        Sources (2009) 787–805. https://doi.org/10.1016/B978-044452745-
        5.00227-6.

[88]   C. Li, M. Iqbal, J. Lin, X. Luo, B. Jiang, V. Malgras, K.C.-W. Wu, J. Kim, Y.
        Yamauchi, Electrochemical deposition: an advanced approach for
        templated synthesis of nanoporous metal architectures, Acc. Chem. Res.
        51 (2018) 1764–1773. https://doi.org/10.1021/acs.accounts.8b00119.

[89] R. Wu, B. Xiao, Q. Gao, Y.-R. Zheng, X.-S. Zheng, J.-F. Zhu, M.-R. Gao, S.-H. Yu, A janus nickel cobalt phosphide catalyst for high-efficiency neutral-pH water splitting, Angew. Chemie Int. Ed. 57 (2018) 15445–15449. https://doi.org/10.1002/anie.201808929.

[90] J.-Q. Chi, K.-L. Yan, Z. Xiao, B. Dong, X. Shang, W.-K. Gao, X. Li, Y.-M. Chai, C.-G. Liu, Trimetallic NiFeCo selenides nanoparticles supported on carbon fiber cloth as efficient electrocatalyst for oxygen evolution reaction, Int. J. Hydrogen Energy. 42 (2017) 20599–20607. https://doi.org/10.1016/j.ijhydene.2017.06.219.

[91] D. Wang, L. Yang, H. Liu, D. Cao, Polyaniline-coated Ru/Ni(OH)$_2$ nanosheets for hydrogen evolution reaction over a wide pH range, J. Catal. 375 (2019) 249–256. https://doi.org/10.1016/j.jcat.2019.06.008.

[92] P.M.B.T.-H. of D.T. for F. and C. (Third E. Martin, ed., Chapter 1 - deposition technologies: an overview, William Andrew Publishing, Boston, (2010) 1–31. https://doi.org/10.1016/B978-0-8155-2031-3.00001-6.

[93] A. Behera, P. Mallick, S.S. Mohapatra, Chapter 13 - Nanocoatings for anticorrosion: an introduction, Micro Nano Technol., Elsevier, (2020) 227–243. https://doi.org/10.1016/B978-0-12-819359-4.00013-1.

[94] A. Vahl, S. Veziroglu, B. Henkel, T. Strunskus, O. Polonskyi, O.C. Aktas, F. Faupel, Pathways to tailor photocatalytic performance of TiO$_2$ thin films deposited by reactive magnetron sputtering, Mater. 12 (2019). https://doi.org/10.3390/ma12172840.

[95] A. Baptista, F. Silva, J. Porteiro, J. Míguez, G. Pinto, Sputtering physical vapour deposition (PVD) coatings: a critical review on process improvement and market trend demands, Coatings. 8 (2018). https://doi.org/10.3390/coatings8110402.

[96] B. Verma, S.K. Mishra, Spectral and structural investigation of layered growth of copper and graphene deposited by sputtering and annealing, Appl. Phys. A. 125 (2019) 534. https://doi.org/10.1007/s00339-019-2837-9.

[97] M. Leskelä, J. Niinistö, M. Ritala, 4.05 - Atomic Layer Deposition, Comprehensive Materials Processing 4 (2014) 101–123. https://doi.org/10.1016/B978-0-08-096532-1.00401-5.
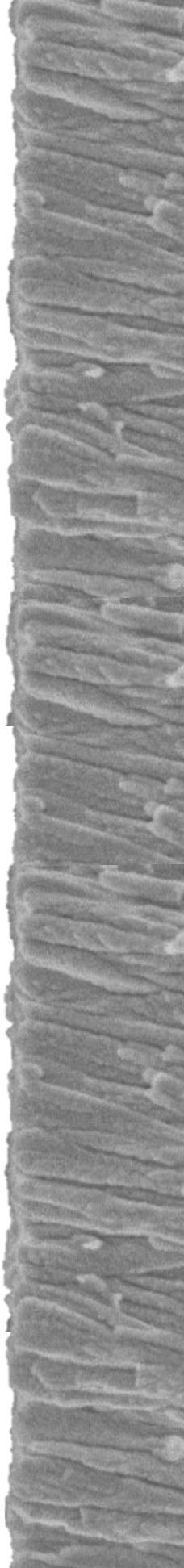
[98]   K.L. Nardi, N. Yang, C.F. Dickens, A.L. Strickler, S.F. Bent, Creating
        highly active atomic layer deposited NiO electrocatalysts for the oxygen
        evolution   reaction,   Adv.   Energy   Mater.   5   (2015)   1500412.
        https://doi.org/10.1002/aenm.201500412.

[99]   M. Tangirala, K. Zhang, D. Nminibapiel, V. Pallem, C. Dussarrat, W. Cao,
        T.N. Adam, C.S. Johnson, H.E. Elsayed-Ali, H. Baumgart, Physical
        analysis of VO_2 films grown by atomic layer deposition and RF
        magnetron sputtering, ECS J. Solid State Sci. Technol. 3 (2014) N89–N94.
        https://doi.org/10.1149/2.006406jss.

[100]   D.M. Mattox, Physical vapor deposition (PVD) processes, Met. Finish. 98
        (2000) 410–423. https://doi.org/10.1016/S0026-0576(00)80350-5.

[101]   A. Barranco, A. Borras, A.R. Gonzalez-Elipe, A. Palmero, Perspectives on
        oblique angle deposition of thin films: From fundamentals to devices,
        Prog.   Mater.   Sci.   76   (2016)   59–153.
        https://doi.org/10.1016/j.pmatsci.2015.06.003.

[102]   W. Phae-ngam, M. Horprathum, C. Chananonnawathorn, T.
        Lertvanithphol, B. Samransuksamer, P. Songsiriritthigul, H. Nakajima, S.
        Chaiyakun, Oblique angle deposition of nanocolumnar TiZrN films via
        reactive magnetron co-sputtering technique: The influence of the Zr
        target   powers,   Curr.   Appl.   Phys.   19   (2019)   894–901.
        https://doi.org/10.1016/j.cap.2019.05.002.

[103]   F. Mwema, E. Akinlabi, P. Oladijo, Sustainability Issues in Sputtering
        Deposition Technology, (2019).

[104]   J. Zhao, E. Baibuz, J. Vernieres, P. Grammatikopoulos, V. Jansson, M.
        Nagel, S. Steinhauer, M. Sowwan, A. Kuronen, K. Nordlund, F.
        Djurabekova, Formation Mechanism of Fe Nanocubes by Magnetron
        Sputtering Inert Gas Condensation, ACS Nano. 10 (2016) 4684–4694.
        https://doi.org/10.1021/acsnano.6b01024.

[105]   Y. Qin, X.-T. Kong, Z. Wang, A.O. Govorov, U.R. Kortshagen, Near-
        infrared plasmonic copper nanocups fabricated by template-assisted
        magnetron   sputtering,   ACS   Photonics.   4   (2017)   2881–2890.
        https://doi.org/10.1021/acsphotonics.7b00866.

[106]   S. Alvi, D.M. Jarzabek, M.G. Kohan, D. Hedman, P. Jenczyk, M.M. Natile,
        A. Vomiero, F. Akhtar, Synthesis and mechanical characterization of a
        CuMoTaWV high-entropy film by magnetron sputtering, ACS Appl.
        Mater.   Interfaces.   12   (2020)   21070–21079.

https://doi.org/10.1021/acsami.0c02156.

[107] S. Hejazi, M. Altomare, S. Mohajernia, P. Schmuki, Composition gradients in sputtered Ti–Au alloys: site-selective Au decoration of anodic TiO_2 nanotubes for photocatalytic H_2 evolution, ACS Appl. Nano Mater. 2 (2019) 4018–4025. https://doi.org/10.1021/acsanm.9b01022.

[108] B. Wei, H. Liang, D. Zhang, Z. Wu, Z. Qi, Z. Wang, CrN thin films prepared by reactive DC magnetron sputtering for symmetric supercapacitors, J. Mater. Chem. A. 5 (2017) 2844–2851. https://doi.org/10.1039/C6TA09985H.

[109] A. Garcia-Valenzuela, S. Muñoz-Piña, G. Alcala, R. Alvarez, B. Lacroix, A.J. Santos, J. Cuevas-Maraver, V. Rico, R. Gago, L. Vazquez, J. Cotrino, A.R. Gonzalez-Elipe, A. Palmero, Growth of nanocolumnar thin films on patterned substrates at oblique angles, Plasma Process. Polym. 16 (2019). https://doi.org/10.1002/ppap.201800135.

[110] D. Deniz, R.J. Lad, Temperature threshold for nanorod structuring of metal and oxide films grown by glancing angle deposition, J. Vac. Sci. Technol. A Vacuum, Surfaces Film. 29 (2011). https://doi.org/10.1116/1.3525882.

[111] D. Deniz, D.J. Frankel, R.J. Lad, Nanostructured tungsten and tungsten trioxide films prepared by glancing angle deposition, Thin Solid Films. 518 (2010) 4095–4099. https://doi.org/10.1016/j.tsf.2009.10.153.

[112] J. Gil-Rostra, M. Cano, J.M. Pedrosa, F.J. Ferrer, F. García-García, F. Yubero, A.R. González-Elipe, Electrochromic Behavior of $W_xSi_yO_z$ Thin Films Prepared by Reactive Magnetron Sputtering at Normal and Glancing Angles, ACS Appl. Mater. Interfaces. 4 (2012) 628–638. https://doi.org/10.1021/am2014629.

[113] M.A. Khan, H. Zhao, W. Zou, Z. Chen, W. Cao, J. Fang, J. Xu, L. Zhang, J. Zhang, Recent Progresses in Electrocatalysts for Water Electrolysis, Electrochem. Energy Rev. 1 (2018) 483–530. https://doi.org/10.1007/s41918-018-0014-z.

[114] Q. Wang, Z. Zhao, H. Li, J. Zhuang, Z. Ma, Y. Yang, L. Zhang, Y. Zhang, One-step RF magnetron sputtering method for preparing $Cu(In, Ga)Se_2$ solar cells, J. Mater. Sci. Mater. Electron. 29 (2018) 11755–11762. https://doi.org/10.1007/s10854-018-9274-y.

[115]   M. Kumar, N.P. Shetti, Magnetron sputter deposited NiCu alloy catalysts
         for production of hydrogen through electrolysis in alkaline water, Mater.
         Sci.   Energy   Technol.   1   (2018)   160–165.
         https://doi.org/10.1016/j.mset.2018.06.010.

[116]   I.V. Tudose, F. Comanescu, P. Pascariu, S. Bucur, L. Rusen, F. Iacomi, E.
         Koudoumas, M.P. Suchea, Chapter 2 - Chemical and physical methods
         for multifunctional nanostructured interface fabrication, Functional
         Nanostructured   Interfaces   for   Environmental   and   Biomedical
         Applications (2019) 15–26. https://doi.org/10.1016/B978-0-12-814401-
         5.00002-5.

[117]   S.M. Park, M.J. Jang, Y.S. Park, J. Lee, J.-Y. Jeong, J. Jung, M.-K. Choi, Y.-
         S. Noh, M.-H. Seo, H.J. Kim, J. Yang, Y.D. Kim, S.M. Choi, Synthesis and
         characterization of the $Cu_{0.72}CO_{2.28}O_4$ catalyst for oxygen evolution
         reaction in an anion exchange membrane water electrolyzer, J. Korean
         Inst.   Met.   Mater.   58   (2020)   49–58.
         https://doi.org/10.3365/KJMM.2020.58.1.49.

[118]   Y.S. Park, M.J. Jang, J. Jeong, S.M. Park, X. Wang, M.H. Seo, S.M. Choi, J.
         Yang, Hierarchical Chestnut-Burr like structure of copper cobalt oxide
         electrocatalyst directly grown on Ni foam for anion exchange membrane
         water   electrolysis,   ACS   Sustain.   Chem.   Eng.   (2020).
         https://doi.org/10.1021/acssuschemeng.9b06767.

[119]   E. Cossar, A.O. Barnett, F. Seland, E.A. Baranova, The performance of
         nickel and nickel-iron catalysts evaluated as anodes in anion exchange
         membrane   water   electrolysis,   Catalysts.   9   (2019).
         https://doi.org/10.3390/catal9100814.

[120]   W. Guo, J. Kim, H. Kim, S.H. Ahn, Cu–Co–P electrodeposited on carbon
         paper as an efficient electrocatalyst for hydrogen evolution reaction in
         anion exchange membrane water electrolyzers, Int. J. Hydrogen Energy.
         (2021). https://doi.org/10.1016/j.ijhydene.2021.03.120.

[121]   J. Hnát, M. Plevova, R.A. Tufa, J. Zitka, M. Paidar, K. Bouzek,
         Development and testing of a novel catalyst-coated membrane with
         platinum-free catalysts for alkaline water electrolysis, Int. J. Hydrogen
         Energy.   44   (2019)   17493–17504.
         https://doi.org/10.1016/j.ijhydene.2019.05.054.

[122]   J. Chang, G. Wang, A. Belharsa, J. Ge, W. Xing, Y. Yang, Stable $Fe_2P_2S_6$
         nanocrystal catalyst for high-efficiency water electrolysis, Small Methods.
         4 (2020) 1900632. https://doi.org/10.1002/smtd.201900632.

Chapter 2

Aims and scope of the thesis

Due to the current necessity to find solutions to the problem of the global energy crisis, and due to the great potential shown by hydrogen as energy vector, research groups from the UCLM and the ICMS have been collaborating the last years to contribute in this important scientific and technological field. This thesis emerges in the framework of the collaboration of these two consolidated scientific teams with the main objective to investigate the possibilities of AEMWE technology.

Despite the fact that water electrolysis is the simplest pathway to produce hydrogen, this process, and in particular AEMWE, has not been extensively used yet due to the high operation cost associated to traditional catalysts and the high overpotential for the oxygen evolution reaction. This thesis work aims to contribute to overcome these limitations with the following partial objectives:

❖ To prepare of Cu-Co mixed oxides, Ni and Ni-Fe based catalyst electrodes with different atomic ratios, microstructures, oxidation states or catalyst loads directly on suitable GDL supports to be used as electrodes in AEMWE cells. This is done with one-step process by MS-OAD at room temperature. The choice of these materials is because they are claimed to be among the most promising non-Pt based catalysts for AEMWE as prepared using traditional wet routes.

❖ To characterize physico-chemically the electrodes as prepared and after electrochemical operation to identify their elemental and chemical composition (surface and bulk), microstructure, and crystallographic structure. These studies guide the preparation process of the electrodes to correlate process parameters (deposition geometry, process atmosphere, target choice, …) with

final physico-chemical properties of the samples. Besides these studies help to justify the obtained electrochemical performances of the manufactured electrodes in electrolyzers and to justify the observed degradation effects.

❖ To test different electrodes in a three-electrode cell configuration, with the main objective to select best electrochemical performance electrodes to scale-up to the AEMWE cells.

❖ To test the anodic and cathodic electrodes in a complete AEMWE cell under realistic operational conditions.

❖ To simplify the manufacture and integration of the catalyst within the electrodes and the complete cells to reduce the cost and other associated problems with the incorporation of additives, such as ionomers, to the traditional manufacture of these electrodes. In this sense, we will study to which extent the addition of ionomers, often a critical point, is required when using MS-OAD to manufacture electrodes for AEMWE cells.

❖ To optimize the different cell components as gas diffusion layers, catalysts loads, anion exchange membranes, or bipolar plates to get optimum performance of a final complete electrolyzer.

❖ To study the long-term stability of complete cells.

❖ To test the electrodes in a hybrid ethanol-water electrolysis system with the objective to reduce the cell required voltage or overall electrical energy consumption to produce hydrogen vs. pure water electrolysis.

Chapter 3

Methods and experimental setups
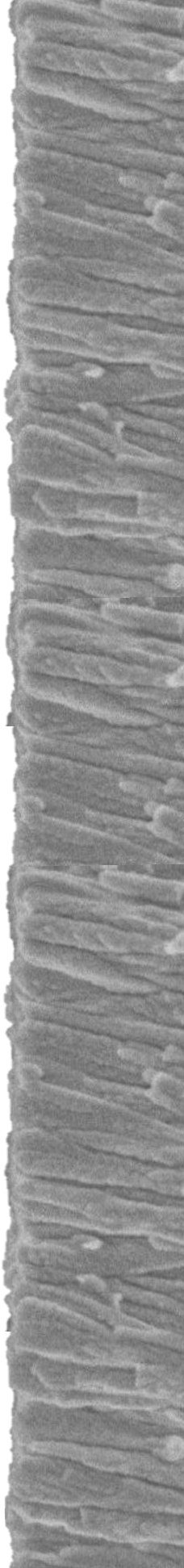
3.1.   Electrodes fabrication by magnetron sputtering

Along this thesis, several Co-Cu mixed oxides, Ni and Ni-Fe nanostructured catalysts were deposited by magnetron sputtering (MS) method at room temperature on conductive gas diffusion layer supports. The deposition reactor used in this thesis was a homemade apparatus shown in **Figure 3.1**.
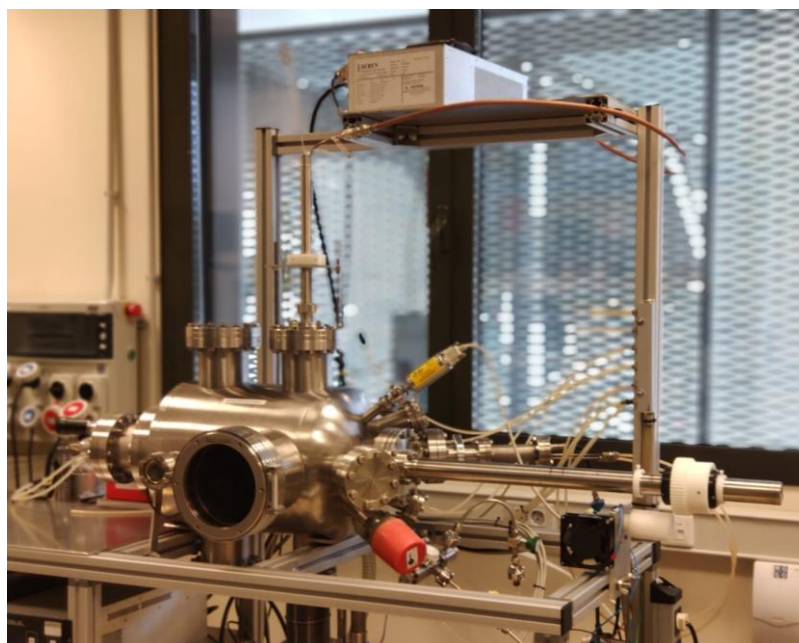
Figure 3.1. *Magnetron sputtering reactor used for the fabrication of the electrodes along this thesis.*

Magnetron sputtering is a vacuum deposition technique to fabricate metals, alloys, and compounds in thin film form. The basic operation and advantages of this method in relation to the final application in water electrolyzers have been described in section 1.6.3. in Chapter 1.

The MS reactor used for the fabrication of catalysts electrodes along this thesis is schematized in **Figure 3.2**. It consists of a stainless-steel

vacuum chamber where suitable pumping system, magnetron heads, gas
inlet and sample holder facilities are implemented.
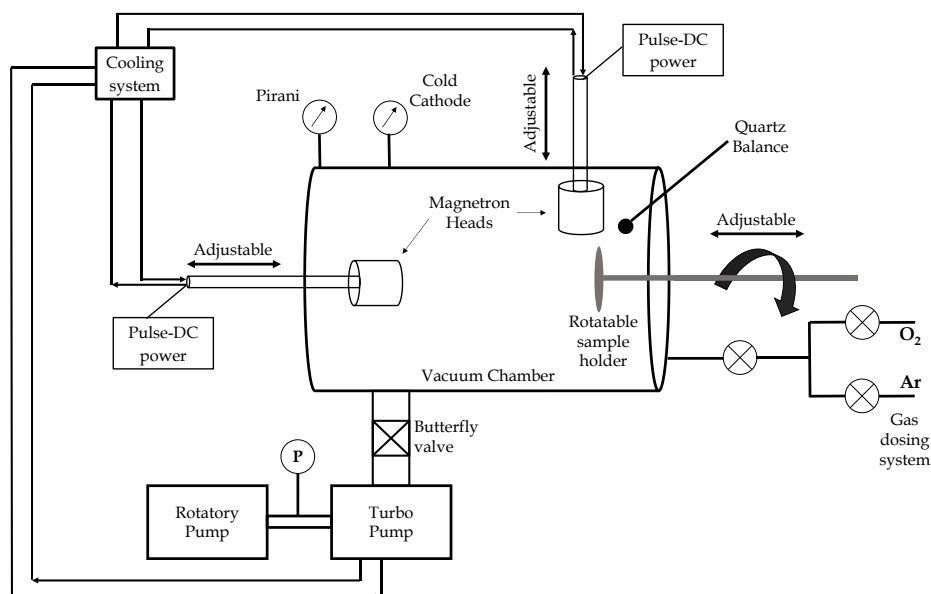
Figure 3.2. Scheme of the MS deposition reactor with its different components.

The pumping system consists of a primary pump (rotatory pump,
TRIVAC D 8 B, Leybold) and a turbo pump (Pfeiffer Vacuum D-35614
Asslar) that allows to achieve base pressures of about $1\text{-}6 \cdot 10^{-6}$ mbar
(overnight pumping). Two vacuum monitors (Pirani gauge and cold
cathode) are used to measure the pressure inside the vacuum chamber.

The gas inlet system consists of independent high purity O_2 and Ar
gases lines controlled by mass flow controllers. Gases in standard cubic
centimeters per minutes (sccm) are displayed on a digital meter.

The deposition sources were two magnetron sputtering heads, as
shown in **Figure 3.3 a)** (GENCOA SW50, 2 inches circular targets), for
normal and oblique deposition. Their exact position within the vacuum

chamber can be selected with an adjustable rod. Two power supplies are connected to the equipment, one pulsed DC power supply (AE Pinnacle+) and other RF power supply (RF Generator 600, AJA International Inc.). A water-cooling system is set to refrigerate the magnetron heads and the turbo pump. Targets of different materials (see **Figure 3.3 b)**) can be used in the MS heads. A photograph of the ignited magnetron plasma can also be seen in **Figure 3.3 c)**.

The sample holder facilities mainly consist of a rotatable magnetic transfer bar where a circular sample holder plate is attached. A motor that continuously rotates the transfer bar is connected to it, allowing the deposits to be homogeneous. The sample holder has a diameter of 10 cm and several substrates can be placed on it (held by screws) for simultaneous deposition within a single batch. The substrates on which the thin films are deposited are placed in the holder as shown in **Figure 3.3 d)**.

As a common feature of all the deposition experiments, a cleaning/conditioning pre-sputtering of the magnetron heads is carried out before the film deposition begins to avoid any target poisoning and to guarantee reproducibility in the deposition process.
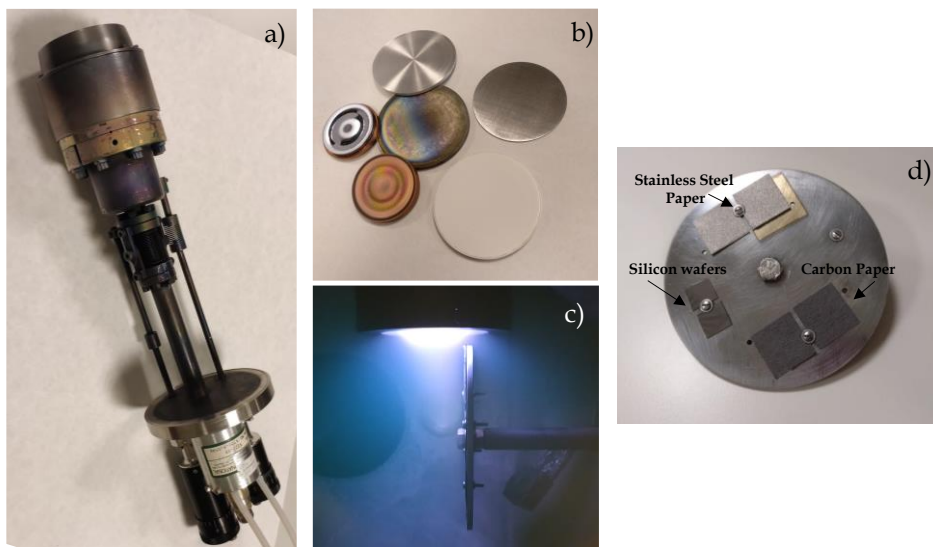
Figure 3.3. Photograph of the a) GENCOA sputtering head, b) several types of targets, c) magnetron plasma discharge in the deposition reactor and d) holder with stainless steel paper, silicon wafers and carbon paper as substrates.

In Chapter 4 and 5, copper-cobalt mixed oxide films were prepared by co-deposition of the two metallic cations by reactive magnetron sputtering. Pure Cu and Co targets of 50 mm diameter (GoodFellow, 99.9%) were used as metallic sources in an O_2/Ar discharge prepared with mass flow controllers set at 15 sccm for both gases. The deposition geometry, schematized in **Figure 3.4**, was as follows: several substrates were placed in the rotatable sample holder. The Cu magnetron head facing the substrates (normal deposition geometry) was aligned with the rotation axis of the sample holder and separated ~19 cm from it. The Co magnetron head was placed perpendicular to the plane holder plate (i.e., in an oblique angle deposition, OAD, geometry) at a distance to the edge of the rotatable holder of ~7 cm (average deposition angle of ~78 °, angle between the normal to the holder plate and the line connecting the center of the holder plate and the center of the magnetron target). During the

deposition process, the sample holder was continuously rotating at a rate of 5 turns per minute to homogenize the deposits.

The Co target was operated by the before defined pulsed DC power supply fixed at 150 W and a frequency of 120 kHz. The Cu target was operated with a RF power supply set between 50 and 200 W to vary the amount of deposited copper within the deposited mixed oxide. The base pressure of the system was $2 \cdot 10^{-6}$ mbar and the deposition pressure $5 \cdot 10^{-3}$ mbar. Under these conditions, the overall deposition rate varies between 4.4 and 7.7 nm min^{-1}, depending on the actual power applied to the copper target. The deposition rate was determined by depositing on a flat substrate, silicon, and measuring the *equivalent thickness* of the deposited film by scanning electron microscopy (SEM) in a cross-sectional configuration for a certain known time.
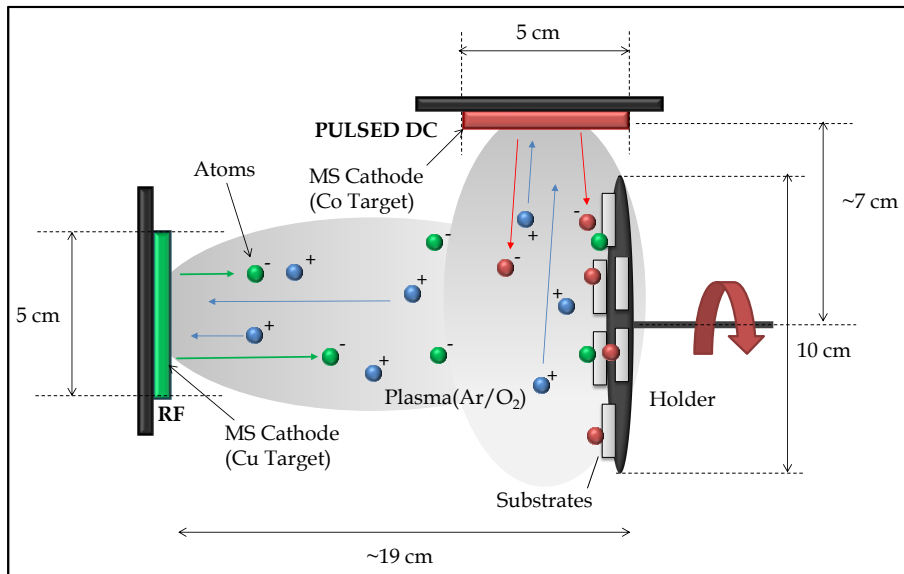

Figure 3.4. Scheme of the co-deposition configuration.

In Chapter 6 to 9 for anodic electrodes and in all chapters for cathodic electrodes, metallic nickel catalysts were deposited on GDL support. A pure Ni circular sheet of 50 mm diameter (GoodFellow, 99.9 %) above a copper target was used as sputtering source. The magnetron head was operated with the pulsed DC power supply fixed at 150 W and working at a frequency of 120 kHz.

The microstructure and composition of electrode films were adjusted using two geometrical deposition configurations and three gas plasma discharges. Compact or porous catalysts deposits were obtained placing the axis of the magnetron head either perpendicular (normal deposition configuration, see **Figure 3.5 a)**) or parallel to the surface of a rotating substrate holder plate (OAD geometry, see **Figure 3.5 b)**). The deposition angle used in the preparation of the OAD electrodes was ~78 $^{\circ}$.

The oxidation state of the nickel-based deposits was controlled adjusting the gas mixture used for the ignition of the magnetron plasma discharge during film growth. Thus metallic nickel Ni, nickel oxide NiO or nickel oxyhydroxide $NiO_x(OH)_y$ films were produced with Ar, Ar/O$_2$, or Ar/O$_2$/H$_2$O plasma gas mixtures, respectively. Ar and O$_2$ gases were supplied to the preparation chamber by mass flow controllers (30 sccm Ar for metallic, 15 sccm Ar and 15 sccm O$_2$ for oxide, and 15 sccm Ar and 4 sccm O$_2$ for oxyhydroxide samples, respectively), while water in the gas mixture was controlled with a leak valve adjusted to dose a constant partial pressure of 5 $\cdot10^{-4}$ mbar in the deposition chamber. In all cases, total deposition pressure was fixed at 5 $\cdot10^{-3}$ mbar (base pressure of the system was 2 $\cdot10^{-6}$ mbar).

The deposition rate was ~30 nm min^{-1} for samples prepared with the Ar discharge, ~8 nm min^{-1} with the O$_2$/Ar discharge and ~31 nm min^{-1}

with the $H_2O/O_2/Ar$ discharges, all of them under the OAD configuration. Deposition rate was ~12 nm min^{-1} for the metallic Ni samples prepared in the normal deposition configuration (note the longer target-substrate distance in this configuration).
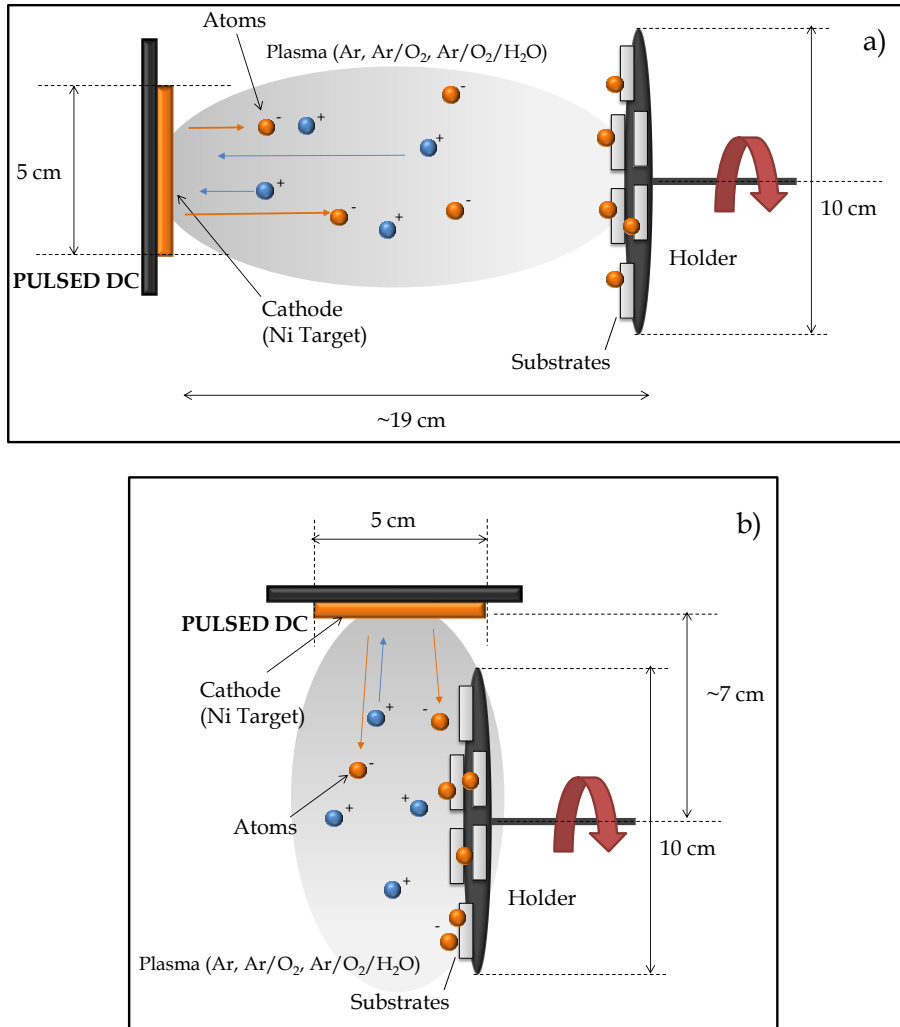
Figure 3.5. *Schemes of the deposition geometries considered in this work a) normal deposition configuration and b) OAD configuration.*

In Chapter 7, bimetallic thin film electrodes made of Ni/Fe mixtures
were prepared by MS at room temperature in an oblique angle deposition
configuration (MS-OAD). A nickel circular sheet (GoodFellow
Cambridge Ltd., 99.9 at. %, 50 mm diameter) with axially wrapped iron
strips (GoodFellow Cambridge Ltd., 99.5 at. %, 1.5 mm width, 0.25 mm
thickness) was used for deposition. The number of iron strips varied
between one and five to obtain electrodes with different Ni/Fe atomic
ratios (see **Figure 3.6**). The other fabrication parameters were similar to
previous explained metallic nickel deposition catalyst.
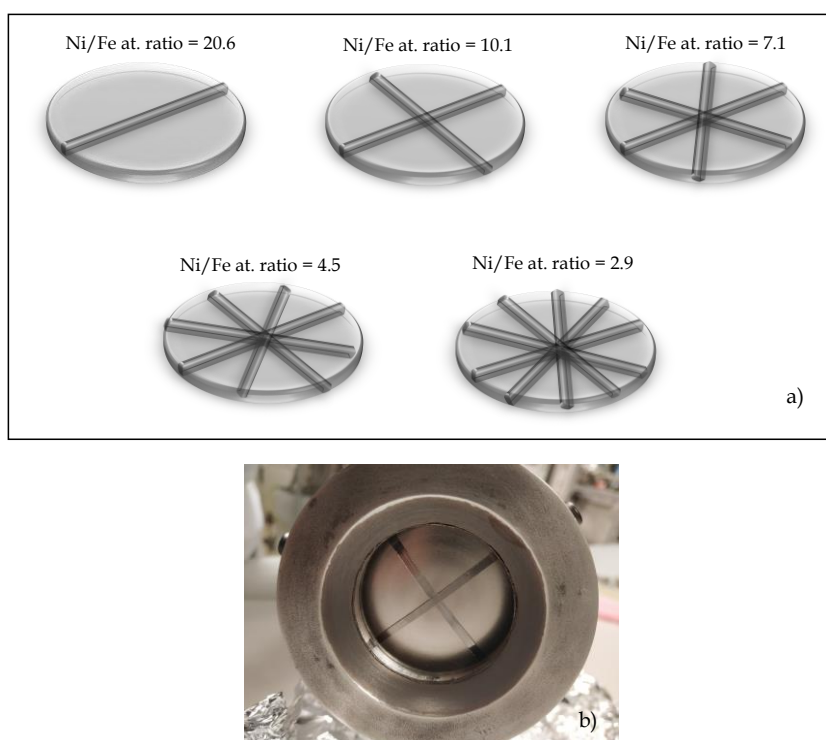
*Figure 3.6. a) Ni-Fe magnetron target configurations showing the axially wrapped iron
strips and indicating the Ni/Fe atomic ratio achieved in the corresponding depositions.
b) Example photograph of a nickel sheet with two axially wrapped iron strips.*

In Chapter 8, the bimetallic Ni-Fe anodic catalysts and the metallic Ni cathodic catalysts were also deposited on stainless steel fiber paper (SSP, Dioxide Materials) to compare with the traditional carbon paper (CP, TGP-H-90, Fuel Cell Earth) support. In **Figure 3.7** the differences between carbon and stainless-steel papers substrates with and without Ni-Fe deposit can be observed. The compositional analysis of the SSP without catalyst determined by energy-dispersive X-ray (EDX) spectroscopy is detailed in **Table 3.1**.

Figure 3.7*. Several carbon and stainless-steel papers with and without Ni-Fe deposit.*

Table 3.1*. Elemental composition of SSP GDL measured by EDX.*

Element	wt. / %	at. / %
Carbon	4.76	18.77
Aluminium	0.94	1.64
Chromium	16.98	15.45
Iron	66.08	55.98
Nickel	8.69	7.00
Molybdenum	2.13	1.05
Tungsten	0.43	0.11
	100.00	100.00

3.2. Physico-chemical characterization

Scanning electron microscopy (SEM)

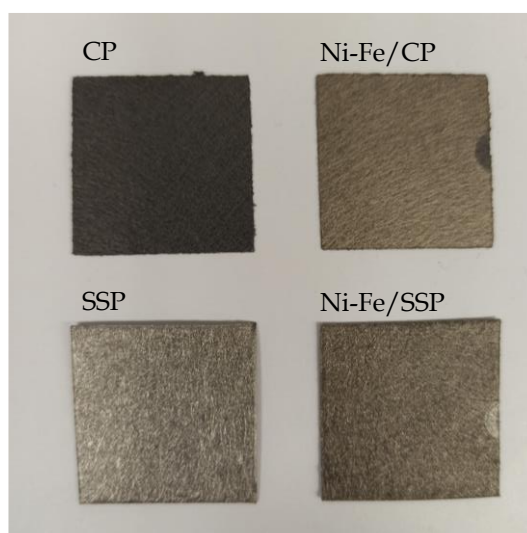Scanning electron microscopy provides microstructural and morphological information on a microscopic scale. A focused electron beam irradiates the surface of the sample to be analysed, and an appropriate detector records the result of the interaction with the sample. Among the different types of signals, secondary electrons, backscattered electrons, or X-Rays are used to obtain the information from the sample.

Along this thesis, two different configurations have been used for the samples characterized by SEM: the top-view was used to examine the film surface deposited on carbon paper, stainless steel fiber paper and flat silicon substrates, and the cross-sectional configuration to determine the *equivalent thickness* of the films deposited on the flat silicon substrates.

Images were taken with a Hitachi S4800 field emission microscope operated at 2 keV. The SEM equipment is a cold cathode field emission gun that allows the images of the morphology and surface texture of the samples with a resolution of 10 nm at 15 kV. SEM equipment is coupled to an energy-dispersive X-ray spectroscopy (EDX) detector (Bruker X-Flash Detector 4010) that allows the elemental analysis and compositional maps.

X-ray diffraction (XRD)

The presence of crystalline structure or structural analysis of the electrodes is carried out by X-ray diffraction technique in a Panalytical X'PERT PRO apparatus. Samples were scanned with an angular step of 0.05 $^{\circ}$ over the range 10 $^{\circ}$ ≤ 2θ ≤ 90 $^{\circ}$ with a scan rate of 4 s·step^{-1}.

In Chapter 4, the crystallization behaviour of the cupper-cobalt oxide samples was followed in situ between room temperature and 600 $^{\circ}$C, at a heating rate of 5 $^{\circ}$C min^{-1}. Sample was kept for 2 h at each recording temperature.

X-ray photoelectron spectroscopy (XPS)

X-Ray photoelectron spectroscopy technique used along the thesis, is employed to analyze the surface stoichiometry and chemistry of the deposits.   The analysis was carried out by a SPECS PHOIBOS-100 spectrometer operated with unmonochromatic Mg Kα radiation as excitation source and 20 eV constant pass energy.

Raman spectroscopy

Chemical structure, phase, crystallinity, and molecular interactions information can be provided by Raman spectroscopy. Raman spectrum features several peaks, with their correspond intensity and wavelength position and corresponding to a specific molecular bond vibration. The Raman spectra was obtained using a SENTERRA spectrometer with an excitation wavelength of 543 nm.

Inductively coupled plasma atomic emission spectroscopy (ICP-AES)

Inductively coupled plasma atomic emission spectroscopy is an emission spectroscopy that quantifies the mass percentage of the components.

Along this thesis, ICP-AES analysis has been carried out using RL Liberty Sequential Varian ICP-AES to analyze the solution after experiments to discard problems of possible delamination of catalyst layers.

Fourier-transform infrared spectroscopy (FTIR)

The infrared light used for scanning the samples, provide an identification of organic, inorganic, and polymeric materials. Changes in the characteristic pattern of absorption bands suggest changes in the material composition. FTIR is useful in identifying and characterizing materials and identifying decomposition and oxidation.

In Chapter 4, FTIR spectra of the films deposited on intrinsic silicon substrates were recorded in transmission mode (400-4000 cm^{-1}) with a Nicolet 510 spectrometer.

X-ray absorption spectroscopy (XAS)

X-ray absorption spectroscopy is an element-specific, short-range probe, providing information about the local structural and compositional environment of an adsorbing atom.

For Chapters 5 and 6 results, XAS measurements were carried out at near ambient pressure photoemission (NAPP) end station of the CIRCE beamline of ALBA Synchrotron Light Source (Barcelona, Spain) (see **Figure 3.8**). The plane grating monochromator covers the energy range 100 - 2000 eV. The energy resolution is ~8000 and the photon flux ~10^{13} ph s^{-1}. For this experiment, silicon membranes (NX10100C, Norcada) were used as substrates to deposit the metallic nickel catalyst (Chapter 6) or the cupper-cobalt mixed oxide films (Chapter 5) with a thickness of approximately 50-60 nm. O K, and Ni L$_{2,3}$ spectra were recorded for nickel films and O K, Co L$_{2,3}$, and Cu L$_{2,3}$ absorption spectra were recorded for Co/Cu films for as prepared samples (i.e., exposed to the air), after their immersion in 1 M KOH electrolyte for 30 minutes and after working as anode for the oxygen evolution reaction (OER) at 750 mV vs. Ag/AgCl

during 30 min. The electrolyte immersed and polarized electrodes were rinsed with distilled water and handled in air for about 5–10 min (maximum exposure time to air) previously to their insertion in the XAS apparatus.
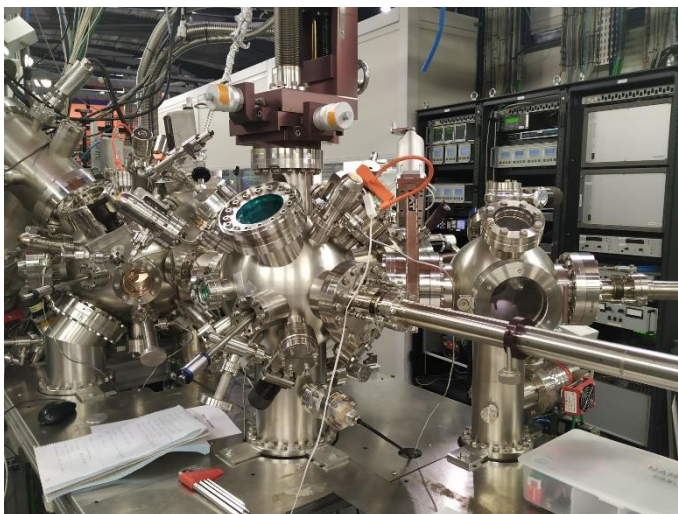
Figure 3.8. Photograph of the vacuum equipment used to carry out the XAS characterization at ALBA Synchrotron Light Source.

Rutherford backscattering spectrometry (RBS)

Elemental composition, in-depth elemental distribution, and metal loading of the films can be estimated by Rutherford backscattering spectrometry.

In Chapters 4, 5 and 6, tandem accelerator (CNA, Seville, Spain) was used to carried out RBS analysis. A beam of alpha particles with 2.8 MeV of energy was used. The backscattered particles were collected with a silicon particle detector placed 165 º off the beam direction. Used as alternative measure of load determination on flat substrates.

3.3. Electrochemical characterization. Three-electrode cell

Electrochemical characterization was carried out in a three-electrode (i.e. half-cell) configuration. The electrochemical characterization measurements, both in the half-cell and in the later explained complete electrolysis cell, are carried out to optimize the production of O_2 and H_2 or to test the stability of the systems. The system consists of a 150 mL glass vessel with three electrodes (working electrode, reference electrode and counter electrode) that fit in a vessel lid. This vessel lid has another opening for the inlet-outlet of nitrogen to inert the solution. The working electrode consists of an electrode support where is placed the electrode to analyze. The geometric area of the exposed electrode is 1.0 cm². An Ag/AgCl electrode (KCl, 3M, Metrohm®) and a platinum foil electrode (Metrohm®) are used as reference and counter, respectively (see **Figure 3.9** for the scheme of the half-cell).
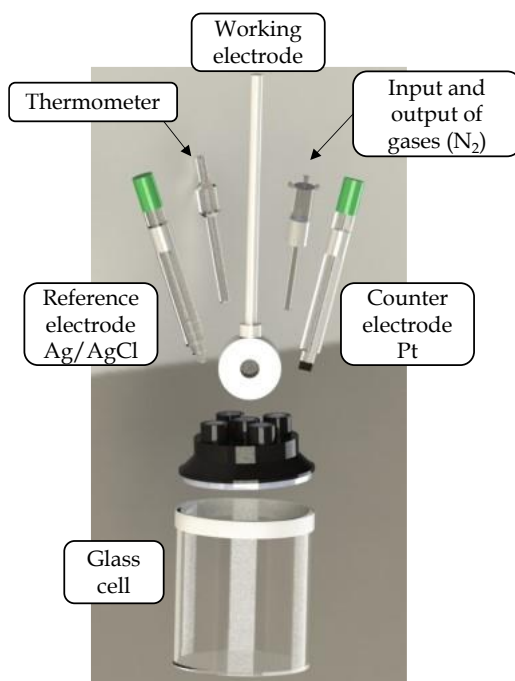

Figure 3.9. Three-electrode cell configuration scheme.

In all chapters, cyclic voltammetry (CV) experiments were used to the electrochemical characterization of the different electrodes. The three-electrode cell is connected to an Autolab potentiostat/galvanostat (PGSTAT30-ECOCHEMIE) to perform the electrochemical tests. A N_2 flow was maintained bubbling for at least 20 minutes prior to all tests and then during the experiment to inert the solution.

CV measurements from 0 to 750 mV vs. Ag/AgCl with a scan rate of 20 mV s^{-1} were carried out to study the OER. To study the influence of the different electrodes towards the hydrogen evolution reaction (HER), CV experiments were carried out from 0 to -1450 mV vs. Ag/AgCl with a scan rate of 10 mV s^{-1}. All the experiments were carried out at room temperature in a 1.0 M KOH-deionized water solution.

In Chapter 5, the electrochemically active surface area (ECSA) was evaluated by means of the double-layer capacitance method [1,2] from the CV plots acquired from 240 to 300 mV vs. Ag/AgCl at scan rate between 2 and 10 mV s^{-1}. The double layer capacitance C_{dl} was obtained from the slope of the linear regression of the current density values vs. scan rate, acquired at 290 mV vs Ag/AgCl. Note that, the C_{dl} values determined in this way are taken as proportional to the ECSA according to [3]:

$$ECSA = \frac{C_{dl}}{L\ C_s} \qquad (3.1)$$

where C_s is the specific electrochemical double-layer capacitance (mF cm^{-2}) and L is the catalyst load (mg cm^{-2}). C_s values typically range between 15-50 mF cm^{-2} and depend on the material. In a previous study related to similar mixed cobalt-copper oxides, we found a value of 40 mF cm^{-2} [4] for this capacitance used as reference.

Furthermore, Tafel slopes were calculated from the data obtained in the cyclic voltammetries according to the approximation of Butler-Volmer equation (**Eq. (3.2)**) [5]. To do this, the representation of logarithm of the current density vs. potential was done. The Tafel slopes are obtained from the linear fits to the initial rise of the OER curves.

$$\eta = b \log \left(\frac{j}{j_o} \right) \qquad (3.2)$$

Where η is the overpotential (V), j is the current density (A cm^{-2}) and b is the Tafel slope, $2.3RT/(\alpha F)$, in V dec^{-1}. R is the gas constant, T the temperature, α is the transfer coefficient and F the Faraday's constant.

In addition, since it is well-known that Pt counter electrodes may present some corrosion problems when working in basic conditions [6,7], we have demonstrated its stability and performance in a separate blank experiment. **Figure 3.10** shows the high stability of a cyclic voltammetry process using a carbon paper as working electrode along a series of OER cyclic voltammetries (see Carbon Paper Cycle 1 and 25 in the figure). This serie of measurements shows that there is not a significant increase of current density along time, thus supporting the negligible influence of the Pt counter electrode in the performance of the electrolysis cell in our conditions. This activity has been compared to a Ni-Fe electrode deposited on the same carbon paper, demonstrating the negligible amount of current provided by the carbon paper substrate without catalyst. This experiment has been carried out in the defined three-electrode cell in 1.0 M KOH solution using a scan rate of 20 mV s^{-1} at room temperature.
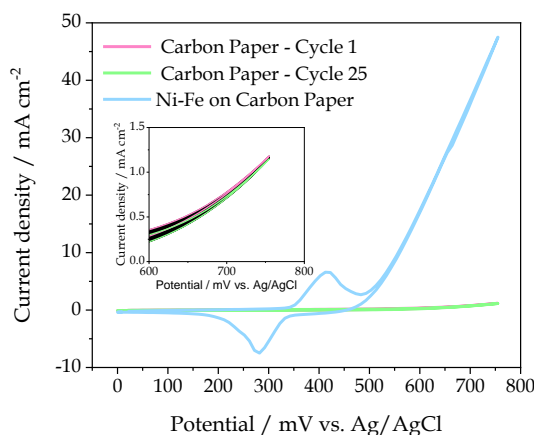
Figure 3.10. *Experiments with and without anodic catalyst.*

Electrochemical impedance spectroscopy (EIS) measurements in half-cell were performed using an impedance module of the used Autolab potentiostat/galvanostat (PGSTAT30-ECOCHEMIE). Data were collected at 700 mV in a frequency range from 100 kHz to 10 mHz. The potential amplitude was 10 mV and the experiments were carried out in 1.0 M KOH at room temperature.

In addition, in Chapter 6, 7 and 8 ECSA for nickel and nickel-iron electrodes has been determined by the procedure proposed by Watzele et al. [8]. For this calculation, a new equivalent circuit was used to determine the ECSA of the different electrodes. Assuming that they are surface oxidized, the value of specific adsorption capacitance of NiO_x deduced by Watzele et al. has been used (C'_a=300 ± 99 µF cm^{-2}, a parameter related to the adsorption/desorption capacity of intermediate species such as *OH, *O and *OOH that are involved in the OER). This specific capacitance is related to the ECSA as follows:

81

$$C_{a'} = \frac{C_a}{ECSA} \qquad (3.3)$$

where C_a is the adsorption capacitance in μF determined by the equivalent electric circuit (**Figure 3.11**) and ECSA is the electrochemical surface area in cm².
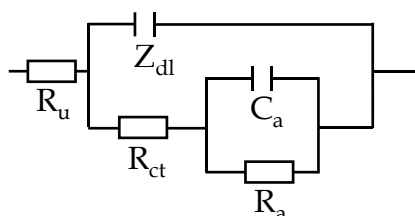
Figure 3.11. Equivalent electric circuit for OER as proposed by Watzele *et al.* [8]. R_u *is the uncompensated resistance, Z_{dl}, the double layer impedance, R_{ct}, the charge transfer resistance, C_a, the adsorption capaciance and R_a, the adsorption resistance.*

3.4.   Setup for anion exchange membrane electrolysis cell configuration

Along this thesis, different electrodes prepared by MS technique and tested in the three-electrode cell have been also studied in a membrane electrode assembly (MEA) configuration. Catalysts supported on different gas diffusion layers were used as anode and cathode electrodes separated by an anion exchange membrane (see **Figure 3.12**).

In Chapter 4, the MEA was sandwiched by hot pressing between two pieces of a stainless-steel frame. Temperature was increased at steps, from room temperature to 120 °C (i.e., 10 °C steps from 20 to 80 °C, followed by 5 °C steps from 80 to 120 °C) and the sample kept for 2 minutes at each intermediate temperature and, after reaching the maximum value of 120 °C, pressure (1 metric ton) was applied for 3 minutes. In the rest of the

chapters, the membrane was simply placed between the electrodes without applying pressure and temperature.
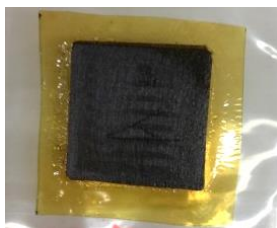
Figure 3.12. Membrane electrode assembly.

In all chapters, Fumapem FAA-3-50 supplied by Fuel Cell Store has been used as commercial anion exchange membrane. In chapter 6, Sustainion® X37-50 (Dioxide Materials) was also compared. The Sustainion® X37-50 anion exchange membrane had 50 microns thickness and an ethylene glycol plasticizer to prevent cracking that is designed to be eliminated during activation. Although a slightly better performance was obtained with the Sustainion membranes, its highly demanding conditioning precluded its systematic use and most results reported in this chapter corresponded to the Fumapem membrane. In chapter 8, Fumasep FAA-3-PK-75® (Fuel Cell Store) and Sustainion® X37-50 (grade T, Dioxide Materials) were also evaluated. In this case, an improved Sustainion® X37-50 (Grade T) membrane was used compared to that used in Chapter 6.

The membrane requires a pretreatment before its use. For the activation treatment of the membranes, they were immersed in a 1.0 M KOH solution for, at least, 24-48 hours at room temperature to replace its Br^- functional groups (Fumapem® FAA-3-50 and Fumasep FAA-3-PK-75®) and chloride form (Sustainion® X37-50) to OH^- groups.

For the electrochemical experiments, an Autolab potentiostat/galvanostat was used. Linear sweep voltammetries (LSVs) were performed between 1.0 to 2.2 V with a scan rate of 5 mV s^{-1}. The stabilities of the electrolyzers were studied by constant-current chronopotentiometry experiments at a fixed current density and cyclic voltammetry experiments (200 cycles, potential range from 1.0 to 2.2 V, scan rate of 50 mV s^{-1}).

Two different electrolysis cells have been used in this thesis. First, a homemade graphitic bipolar plate AEMWE cell (see **Figure 3.13 a)**) was used for Chapters 4, 5 and 6. In a second stage (Chapters 7, 8 and 9), to avoid the problems associated with the graphitic bipolar plate in an alkaline medium, a commercial AEMWE cell with nickel bipolar plate was acquired (see **Figure 3.13 b)**). A scheme of the plates AEMWE cell assembly and their components used in this thesis is included in **Figure 3.14 a)**. The active geometric area of the electrode in the cell was 5 cm^2 and 6.25 cm^2 for the nickel and graphitic AEMWE cell, respectively. Both bipolar plates have channel groves to supply the liquid solution uniformly in the complete electrode in both sides of the MEA (see **Figure 3.14 b)** and **c)**). The bipolar plates were used as current collectors and as distributors of reactants and products. External teflon gaskets were placed on both sides of the bipolar plates to seal the cell and to avoid short-circuiting.
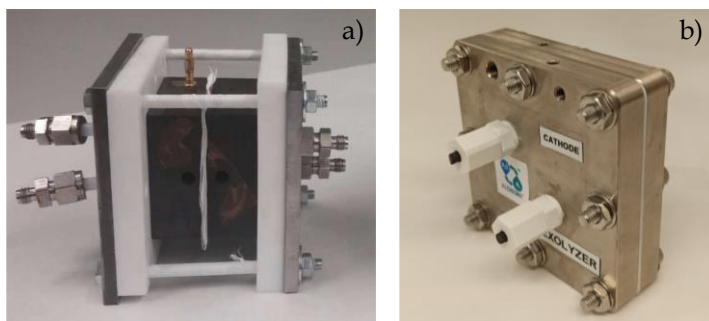
Figure 3.13. a) Graphitic bipolar plate and b) nickel bipolar plate AEMWE cells.
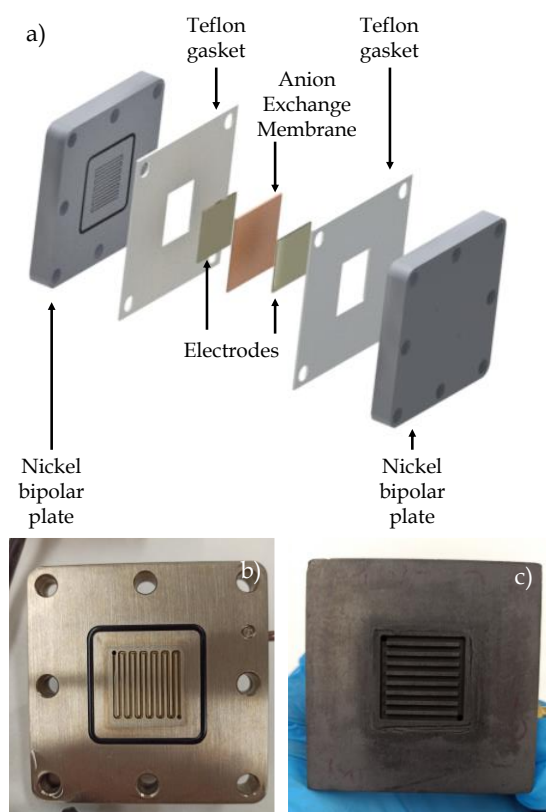
Figure 3.14. a) Schematic view of the AEMWE cell assembly and their components. A detail of the channels of the bipolar plates of b) nickel and c) graphite.

85

The AEMWE complete set up, schemed in **Figure 3.15**, consisted of a feeding unit, a reaction system, and a polarization system.

The feeding unit consists of two liquid reservoirs and a multichannel peristaltic pump (Pump drive 5001, Heidolph) to impulse the liquid from two compartments of 1 L of volume and recirculating the streams to the feed reservoirs. Anode and cathode chambers were fed with different concentration of KOH-deionized water solutions flowing at a constant flow rate of 2 mL min^{-1} using the peristaltic pump.

The AEMWE cell or reaction system has been explained above.

The polarization unit is an Autolab potentiostat/galvanostat (PGSTAT30-ECOCHEMIE) analyzer that allows the application of electric current or potential between both electrodes.
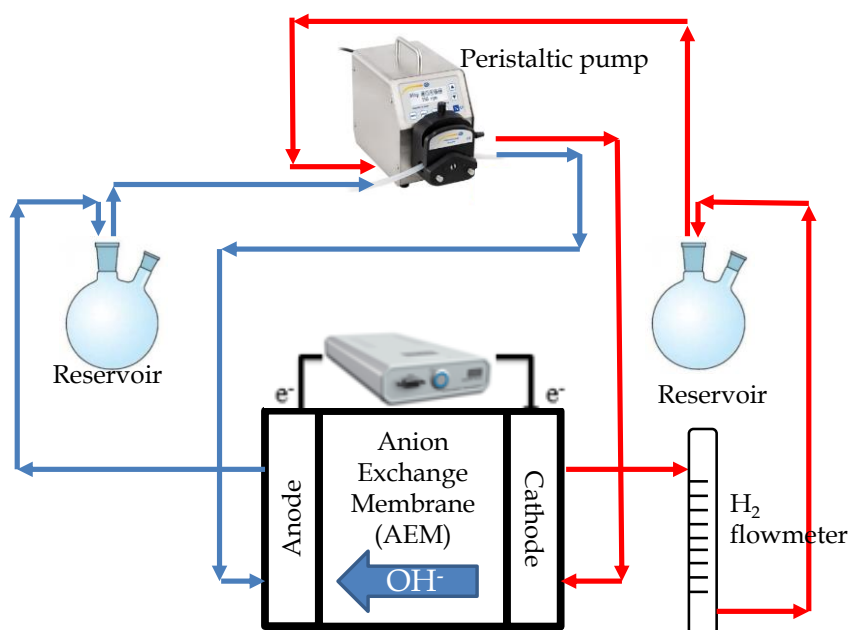
Figure 3.15. AEMWE complete experimental set up scheme.

3.5. References

[1] M. Sun, Z. Wang, B. Gao, S. Wang, C. Wang, X. Song, D. Lin, Electrocatalytic hydrogen evolution properties of anionic NiS_2-$Ni(OH)_2$ nanosheets produced on the surface of nickel foam, Int. J. Energy Res. 44 (2020) 4827–4836. https://doi.org/10.1002/er.5275.

[2] S. V Mohite, R. Xing, B. Li, S.S. Latthe, Y. Zhao, X. Li, L. Mao, S. Liu, Spatial Compartmentalization of Cobalt Phosphide in P-Doped Dual Carbon Shells for Efficient Alkaline Overall Water Splitting, Inorg. Chem. 59 (2020) 1996–2004. https://doi.org/10.1021/acs.inorgchem.9b03363.

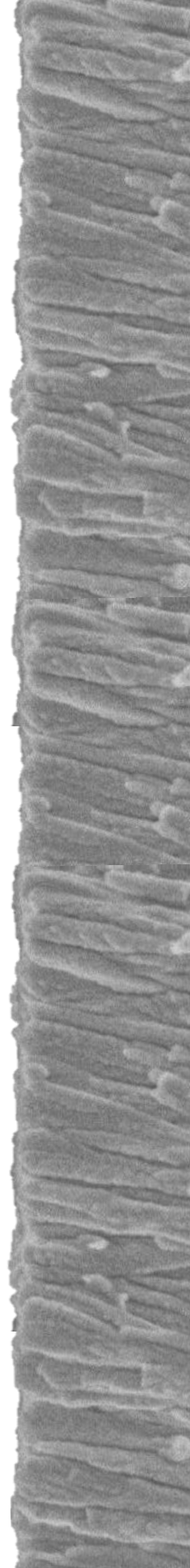[3] G. Li, L. Anderson, Y. Chen, M. Pan, P.-Y. Abel Chuang, New insights into evaluating catalyst activity and stability for oxygen evolution reactions in alkaline media, Sustain. Energy Fuels. 2 (2018) 237–251. https://doi.org/10.1039/C7SE00337D.

[4] S.K. Bikkarolla, P. Papakonstantinou, $CuCo_2O_4$ nanoparticles on nitrogenated graphene as highly efficient oxygen evolution catalyst, J. Power Sources. 281 (2015) 243–251. https://doi.org/10.1016/j.jpowsour.2015.01.192.

[5] R.F. Mann, J.C. Amphlett, B.A. Peppley, C.P. Thurgood, Application of Butler–Volmer equations in the modelling of activation polarization for PEM fuel cells, J. Power Sources. 161 (2006) 775–781. https://doi.org/10.1016/j.jpowsour.2006.05.026.

[6] M. Schalenbach, O. Kasian, M. Ledendecker, F.D. Speck, A.M. Mingers, K.J.J. Mayrhofer, S. Cherevko, The electrochemical dissolution of noble metals in alkaline media, Electrocatalysis. 9 (2018) 153–161. https://doi.org/10.1007/s12678-017-0438-y.

[7] P.P. Lopes, D. Strmcnik, D. Tripkovic, J.G. Connell, V. Stamenkovic, N.M. Markovic, Relationships between atomic level surface structure and stability/activity of platinum surface atoms in aqueous environments, ACS Catal. 6 (2016) 2536–2544. https://doi.org/10.1021/acscatal.5b02920.

[8] S. Watzele, P. Hauenstein, Y. Liang, S. Xue, J. Fichtner, B. Garlyyev, D. Scieszka, F. Claudel, F. Maillard, A.S. Bandarenka, Determination of electroactive surface area of Ni-, Co-, Fe-, and Ir-based oxide electrocatalysts, ACS Catal. 9 (2019) 9222–9230. https://doi.org/10.1021/acscatal.9b02006.

Chapter 4

$Cu_xCo_yO_z$ anodes for anion exchange membrane water electrolysis
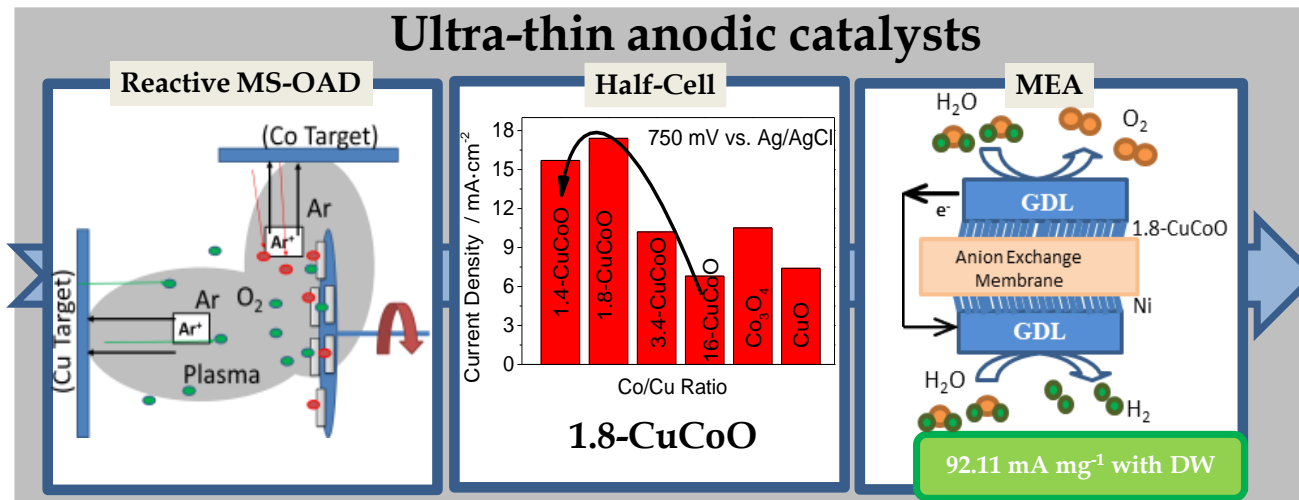
The content of this chapter has been published in:

4.1. Introduction

The growing demand for hydrogen produced in conjunction with renewable sources has encouraged the development of sustainable and environmentally friendly production pathways. Among the hydrogen production methods, water electrolysis is considered the most efficient and practical method in combination with other renewable energy sources [1,2]. AEMWE combines the advantages of the other forms of water electrolysis and solves their associated problems [1,3].

Cobalt based oxides are considered good catalysts for the oxygen evolution reaction (OER) in alkaline media because of their optimum electrochemical behavior, high electrical conductivity, high stability, low cost, and environmental compatibility [3,4]. In the quest for more efficient electrodes, it has been demonstrated that performance increases by the addition of a second element, such as Li, Ni or Cu, to form binary mixed oxide catalyst anodes [5]. In particular, previous studies with half-cells have shown that the incorporation of Cu into the Co$_3$O$_4$ spinel lattice leads to more negative OER onset potentials [3].

Traditional electrode fabrication techniques of catalyst layers for this type of electrolyzers consist of dripping a catalyst ink onto a porous electrode support (usually carbon paper) [3,6,7]. This method makes use of catalyst powders, usually prepared by thermal decomposition of precipitated metal precursors salts, giving rise to inhomogeneous electrodes with high metal loadings in the range of few or even tens of mg cm^{-2} [2,8]. Additionally, the low reproducibility of this kind of preparation techniques hinders their straightforward scaling to stack configuration and larger areas.

Physical vapor deposition by magnetron sputtering (MS) could be a feasible way to solve some of these limitations. MS deposition gives rise to homogeneous films of controlled low metal loading and thickness, operates at room temperature, and it is easily scalable and quite reproducible [9–13]. The compactness of the deposited material with this technique can be tuned through deposition geometry, i.e., angle between the flux of sputtered particles from the target and substrate normal [13]. Thus, MS at oblique angle deposition (MS-OAD) renders mesoporous films with open microstructure (compared with normal deposition configuration that gives in general compact thin films [12]) producing electrodes with enhanced electrocatalytic activity in water electrolysis [9,12,14].

In this chapter, a study of copper-cobalt mixed oxides anodic films prepared by MS-OAD method is presented. These catalyst electrodes are characterized by a series of physicochemical techniques (SEM, EDX, XPS, XRD, and FTIR) before and after their use as anodic electrodes and tested as OER catalysts. These studies provide interesting clues about the nature of the most active sites of these catalysts for the OER. Thus, porous and amorphous samples with a strict control of the total catalyst load and Co/Cu ratio were fabricated. Electrocatalytic tests showed a maximum performance for the OER at Co/Cu atomic ratio around 1.8. Besides, it is found, through crystallization studies, that a particular local chemical environment around the Co and Cu sites acts as an efficient catalytic site for the oxygen evolution reaction. The high performance found for these electrodes in terms of current density vs. catalyst load, and their long-term stability and reproducibility, support the potential of the MS-OAD technique for the preparation of a new generation of highly reliable AEMWE electrodes.

4.2. Experimental

Magnetron sputtering fabrication method previously described in Chapter 3 has been used to prepare the cupper-cobalt mixed oxides electrodes. The deposition process took place simultaneously in pieces of polished silicon wafers (Si) and fused silica used as substrates for film characterization and commercially available carbon paper (TGP-H-90, Fuel Cell Earth) used as gas diffusion layer support and indium tin oxide (ITO) glass panes for the electrochemical tests.

To study the effect of catalyst crystallization, selected samples were annealed in air up to 500 °C, at a rate of 5 °C min^{-1} and maintained for 2 hours at this temperature. For the annealing, it is used a tubular furnace that allows to control the reaction atmosphere associated with a thermal controller-programmer.

In addition, (Co$_3$O$_4$/CuO)^{10} multilayered samples were prepared by sequential deposition of the single oxides with the same process parameters than for the mixed oxides fixed 150 W applied to the target. The first deposited layer was CuO followed by Co$_3$O$_4$, and the stack terminated in Co$_3$O$_4$. Each layer had an *equivalent thickness* of 25 nm, and the total number of layers was 20. We define *equivalent thickness* as the physical thickness determined by cross-sectional SEM analysis for the thin films deposited simultaneously on a flat silicon wafer substrate.

A Ni thin film supported on carbon paper used as cathode was also prepared by MS-OAD as has been explained in Chapter 3.

The microstructures of the films deposited on carbon paper and silicon substrates were examined by SEM in planar view and cross-sectional configurations. Surface chemistry and stoichiometry of the deposits on

carbon paper were evaluated by XPS. Elemental composition, in-depth elemental distribution, and total metal loading of the films deposited on polished silicon wafers were evaluated by RBS. Crystallinity and phase analysis were performed by XRD. FTIR spectra of the films deposited on intrinsic silicon substrates were also recorded. All the physico-chemical characterization techniques used in this chapter have been previously explained in Chapter 3.

In addition, DC electrical measurements, performed at room temperature by the four-point probe technique in a square configuration, were carried out on samples deposited on fused silica in this chapter. A Keithley 2635A equipment was used for these measurements.

Anodic samples have been labelled as *YY-CuCoO-thickness/CP*, *YY-CuCoO-thickness/Si*, or *YY-CuCoO-thickness/ITO* where YY refers to the Co/Cu atomic ratio obtained by EDX analysis of samples prepared on carbon paper, polished silicon wafer, or ITO, respectively. On the other hand, the pure copper and cobalt samples will be named as *CuO-thickness/CP* and *Co$_3$O$_4$-thickness/CP*, respectively.

Electrochemical characterization in the half-cell configuration was carried out as has been described in Chapter 3. Finally, a MEA consisted of an anion exchange membrane (Fumapem FAA-3-50), the $Cu_xCo_yO_z$ (Cu/Co at. ratio of 1.8) thin film supported on carbon paper working as anode and the Ni thin film supported on carbon paper working as cathode was prepared. The catalyst loading was 0.18 mg cm^{-2} (500 nm *equivalent thickness*) for the anode and 0.72 mg cm^{-2} (1000 nm *equivalent thickness*) for the cathode.

Water electrolysis experiments were carried out in the experimental setup described in Chapter 3. The temperature of the cell was varied

between 25 and 70 °C. Chronopotentiometric experiments were subsequently performed during 18 hours at 40 °C. Gas-volume measurements were carried to determine the hydrogen production rate during the water electrolysis. Data were cross-checked via Faraday's Law. KOH concentration in the anode and cathode chambers was changed to study the effect of electrolyte concentration. The possible use of tap water and milli-Q water as electrolytes was also investigated. Electrochemical impedance spectroscopy (EIS) measurements were carried out at two potentials (1.7 and 2.0 V) in a 1.0 KOH solution at 40 °C.

4.3.   Results and discussions

4.3.1.   Physico-chemical characterization of $Cu_xCo_yO_z$ thin films

Several techniques were used to characterise the anodic $Cu_xCo_yO_z$ catalyst films. For the different batches of anodic thin films, **Table 4.1** shows the experimental parameters used for their synthesis (i.e., the power applied to the magnetron heads), the Co/Cu atomic ratios determined from either EDX or XPS analysis, the *equivalent thickness* determined by SEM, the total metal atom load (number of atoms per cm^{-2}) determined by RBS and the DC films electrical resistivity. The catalyst load, expressed in mg cm^{-2}, was calculated from the number of atoms per cm^2 obtained by RBS. Data in this table show that the Co/Cu atomic ratio in the films varies with the ratio of powers applied to the copper and cobalt targets during the co-deposition process. The mismatch in Co/Cu atomic ratio obtained with XPS and EDX might be attributed to the different probing depths of these techniques (XPS analyses just the upmost ~3 nm zone, while EDX analyses the whole film thickness). The

films electrical properties varied also with their composition: the single oxide films present the highest resistance values and for the $Cu_xCo_yO_z$ thin films, this parameter decreases continuously with the Co/Cu atomic ratio. This tendency agrees with previous studies evidencing that the addition of Cu to $Cu_xCo_yO_z$ improves its electrical conductivity [15], while pure Co_3O_4 and CuO behave as semiconductor materials and have relatively higher electrical resistance. From the point of view of the use of these thin films as anodes, these low resistance values support that the electrochemical performance will not be significantly affected by high electrode impedances [15]. It is noteworthy that the films *equivalent thickness*, their atom density per unit surface and the metal load are very similar for all investigated electrodes, which evidences an accurate control of the MS deposition process and supports those electrochemical results can be properly compared. It should be mentioned that the total metal load and atomic ratio distribution were homogeneous through the whole deposition area, the former is much lower than in powder based OER electrodes [1,16,17]. The homogeneous deposition in the elemental mapping obtained for sample *1.8-CuCoO-450/CP* can be observed in **Figure 4.1**.

Table 4.1. Summary of the physico-chemical characterization of the prepared anodes.

Sample label	Power (W_{Co}/W_{Cu})	Co/Cu at. ratio		Thickness (SEM) (nm)	Catalyst Load (RBS)		DC Resistance (Ω)
		EDX	XPS		Metal content (at cm^{-2})	Metal content (mg cm^{-2})	
Co$_3$O$_4$-540/CP	150/0	-	-	450	$4.05 \cdot 10^{18}$	0.20	$1.3 \cdot 10^{-2}$
16-CuCoO-450/CP	150/50	16	9.7	454	$3.79 \cdot 10^{18}$	0.19	$3.0 \cdot 10^{-4}$
3.4-CuCoO-450/CP	150/100	3.4	1.6	488	$3.83 \cdot 10^{18}$	0.19	$1.6 \cdot 10^{-4}$
1.8-CuCoO-450/CP	150/150	1.8	1.0	441	$3.40 \cdot 10^{18}$	0.18	$2.3 \cdot 10^{-6}$
1.4-CuCoO-450/CP	150/200	1.4	0.8	438	$3.75 \cdot 10^{18}$	0.21	$7.6 \cdot 10^{-7}$
CuO-450/CP	0/150	0	0	469	$3.00 \cdot 10^{18}$	0.18	$8.7 \cdot 10^{-2}$
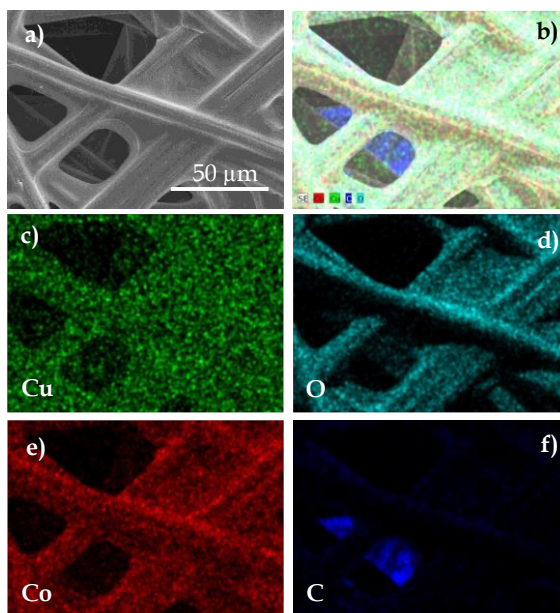
Figure 4.1. a) SEM image of 1.8-CuCoO-450/CP electrode and EDX mapping images showing the corresponding elemental c) Cu, d) O, e) Co, and f) C distributions and their combined image b).

Figure 4.2 shows selected SEM images of *1.8-CuCoO* films deposited on polished silicon wafer (*1.8-CuCoO-450/Si*) and carbon paper (*1.8-CuCoO-450/CP*) substrates. The cross sectional and normal SEM micrographs in **Figures 4.2 a)** and **b)** reveal that the film deposited on polished silicon wafer is formed by vertically aligned nanocolumns, which is the typical microstructure of MS-OAD thin films prepared in these experimental conditions [11,18,19]. The open porosity of these films supports their use as electrodes, where a high surface area in contact with the medium is a key requirement. When deposited on carbon paper, the film material grows only onto the most external fibres of the substrate (c.f **Figure 4.2 c)**), but it still keeps a high porosity, as revealed by the high magnification image in **Figure 4.2 d)** where agglomerated grains corresponding to the tips of the nanocolumns can be appreciated. It is

expected that decoration of the outer fibres of the carbon paper substrates with these tiny aggregates provides a high electrochemical active surface area [20]. Composition was homogenous in all deposited zones, not only laterally, but also in the first and second layer of fibres, as evidenced by EDX mapping of the electrode surfaces (see Figure 4.1).
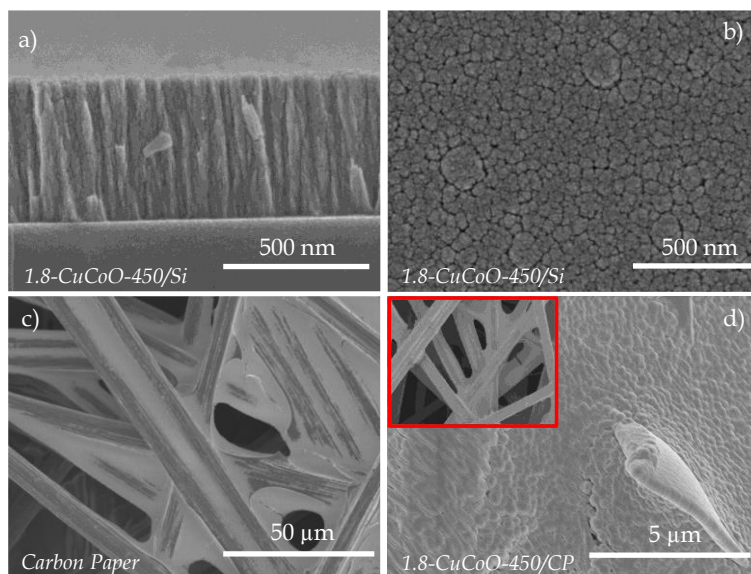
Figure 4.2. SEM images of: 1.8-CuCoO-450/Si sample a) in a cross-sectional configuration and b) in planar view; c) bare carbon paper and d) 1.8-CuCoO-450/CP sample supported on carbon paper in planar view. The inset shows the same sample with a different scale.

Chemical state of catalyst films was typical of copper and cobalt oxides, as determined by XPS and FTIR. **Figure 4.3** presents the Cu $2p_{3/2}$ and Co 2p photoelectron spectra recorded for the studied as prepared samples. The binding energy of the Cu $2p_{3/2}$ peak at 934.0 eV and the strong satellite at 940-944 eV confirm that copper is in the form of Cu^{2+} [21]. Meanwhile, the overall Co 2p peak shape and Co $2p_{3/2}$ binding

energy at approximately 780 eV are typical of Co^{n+} (n=2,3) in Co_3O_4 [15,22–24].
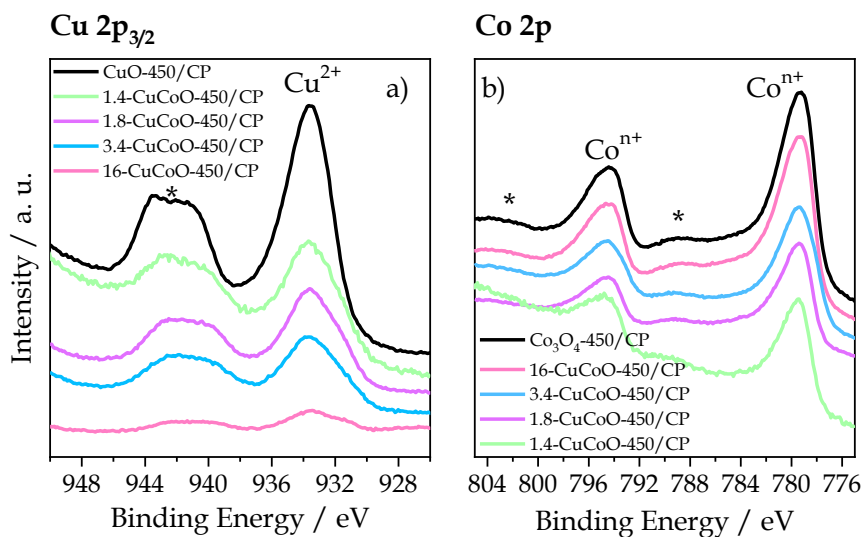
Figure 4.3. *XPS spectra of a) Cu $2p_{3/2}$ and b) Co 2p for YY-CuCoO-450/CP samples. * denotes so-called shake-up satellite peaks which are typical of the Cu^{2+} and Co^{n+} oxidation states of Cu and Co, respectively.*

This assignment was confirmed by the FTIR analysis, that depicted spectra where Co^{3+}-$O^=$ and Cu^{2+}-$O^=$ characteristic bands [25–27] are clearly identified (see **Figure 4.4**). The most significant result of this characterization is the presence of strong absorption bands at 3200-3500 cm^{-1}, that corresponds to the –OH groups [25,26], for the *YY-CuCoO-450/Si* samples (those prepared in MS-OAD geometry), and its absence for the CuO samples (prepared in normal MS deposition geometry). The presence of this band is an additional prove of the porosity of the *YY-CuCoO* films. Bands in the 1410-1564 cm^{-1} range relate the presence of C=O [26]. The two absorption bands occurred at 568 and 662 cm^{-1}

correspond to the vibration of Co-O functional group in the Co_3O_4 [27]. Finally, an absorption band at 532 cm^{-1} corresponds to the vibration of Cu-O functional group in the electrodes with Cu [26].

In addition, indirect evidence gained by XRD and the electrochemical behavior of the multilayer $(CuO/Co_3O_4)^{10}$ electrodes (see below) sustains that, in the as prepared *YY-CuCoO-450/CP* samples, copper and cobalt oxides are mixed in a common amorphous lattice (i.e., in the form of a $Cu_xCo_yO_z$ mixed oxide network).
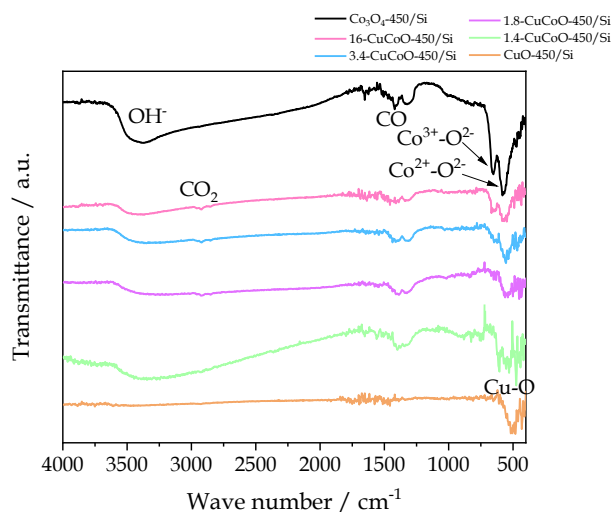
Figure 4.4. FTIR spectra of the different Co/Cu atomic ratios electrodes.

4.3.2. Influence of the Co/Cu atomic ratio on the oxygen evolution reaction

To retrieve information about the influence of the cobalt/copper atomic ratio in the OER, preliminary electrochemical analysis was carried out in the three-electrode cell (i.e., half-cell configuration) with the *YY-CuCoO-450/CP* anodic catalysts. **Figure 4.5 a)** shows cyclic voltammetry diagrams as a function of the Co/Cu atomic ratio. In some voltammetry

curves, such as in the case of pure Co$_3$O$_4$ sample, a small anodic feature at approximately 500 mV has been attributed to the Co(III)/Co(IV) redox couple [28,29]. In addition, the corresponding cathodic peaks in the potential about 400-200 mV obtained on the reverse scan are due to Co(IV)/Co(III) redox reactions [3,17,28]. The onset potential for the OER was found between 500 and 600 mV, similar to that found for other copper and cobalt oxides systems prepared by alternative routes [3,17,30]. From the set of studied Cu$_x$Co$_y$O$_z$ thin films, sample *1.8-CuCoO-450/CP* rendered the highest current density and therefore the fastest OER kinetics within the explored potential range. A bulk Co/Cu atomic ratio of 1.8 is within the optimal compositions reported in literature for Cu-cobaltite electrodes [3,15,21,28]. However, surface Co/Cu atomic ratio in this sample is close to 1 (see XPS value in Table 4.1) which suggests a preferential surface segregation of copper and that a particular local chemical environment around the Cu and Co sites yields a maximum catalytic activity.

Long-term stability under operation conditions of sample *1.8-CuCoO-450/CP* was proved by an accelerated life testing of repetitive cyclic voltammetry (200 cycles). The comparison in **Figure 4.5 b)** of the 1st and 200th cycle reveals no distinctive difference after the aging test and supports that, despite their amorphous character, the MS-OAD Cu-cobaltite thin films exhibit a satisfactory stability as OER electrocatalysts. This behavior is similar to that found for crystalline Cu-cobaltite anodic catalysts prepared by thermal decomposition of precursors [3,7].
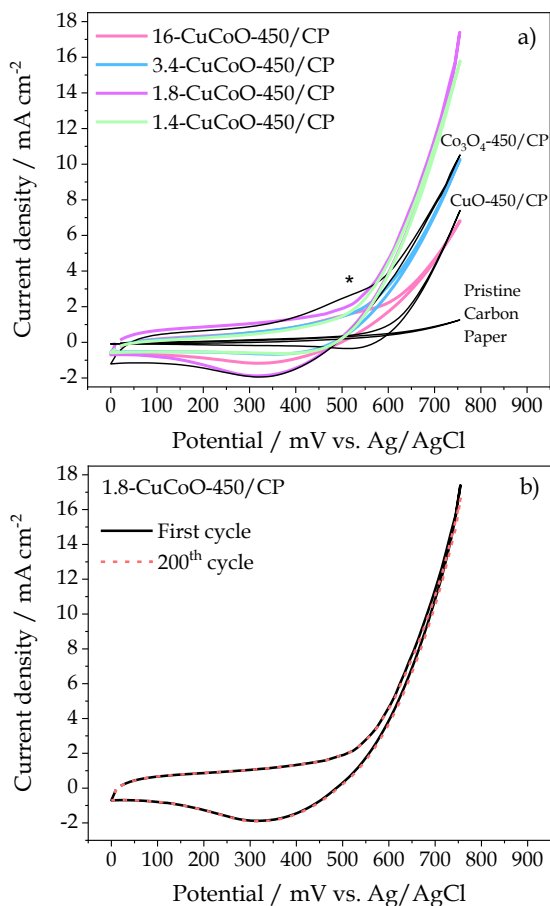
Figure 4.5. *a) Cyclic voltammetry experiments of YY-CuCoO-450/CP samples (**
denotes Co(III)/Co(IV) redox couple) and b) comparison of the 1ˢᵗ and the 200ᵗʰ cycle of
1.8-CuCoO-450/CP sample at room temperature, with scan rate 20 mV s⁻¹ in 1.0 M
KOH solution.

To further investigate the surface properties of the *1.8-CuCoO-450/CP*
electrode after this accelerated aging test, used electrocatalyst samples
were analyzed by XPS. Surprisingly, the Co/Cu atomic ratio had changed
to ca. 2.2, i.e., doubling the Co/Cu ratio of the as prepared sample, c.f.,
Table 4.1. A similar change occurred when the samples were just

immersed in the KOH electrolyte solution for a time period equivalent to that of the electrocatalytic tests. The shapes of the Cu $2p_{3/2}$ and the Co 2p photoemission peaks did not vary after these electrolyte immersion tests and only differences were found in the O 1s signal with the appearance of a prominent peak at 531.0 eV attributed to a surface enrichment in OH^- groups [25,31,32] (see **Figure 4.6**). We attribute the observed change in Co/Cu atomic ratio at the outmost surface region of the samples to some surface atom redistribution/segregation and/or to some preferential leaching into the electrolyte solution rather than to any selective delamination of the deposited anodic catalyst after the aging process. This is justified because the fluorine content (due to the Teflon coating of the fibers in the carbon paper [31,33]) detected by XPS did not vary significantly after immersion. Thus, the Co/Cu ratio of 2.2 measured for the used samples supports that the most active surface electrocatalytic sites may consist of a three cations bonding arrangements of the type Co(O)Cu(O)Co rather than the binary Cu(O)Co bonding structure suggested by the XPS surface analysis of the pristine sample. This point deserves further confirmation by local order studies around the Cu and Co sites.
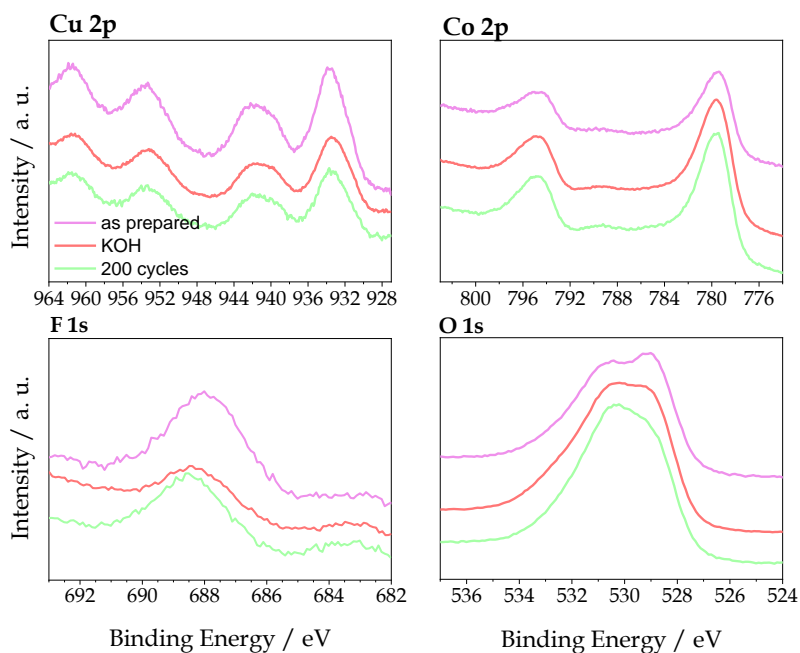
Figure 4.6. *XPS spectra of 1.8-CuCoO-450/CP sample in its as prepared form, after the immersion in KOH solution, and after its accelerated aging test consisting of 200 cycles of repetitive cyclic voltammetry experiments.*

The higher efficiency of catalytic sites involving neighboring Co^{n+} and Cu^{2+} cations was further demonstrated by an experiment with the *(Co₃O₄/CuO)¹⁰/CP* multilayer electrode, where copper and cobalt are separately distributed in a multilayer stack. The maximum current density found in this case was half that obtained for sample *1.8-CuCoO-450/CP* (see **Figure 4.7**), in line with our proposal that most efficient electrocatalytic sites are formed by local arrangements of Cu and Co atoms.
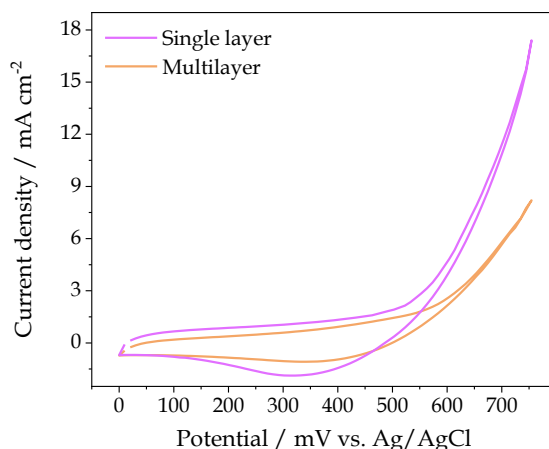
Figure 4.7. *Comparative of the cyclic voltammetry experiments of 1.8-CuCoO-450/CP film and a (Co$_3$O$_4$/CuO)^{10}/CP multilayer electrodes performed at room temperature, with scan rate 20 mV s^{-1} in 1 M KOH solution.*

4.3.3.   Influence of the crystallinity on the oxygen evolution reaction

The Cu$_x$Co$_y$O$_z$ thin films prepared by MS-OAD at room temperature were amorphous, a feature that contrasts with the crystalline character of equivalent electrocatalysts reported in literature prepared by thermal decomposition of precursor solutions [8,16,17]. To assess the influence of the electrode crystalline structure of the electrodes on the OER, we have studied the crystallization behavior of the as prepared samples upon annealing in air at increasing temperatures. **Figure 4.8** shows XRD diagrams of the *1.8-CuCoO-450/CP* sample measured after its annealing at increasing temperatures. No well-defined diffraction peaks due to crystalline phases were detected for annealing temperatures below 400 ºC. This result confirms that the deposited electrodes, formed by a random solid solution of the Cu^{2+} and Co^{n+} cations, are amorphous and do not present long range order in their structure. At temperatures above

450 $^{\circ}$C, diffraction peaks of CuO and $Cu_{0.7}Co_{2.3}O_4$ phases start to develop and they become clearly observed at higher temperatures [2,21]. The presence of some minor Co_3O_4 contribution cannot be discharged. The formation of CuO crystallites indicates that the observed phase separation process will significantly alter the average distribution of atoms at the electrocatalyst surface, at least for the grains of the pure oxides. This effect, together with the possible sintering processes occurring at high temperature, suggests that the OER activity might be modified after electrode annealing. This point was checked by measuring the electrochemical performance of a *1.8-CuCoO* film supported on two different substrates, carbon paper (*1.8-CuCoO-450/CP*) and ITO (*1.8-CuCoO-450/ITO*), after heating these samples for two hours at 500 $^{\circ}$C. To control any possible secondary effect resulting from substrate heating, these ones were heated at 500 $^{\circ}$C before the deposition of the amorphous anodic film. Electrocatalytic OER activities of these systems were examined by cyclic voltammetry in the half cell configuration.
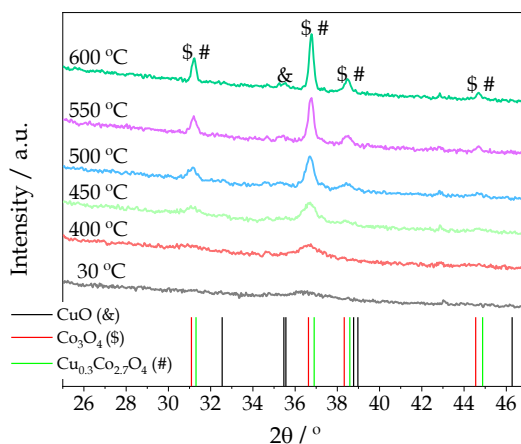
Figure 4.8*. X-Ray patterns of 1.8-CuCoO-450/CP sample annealed at increasing
temperatures. Most significant diffraction lines of CuO (PDF: 01-080-1268), Co_3O_4
(PDF: 01-080-1535), and $Cu_{0.3}Co_{2.7}O_4$ (PDF: 00-025-0270) phases are included.*

Figure 4.9 shows the cyclic voltammetry curves obtained for as
deposited and 500 °C annealed samples deposited on carbon paper and
ITO substrates, respectively. The higher electrocatalytic activity found
with carbon paper can be attributed to the higher electrical conductivity
and easier electrolyte accessibility in this substrate. However, in the two
cases, the electrocatalytic activity decreased after annealing at 500 °C, thus
supporting our considerations about the nature of the most efficient
catalyst sites and/or pointing out a possible detrimental effect due to
sintering [28]. From a practical point of view, these results disregard the
need of any annealing treatment when using MS-OAD thin films as
electrodes, thus simplifying their manufacturing procedure.
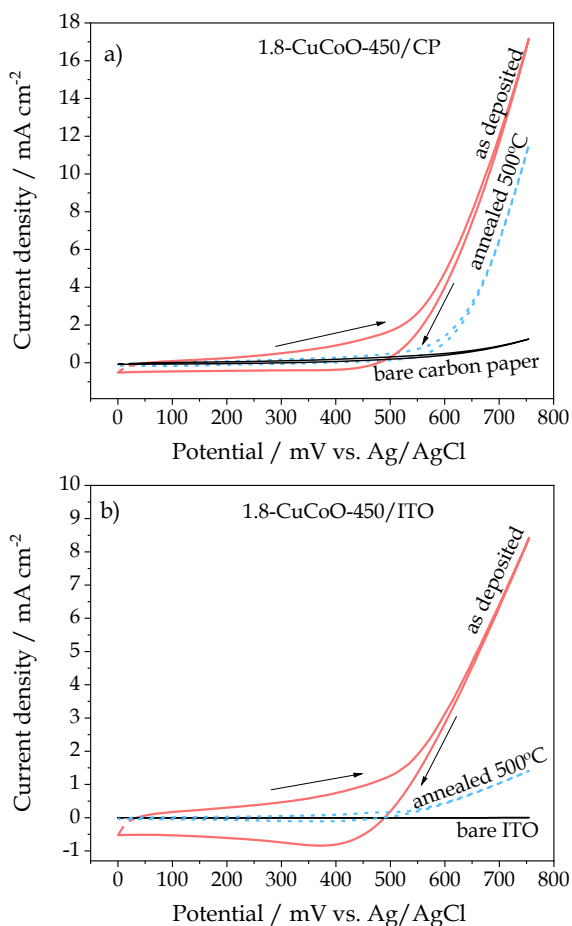
Figure 4.9. Cyclic voltammetry curves of as deposited and crystallized a) 1.8-CuCoO-450/CP and b) 1.8-CuCoO-450/ITO samples evaluated with scan rate 20 mV s⁻¹ in 1.0 M KOH solution at room temperature.

4.3.4.   Scale-up to anion exchange membrane water electrolysis cell

To test the performance of the $Cu_xCo_yO_z$ anodic thin films under real operation conditions, experiments were carried out with the *1.8-CuCoO-450/CP* electrode integrated in a single electrolysis cell, provided with an anion exchange membrane in a MEA configuration and Ni thin film acting as cathode. The linear voltammetry curves in **Figure 4.10 a)** were

obtained at several temperatures with 1.0 M KOH solution, while in
Figure 4.10 b) the curves correspond to various electrolyte solutions at 40
^oC. In good agreement with other studies [17], recorded density curves
show that a first activation exponential region is triggered at a potential
threshold around 1.5 V (see Figure 4.10 a)) and then, it is followed by a
lineal ohmic region, for current densities higher than 30 mA cm^{-2}. As
expected, at constant intensity, cell potential decreased with increasing
temperature due to an increase in both: the hydroxyl ion conductivity
through the membrane and in the rate of catalytic hydrogen and oxygen
evolution [34]. It can be also observed in Figure 4.10 a) that the electrolysis
onset potential slightly decreases from 1.60 V at 25 ^oC to 1.56 V at 70 ^oC.
The highest cell performance was found at 70 ^oC, when it reached a
current density of 110 mA cm^{-2} at 2.2 V. It is worth stressing that this value
is close to that reported in literature for highly performance cells and
electrodes incorporating anion exchange membranes (AEM) and much
higher catalyst loads [16,30].

Figure 4.10 b) also shows that an increase in KOH concentration
enhances the electrolyzer performance, an effect that can be attributed to
both an increase in ion conductivity through the membrane and in the
anode electrocatalyst activity at higher pH values [8]. This behavior
agrees with previous results reporting a lower internal resistance of the
cells at higher pHs [34–37]. A significant influence of ion conductivity in
the experiments in Figure 4.10 b) can be traced from the decrease in onset
potential from 1.65 V for deionized water to 1.55 V for 2.0 M KOH
solution, and by the fact that the lowest electrocatalytic performance was
obtained with pure deionized water (pH=6.0) and, therefore, a negligible
concentration of OH$^-$ ions.
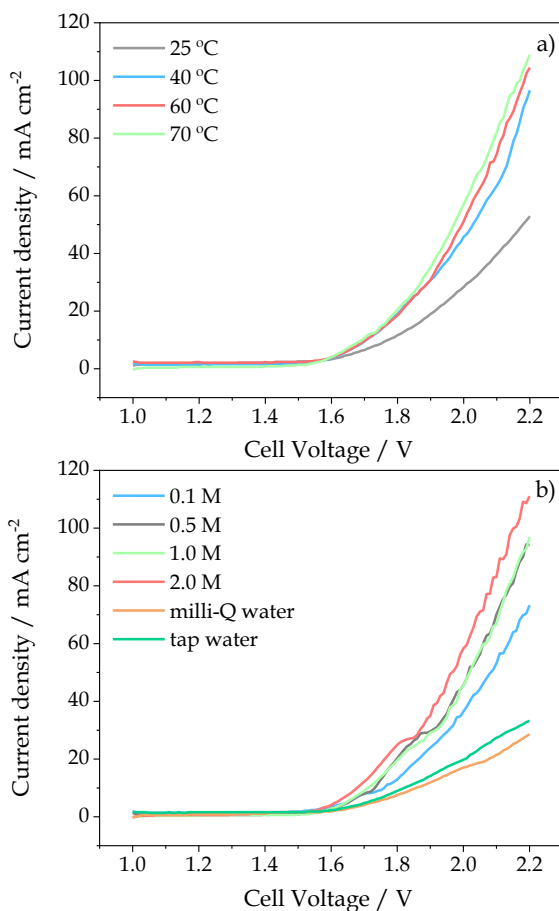
Figure 4.10. Influence of a) the temperature (1.0 M KOH solution at temperature of 25, 40, 60, 70 ºC) and b) the electrolyte (at 40 ºC using different KOH concentration and water) on the polarization curves of the electrolysis cell.

As part of this analysis of the MEA, experiments similar to those in Figure 4.10 carried out with annealed anode films (at 500 ºC) revealed a clear decrease in performance in this case (see the i-V curves as a function of temperature and electrolyte type in **Figure 4.11**). This behavior confirmed the results in Figure 4.9 about the deleterious effect on catalytic

performance of segregation and/or crystallization processes occurring
during heating.
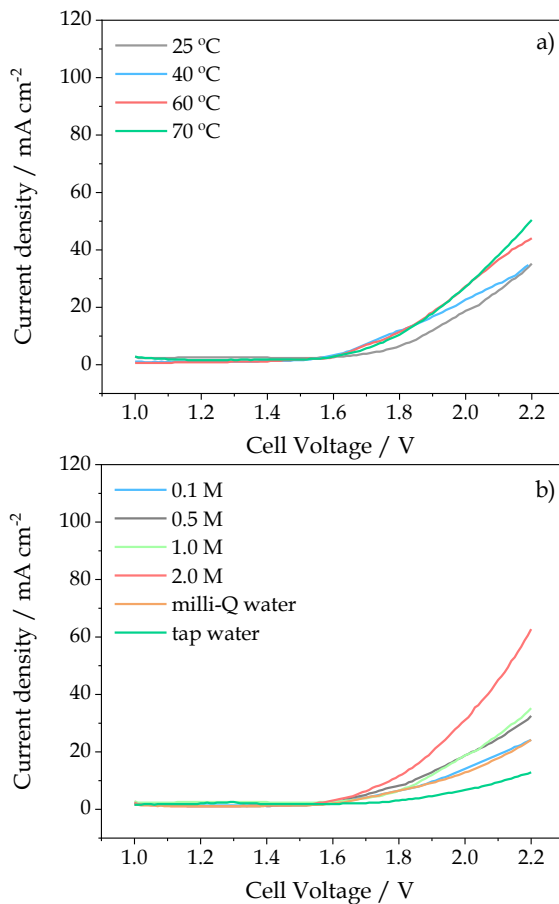
Figure 4.11. *Influence of a) the temperature (1 M KOH solution at temperature of 25,
40, 60, 70 °C) and b) the electrolyte (at 40 °C using different KOH concentration and
water) on the polarization curves of the electrolysis cell.*

A decrease in performance could be also consistent to the observed EIS
analysis carried out with the MEA incorporating either as deposited or
annealed anodes (see **Figure 4.12** and the resistance values in **Table 4.2**
derived according to the equivalent RC circuit included as an inset in the

figure [38,39]). Thus, the anodic charge transfer resistance [38,39] of the
annealed anode at 1.7 V was higher than that of the as deposited anode
(3.0 Ω vs 1.89 Ω, see Table 4.2), which justify the observed lower OER
performance of the annealed anode.
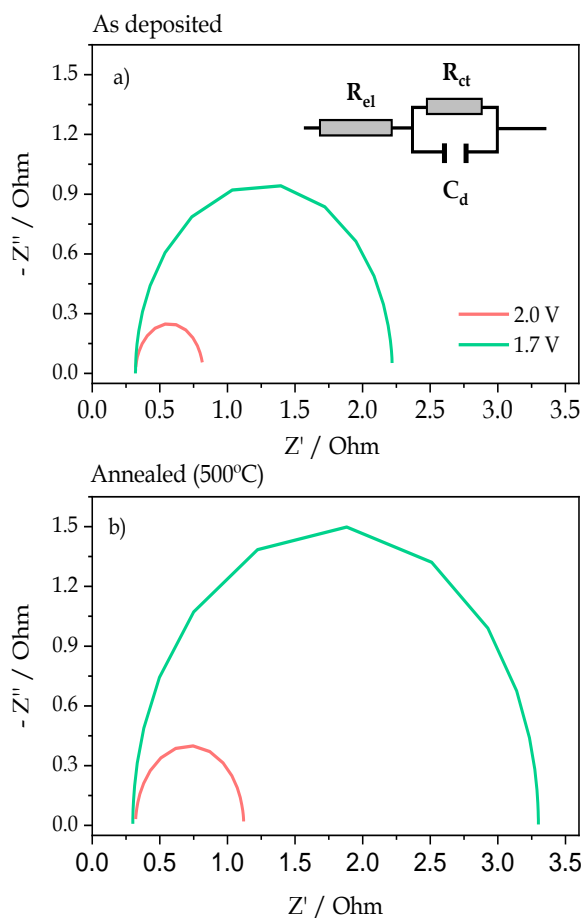
*Figure 4.12. Simulation of the impedance spectra of the cell at a constant potential of
1.7 V and 2.0 V with as deposited a) and annealed b) 1.8-CuCoO-450/CP electrode.
The inset shows the RC circuit used for the fitting of the experimental data (R_{el}: ohmic
resistance of the membrane; R_{ct} charge transfer resistance at the anode; C_d double layer
capacity at the anode)*

Table 4.2. *Ohmic resistance of the membrane electrolyte R_{el} and combined mass and charge transfer resistance at the anode R_{ct} obtained from simulated Nyquist plots in Figure 4.12.*

		R_{el} / Ω	R_{ct} / Ω
As deposited	**1.7 V**	0.32	1.89
	2.0 V	0.32	0.49
Annealed (500 ºC)	**1.7 V**	0.30	3.00
	2.0 V	0.32	0.80

Stability tests were also carried out with the MEA at an intermediate electrolyte concentration of 1.0 M and 40 ºC to avoid a too corrosive environment [40]. Under these conditions, the V-t plot in **Figure 4.13** shows the stability of the cell for 18 hours operation at 25 mA cm^{-2} constant current. The curve depicts a sharp voltage increase at the beginning of the experiment that is followed by a rather constant voltage at the end of the experiment [6,41]. Since the generated volume of hydrogen as a function of time followed the linear tendency predicted by the Faraday law (see inset in Figure 4.13, corresponding to the H_2 evolution during the first 30 minutes of operation), and a longer stability of the anode was proved by the three-electrode cell experiments (Figure 4.5 b)), we attribute the observed slight deactivation with time to a certain degradation of the membrane (e.g., affecting the polymer backbone or the ion exchange groups). Nonetheless, the hydrogen energy production yield of 51 kW (kgH$_2$)$^{-1}$ determined in this experiment is similar to other values obtained with AEM electrolyzers and conventional electrode materials [35].
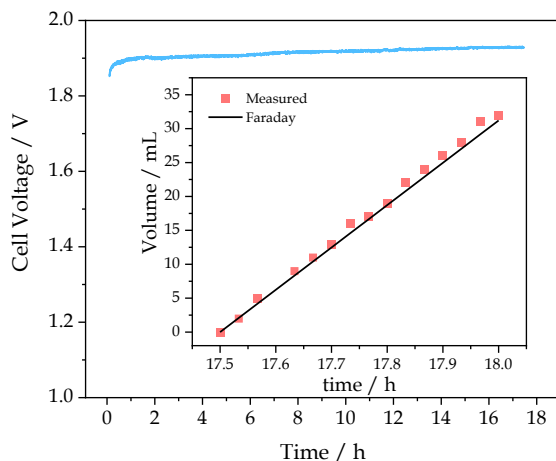
Figure 4.13. Chronopotentiometry experiment using a constant current density of 25 mA cm^{-2} at 40 °C in a 1.0 M KOH solution. Inset: comparison of the measured and Faradaic hydrogen production.

To put in context the MEA performance herein obtained, **Table 4.3** summarizes a series of published AEM electrolysis results carried out with similar catalysts and working conditions, except for the use of different ionomers (ionomers are compounds used to enhance electrolysis performance by creating transport pathways between membrane and reaction sites [1,35]). Although the absolute electrocatalytic activity of our system is lower than that reported in these MEAs studies (for example in ref. [3] using 3 mg cm^{-2} Cu$_x$Co$_y$O$_z$ well-crystallized nanoparticles as anode and 1 mg Pt cm^{-2} as cathode they obtained 1000 mA cm^{-2} at 1.8 V), the extremely low amount of metal loading in our systems makes them the most efficient in terms of catalyst load. This high performance might be due to particular mesoporous microstructure of the deposited catalysts by MS-OAD. An additional advantage in terms of costs is the use of low load of Ni cathode catalyst, also prepared at room temperature by MS. Finally, also to mention that

the cost associated with the traditional annealing processes needed to obtain a well crystallize mixed cobaltite catalysts is also removed.

Table 4.3. Comparison of our results with previous studies using milli-Q water as anodic feeding stream. *Normalized current at 2.0 V with milli-q water.

Anode	Membrane	Cathode	Ionomer	Normalized Current* (mA mg^{-1})	Temperature (°C)	Ref.
Co_3O_4-CuO	Fumapem FAA-3-50	Ni	No	92.11	40	This study
$Cu_{0.7}Co_{2.3}O_4$	mm-qPVBz/Cl-	Ni	Yes	25.00	40	[16]
CuCoOx	Tokuyama A-201	Ni/(CeO$_2$-La$_2$O$_3$)/C	Yes	11.67	60	[1]
CuCoOx	QAPPO membrane	Ni/(CeO$_2$-La$_2$O$_3$)/C	Yes	74.00	60	[42]
$Cu_{0.7}Co_{2.3}O_4$	Prepared	Pt	Yes	73.33	25	[3]
$Cu_xMg_{0.9-x}Co_{2.1}O_4$	Prepared	Pt	Yes	66.67	40	[30]
$Cu_{0.7}Co_{2.3}O_4$	Cranfield-membrane	Ni	Yes	50.00	25	[43]

4.4.   Conclusions

The results obtained in this chapter have demonstrated, for the first time in the literature that active and stable $Cu_xCo_yO_z$ ultrathin electrodes can be prepared by MS-OAD at room temperature for their use in AEMWE cells. In fact, the normalized electrocatalytic activity per mass of metal load for the most active catalysts formulation reported here (i.e., Co/Cu atomic ratio of 1.8) exceeds the values obtained for other similar electrocatalyst systems. From a fundamental point of view, the electrochemical performance of the as deposited electrodes, together with the characterization of the used catalyst surfaces suggest that local arrangements combining one Cu and two Co cations constitute surface sites providing a maximum catalytic activity for the OER. Although further studies are still required to make the overall density current values competitive, the present chapter proves the feasibility of this preparation technique for OER catalyst fabrication and the development

of cheap and reliable electrolysis devices. The stability tests carried out in a three-electrode cell system and the MEA device confirm the suitability of this ultra-thin electrocatalysts for practical applications and support the use of MS-OAD for large area electrode fabrication.

4.5. References

[1]   I. Vincent, A. Kruger, D. Bessarabov, Development of efficient membrane electrode assembly for low cost hydrogen production by anion exchange membrane electrolysis, Int. J. Hydrogen Energy. 42 (2017) 10752–10761. https://doi.org/10.1016/j.ijhydene.2017.03.069.

[2]   K.E. Kang, C.H. Kim, M.S. Lee, C.W. Jung, Y. Do Kim, J.H. Lee, Stability of a $Cu_{0.7}Co_{2.3}O_4$ electrode during the oxygen evolution reaction for alkaline anion-exchange membrane water electrolysis, J. Korean Phys. Soc. 72 (2018) 52–56. https://doi.org/10.3938/jkps.72.52.

[3]   X. Wu, K. Scott, $Cu_xCo_{3-x}O_4$ ($0 \leq x < 1$) nanoparticles for oxygen evolution in high performance alkaline exchange membrane water electrolysers, J. Mater.   Chem.   21   (2011)   12344–12351. https://doi.org/10.1039/c1jm11312g.

[4]   M. Hamdani, R.N. Singh, P. Chartier, Co_3O_4 and co-based spinel oxides bifunctional oxygen electrodes, Int. J. Electrochem. Sci. 5 (2010) 556–577.

[5]   I. Nikolov, R. Darkaoui, E. Zhecheva, R. Stoyanova, N. Dimitrov, T. Vitanov, Electrocatalytic activity of spinel related cobalties $M_xCo_{3-x}O_4$ (M = Li, Ni, Cu) in the oxygen evolution reaction, J. Electroanal. Chem. 429 (1997) 157–168. https://doi.org/10.1016/S0022-0728(96)05013-9.

[6]   M.K. Cho, A. Lim, S.Y. Lee, H.-J. Kim, S.J. Yoo, Y.-E. Sung, H.S. Park, J.H. Jang, A Review on membranes and catalysts for anion exchange membrane water electrolysis single cells, J. Electrochem. Sci. Technol. 8 (2017) 183–196. https://doi.org/10.5229/JECST.2017.8.3.183.

[7]   A. Calcerrada Martínez, A. De la Osa, H. Dole, F. Dorado, E. Baranova, A. Lucas-Consuegra, Stability testing of Pt_xSn_{1-x}/C anodic catalyst for renewable hydrogen production via electrochemical reforming of ethanol, Electrocatalysis. 9 (2018). https://doi.org/10.1007/s12678-017-0428-0.

[8] G. Gupta, K. Scott, M. Mamlouk, Performance of polyethylene based radiation grafted anion exchange membrane with polystyrene-b-poly (ethylene/butylene)-b-polystyrene based ionomer using NiCo$_2$O$_4$ catalyst for water electrolysis, J. Power Sources. 375 (2018) 387–396. https://doi.org/10.1016/j.jpowsour.2017.07.026.

[9] A. Barranco, A. Borras, A.R. Gonzalez-Elipe, A. Palmero, Perspectives on oblique angle deposition of thin films: From fundamentals to devices, Prog. Mater. Sci. 76 (2016) 59–153. https://doi.org/10.1016/j.pmatsci.2015.06.003.

[10] J.-P. Biethan, D. Arhilger, J. Pistner, H. Reus, M. Stapp, H. Hagedorn, High precision optical filter based on magnetron sputtering, Vak. Forsch. Und Prax. 29 (2017) 26–31. https://doi.org/10.1002/vipr.201700654.

[11] J. Gil-Rostra, F. García-García, F. Yubero, A.R. González-Elipe, Tuning the transmittance and the electrochromic behavior of Co$_x$Si$_y$O$_z$ thin films prepared by magnetron sputtering at glancing angle, Sol. Energy Mater. Sol. Cells. 123 (2014) 130–138. https://doi.org/10.1016/j.solmat.2013.12.020.

[12] J. Gil-Rostra, M. Cano, J.M. Pedrosa, F.J. Ferrer, F. García-García, F. Yubero, A.R. González-Elipe, Electrochromic behavior of W$_x$Si$_y$O$_z$ thin films prepared by reactive magnetron sputtering at normal and glancing angles, ACS Appl. Mater. Interfaces. 4 (2012) 628–638. https://doi.org/10.1021/am2014629.

[13] J. Gil-Rostra, F.J. García-García, F.J. Ferrer, A.R. González-Elipe, F. Yubero, Microstructure of mixed oxide thin films prepared by magnetron sputtering at oblique angles, Thin Solid Films. 591 (2015) 330–335. https://doi.org/10.1016/j.tsf.2015.01.058.

[14] R. Alvarez, J.M. Garcia-Martin, M.C. Lopez-Santos, V. Rico, F.J. Ferrer, J. Cotrino, A.R. Gonzalez-Elipe, A. Palmero, On the deposition rates of magnetron sputtered thin films at oblique angles, Plasma Process. Polym. 11 (2014) 571–576. https://doi.org/10.1002/ppap.201300201.

[15] J. Jia, X. Li, G. Chen, Stable spinel type cobalt and copper oxide electrodes for O$_2$ and H$_2$ evolutions in alkaline solution, Electrochim. Acta. 55 (2010) 8197–8206. https://doi.org/10.1016/j.electacta.2010.04.026.

[16] Y.-C. Cao, X. Wu, K. Scott, A quaternary ammonium grafted poly vinyl benzyl chloride membrane for alkaline anion exchange membrane water electrolysers with no-noble-metal catalysts, Int. J. Hydrogen Energy. 37

(2012) 9524–9528. https://doi.org/10.1016/j.ijhydene.2012.03.116.

[17]   X. Wu, K. Scott, A Li-doped Co_3O_4 oxygen evolution catalyst for non-precious metal alkaline anion exchange membrane water electrolysers, Int. J. Hydrogen Energy. 38 (2013) 3123–3129. https://doi.org/10.1016/j.ijhydene.2012.12.087.

[18]   P. Salazar, F.J. Garcia-Garcia, F. Yubero, J. Gil-Rostra, A.R. González-Elipe, Characterization and application of a new pH sensor based on magnetron sputtered porous WO_3 thin films deposited at oblique angles, Electrochim. Acta. 193 (2016) 24–31. https://doi.org/10.1016/j.electacta.2016.02.040.

[19]   F.J. Garcia-Garcia, P. Salazar, F. Yubero, A.R. González-Elipe, Non-enzymatic Glucose electrochemical sensor made of porous NiO thin films prepared by reactive magnetron sputtering at oblique angles, Electrochim. Acta. 201 (2016) 38–44. https://doi.org/10.1016/j.electacta.2016.03.193.

[20]   A. de Lucas-Consuegra, A.R. de la Osa, A.B. Calcerrada, J.J. Linares, D. Horwat, A novel sputtered Pd mesh architecture as an advanced electrocatalyst for highly efficient hydrogen production, J. Power Sources. 321 (2016) 248–256. https://doi.org/10.1016/j.jpowsour.2016.05.004.

[21]   M. Polyakov, A.-E. Surkus, A. Maljusch, S. Hoch, A. Martin, Impact of Co:Cu ratio of CoCu-containing oxidic solids on their activity for water splitting reaction, ChemElectroChem. 4 (2017). https://doi.org/10.1002/celc.201700124.

[22]   M.E.A. Warwick, G. Carraro, D. Barreca, A. Gasparotto, C. Maccato, TiO_2-Fe_2O_3 and Co_3O_4-Fe_2O_3 nanocomposites analyzed by X-ray photoelectron Spectroscopy, Surf. Sci. Spectra. 22 (2015) 34–46. https://doi.org/10.1116/1.4934573.

[23]   V.M. Jiménez, A. Fernández, J.P. Espinós, A.R. González-Elipe, The state of the oxygen at the surface of polycrystalline cobalt oxide, J. Electron Spectros. Relat. Phenomena. 71 (1995) 61–71. https://doi.org/10.1016/0368-2048(94)02238-0.

[24]   J.P. Espinós, J. Morales, A. Barranco, A. Caballero, J.P. Holgado, A.R. González-Elipe, Interface effects for Cu, CuO, and Cu_2O deposited on SiO_2 and ZrO_2. XPS determination of the valence state of copper in Cu/SiO_2 and Cu/ZrO_2 catalysts, J. Phys. Chem. B. 106 (2002) 6921–6929.

https://doi.org/10.1021/jp014618m.

[25]   A. Shanmugavani, R.K. Selvan, Improved electrochemical performances of $CuCo_2O_4/CuO$ nanocomposites for asymmetric supercapacitors, Electrochim. Acta. 188 (2016) 852–862. https://doi.org/10.1016/j.electacta.2015.12.077.

[26]   A. El-Trass, H. ElShamy, I. El-Mehasseb, M. El-Kemary, CuO nanoparticles: Synthesis, characterization, optical properties and interaction with amino acids, Appl. Surf. Sci. 258 (2012) 2997–3001. https://doi.org/10.1016/j.apsusc.2011.11.025.

[27]   L. Wei, X. Dong, M. Ma, Y. Lu, D. Wang, S. Zhang, D. Zhao, Q. Wang, Co_3O_4 hollow fiber: An efficient catalyst precursor for hydrolysis of sodium borohydride to generate hydrogen, Int. J. Hydrogen Energy. 43 (2018) 1529–1533. https://doi.org/10.1016/j.ijhydene.2017.11.113.

[28]   Q. Zhang, Z.D. Wei, C. Liu, X. Liu, X.Q. Qi, S.G. Chen, W. Ding, Y. Ma, F. Shi, Y.M. Zhou, Copper-doped cobalt oxide electrodes for oxygen evolution reaction prepared by magnetron sputtering, Int. J. Hydrogen Energy. 37 (2012) 822–830. https://doi.org/10.1016/j.ijhydene.2011.04.051.

[29]   B. Chi, H. Lin, J. Li, Cations distribution of $Cu_xCo_{3-x}O_4$ and its electrocatalytic activities for oxygen evolution reaction, Int. J. Hydrogen Energy. 33 (2008) 4763–4768. https://doi.org/10.1016/j.ijhydene.2008.05.032.

[30]   X. Wu, K. Scott, A non-precious metal bifunctional oxygen electrode for alkaline anion exchange membrane cells, J. Power Sources. 206 (2012) 14–19. https://doi.org/10.1016/j.jpowsour.2011.12.052.

[31]   X. Li, R. Ding, W. Shi, Q. Xu, D. Ying, Y. Huang, E. Liu, Hierarchical porous $Co(OH)F/Ni(OH)_2$: A new hybrid for supercapacitors, Electrochim. Acta. 265 (2018) 455–473. https://doi.org/10.1016/j.electacta.2018.01.194.

[32]   H.-X. Li, W. Hao, J. Hu, H. Wu, A photoelectrochemical sensor based on nickel hydroxyl-oxide modified n-silicon electrode for hydrogen peroxide detection in an alkaline solution, Biosens. Bioelectron. 47C (2013) 225–230. https://doi.org/10.1016/j.bios.2013.03.028.

[33]   L. Zhu, Y. Zheng, T. Hao, X. Shi, Y. Chen, J. Ou-Yang, Synthesis of hierarchical ZnO nanobelts via Zn(OH)F intermediate using ionic liquid-

assistant microwave irradiation method, Mater. Lett. - MATER LETT. 63
(2009) 2405–2408. https://doi.org/10.1016/j.matlet.2009.07.062.

[34]   C.C. Pavel, F. Cecconi, C. Emiliani, S. Santiccioli, A. Scaffidi, S.
Catanorchi, M. Comotti, Highly efficient platinum group metal free based
membrane-electrode assembly for anion exchange membrane water
electrolysis, Angew. Chemie Int. Ed. 53 (2014) 1378–1381.
https://doi.org/10.1002/anie.201308099.

[35]   I. Vincent, D. Bessarabov, Low cost hydrogen production by anion
exchange membrane electrolysis: A review, Renew. Sustain. Energy Rev.
81 (2018) 1690–1704. https://doi.org/10.1016/j.rser.2017.05.258.

[36]   L. Zeng, T.S. Zhao, Integrated inorganic membrane electrode assembly
with layered double hydroxides as ionic conductors for anion exchange
membrane water electrolysis, Nano Energy. 11 (2015) 110–118.
https://doi.org/10.1016/j.nanoen.2014.10.019.

[37]   Ö.F. Selamet, F. Becerikli, M.D. Mat, Y. Kaplan, Development and testing
of a highly efficient proton exchange membrane (PEM) electrolyzer stack,
Int. J. Hydrogen Energy. 36 (2011) 11480–11487.
https://doi.org/10.1016/j.ijhydene.2011.01.129.

[38]   H. Ju, S. Giddey, S.P.S. Badwal, R.J. Mulder, Electro-catalytic conversion
of ethanol in solid electrolyte cells for distributed hydrogen generation,
Electrochim. Acta. 212 (2016) 744–757.
https://doi.org/10.1016/j.electacta.2016.07.062.

[39]   N. Wagner, M. Schulze, Change of electrochemical impedance spectra
during CO poisoning of the Pt and Pt–Ru anodes in a membrane fuel cell
(PEFC), Electrochim. Acta. 48 (2003) 3899–3907.
https://doi.org/10.1016/S0013-4686(03)00528-0.

[40]   A. Lim, M.K. Cho, S.Y. Lee, H.-J. Kim, S.J. Yoo, Y.-E. Sung, J.H. Jang, H.S.
Park, A review of industrially developed components and operation
conditions for anion exchange membrane water electrolysis, J.
Electrochem. Sci. Technol. 8 (2017) 265–273.
https://doi.org/10.5229/JECST.2017.8.4.265.

[41]   P. Ganesan, A. Sivanantham, S. Shanmugam, Nanostructured nickel–
cobalt–titanium alloy grown on titanium substrate as efficient
electrocatalyst for alkaline water electrolysis, ACS Appl. Mater.
Interfaces. 9 (2017) 12416–12426.
https://doi.org/10.1021/acsami.7b00353.

[42] L. Zeng, T.S. Zhao, An effective strategy to increase hydroxide-ion conductivity through microphase separation induced by hydrophobic-side chains, J. Power Sources. 303 (2016) 354–362. https://doi.org/10.1016/j.jpowsour.2015.11.019.

[43] X. Wu, K. Scott, A polymethacrylate-based quaternary ammonium OH⁻ ionomer binder for non-precious metal alkaline anion exchange membrane water electrolysers, J. Power Sources. 214 (2012) 124–129. https://doi.org/10.1016/j.jpowsour.2012.03.069.

Chapter 5

Optimization of $Cu_xCo_yO_z$ anodic electrodes and active sites chemical analysis
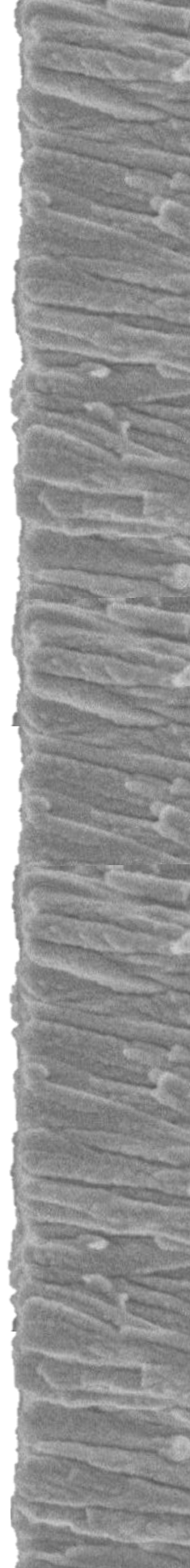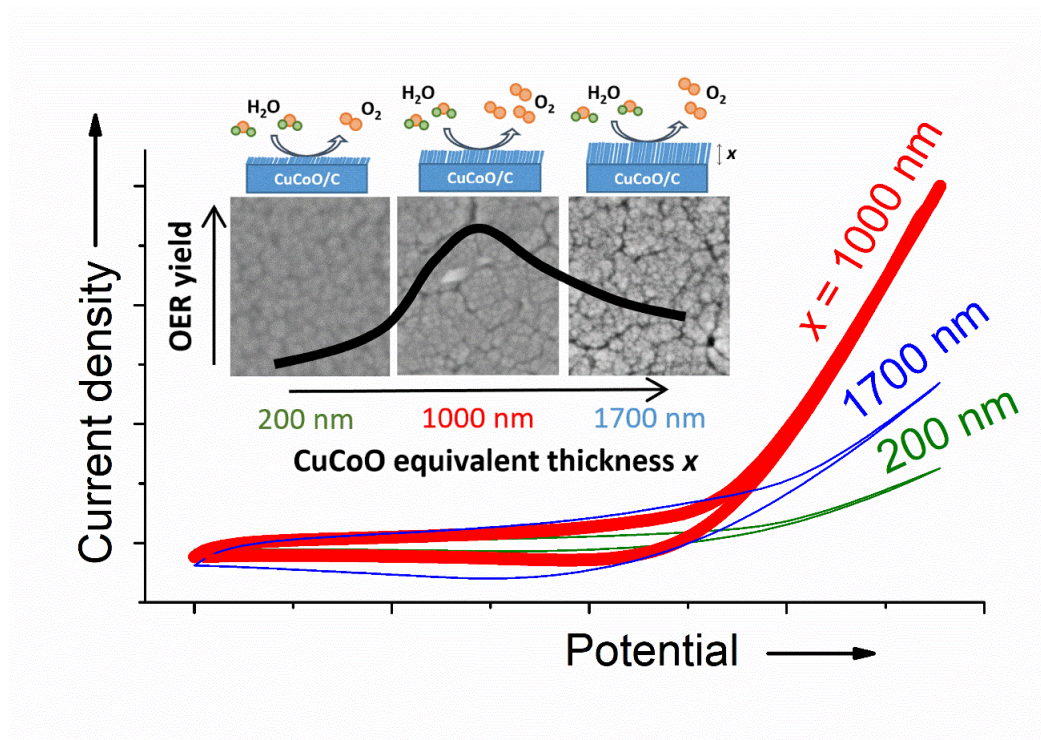
The content of this chapter has been published in:

5.1. Introduction

In Chapter 4, we have demonstrated that copper-cobalt mixed oxides anode catalysts with Co/Cu atomic ratio of 1.8 prepared by magnetron sputtering in an oblique angle configuration (MS-OAD) at room temperature are a good choice for AEMWE cells [1]. Herein, besides deepening our understanding of this type of anode catalysts, we report on critical electrode characteristics that contribute to control the AEMWE cell performance, such as the morphology and chemical properties of the mixed oxide electrodes. For this purpose, we first have investigated the chemical characteristics of the active sites involved in the OER following, by means of X-ray absorption spectroscopy (XAS) the O K, Co $L_{2,3}$ and Cu $L_{2,3}$ edges [2], the changes induced when various $Cu_xCo_yO_z$ anodes are immersed in the alkaline water solution electrolyte and thereafter subjected to a positive polarization (i.e., oxygen evolution reaction, OER, conditions).

Then, using a three-electrode cell configuration, we have studied how the catalyst thickness (or load), electrochemical surface area and other morphological properties of the electrodes contribute to increase the current density.

The information provided by XAS and that stemming from the electrochemical tests carried out in a three-electrode cell configuration has been complemented with a thorough electrochemical analysis in a membrane electrode assembly (MEA) with a design typical of AEMWE final devices. The optimum thickness and microstructure of the copper-cobalt mixed oxide anodes have also revealed to be highly performant in a MEA. The chemical, structural and microstructural factors controlling the final behavior of these anodes and accounting for this maximization

of the reaction yield are discussed based on these results and as a function
of preparation variables of the electrodes and operating conditions of the
cell.

5.2. Experimental

Copper-cobalt mixed oxide catalyst anodes with the optimum Co/Cu
atomic ratio of 1.8 towards OER identified in Chapter 4 were prepared by
co-deposition from two independent sources (Cu and Co targets) with the
experimental procedure described in Chapter 3. On the other hand,
metallic nickel cathode catalysts deposited on carbon paper gas diffusion
layer (GDL) were prepared as herein described in Chapter 3 and used as
cathodic electrodes in the electrochemical analysis of complete
electrolyzer cells.

Anode samples will be named as *1.8-CuCoO-thickness/XX* and *Co$_3$O$_4$-
thickness/XX,* where the first number in the label of the mixed oxide refers
the Co/Cu atomic ratio determined by EDX. Cathode samples will be
named as *Ni-thickness/XX. XX* is the support used in each electrode, *CP*
for carbon paper and *Si* for silicon substrate. In all cases thickness refers
to the *equivalent thickness* (in nanometers) determined on a polished
silicon wafer substrate located at an equivalent position of the sample
holder than the GDL substrates used in the electrochemical
characterizations.

The *equivalent thicknesses* of the mixed copper-cobalt oxide samples
varied between 100 and 1700 nm for the *1.8-CuCoO-100* and *1.8-CuCoO-
1700* samples, respectively. These thicknesses correspond to catalyst
loads of 0.04 and 0.68 mg cm^{-2}, as determined by RBS and confirmed by

weighting the electrodes before and after catalysts deposition. **Table 5.1** shows the calibration relationship found between the *equivalent thickness* and the catalyst load of the samples considered in this work. It is noteworthy that in all cases catalyst load was lower than 1.0 mg cm^{-2}.

Table 5.1. *Calibration between equivalent thickness and catalyst load of the different electrodes used in this work.*

Sample	Equivalent Thickness / nm	Catalyst Load / mg cm^{-2}
1.8-CuCoO-100/CP	100	0.04
1.8-CuCoO-200/CP	200	0.08
1.8-CuCoO-450/CP	450	0.18
1.8-CuCoO-1000/CP	1000	0.40
1.8-CuCoO-1700/CP	1700	0.68

The microstructure of the different catalysts deposited both onto carbon paper GDL and silicon wafer substrates was characterized by scanning electron microscopy (SEM). In the latter case, both top and cross-section views were acquired.

XAS measurements were carried out at the CIRCE beam line of ALBA Synchrotron Light Source (Barcelona, Spain). In these experiments, *1.8-CuCoO-50/Si* and *Co₃O₄-50/Si* thin films, prepared in the same manner for comparative purpose, were studied. The small thickness of these electrodes was selected to approximately fit the probing depth of the technique. O *K*, Co *L$_{2,3}$*, and Cu *L$_{2,3}$* absorption spectra were recorded for the as prepared samples (i.e., exposed to the air), after their immersion in 1.0 M KOH electrolyte for 30 minutes, and after working as anode for the OER at 750 mV vs. Ag/AgCl for 30 minutes. The electrolyte immersed and polarized electrodes were rinsed with distilled water and handled in air for about 5-10 minutes (maximum exposure time to air) previously to their insertion in the XAS apparatus.

All the physico-chemical characterization techniques used in this study have been previously explained in Chapter 3.

The effect of the load of $Cu_xCo_yO_z$ mixed oxide catalyst deposited on carbon paper in the OER performance, the determination of electrochemical surface area (ECSA) and impedance analysis were determined by electrochemical experiments performed in a three-electrode cell as has been previously explained in Chapter 3.

Finally, the study of the electrochemical performance of the MEA in AEMWE configuration was carried out with the mixed copper-cobalt oxide electrode given the best OER performance in the half-cell configuration analysis (i.e., *1.8-CuCoO-1000/CP*, catalyst load 0.40 mg cm^{-2}). These results have been comparatively discussed in relation with previously reported results by our group [1] (Chapter 4 in this thesis). The cathode of these MEAs was a *Ni-540/CP* (catalyst load of 0.38 mg cm^{-2}). Experiments were performed at temperatures varying from 30 to 70 $^{\circ}$C. A 1.0 M KOH electrolyte solution was fed into both anode and cathode compartments. The device stability was studied by means of 200 cyclic voltammetry (CV) experiments and constant-current (25 mA cm^{-2}) chronopotentiometric measurements for 45 hours, both experiments performed at 40 $^{\circ}$C.

5.3.   Results and discussion

5.3.1.   XAS characterization of the chemical state of the $Cu_xCo_yO_z$ anodes

In the previous chapter of this thesis [1], we found a maximum OER performance for a Co/Cu atomic ratio of 1.8, the same stoichiometry selected here for analysis. In the course of the current investigation, we

have deeply studied the chemical state of these electrodes by XAS. **Figure 5.1** shows the Co L_3 and O K absorption edge spectra recorded for *1.8-CuCoO-50/Si* and *Co₃O₄-50/Si* electrodes, this latter used as reference. Spectra are reported for the as prepared samples, after their immersion in 1.0 M KOH aqueous electrolyte solution, and after they were subjected to positive polarization in an electrochemical cell under OER conditions. In previous surface studies in Chapter 4 of these samples by XPS, it was determined that Co³⁺ species are majority in the two cases although, as for pure and crystalline Co_3O_4 spinel [3], the presence of Co²⁺ species could not be discarded just by analysis of the Co *2p* photoemission spectra. Single and mixed cobalt oxides have been relatively well studied in the literature by XAS and several works relate the relative intensity of their main spectral features with the partition of Co³⁺/Co²⁺ cations in the oxides [3–5]. In line with these previous works, it appears that the shape of the Co L_3 edges in **Figure 5.1 a**), and particularly the main peak position of the Co L_3 edge at 782.7 eV, can be attributed to the presence of Co³⁺ ions, while the feature at 781.0 eV, as well as the shoulder at approximately 785.0 eV, are indications of the presence of Co²⁺ ions. This assignment of spectral features indicates that, with respect to sample *Co₃O₄-50/Si* where a mixture of Co³⁺ and Co²⁺ cations is expected, the concentration of Co²⁺ species in sample *1.8-CuCoO-50/Si* is depleted, very likely because of the presence of copper in its structure. Since the shape of the Cu $L_{2,3}$ absorption edge of these samples (see **Figure 5.2 a)**) is similar to that of Cu²⁺ species in CuO [6], we can argue that the incorporation of the Cu²⁺ cation in the mixed oxide structure plays an equivalent structural role than Co²⁺ ions in the pure spinel oxide and contributes to stabilize a relatively higher concentration of Co³⁺ species in the mixed oxide. It is noteworthy in this regard that the intensity of features associated to Co²⁺

progressively decreased in intensity as the concentration of copper in the films increased (e.g., see a comparison of samples *1.8-CuCoO-50/Si* and *0.9-CuCoO-50/Si* in **Figure 5.2 b)**).

The analysis of the O K absorption edges in **Figure 5.1 b)** also suggests a decrease in the relative concentration of Co^{2+} species in sample *1.8-CuCoO-50/Si* with respect to sample *Co_3O_4-50/Si*. Reported spectra of CoO_x oxides with a variable value of x [7] reveal a progressive decrease in the 3s and 3p contribution to the empty states of the system when the concentration of Co^{2+} species decreases. According to these studies, this entails an increase in the intensity of the spectral features at around 539.0 eV. The increase in the intensity of the small features at around 529.8 eV before the large and well-defined peak at 531.7 eV, resulting from the overlapping with 3d empty states of cobalt, further supports a decrease in the relative concentration of Co^{2+} species in sample *1.8-CuCoO-50/Si* with respect to *Co_3O_4-50/Si*.
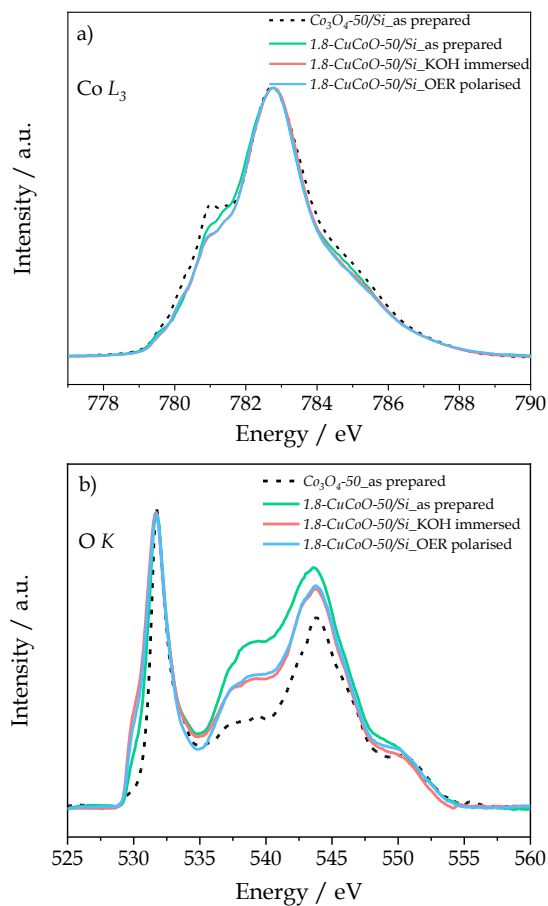
Figure 5.1. *a) Co L$_3$ and b) O K absorption spectra of an as prepared 1.8-CuCoO-50/Si sample anode, after immersion in 1.0 M KOH electrolyte, and after polarization at 750 mV (i.e., OER conditions). Reference spectra for an as prepared Co$_3$O$_4$-50/Si sample (dashed lines) are included for comparison.*
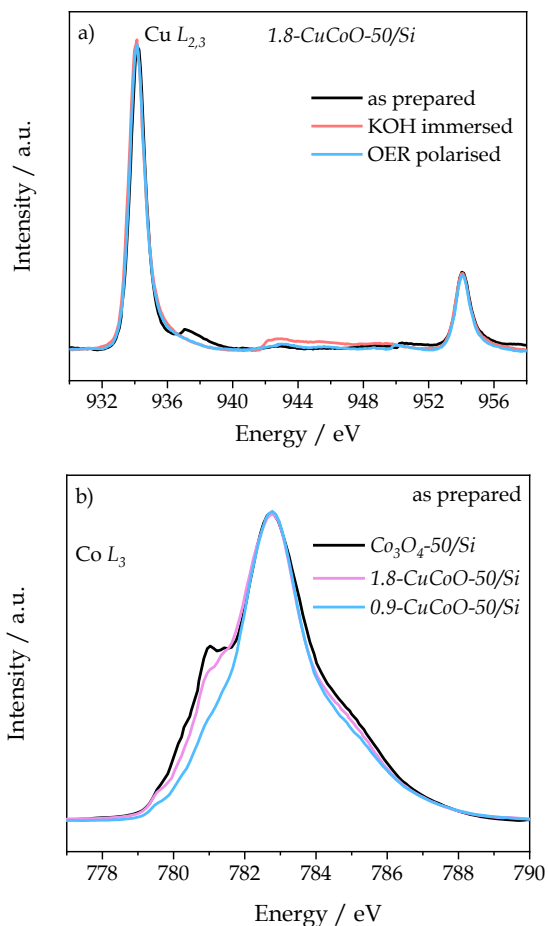
F*igure* 5.2. *a) Cu L$_{2,3}$ absorption spectra of 1.8-CuCoO-50/Si anode sample as prepared, after immersion in 1.0 M KOH electrolyte, and after polarization at 750 mV (i.e., OER conditions) in the same medium, b) Co L$_3$ absorption spectra of 1.8-CuCoO-50/Si, 0.9-CuCoO-50/Si and Co$_3$O$_4$-50/Si as prepared anode samples.*

Interestingly, when the *1.8-CuCoO-50/Si* electrode was immersed in the 1.0 M KOH basic solution and subjected to positive polarization (OER conditions), certain decrease in the intensity of the Co *L$_3$* feature at 781.0 eV and a significant decrease in the O *K* edge feature at ~543.8 eV were observed (see Figure 5.1). These changes suggest an increase in the

relative concentration of Co^{2+} species after these treatments. In this regard, a certain contradiction appears when comparing the previous changes with the increase in intensity of the shoulder at 529.8 eV observed at the O K edge in sample *1.8-CuCoO-50/Si* after immersion/polarization in the basic electrolyte solution. This contradiction can be released by admitting a certain modification of the coordination state of part of the tetrahedral Co^{2+} species into octahedral or D4h planar sites as recently reported for CoO thin film layers [5]. This XAS analysis revealed that, unlike the high stability found for sample *Co$_3$O$_4$-50/Si* (their Co L_3 and O K absorption spectra did not change when it was immersed in the basic solution and polarized at 750 mV vs. Ag/AgCl, see **Figure 5.3**), sample *1.8-CoCuO-50/Si* was rather labile and can experience surface transformations that bring its Co^{2+}/Co^{3+} ratio to a surface state close, but not identical, to that in sample *Co$_3$O$_4$-50/Si*. In particular, the observed increase in the concentration of Co^{2+} species is likely linked with the reported increase in the Co/Cu ratio at the surface of these electrodes determined by XPS after immersion in the basic solution in our previous study in Chapter 4 [1]. We would like to stress that the chemical lability of *1.8-CuCoO* electrodes deduced from this study does not imply a loss of stability as demonstrated by the straightforward cyclability of these electrodes, c.f. **Figure 5.4 a)** and suggests that this may be a good characteristic to maximize their OER performance. In a recent publication by Yan et al [3] dealing with the OER in acid medium using modified CoO$_x$ anodes, these authors found an increase in current density for processing conditions of the anode rendering a certain amount of Co^{2+} species. Our results here sustain the importance of mixed valence (i.e., Co^{2+}/Co^{3+}) active sites in the promotion of the OER, although at this stage is still unclear the type of involvement of the low valence cobalt cations.

The fact that the un-doped Co_3O_4 electrode does not perform well regarding OER and, at the same time, further quite stable from the viewpoint of XAS analysis supports this assumption (see **Figure 5.4 b)**).
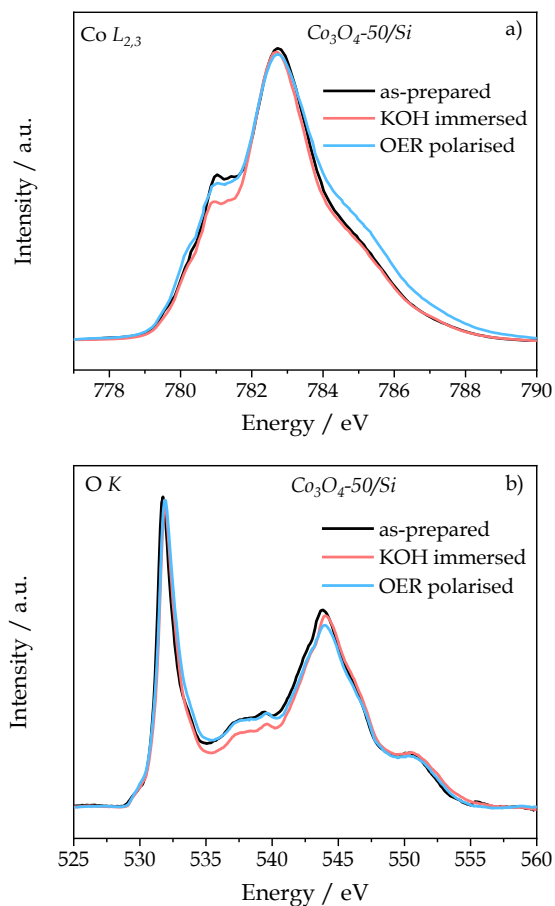
Figure 5.3. *a) Co L_3 and b) O K absorption edges acquired for Co_3O_4-50/Si sample as prepared, after immersion in 1.0 M KOH electrolyte, and after polarization at 750 mV (i.e., OER conditions) in the same medium.*
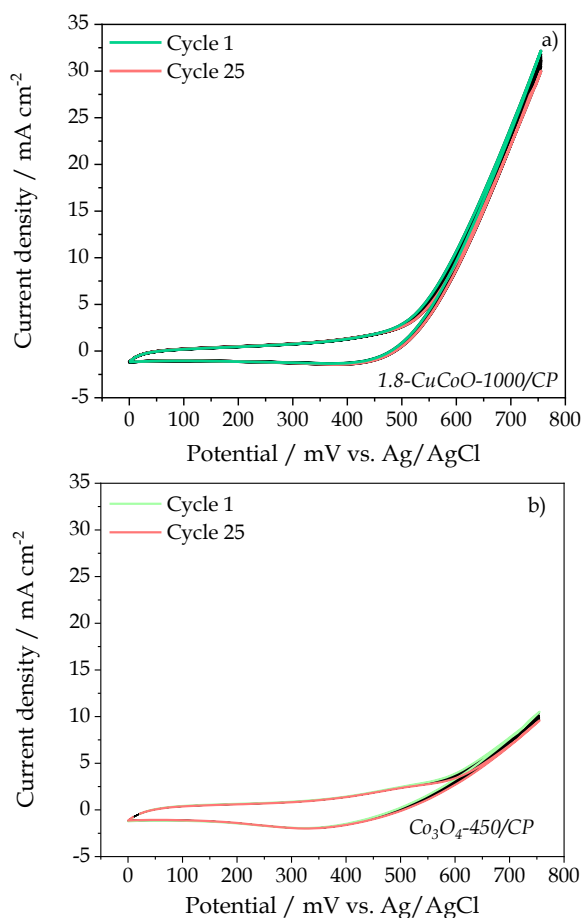
Figure 5.4. *Comparison of the first 25 CV experiments of a) 1.8-CuCoO-1000/CP and b) Co$_3$O$_4$-450/CP anode samples at 1.0 M KOH solution (Scan rate: 20 mV s^{-1}; voltage range: 0 to 750 mV vs. Ag/AgCl). 1st and 25th cycles are highlighted in green and red, respectively.*

5.3.2 Microstructure and effective electrochemical area of catalyst thin films

The influence of the amount of anodic catalyst on the OER efficiency has been studied analysing a series of *1.8-CoCuO* electrodes with different *equivalent thickness*. Owing to the importance of porosity and

135

microstructure on the performance of this type of electrodes, we have firstly investigated whether the surface microstructure of the catalyst films varies with thickness. We have carried out this analysis both on flat polished silicon wafers and on carbon paper GDL substrates utilized for the electrochemical analysis. **Figure 5.5** shows top view and cross section SEM images of *1.8-CuCoO-200*, *1.8-CuCoO-1000* and *1.8-CuCoO-1700* samples deposited on polished silicon substrates (Si), and the corresponding standard SEM images for the same loads on carbon paper GDL substrates (CP). Although, in general, the microstructure of the films deposited on flat substrates looks rather similar independently of the deposited thickness (see **Figures 5.5 a), d)** and **g)**), some particle agglomerations are observed in the thickest films. The films are formed by nanocolumns separated by voids as expected for a porous microstructure typical of MS-OAD preparation conditions (see **Figures 5.5 b), e)** and **h)**) [8–11]. In this kind of preparation, porosity and film roughness stem from shadow effects of deposited species during the growth of the films and the images of the examined thin films deposited on silicon prove that these shadow mechanisms are little affected upon deposition on flat substrates. The situation is rather different when the deposition is carried out on the carbon paper substrate used for the electrocatalytic studies. A common phenomenon observed during the MS-OAD of thin films on non-planar substrates, membranes or similar substrates is a change in the growth regime depending on the roughness characteristic of the support [12] and the thickness of the deposited layer [13]. According to SEM images of films deposited on carbon paper (**Figures 2 c), f)** and **i)**), an increase in *equivalent thickness* gives rise to a certain agglomeration into large-sized aggregates [14], as it can be observed in sample *1.8-CuCoO-1700/CP*. This evolution in the electrode

microstructure might entail a relative decrease in the number of surface-active sites and a certain loss of electrical conductivity due to a poorer grain connectivity, both features being detrimental for the OER activity.
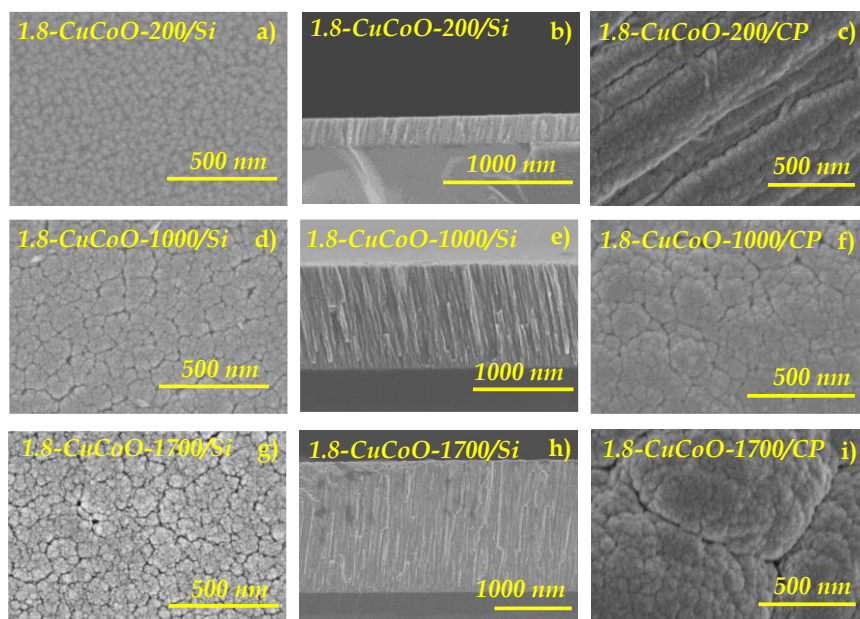
Figure 5.5. *Top view (left column) and cross section (middle column) SEM images of 1.8-CuCoO-200, 1.8-CuCoO-1000 and 1.8-CuCoO-1700 samples deposited on polished silicon substrates (Si). Right column: corresponding standard SEM images of the same catalyst loads deposited on carbon paper (CP) substrates.*

To assess the evolution of the surface active sites with increased electrode *equivalent thickness*, we assume their direct correlation with the ECSA determined using the electrochemical double-layer capacitance method [15–18]. Double layer capacitance C_{dl} was obtained from CV experiments performed in 1.0 M KOH electrolyte solution as described in the Chapter 3 of experimental details. **Figure 5.6 a)** shows CV curves for *1.8-CuCoO-1000/CP* sample recorded at several scan rates. The CV curves of the other examined samples are shown in **Figure 5.7**. The double layer capacitance C_{dl} was obtained from the slope of the linear regression of the

current density values vs. scan rate, acquired at 290 mV vs. Ag/AgCl (see **Figure 5.6 b)**). Note that, the C_{dl} values determined in this way are taken as proportional to the ECSA according to **Eq. (3.1)** of Chapter 3 [18]. In a previous study related to similar mixed cobalt-copper oxides, we found a C_s value of 40 mF cm^{-2} [16,19] for this capacitance used as reference.
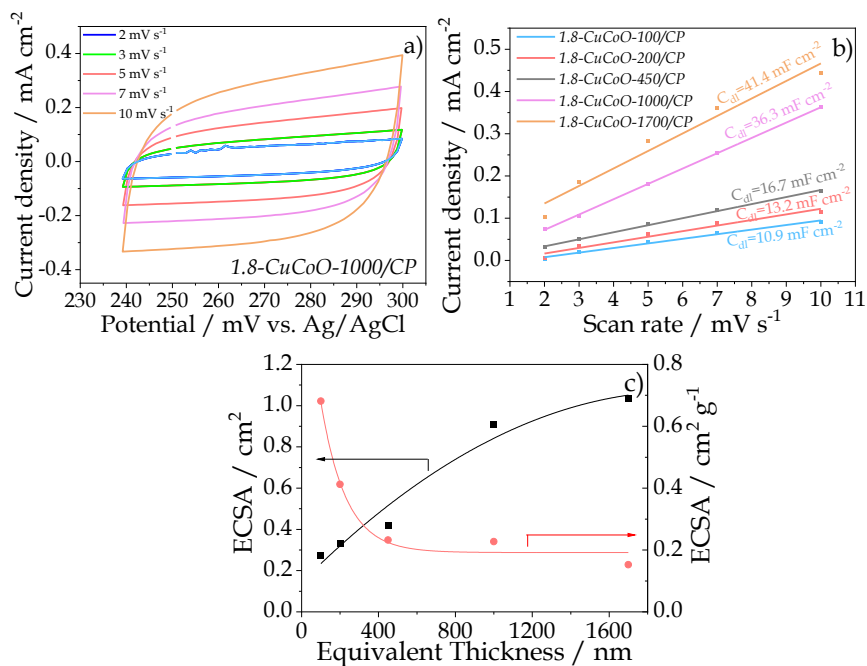
Figure 5.6. a) CV plots recorded at scan rates ranging from 2 to 10 mV s^{-1} for the 1.8-CuCoO-1000/CP electrode sample with a 1.0 M KOH solution. b) Current density vs. scan rate determined from CVs of the indicated electrodes. The slopes of the least square linear regressions define the double layer capacitance C_{dl} in each case. c) ECSA values (expressed in either cm^2 or cm^2 g^{-1} units) for several loads of 1.8-CuCoO-thickness/CP anodes.
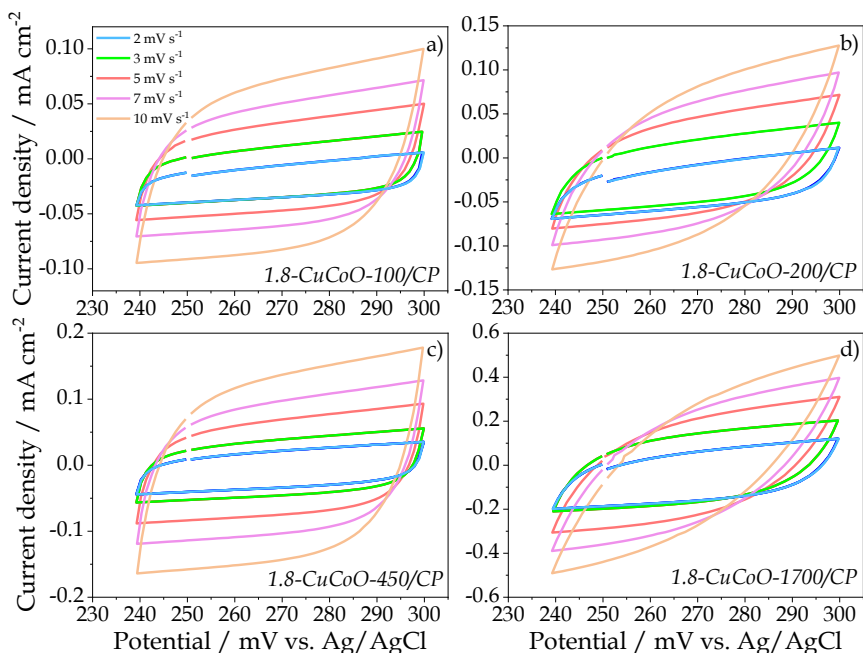
Figure 5.7. *CV plots acquired for 1.8-CuCoO-thickness/CP anodes with different loads,
a) 100 nm, b) 200 nm, c) 450 nm, and d) 1700 nm equivalent thicknesses, recorded at
various scan rates, as indicated at 1.0 M KOH solution (Scan rate from 2 to 10 mV s^{-1}).*

ECSA values expressed in area units, as determined by **Eq. (3.1)** (see
Figure 5.6 c)), increase about linearly with the amount of deposited
catalyst up to 1000 nm *equivalent thickness*, indicating that blocking of the
available active sites is not critical for this range of loads. For higher loads,
i.e., 1700 nm, ECSA keeps increasing, but at lower rate. We attribute this
feature to the agglomeration of the electrode material. This is clearly
evidenced when representing the ECSA in normalized area units to the
catalyst load (also in Figure 5.6 c)) showing a progressive decrease with
the amount of active phase. It is noteworthy that these ECSA values are
similar or even higher than those previously reported for other Cu-
incorporated cobalt oxide catalysts [16].

5.3.3. <u>Anode electrochemical performance for oxygen evolution reaction</u>

A main objective of the present chapter was to determine the morphological and electrochemical factors contributing to maximize the OER yield with *1.8-CuCoO* electrodes. In this section, we firstly analyse the evolution of performance with the electrode thickness and secondly, we correlate the observed evolutions with the morphological and electrical characteristics of the electrodes.

Figure 5.8 a) shows the electrochemical cycling behaviour of various electrodes with *equivalent thickness* between 100 and 1700 nm. The experiments were carried out at room temperature in a 1.0 M KOH electrolyte solution. In this set of CVs a sharp current increase starts at voltages above 500 mV vs. Ag/AgCl, i.e., corresponding to the OER onset potential [20–22], and the curves present different slopes and maximum current density values depending on the *equivalent thickness* of the anode. The highest current density values were found for sample *1.8-CoCuO-1000/CP.* An increase in the electrocatalytic OER yield (i.e., value of the corresponding current density) can be associated to an increase in the amount of catalyst and/or to the increase in the number of the available electrocatalytic active sites at the surface [23]. The series of cyclic voltammetries in Figure 5.8 a) clearly show an increase in current density for higher catalyst loads. This tendency breaks down for an anode *equivalent thickness* higher than 1000 nm. Tentatively, we associate the decrease in current density found for sample *1.8-CoCuO-1700/CP* with an increase in the agglomeration degree of the catalyst deposits as observed by SEM (c.f., Figure 5.5) (a similar effect has been reported in refs. [14,24]). In fact, an increase in the charge transfer resistance through the electrode may contribute to this effect as will be shown by EIS analysis below [25].
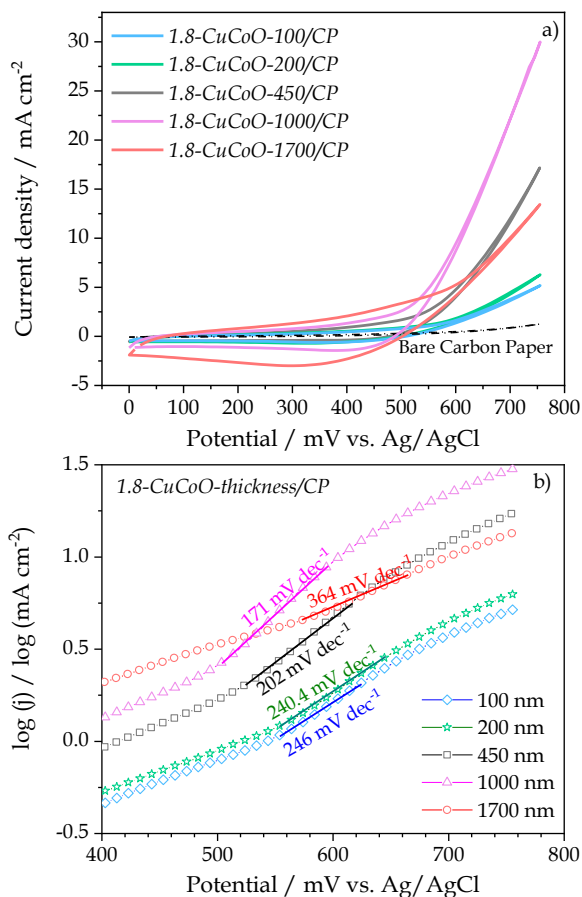
Figure 5.8. a) Cyclic voltammograms recorded for 1.8-CuCoO-thickness/CP anode samples with increasing equivalent thickness (1.0 M KOH solution, scan rate 20 mV s^{-1}). The behaviour of a bare carbon paper is included for comparison. b) Log (j) vs. mV Tafel plots corresponding to 1.8-CuCoO-thickness/CP anodes with different loads, identified by their equivalent thickness. The Tafel slopes obtained from the linear regression to the onset of the OER are indicated.

A closer look to the cyclic voltammetries in Figure 5.8 a) reveals that the minimum onset potential for OER found in sample *1.8-CuCoO-1000/CP* (i.e., around 500 mV vs. Ag/AgCl) is similar or even lower than that reported in previous studies for cobalt/copper mixed oxides [26–28]. In addition, this analysis reveals the development of small and broad

141

anodic and cathodic spectral features with a different intensity depending on the electrode thickness. They appear at approximately 500 mV and 300 mV vs. Ag/AgCl and can be attributed to the Co(III)/Co(IV) oxidation and the reverse reduction redox couples, respectively, as has been previously explained in Chapter 4 [20,29,30]. These features depicted maximum intensities for sample *1.8-CuCoO-1700/CP*, thus inducing a shift in the OER onset potential to around 600 mV vs. Ag/AgCl that suggests the existence of a certain overpotential and/or a poorer electrocatalytic activity for this reaction.

A systematic way to assess the electrocatalytic activity of this kind of electrodes entails the determination of the corresponding Tafel slopes. Higher Tafel slopes are related to a lower electrocatalytic activity and a slower kinetic of the electron exchange process [17,31]. Using the Butler-Volmer equation, we have calculated the Tafel slopes from the cyclic voltammetry curves in Figure 5.8 a) (see **Figure 5.8 b)**). The lowest observed value of the Tafel slope (171 mV dec^{-1} for the *1.8-CuCoO-1000/CP* sample) was similar to the best values obtained in other equivalent studies in the literature [29,32,33]. Furthermore, such a low value for the Tafel slope supports a high electrocatalytic activity for this sample. Meanwhile, sample *1.8-CuCoO-1700/CP* presented the highest value (363 mV dec^{-1}) in agreement with its poorer OER performance.

The electrical characteristics of the electrodes under operational working conditions can be analysed by EIS and a systematic study with this technique was carried out for the different electrodes investigated in this chapter. **Figure 5.9 a)** shows Nyquist plots obtained under OER working conditions (1.0 M KOH solution) at a potential of 700 mV vs. Ag/AgCl. The impedance curves adjust to two semicircles, a shape that is typical for this type of processes and that can be straightforwardly

fitted to an equivalent circuit model. In some cases, these two semicircles are not clearly observed due to their overlap. Herein, we have used the RC diagram reported in the inset in **Figure 5.9 b)** that is typically used for this kind of analysis [18,34]. Values of fitting parameters relying on this equivalent circuit are collected in **Table 5.2** and Figure 5.9 b). R_1 is generally associated with the resistance of the solution or electrolyte, R_2 with the layer resistance to the formation of active intermediates at the surface and R_3 with the charge transfer resistance during OER [18,34]. Meanwhile, the sum of these two parameters ($R_T = R_1 + R_2$) represents the overall internal resistance of the electrodes to the exchange of current during OER. The minimization of this parameter would maximize the yield of the system regarding the production of oxygen. The obtained R_1 values were about the same, within a 20 % variation, for all samples indicating a similar contact resistance with the electrolyte. The lowest values of R_2 and R_3 (both in the range of 1 ohm cm^{-2}) were found for sample *1.8-CuCoO-1000/CP*, suggesting that the formation of active OER catalytic intermediate species was more effective and that anodic charge transfer is favoured on the surface of this sample. A reasonable assumption is to associate the first feature to the characteristic surface evolution deduced from the XAS analysis (c.f., Figure 5.1) and the second to an optimum growth regime of domains during the MS-OAD for this electrode load (c.f. Figure 5.5). Since R_2 and R_3 values were the lowest in sample *1.8-CuCoO-1000/CP*, its activity results to be the highest from the whole series. This result might in principle contradict the intuitive idea that the larger the amount of electrocatalytic active phase, the higher the electrochemical activity. This could indeed be deduced from the slight increase in ECSA found for the electrode with highest catalyst load in comparison with the value in sample *1.8-CuCoO-1000/CP* (note however,

143

the tendency to saturation highlighted when analysing this parameter in Figure 5.6 c)). In this regard, the higher R_3 values found for *1.8-CuCoO-1700/CP* sample supports that a higher agglomeration degree of particles as that found in this sample (see Figure 5.5) degrades the domain connectivity and therefore increases the grain boundary resistance to charge transfer.
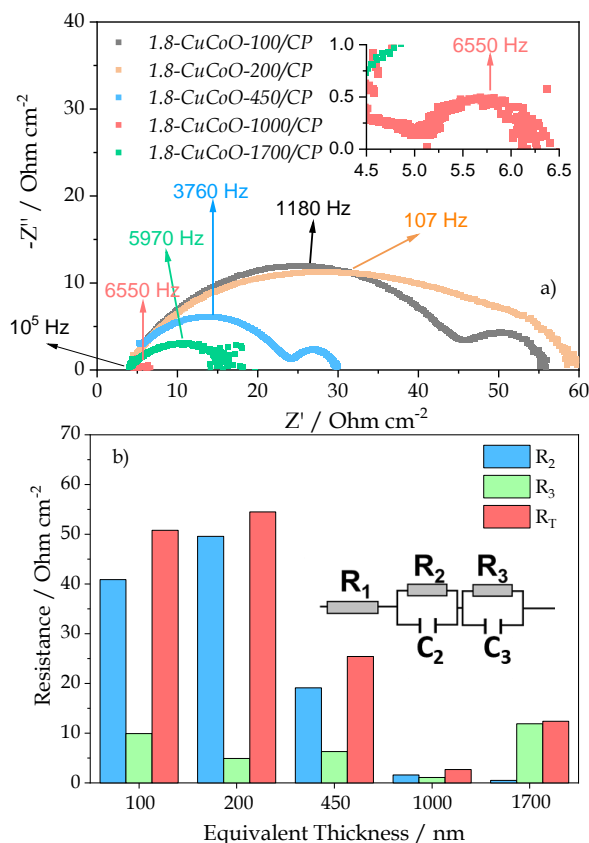
Figure 5.9*. a) Nyquist plots for 1.8-CuCoO-thickness/CP samples with different equivalent thickness obtained in the three-electrode cell (1.0 M KOH solution, 10 mV ac potential amplitude, 100 kHz to 10 mHz frequency range). b) R_2, R_3 and total resistance R_T ($R_T=R_2+R_3$) evaluated at 700 mV vs. Ag/AgCl obtained through the fitting of the experimental Nyquist plots according to the equivalent electrical circuit R_1-R_2C_2-R_3C_3 included as an inset.*

Table 5.2. *Electrical parameter values obtained by fitting the Nyquist plots in Figure 5.9 at 700 mV vs. Ag/AgCl.*

Sample	$R_1 / \Omega\ cm^{-2}$	$R_2 / \Omega\ cm^{-2}$	$R_3 / \Omega\ cm^{-2}$
1.8-CuCoO-100/CP	5.0	40.9	9.9
1.8-CuCoO-200/CP	4.4	49.6	4.9
1.8-CuCoO-450/CP	4.3	19.1	6.3
1.8-CuCoO-1000/CP	3.5	1.6	1.1
1.8-CuCoO-1700/CP	4.0	0.5	11.9

5.3.4. <u>Electrochemical test in anion exchange membrane water electrolysis cell</u>

The *1.8-CuCoO-1000/CP* sample electrode, showing best electrochemical performance in the three-electrode cell configuration, was incorporated for further evaluation into a MEA electrolyzer with a Ni thin film cathodic electrode prepared by MS-OAD and an anion exchange membrane between both electrodes. **Figure 5.10** shows that this assembly rendered an increase in the current density and a decrease in the onset potential as the operational temperature increased. This tendency can be attributed to a temperature activation of the hydroxyl ion conductivity through the membrane and to a higher rate of oxygen and hydrogen evolutions [35,36]. Compared with results of a previous study using a thinner electrode (i.e. *1.8-CuCoO-450/CP)* in Chapter 4 of this thesis [1], an increase in current density of about 9, 32, and 50 % was found for the *1.8-CuCoO-1000/CP* anode at 40 °C, 60 °C, and 70 °C, and a polarization of 2.2 V. This progressive increase in differential performance with temperature for the optimized anode occurs for conditions at which the diffusion of hydroxyl groups through the membrane is not the main limiting step of the reaction process. This comparative assessment based on MEA results confirms the superior

performance found for the *1.8-CuCoO-1000/CP* anode in the three-electrode cell configuration and indicates that the chemical and morphological characteristics of this electrode are preserved when integrated in the MEA assembly.
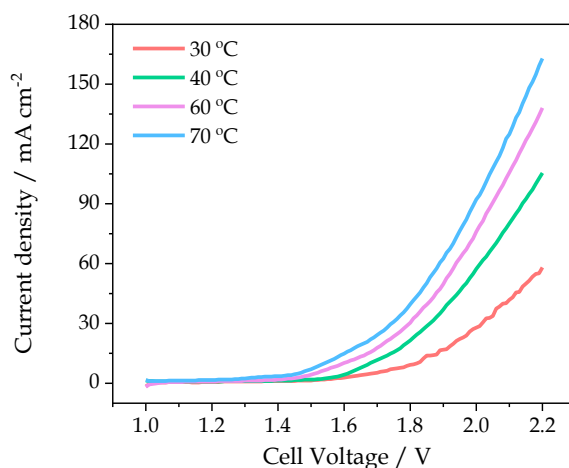
Figure 5.10. *Temperature dependence of the polarization curves of the MEA prepared using a 1.8-CuCoO-1000/CP anodic electrode (1.0 M KOH, scan rate of 5 mV s^{-1}).*

It is noteworthy that the current yield per amount of catalyst at 40 °C (150 mA mg^{-1} at 2.0 V) using the *1.8-CuCoO-1000/CP* anode is superior than that reported in previous studies with cobalt doped oxides catalysts and similar electrolysis conditions. For example, values of 80, 60 or 57 mA mg^{-1} have been reported at the same potential in other works [37–39] (see a more complete list of literature data **Table 5.3**).

Table 5.3. *Literature review about copper-cobalt oxide anodes used in the AEM electrolysis at 2.0 V with 1.0 M KOH.*

Catalyst Loading (mg cm^{-2})	Specific current (mA mg^{-1})	Reference
0.4	150	This MEA
3	57	[39]
10	100	[40]
10	80	[37]
36	17	[41]
30	13	[42]
23	60	[38]

Stability tests carried out under these conditions showed a very good reproducibility during cyclic voltammetry (polarization between 1.0 and 2.2 V, scan rate 50 mV s^{-1}, 200 cycles) as illustrated in **Figure 5.11 a)**. A high stability after long periods (45 hours) of continuous operation at 25 mA cm^{-2} constant current (at voltage around 2 V) in 1.0 M KOH solution and 40 °C can be also appreciated in **Figure 5.11 b)**. In this latter experiment, the cell voltage remained about constant and the initial response only decreased by 0.12 % V h^{-1}, a lower decrease than that previously reported for sample *1.8-CuCoO-450/CP* under the same electrochemical conditions (Chapter 4) [1]. This performance decrease is also lower than that reported in other studies in the literature [43,44], thus sustaining the feasibility of the MS-OAD techniques for the preparation of AEMWE electrodes.
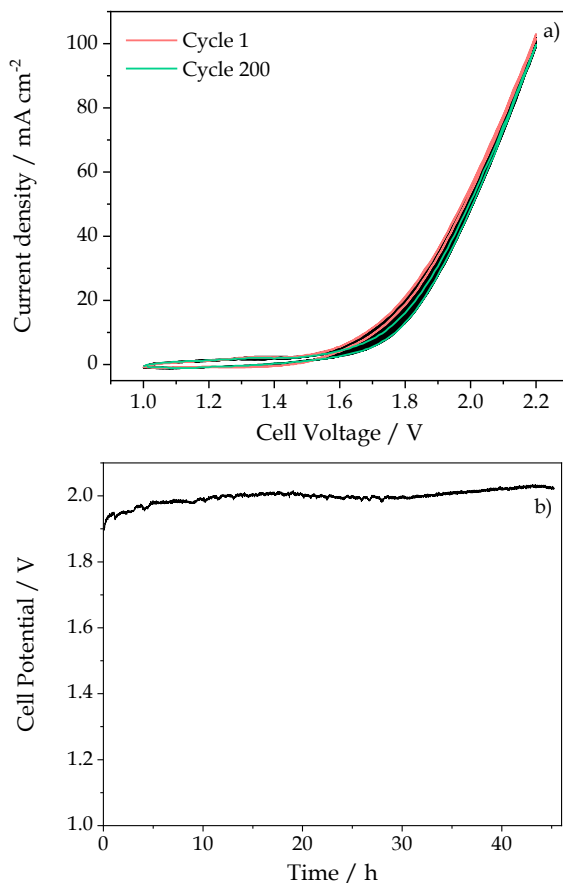
Figure 5.11. *Stability tests of 1.8-CuCoO-1000/CP anode sample in MEA
configuration. a) Cyclic voltammetry experiments: comparison of the first 200 cycles
(1st and 200th cycles highlighted in red and green, respectively). b) Constant current
chronopotentiometry acquired at 25 mA cm-2. Both set of measurements carried out at
40 ºC in a 1.0 M KOH solution.*

5.4. Conclusions

We have studied the electrochemical and morphological properties of
copper-cobalt mixed oxides catalysts prepared by MS-OAD to be used as
anodes in an AEMWE cell with the purpose of determining their
optimum characteristics and maximise the OER yield under operation

148

conditions. Unlike the common idea that increasing the catalyst load will contribute to improve the OER performance, our results have shown that there is a maximum yield for intermediate loads, around 1 micron *equivalent thickness* (0.4 mg cm^{-2}), for which the electrochemically active surface area and the electrical resistivity through the catalyst layer become optimum. It is found that larger catalysts loads can be detrimental for the reaction yield because a slightly higher value of the active surface area results insufficient to compensate the increase of electrical resistivity detected for amounts of deposited catalyst beyond a certain limit. This evidence is of course valid for the particular conditions used for the synthesis of the electrode films in this chapter (i.e., characteristics of the carbon paper GDL supports and the catalysts growth conditions during MS-OAD), but the idea would also apply for other preparation techniques.

In addition, our analysis by XAS has shown that a partial exchange between Co^{2+} and Co^{3+} species, likely maximized for a Co/Cu atomic ratio of 1.8, is a very important factor to increase the surface activity of the catalysts. This condition appears also maximized in the sample with the optimum thickness and contributes to increase the overall reaction yield.

Finally, our results obtained with the MEA configuration have demonstrated that these findings are also valid under experimental conditions close to those required in a compact water electrolyser. Inserted in the MEA the electrodes maintain their microstructural characteristics, providing a good electrochemical activity and stability as compared with other literature data, especially if the comparison of the performance is normalised to the amount of catalyst.

5.5.   References

[1]   E. López-Fernández, J. Gil-Rostra, J.P. Espinós, A.R. González-Elipe, F. Yubero, A. de Lucas-Consuegra, $Cu_xCo_{3-x}O_4$ ultra-thin film as efficient anodic catalysts for anion exchange membrane water electrolysers, J. Power Sources. 415 (2019) 136–144. https://doi.org/10.1016/j.jpowsour.2019.01.056.

[2]   J. Simböck, M. Ghiasi, S. Schönebaum, U. Simon, F.M.F. de Groot, R. Palkovits, Electronic parameters in cobalt-based perovskite-type oxides as descriptors for chemocatalytic reactions, Nat. Commun. 11 (2020) 652. https://doi.org/10.1038/s41467-020-14305-0.

[3]   K.-L. Yan, J.-F. Qin, J.-H. Lin, B. Dong, J.-Q. Chi, Z.-Z. Liu, F.-N. Dai, Y.-M. Chai, C.-G. Liu, Probing the active sites of Co_3O_4 for the acidic oxygen evolution reaction by modulating the Co^{2+}/Co^{3+} ratio, J. Mater. Chem. A. 6 (2018) 5678–5686. https://doi.org/10.1039/C8TA00070K.

[4]   M. Driess, A. Indra, P. Menezes, C. Das, C. Goebel, M. Tallarida, D. Schmeißer, A facile corrosion approach to highly active CoO_x water oxidation catalysts, J. Mater. Chem. A. (2017). https://doi.org/10.1039/C6TA10650A.

[5]   C. Morales, D. Diaz, R.J.O. Mossanek, M. Abbate, J. Méndez, V. Pérez-Dieste, C. Escudero, J. Rubio Zuazo, P. Prieto, L. Soriano, Controlled ultra-thin oxidation of Graphite promoted by cobalt oxides: influence of the initial 2D CoO wetting layer, Appl. Surf. Sci. 509 (2019) 145118. https://doi.org/10.1016/j.apsusc.2019.145118.

[6]   K. Kvashnina, S. Butorin, A. Modin, I. Soroka, M. Marcellini, J. Guo, L. Werme, J. Nordgren, Changes in electronic structure of copper films in aqueous solutions, J. Phys. Condens. Matter. 19 (2007) 226002. https://doi.org/10.1088/0953-8984/19/22/226002.

[7]   L. Soriano, M. Abbate, A. Fernández, A.R. González-Elipe, F. Sirotti, J.M. Sanz, Oxidation state and size effects in CoO nanoparticles, J. Phys. Chem. B. 103 (1999) 6676–6679. https://doi.org/10.1021/jp990423r.

[8]   A. Barranco, A. Borras, A.R. Gonzalez-Elipe, A. Palmero, Perspectives on oblique angle deposition of thin films: From fundamentals to devices, Prog. Mater. Sci. 76 (2016) 59–153. https://doi.org/10.1016/j.pmatsci.2015.06.003.

[9]   J. Gil-Rostra, M. Cano, J.M. Pedrosa, F.J. Ferrer, F. García-García, F. Yubero, A.R. González-Elipe, Electrochromic behavior of $W_xSi_yO_z$ thin

films prepared by reactive magnetron sputtering at normal and glancing angles, ACS Appl. Mater. Interfaces. 4 (2012) 628–638. https://doi.org/10.1021/am2014629.

[10] D. Deniz, D.J. Frankel, R.J. Lad, Nanostructured tungsten and tungsten trioxide films prepared by glancing angle deposition, Thin Solid Films. 518 (2010) 4095–4099. https://doi.org/10.1016/j.tsf.2009.10.153.

[11] D. Deniz, R.J. Lad, Temperature threshold for nanorod structuring of metal and oxide films grown by glancing angle deposition, J. Vac. Sci. Technol. A Vacuum, Surfaces Film. 29 (2011). https://doi.org/10.1116/1.3525882.

[12] G. Sievers, T. Vidakovic-Koch, C. Walter, F. Steffen, S. Jakubith, A. Kruth, D. Hermsdorf, K. Sundmacher, V. Brüser, Ultra-low loading Pt-sputtered gas diffusion electrodes for oxygen reduction reaction, J. Appl. Electrochem. 48 (2018) 221–232. https://doi.org/10.1007/s10800-018-1149-7.

[13] E. López-Fernández, J. Gil-Rostra, J.P. Espinós, A.R. González-Elipe, A. de Lucas Consuegra, F. Yubero, Chemistry and electrocatalytic activity of nanostructured nickel electrodes for water electrolysis, ACS Catal. 10 (2020) 6159–6170. https://doi.org/10.1021/acscatal.0c00856.

[14] Y.T. Lee, R.P. Gautam, S.M. Islam, C.J. Barile, Cuprous oxide electrodeposited with nickel for the oxygen evolution reaction in 1 M NaOH, J. Phys. Chem. C. 123 (2019) 1287–1292. https://doi.org/10.1021/acs.jpcc.8b10413.

[15] S. Xiong, P. Li, Z. Jin, T. Gao, Y. Wang, Y. Guo, D. Xiao, Enhanced catalytic performance of ZnO-CoO$_x$ electrode generated from electrochemical corrosion of Co-Zn alloy for oxygen evolution reaction, Electrochim. Acta. 222 (2016) 999–1006. https://doi.org/10.1016/j.electacta.2016.11.068.

[16] I. Vincent, D. Bessarabov, Electrochemical characterization and oxygen reduction kinetics of Cu-incorporated cobalt oxide catalyst, Int. J. Electrochem. Sci. 11 (2016) 8002–8015. https://doi.org/10.20964/2016.09.12.

[17] M. Sun, Z. Wang, B. Gao, S. Wang, C. Wang, X. Song, D. Lin, Electrocatalytic hydrogen evolution properties of anionic NiS$_2$-Ni(OH)$_2$ nanosheets produced on the surface of nickel foam, Int. J. Energy Res. 44 (2020) 4827–4836. https://doi.org/10.1002/er.5275.

[18] L. Guangfu, L. Anderson, Y. Chen, M. Pan, P.-Y. Chuang, New insights

into evaluating catalyst activity and stability of oxygen evolution reactions in alkaline media, Sustain. Energy Fuels. 2 (2017). https://doi.org/10.1039/C7SE00337D.

[19]   S.K. Bikkarolla, P. Papakonstantinou, $CuCo_2O_4$ nanoparticles on nitrogenated graphene as highly efficient oxygen evolution catalyst, J. Power Sources. 281 (2015) 243–251. https://doi.org/10.1016/j.jpowsour.2015.01.192.

[20]   X. Wu, K. Scott, $Cu_xCo_{3-x}O_4$ (0 ≤ x < 1) nanoparticles for oxygen evolution in high performance alkaline exchange membrane water electrolysers, J. Mater. Chem. 21 (2011) 12344–12351. https://doi.org/10.1039/c1jm11312g.

[21]   X. Wu, K. Scott, A Li-doped Co_3O_4 oxygen evolution catalyst for non-precious metal alkaline anion exchange membrane water electrolysers, Int. J. Hydrogen Energy. 38 (2013) 3123–3129. https://doi.org/10.1016/j.ijhydene.2012.12.087.

[22]   X. Wu, K. Scott, A non-precious metal bifunctional oxygen electrode for alkaline anion exchange membrane cells, J. Power Sources. 206 (2012) 14–19. https://doi.org/10.1016/j.jpowsour.2011.12.052.

[23]   S. Ahn, B.-S. Lee, I. Choi, S. Yoo, H.-J. Kim, E. Cho, D. Henkensmeier, S. Nam, J. Jang, Development of a membrane electrode assembly for alkaline water electrolysis by direct electrodeposition of nickel on carbon papers, Appl. Catal. B Environ. s 154–155 (2014) 197–205. https://doi.org/10.1016/j.apcatb.2014.02.021.

[24]   S. Cui, X. Liu, Z. Sun, P. Du, Noble metal-free copper hydroxide as an active and robust electrocatalyst for water oxidation at weakly basic pH, ACS Sustain. Chem. Eng. 4 (2016) 2593–2600. https://doi.org/10.1021/acssuschemeng.6b00067.

[25]   M. Qian, X. Liu, S. Cui, H. Jia, P. Du, Copper oxide nanosheets prepared by molten salt method for efficient electrocatalytic oxygen evolution reaction with low catalyst loading, Electrochim. Acta. 263 (2018) 318–327. https://doi.org/10.1016/j.electacta.2018.01.053.

[26]   S. Asadizadeh, M. Amirnasr, S. Meghdadi, F. Fadaei Tirani, K. Schenk, Facile synthesis of Co_3O_4 nanoparticles from a novel tetranuclear cobalt(III) complex. Application as efficient electrocatalyst for oxygen evolution reaction in alkaline media, Int. J. Hydrogen Energy. 43 (2018) 4922–4931. https://doi.org/10.1016/j.ijhydene.2018.01.104.

[27]   X. Li, Y. Fang, L. Wen, F. Li, G. Yin, W. Chen, X. An, J. Jin, J. Ma,

Co@Co₃O₄ core–shell particle encapsulated N-doped mesoporous carbon cage hybrids as active and durable oxygen-evolving catalysts, Dalt. Trans. 45 (2016) 5575–5582. https://doi.org/10.1039/C6DT00102E.

[28]   M. Kuang, P. Han, Q. Wang, J. Li, G. Zheng, CuCo hybrid oxides as bifunctional electrocatalyst for efficient water splitting, Adv. Funct. Mater. 26 (2016) 8555–8561. https://doi.org/10.1002/adfm.201604804.

[29]   R.A.E. Acedera, M.D.L. Balela, Hierarchical Urchin-like spinel $Cu_xCo_{3-x}O_4$ particles as oxygen evolution reaction catalysts in alkaline medium, IOP Conf. Ser. Mater. Sci. Eng. 617 (2019) 12004. https://doi.org/10.1088/1757-899x/617/1/012004.

[30]   F. Švegl, B. Orel, I. Grabec-Švegl, V. Kaučič, Characterization of spinel Co₃O₄ and Li-doped Co₃O₄ thin film electrocatalysts prepared by the sol–gel route, Electrochim. Acta. 45 (2000) 4359–4371. https://doi.org/10.1016/S0013-4686(00)00543-0.

[31]   S. V Mohite, R. Xing, B. Li, S.S. Latthe, Y. Zhao, X. Li, L. Mao, S. Liu, Spatial compartmentalization of cobalt phosphide in P-doped dual carbon shells for efficient alkaline overall water splitting, Inorg. Chem. 59 (2020) 1996–2004. https://doi.org/10.1021/acs.inorgchem.9b03363.

[32]   Q. Zhou, T.-T. Li, F. Guo, Y.-Q. Zheng, Construction of hierarchically structured CuO@CoP anode for efficient oxygen evolution reaction, ACS Sustain. Chem. Eng. 6 (2018) 11303–11312. https://doi.org/10.1021/acssuschemeng.8b00802.

[33]   D. Xu, B. Liu, G. Liu, K. Su, C. Yang, H. Tong, D. Qian, J. Li, N-doped bamboo-like CNTs combined with CoFe–CoFe₂O₄ as a highly efficient electrocatalyst towards oxygen evolution, Int. J. Hydrogen Energy. 45 (2020) 6629–6635. https://doi.org/10.1016/j.ijhydene.2019.12.180.

[34]   Q. Zhang, Z.D. Wei, C. Liu, X. Liu, X.Q. Qi, S.G. Chen, W. Ding, Y. Ma, F. Shi, Y.M. Zhou, Copper-doped cobalt oxide electrodes for oxygen evolution reaction prepared by magnetron sputtering, Int. J. Hydrogen Energy. 37 (2012) 822–830. https://doi.org/10.1016/j.ijhydene.2011.04.051.

[35]   H.A. Miller, K. Bouzek, J. Hnat, S. Loos, C.I. Bernäcker, T. Weißgärber, L. Röntzsch, J. Meier-Haack, Green hydrogen from anion exchange membrane water electrolysis: A review of recent developments in critical materials and operating conditions, Sustain. Energy Fuels. 4 (2020) 2114–2133. https://doi.org/10.1039/c9se01240k.

[36]   A.B. Calcerrada, A.R. de la Osa, E. Lopez-Fernandez, F. Dorado, A. de

Lucas-Consuegra, Influence of the carbon support on the Pt–Sn anodic catalyst for the electrochemical reforming of ethanol, Int. J. Hydrogen Energy. 44 (2019) 10616–10626. https://doi.org/10.1016/j.ijhydene.2019.03.011.

[37]   L. Zeng, T.S. Zhao, An effective strategy to increase hydroxide-ion conductivity through microphase separation induced by hydrophobic-side chains, J. Power Sources. 303 (2016) 354–362. https://doi.org/10.1016/j.jpowsour.2015.11.019.

[38]   Y.S. Park, M.J. Jang, J. Jeong, S.M. Park, X. Wang, M.H. Seo, S.M. Choi, J. Yang, Hierarchical Chestnut-Burr like structure of copper cobalt oxide electrocatalyst directly grown on Ni foam for anion exchange membrane water electrolysis, ACS Sustain. Chem. Eng. (2020). https://doi.org/10.1021/acssuschemeng.9b06767.

[39]   X. Wu, K. Scott, A polymethacrylate-based quaternary ammonium OH⁻ ionomer binder for non-precious metal alkaline anion exchange membrane water electrolysers, J. Power Sources. 214 (2012) 124–129. https://doi.org/10.1016/j.jpowsour.2012.03.069.

[40]   S.M. Park, M.J. Jang, Y.S. Park, J. Lee, J.-Y. Jeong, J. Jung, M.-K. Choi, Y.-S. Noh, M.-H. Seo, H.J. Kim, J. Yang, Y.D. Kim, S.M. Choi, Synthesis and characterization of the $Cu_{0.72}CO_{2.28}O_4$ catalyst for oxygen evolution reaction in an anion exchange membrane water electrolyzer, J. Korean Inst. Met. Mater. 58 (2020) 49–58. https://doi.org/10.3365/KJMM.2020.58.1.49.

[41]   C.C. Pavel, F. Cecconi, C. Emiliani, S. Santiccioli, A. Scaffidi, S. Catanorchi, M. Comotti, Highly efficient platinum group metal free based membrane-electrode assembly for anion exchange membrane water electrolysis, Angew. Chemie Int. Ed. 53 (2014) 1378–1381. https://doi.org/10.1002/anie.201308099.

[42]   I. Vincent, A. Kruger, D. Bessarabov, Development of efficient membrane electrode assembly for low cost hydrogen production by anion exchange membrane electrolysis, Int. J. Hydrogen Energy. 42 (2017) 10752–10761. https://doi.org/10.1016/j.ijhydene.2017.03.069.

[43]   P. Ganesan, A. Sivanantham, S. Shanmugam, Nanostructured nickel–cobalt–titanium alloy grown on titanium substrate as efficient electrocatalyst for alkaline water electrolysis, ACS Appl. Mater. Interfaces. 9 (2017) 12416–12426. https://doi.org/10.1021/acsami.7b00353.

[44] J. Hnát, M. Plevova, R.A. Tufa, J. Zitka, M. Paidar, K. Bouzek, Development and testing of a novel catalyst-coated membrane with platinum-free catalysts for alkaline water electrolysis, Int. J. Hydrogen Energy. 44 (2019) 17493–17504. https://doi.org/10.1016/j.ijhydene.2019.05.054.

Chapter 6

Nickel electrodes for anion exchange membrane water electrolysis
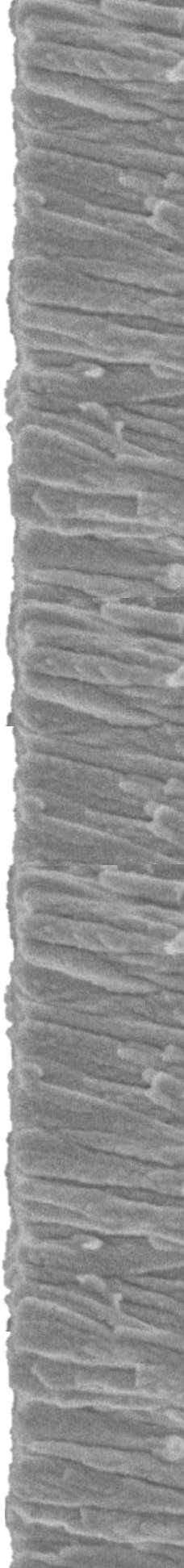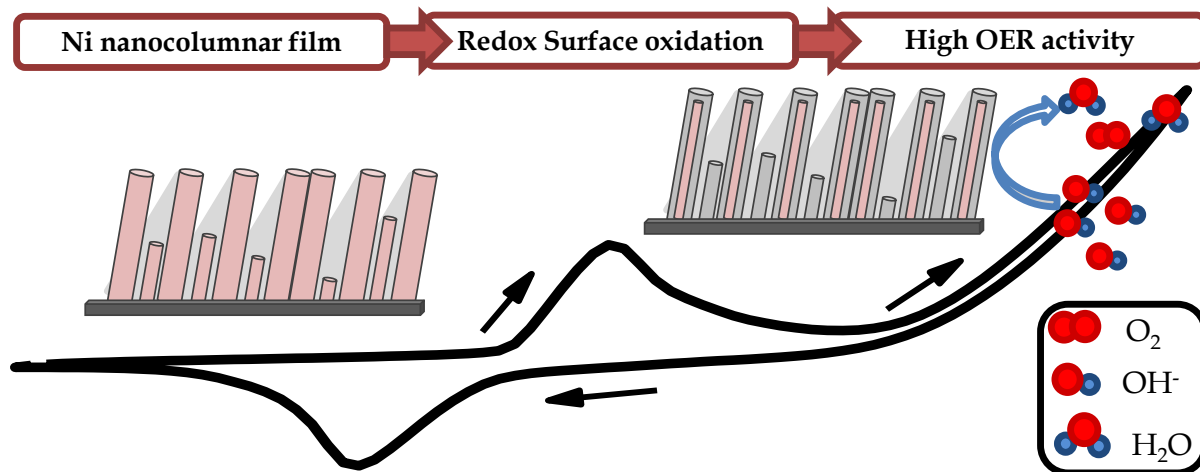
Ni nanocolumnar film → Redox Surface oxidation → High OER activity

O₂
OH⁻
H₂O

The content of this chapter has been published in:

6.1.   Introduction

In addition to the Co-based anodes studied in Chapter 4 and 5, nickel and Ni-alloy based catalysts have demonstrated high activity and stability as both anodes and cathodes in electrolyzers working in alkaline media [1–4]. Commonly, the anode catalyst load is incorporated onto a gas diffusion layer support employing wet routes, in most cases as oxides or hydroxides [5,6] since these are believed to be the chemical forms of the active catalytic phase required to promote the oxygen evolution reaction (OER).

In the present study, we have used magnetron sputtering (MS) to achieve a strict control of oxidation state, load, and microstructure of nickel-based catalysts. The aim is to determine the most favorable nickel oxidation state to promote the efficient operation of AEMWE cells, particularly to enhance the OER activity of the anodes. In this regard, we have adapted the deposition conditions in our MS reactor to prepare electrode catalyst layers with either metallic Ni [7,8], oxide NiO [6] or oxyhydroxide $NiO_x(OH)_y$ [5,9] compositions and a similar porous microstructure. Although it is well known that the nickel oxyhydroxide is the active phase for OER [10,11], it is not clear whether a homogeneous chemical distribution or a mixture of various phases is the most convenient configuration of the nickel anode catalyst when they are incorporated to the GDL. Note that this point can hardly be checked when electrodes are prepared by chemical or electrochemical methods due to the fact that a change in oxidation state generally entails a different morphology and porosity, and vice versa.

Unlike this situation with electrodes prepared by chemical methods, MS-OAD permits the preparation of thin films with different oxidation

states but a similar microstructure, thus providing a unique way to study the response toward the OER of nickel based catalysts [12–14]. Thus, the chemistry of the deposits, from metal to oxide or oxyhydroxide, has been controlled modifying the composition of the gas mixture in the magnetron plasma discharge during the deposition process [15]. We have customized the nickel anode composition and layer distribution (metal, oxide or oxyhydroxide phases within single layer or bilayer structures) to determine the best anode configuration/chemical state to maximize the OER yield. This feature and the preparation of bilayer metal/oxide electrodes at room temperature are hardly achievable through wet or ceramic routes if the preservation of well-defined of interfaces and chemical compositions is a requirement.

The chemistry and microstructure of the electrode films and surfaces (as prepared and used samples) have been characterized by XPS, XAS, XRD and SEM, while their performance as OER catalysts has been electrochemically tested using a three-electrode electrochemical cell configuration. To complete this study, the best anode electrodes have been incorporated to a MEA provided with a metallic Ni cathode prepared by the same procedure. The MEA performance has been critically assessed in relation to the catalyst load both in the anode and cathode electrodes and with the chemical state of nickel in the former, either at the surface or in the bulk. As a result of this investigation, we show that among the different oxidation states of nickel-based anode catalysts, those prepared as metallic and covered with a thin oxide/oxyhydroxide layer developed in the electrolyte solution during its electrochemical activation show best performance towards OER.

6.2.   Experimental

Magnetron sputtering method previously explained in Chapter 3 has been used to prepare the nickel-based electrodes. Carbon paper and polished silicon wafers were used as substrates. The microstructure and composition of electrode films were adjusted using two geometrical deposition configurations and three gas plasma discharges also previously explained in Chapter 3.

Along this chapter, the identification label of electrodes will be as follows: *XX-YYw/ZZ*, where *XX* refers to the chemical nature of the deposited nickel-based films (i.e., metallic *Ni*, oxide *NiO* or oxyhydroxide *NiOOH*), *YY* refers to their *equivalent thickness* (in nanometers), *w* refers to the fabrication geometry (i.e., normal *n* or oblique *o*) and *ZZ* is the support used in each electrode. For example, *Ni-540o/CP* refers to an electrode fabricated using an Ar plasma discharge (metallic Ni), with an *equivalent thickness* of 540 nm that was deposited in an OAD configuration on carbon paper.

All the physico-chemical characterization techniques used in this study has been previously explained in Chapter 3.

With the XPS analysis we aimed at comparing the surface state of the electrodes before and after electrochemical cycling. For this analysis, various cyclic voltammetry (CV) experiments from 0 to 750 mV vs. Ag/AgCl (scan rate 20 mV s^{-1} in a 1.0 M KOH solution, 25 cycles) were carried out up to reach steady state conditions and then stopped at 0 V vs. Ag/AgCl. Then, the nickel electrode used as anode was rinsed with distilled water and exposed to ambient air for about 10 minutes (maximum exposure time to air) previously to their insertion in the XPS apparatus.

XAS was carried out at near ambient pressure photoemission (NAPP) end station of the CIRCE beamline of ALBA Synchrotron Light Source (Barcelona, Spain). For this experiment, Si_3N_4 membranes (NX10100C, Norcada) were used as substrates to deposit the metallic nickel catalyst film with a thickness of approximately 60 nm (i.e., sample *Ni-60o/Si)*, trying to adjust its thickness to the probing depth of the technique. O K, and Ni $L_{2,3}$ absorption spectra were recorded (drain current measurements) for these films as prepared samples (i.e., exposed to the air) and after their immersion in 1.0 M KOH electrolyte for 30 minutes.

To study the influence of the microstructure, chemistry and nickel loading of deposits on the performance of electrodes for the OER, electrochemical experiments were carried out in a three-electrode cell previously defined in Chapter 3. OER and hydrogen evolution reaction (HER) efficiencies were studied by CV. The nickel-based deposits acting as anodes and cathodes were pre-conditioned by a series of successive CVs before their use to activate the OERs or HERs. This electrochemical conditioning consisted of 25 CVs in 1.0 M KOH electrolyte with a scan rate of 20 mV s^{-1}. A similar pre-treatment was also applied to the nickel oxide and oxyhydroxide electrodes.

The influence of the amount (i.e., thickness) of Ni electrocatalyst was also studied in a MEA configuration. In this system, different Ni metallic catalysts supported on carbon paper were used as anode and cathode electrodes separated by an anion exchange membrane (either Fumapem FAA-3-50 or Sustainion® X37-50). The catalyst loading varies from 0.09 mg cm^{-2} (for 140 nm *equivalent thickness* electrode) to 1.45 mg cm^{-2} (for 2000 nm *equivalent thickness* electrode) measured by RBS and confirmed by weighing of the electrodes before and after of the deposition of the catalysts.

Experiments were performed between 25 and 60 °C. A 1.0 M KOH in distilled water electrolyte solution was fed into both anode and cathode compartments. Finally, to investigate the stability of the cell, two types of experiments were carried out: constant-current chronopotentiometric experiments (current density 32 mA cm^{-2}, elapsed time 14 hours) and 200 CVs, both at a temperature of 40 °C.

6.3.   Results and discussion

6.3.1.   Influence of microstructure on oxygen evolution reaction performance

To study the influence of microstructure of metallic nickel deposits on the nickel redox behaviour and OER efficiency, we compared the results obtained with electrode films prepared either in a normal or an OAD configuration. According to the SEM images of *Ni-540n/CP* and *Ni-540o/CP* films (c.f., **Figures 6.1 a)** and **6.1 b)**), the latter has a less compact microstructure than the former. A higher porosity in an OAD configuration was confirmed by the observation of the SEM images of *Ni-540n/Si* and *Ni-540o/Si* films deposited on flat polished silicon substrates (see normal micrographs in **Figure 6.1 c)** and **d)**). The latter consists of nanocolumns separated by large voids, explained with more details in previous chapters, while in the former the deposited material appears as a more compacted layer [16]. Although still insufficiently studied in literature, an enhancement of porosity and the development of a kind of columnar growth have been reported for other authors when using an OAD configuration and different supports in the form of membranes, metal foams, porous silicon, porous alumina membranes, nanotubes, and other substrates or nanostructured surfaces [17–22].
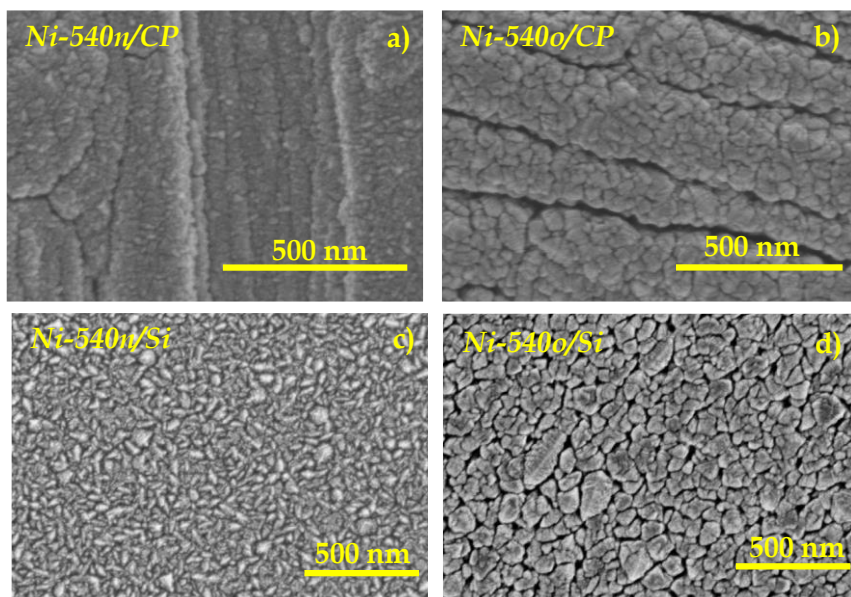
Figure 6.1. SEM images of samples a) Ni-540n/CP, b) Ni-540o/CP, c) Ni-540n/Si and d) Ni-540o/Si.

According to **Figure 6.2 a)** showing the electrochemical cycling behavior of a *Ni-540o/CP* electrode taken as example, electrochemical CV activation resulted in progressively more intense anodic and cathodic peaks at around 380 and 220 mV, respectively. Stable conditions were obtained after the first 20th cycles. The anodic peak can be attributed to oxidation processes to NiOOH taking place at the oxidized surface layers formed onto the metal nickel electrodes by their air/moisture exposure (see below the XPS/XAS analysis of this sample), and the cathodic peak to the reduction of NiOOH to NiO/Ni(OH)$_2$ according to the reversible reaction Ni(OH)$_2$ + OH$^-$ ⇆ NiOOH + e$^-$ [6,23,24]. The observed progressive voltage shift in the redox anodic and cathodic peaks and the increase in the current density values in Figure 6.2 a) agree with previous studies [24], suggesting the building up of an increasingly thicker surface

164

oxide or oxyhydroxide layer. Interestingly, the comparison in **Figure 6.2 b)** of samples *Ni-540o/CP* and *Ni-540n/CP* shows that the CVs of the latter depict a broader profile and higher peak voltage values for the oxidation and reduction peaks. In agreement with the more porous structure and higher surface area of sample *Ni-540o/CP*, its narrower peaks must be attributed to a faster electrolyte diffusion rate up to the active sites at its surface [24]. In addition, according to Figure 6.2 a), the enhancement of the electrocatalytic OER reaction yield (i.e., maximum anodic current intensity at 700 mV vs. Ag/AgCl) in this sample in comparison with that of sample *Ni-540n/CP* must be also attributed to its open and porous microstructure. Although for both samples the onset potential for the OER reaction appears in the range 500-600 mV vs. Ag/AgCl, as previously reported in other studies [23–26], the actual voltage is lower for sample *Ni-540o/CP* (approximately 530 mV vs. Ag/AgCl), a feature in line with the higher current densities measured above 600 mV vs. Ag/AgCl (i.e., when the OER is taking place). Tafel slopes, calculated (see **Figure 6.2 c)**) according to Butler-Volmer equation for CV experiments, were smaller for *Ni-540o/CP* (157 mV dec^{-1}) than for *Ni-540n/CP* (259 mV dec^{-1}) electrodes. A lower value of the Tafel slope indicates a higher electrocatalytic activity or a faster kinetic of the electron exchange process [27]. Therefore, the herein found tendency for the electrodes studied in this chapter indicates a faster and more efficient OER process [27] for the OAD electrodes. This result is consistent with the highest absolute electrocatalytic activity found for this type of electrodes.
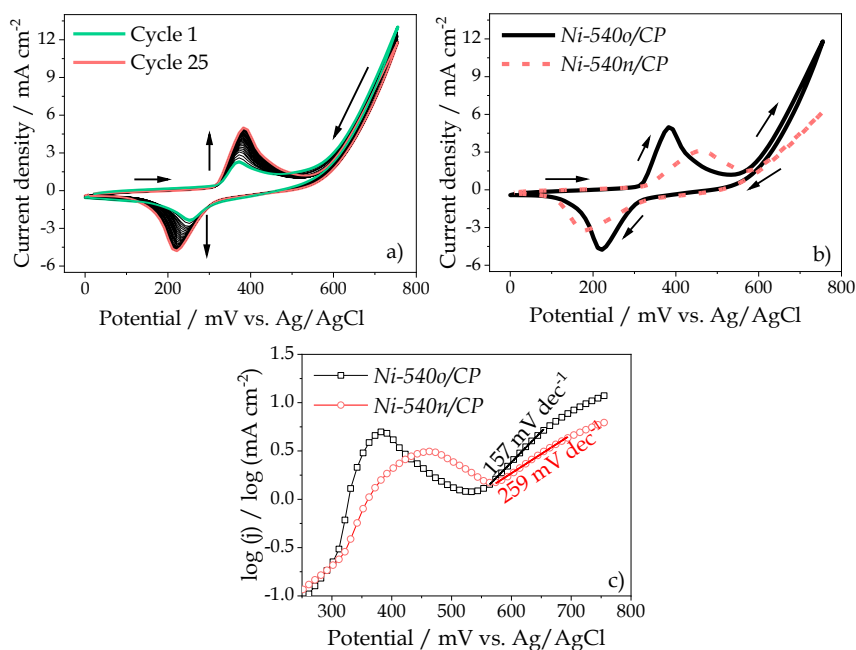
Figure 6.2. *a) Electrochemical activation of a Ni-540o/CP electrode by cyclic voltammetry (ambient temperature, 1.0 M KOH electrolyte, scan rate of 20 mV s^{-1}) from the 1st to the 25th cycle. b) Comparison of cyclic voltammograms taken for the two samples in the three-electrode cell after 25 cycles conditioning. c) Log (j) vs. mV Tafel plots of Ni-540o/CP and Ni-540n/CP. The Tafel slopes obtained from the linear fits to the initial rise of the OER curves are indicated in the plots.*

To further investigate the higher electrocatalytic activity of the OAD films, an EIS analysis was carried out in the three-electrode cell at 700 mV vs. Ag/AgCl. **Figure 6.3** shows the Nyquist plots obtained under OER working conditions (i.e., 1.0 M KOH electrolyte and 700 mV vs. Ag/AgCl) and the equivalent electrical circuit accounting for the observed electrochemical behavior. Values of electrical parameters obtained after fitting analysis are shown in the inset table.
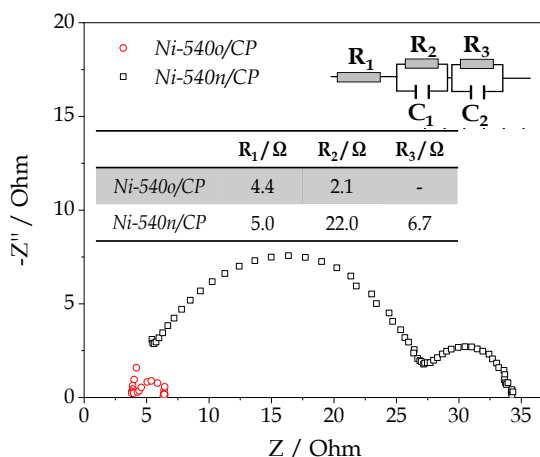
Figure 6.3. Nyquist plots for samples Ni-540o/CP (red open circles) and Ni-540n/CP (black open squares) obtained in the three-electrode cell. The equivalent electrical circuit used for fitting Nyquist plots is included as inset.

The equivalent circuit reproducing the Nyquist plots consists of an ohmic resistance R_1 associated to the electrolyte and two additional RC (resistor-capacitor) elements [28]. The resistances R_2 and R_3 can be respectively associated with the restrictions to the transfer of charge through the electrode and with the formation of surface intermediates, both during OER [9,29]. Interestingly, the very small values of R_2 and, to a lesser extent R_3, for sample *Ni-540o/CP* supports that, in agreement with previous results in literature [29,30], a favoured transfer of charge through the electrode is the main responsible for the enhanced OER activity of these samples. Since the metallic Ni electrodes prepared by OAD presented the best OER electrocatalytic activity, we have adopted this geometry for the preparation of the nickel oxide and oxyhydroxide electrodes.

Watzele et al. [31] have recently proposed a procedure based on an alternative interpretation of Nyquist plots to deduce values of the

electrochemical surface area (ECSA) of electrodes. This procedure has been previously explained in Chapter 3. Using the same approach, we have calculated the effective ECSA values for the *Ni-540o/CP* and for *Ni-540n/CP* electrodes. Considering the equivalent circuit in Figure 3.11 and the Eq. (3.3) of Chapter 3, C_a values for the different fabrication configuration electrodes were estimated in 1.84 mF and 1.62 mF for *Ni-540o/CP* and *Ni-540n/CP*, respectively, providing 6.13 and 5.40 cm² of ECSA values. These values support a slightly higher effective area in the electrode prepared in the OAD.

6.3.2. Influence of electrode chemical composition on oxygen evolution reaction performance

The MS technique offers the possibility to tailor the chemistry of deposited films while preserving a given microstructure. In this section we will firstly present a series of characterization results of the thin film electrodes prepared with pure Ar or mixtures Ar/O_2 and $Ar/O_2/H_2O$ as plasma gas to, in a second part, comparatively discuss their electrochemical performance.

A thorough characterization by XRD (c.f., **Figure 6.4)**) has been carried for the different nickel-based electrodes both as prepared and after their use as OER electrodes.

Peaks of the deposited nickel films appear superimposed on characteristic peaks of the carbon paper at ~54.6 º and ~86.9 º [32], which are labelled as *[e]* in the figure. The diagram of the *Ni-540o/CP* sample in the **Figure 6.4 a)** shows two diffraction peaks at 44.6 º and 51.9 º (labelled as *[a])* that are not detected in the other two samples and that can be

assigned to metallic nickel [33]. Besides, this sample and samples *NiO-540o/CP* and *NiOOH-540o/CP* depict diffraction peaks at 37.2 $^{\circ}$ and 43.2 $^{\circ}$ (labelled as *[b]*), that can be assigned to NiO or $NiO_x(OH)_y$ [34,35]. For the samples prepared in oxygen containing plasma discharges (samples NiO and NiOOH) this agrees with the formation of nickel oxide during preparation, while for the metallic nickel sample the relatively small size of peaks *[b]* can be attributed to the fact that they stem from the air oxidation of metallic nickel, taking place mainly at the surface. In addition, the diffraction peak at 62.7 $^{\circ}$ (labelled as *[d]*) only appears in sample *NiOOH-540o/CP* that, fabricated with H_2O to the plasma discharge, points to the formation of a $Ni(OH)_2$ phase [36]. In the diagram of the activated samples (**Figure 6.4 b)**) there are two new peaks attributed to KOH (labelled as *[f]*) and K_2CO_3 (labelled as *[g]*) that must be due to residual KOH remaining onto the surface of the electrodes after their use. It is noteworthy from this XRD analysis that, even for the metallic Ni electrodes, their crystallographic structure (i.e., features *[a]-[c]*) remained practically unaffected after activation, thus confirming that the electrochemical oxidation processes in Figure 6.2 a) only affect to the surface of the metal films acting as electrodes**.**
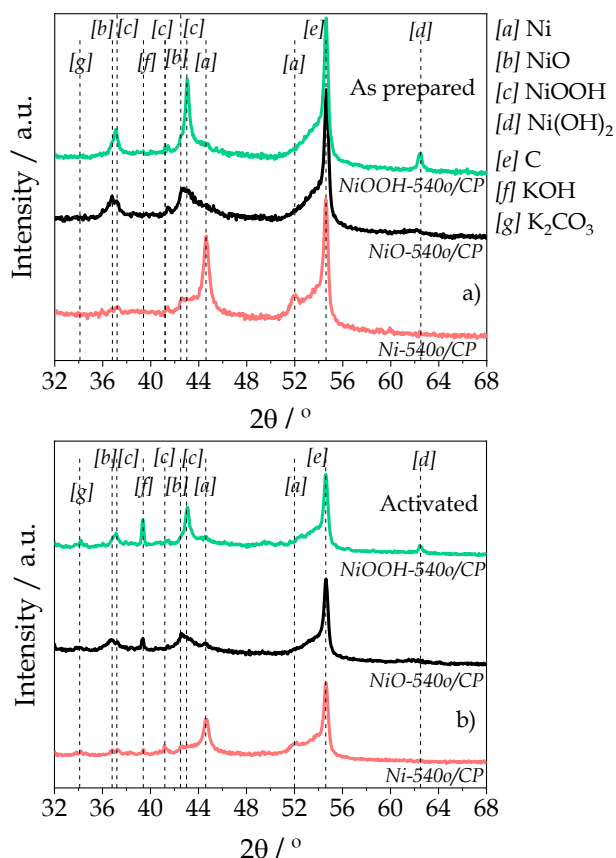
Figure 6.4. X-ray diffractograms of several nickel-based electrode films prepared by MS in OAD configuration with different plasma discharges a) as prepared samples and b) after electrochemical CV activation.

Surface chemical state of the electrodes, as deposited and after activation, was studied by XPS analysis. The recorded spectra confirmed the presence of oxygen, nickel, carbon (from airborne hydrocarbons and some carbonate) and potassium on the surface of the electrodes, this latter for the samples immersed in the basic medium. Based on this analysis, any contamination of the electrodes coming from platinum of the counter electrode or other components of the cell can be discarded. **Figures 6.5**

a)-d) show the Ni $2p_{3/2}$ and O 1s spectra obtained for *Ni-540o/CP*, *NiO/540/o*, and *NiOOH-540o/CP* electrodes, as prepared and after electrochemical cycling (i.e., after 25 CVs in 1 M KOH).

The Ni $2p_{3/2}$ and O 1s spectra of the as prepared electrodes were rather similar for samples *NiO-540o/CP* and *NiOOH-540o/CP* but differ for sample *Ni-540o/CP*. In general, the Ni $2p_{3/2}$ spectra are characterised by a peak plus satellite structure typical of NiO [37]. In addition, the *Ni-540o/CP* sample has an extra contribution at ~853.3 eV binding energy typical of Ni^0. Due to the surface character of the XPS technique and the XRD data in Figure 6.4 for this sample, we attribute this feature to the fact that in the original samples the pristine oxide layer is very thin and the metal core of the nanocolumns is still visible with this surface technique. In agreement with this attribution, the O 1s spectra of the as prepared *Ni-540o/CP* samples in Figure 6.5 c) depicts a main contribution at 531.7 eV attributed to OH^- groups (adsorbed carbonates might also contribute to this peak) and another one at 529.7 due to $O^=$ ions (i.e., oxide anions from the network). Unlike this situation in the metallic nickel sample, the OH^- contribution is majority in samples *NiO-540o/CP* and *NiOOH-540o/CP*.
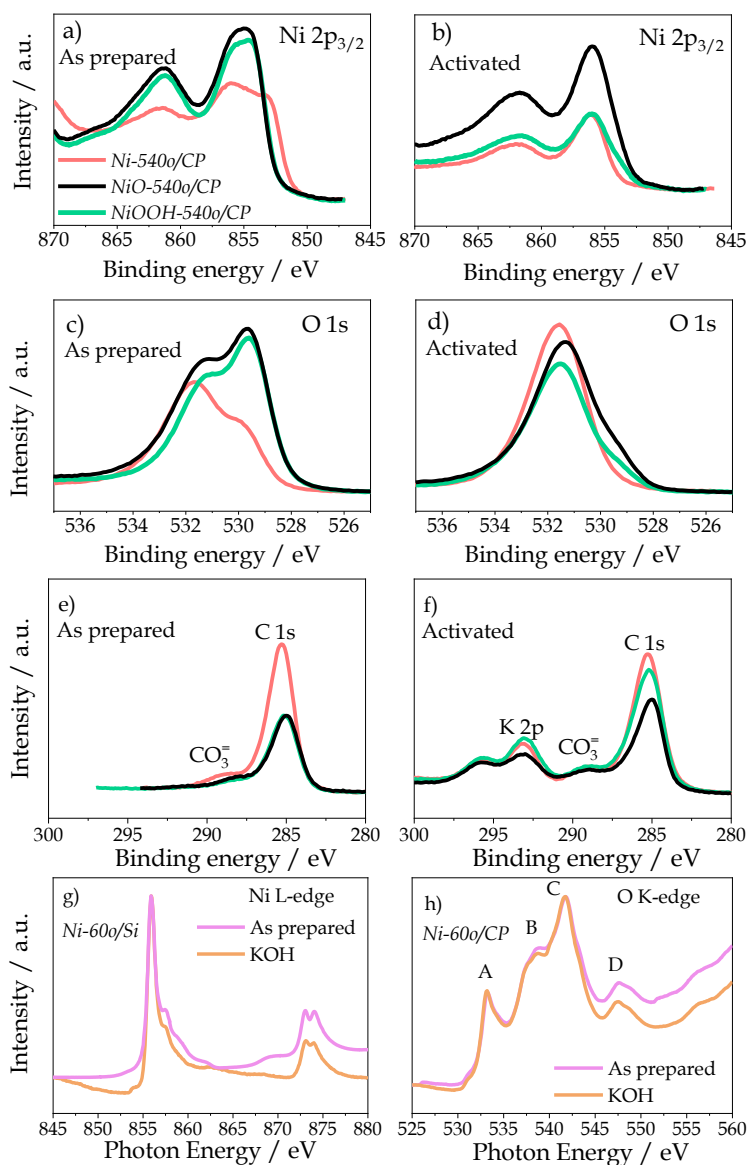
Figure 6.5. *a) Ni 2p$_{3/2}$, c) O 1s, e) C 1s and K 2p XPS spectra of Ni-540o/CP, NiO-540o/CP and NiOOH-540o/CP as prepared samples and b), d), f) after their electrochemical activation, respectively. Normalized g) Ni L$_{2,3}$ and h) O K XAS spectra of Ni-60o/CP sample as prepared and after 30 minutes immersion in 1 M KOH.*

The spectra of the electrochemically activated samples (Figure 6.5, b) and d)) reveal changes in the Ni $2p_{3/2}$ and O 1s spectra. The shape of the former, rather similar for all samples, is characterized by a main peak and a satellite as those depicted by nickel hydroxides and oxyhydroxides [37–39]. Meanwhile, all O 1s spectra appear now formed by a single band at 530 eV due to OH$^-$ groups [38,40]. The built up of an hydroxide layer has been previously observed in other OER oxide anodes electrochemically cycled in a basic medium [25]. This finding also suggests that the active catalytic phase for the OER is a nickel oxide/hydroxide formed at the surface of the electrodes. It is also noteworthy that XPS also showed the incorporation of K$^+$ ions onto the surface of activated samples (K 2p and C 1s are shown in **Figure 6.5 e)** and **f)**).

The oxide character of the surface of nanostructured nickel electrodes is further confirmed by the XAS analysis of sample *Ni-60o/Si*. This sample was thinner than that utilized for the XPS analysis both to verify the extension of oxidation and to adjust its thickness to the proving depth of the technique. **Figures 6.5 g)** and **h)** show the typical XAS spectra at the Ni $L_{2,3}$ and O K absorption edges for this kind of films. The Ni $L_{2,3}$ spectrum (Figure 6.5 g)) is composed by two regions, the Ni L_3 at ~855 eV and the Ni L_2 at ~872 eV, resulting from dipole excited electronic transitions from the Ni $2p_{3/2}$ and Ni $2p_{1/2}$ core levels of nickel to empty states in the conduction band. The intensity ratio of the double-peak in Ni L_3 region depends on the oxidation state of the Ni atoms [41] and it is similar to other electrodes where Ni occupies octahedral sites with an oxidation state of Ni^{+2} [42–44]. On the other hand, the O K absorption spectrum in Figure 6.5 h) corresponds to electronic transitions from a O 1s core level to the empty O 2p states at the conduction band of the system [45]. The four features observed in the recorded spectrum (labelled as A,

B, C and D) can be attributed to the transition into O-p state hybridized with Ni-3d state (feature A) or O-p states hybridized with Ni-4s and Ni-4p states [46] (features B, C and D). These spectral shapes of the Ni $L_{2,3}$ and O K spectra confirm the formation of an oxidized layer in this sample that likely extents through the whole thickness of these films. The similar spectra recorded for sample *Ni-60o/Si* as prepared and after its immersion in KOH solution indicate that changes are slight and only give rise to subtle differences on the high-energy side of L_3 and L_2 spectral edges. These changes can be related to a modulation in the ligand-to-metal charge-transfer and a modification in the electronic structure at the Ni site [47], which we attribute to an additional hydroxylation of the surface. However, the most important from this analysis is the fact that this very thin sample appears to be fully oxidized, which we relate to a result of the exposure to air of this type of highly porous and nanocolumnar OAD samples.

A premise for a straightforward comparison of the performance of electrodes with different chemical composition in the bulk is to ensure that they present a similar microstructure. **Figure 6.6 a-f)** shows SEM images of as deposited *Ni-540o/CP*, *NiO-540o/CP* and *NiOOH-540o/CP* samples. These images confirm that all MS-OAD electrodes present a similar microstructure consisting of a nanocolumnar layer with some minor differences in column size and shape depending on plasma discharge characteristics. This microstructure remained intact after the CV activation although, in some cases, a small area delamination of the nickel phase was found in samples *NiO-540o/CP* and *NiOOH-540o/CP* (see **Figure 6.6 g-i)**).
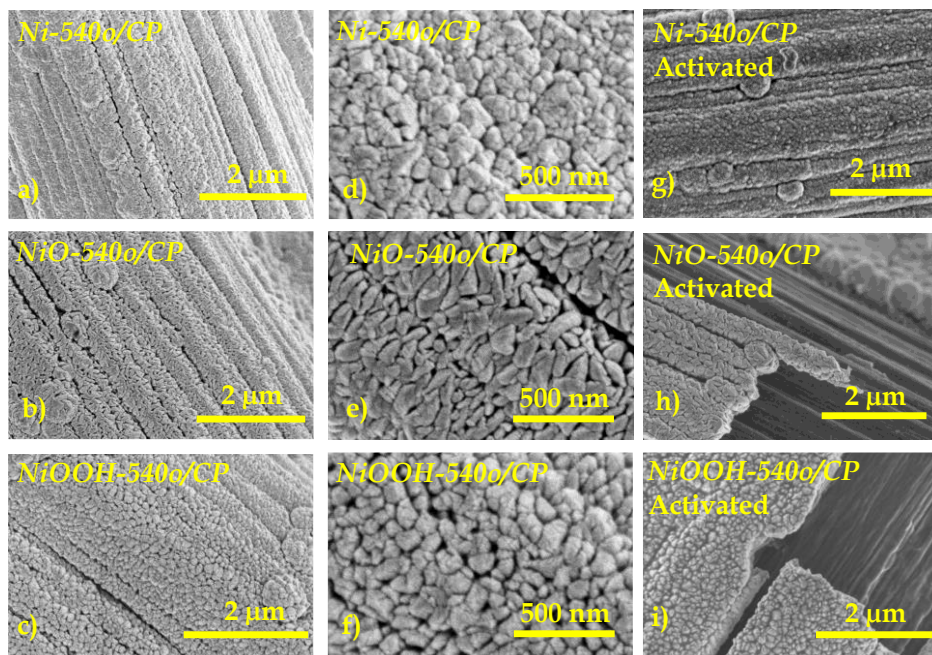
Figure 6.6. *SEM images of a) and d) as deposited Ni-540o/CP, b) and e) NiO-540o/CP and c) and f) NiOOH-540o/CP samples at low and high magnifications. SEM image details of activated g) Ni-540o/CP, h) NiO-540o/CP and i) NiOOH-540o/CP electrode samples taken in zones where a partial delamination has taken place.*

The electrode chemical state had much influence on the electrode performance. **Figure 6.7 a)** shows a series of CVs for samples with a similar *equivalent thickness* but different bulk compositions. Unlike the relatively low anodic redox voltage found for sample *Ni-540o/CP*, a shift to higher voltages was observed for samples *NiO-540o/CP* and *NiOOH-540o/CP*. In addition, the *Ni-540o/CP* electrode presented a higher electrocatalytic intensity yield at 700 mV vs. Ag/AgCl (i.e. under conditions of the OER). Similarly to previous analysis for Ni electrodes, the influence of the chemical nature in the OER performance has been studied by monitoring the Tafel slopes in the CV diagrams. In this case, values of Tafel slopes for *Ni-540o/CP*, *NiO-540o/CP* and *NiOOH-540o/CP*

electrodes were 157, 299 and 311 mV dec^{-1}, respectively (see **Figure 6.7 c)**).
The lowest Tafel slope obtained for the *Ni-540o/CP* electrodes supports
that they perform faster and more efficiently regarding the OER process
[27] than the electrodes manufactured in the form of oxides or
oxyhydroxides.
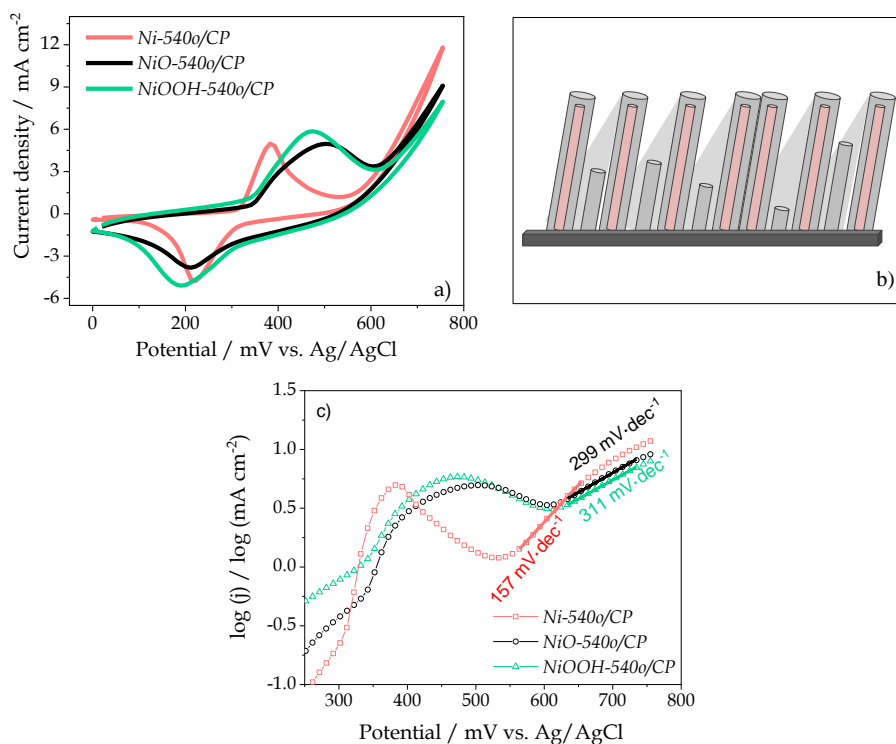
*Figure 6.7. a) CVs of Ni-540o/CP, NiO-540o/CP and NiOOH-540o/CP samples. b)
Morphological scheme of the OAD thin films and of the involvement of the most
external layers of nanocolumns in the electrocatalytic processes. c) Log (j) vs. mV Tafel
plots of Ni-540o/CP, NiO-540o/CP and NiOOH-540o/CP samples. The Tafel slopes
obtained from the linear fits to the initial rise of the OER curves are indicated in the
plots.*

A morphological scheme of the structure of the nanocolumnar films
and the participation of the most external layers of nanocolumns in the
electrochemical processes is reported in **Figure 6.7 b)** showing the

formation of an outer oxidized layer covering the nanocolumns. From the areas of the redox oxidation peaks (i.e. the transferred charge due to the reaction $Ni(OH)_2 + OH^- \leftrightarrows NiOOH + e^-$), it is possible to estimate the atomic ratio between the surface nickel ions that are oxidised to NiOOH according to the reaction and the total amount of nickel atoms present in the electrodes as determined by RBS (see **Figure 6.8**).

The thickness of the oxidized layer built up by electrochemical activation of the as prepared nickel-based catalyst (letters a-c in Figure 6.8) is estimated according to the following considerations. First, considering the scan rate and the area of the oxidation peak of the curves reported in Figure 6.7 a) and knowing that a coulomb is equivalent to the charge of $6.24 \cdot 10^{18}$ electrons, it is possible to calculate the number of atoms that become oxidized per cm^2 of sample. Then, considering the atom surface density (i.e. number of atoms per cm^2 obtained by RBS) in the original samples, it can be calculated the percentage of atoms that become oxidized. Using the SEM measurements, it is possible to estimate the width of the nanocolumns (D_1-D_3 in Figure 6.8) and from this and the geometrical model in Figure 6.8, the approximate thickness of the NiOOH layer. This calculation renders values of 3.6 %, 5.2 % and 7.8 % atoms for the *Ni-540o/CP*, *NiO-540o/CP* and *NiOOH-540o/CP* samples, respectively. From this data it is possible to estimate a thickness of the surface layer undergoing the redox reaction. Assuming that the films microstructure is formed by cylindrical nanocolumns (under this oversimplified assumption, we have considered cylinders with diameters of 86, 100 and 120 nm as deduced from the SEM observation of the head terminations of nanocolumns at the surface of the films), the thickness of the nanocolumns layer affected by redox reaction at the surface has been estimated in 1.0, 1.8 and 3.2 nm for the *Ni-540o/CP, NiO-540o/CP* and

NiOOH-540o/CP samples, respectively. These values must be taken as a crude approximation just useful for comparative purposes because the width of nanocolumns in OAD thin films use to evolve from a very narrow distribution at the beginning of the deposition process to larger width after a kind of cannibalization mechanism by which some nanocolumns grow in width and height in detriment to other [48] (see scheme in Figure 6.7 b)).
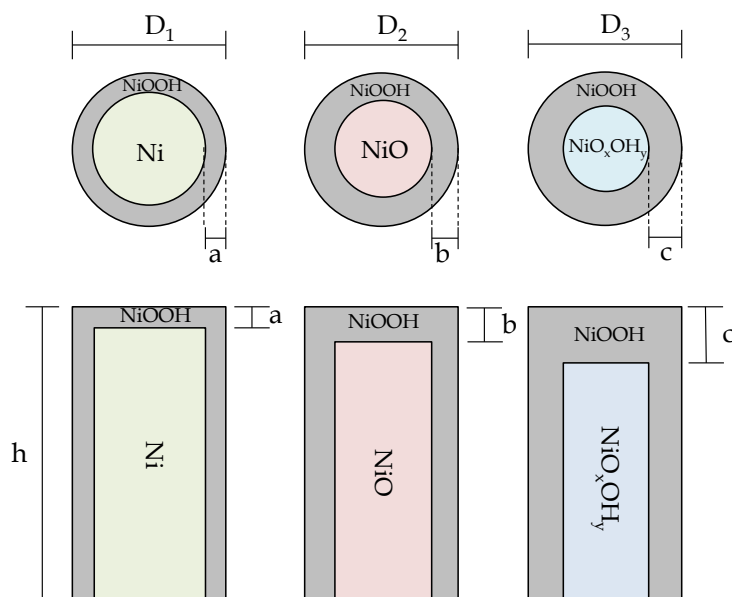
Figure 6.8. Scheme of the nanocolumnar structures proposed for the different electrodes after electrochemical redox partial oxidation.

It is thus likely that the very thin and highly porous nanocolumns (see **Figure 6.9**) formed at the initial stages of the deposition process of the Ni electrodes may become completely oxidized as revealed by the XAS analysis of sample *Ni-60o/Si* (c.f., Figure 6.5 g) and h)). The width of the nanocolumn heads in sample *Ni-60o/Si* is about 15 nm making the initially deposited layer of Ni more prompt to complete oxidation.
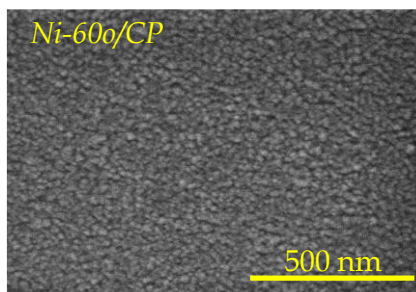
Figure 6.9. *SEM images of Ni-60o/Si supported on Si$_3$N$_4$ membrane*

To avoid possible delamination problems (see Figure 6.6 h) and i))
which seem to affect the Carbon-NiO (NiO$_x$OH$_y$) interfaces in the
examined samples, two more electrodes were fabricated and tested in the
half-cell configuration. They consisted of a bilayer structure formed by
metallic Ni (140 nm *equivalent thickness)* in contact to the carbon fibers of
the GLD and in a second layer of either NiO or NiO$_x$(OH)$_y$ until achieving
a total *equivalent thickness* of 540 nm. It is noteworthy that preparation of
this bilayer structure is straightforward with the MS method of
preparation and that delamination problems of the active nickel phase
were avoided in these bilayer electrodes. However, from the point of
view of their electrochemical performance these bilayer electrodes
behaved similarly to samples *NiO-540o/CP* and *NiOOH-540o/CP* (**see
Figure 6.10 a)**).
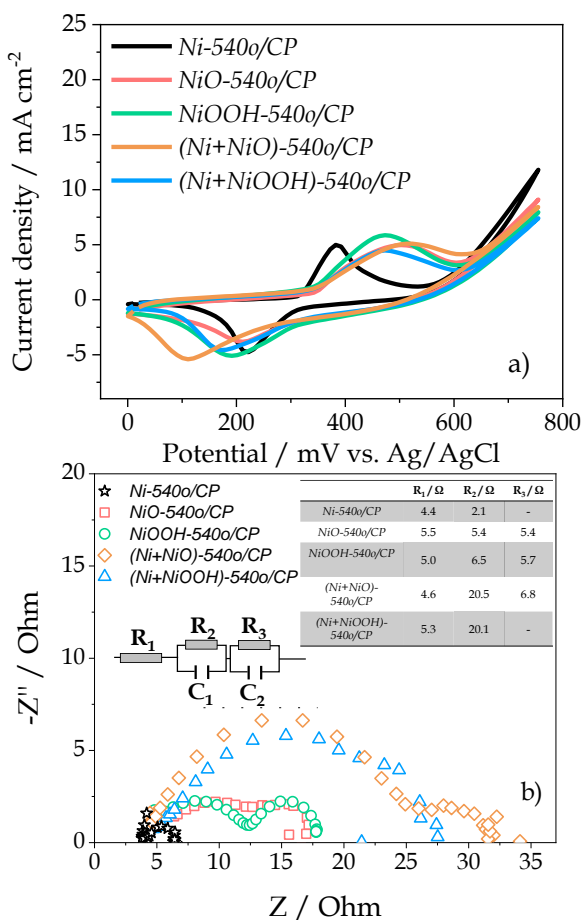
Figure 6.10. a) CV measurements in the half-cell configuration taken for nickel single layer and bilayer based electrodes (1.0 M KOH solution using a scan rate of 20 mV s^{-1}). b) EIS analysis in the form of Nyquist plots for the indicated single layer and bilayer nickel-based electrodes carried out in the three-electrode cell at 700 mV vs. Ag/AgCl. The equivalent electrical circuit used for fitting the Nyquist plots is included as inset.

The XPS analysis of the cycled electrodes in Figure 6.5 and their electrochemical CV characterization in Figure 6.2 and Figure 6.7 might seem contradictory in the sense that a similar surface composition of the active catalytic surface layer renders a different electrochemical behaviour depending on the bulk composition of the nickel phase. To

shed some light into this point we have carried out an EIS analysis of the electrochemical process. **Figure 6.10 b)** shows the corresponding Nyquist plots and the equivalent circuit. The values of the electrical resistances within the fitted equivalent circuit determined for the three single layers and bilayers electrodes are shown in the inset table.

The lowest polarization resistance R_2 was found in sample *Ni-540o/CP*, indicating that charge transfer through the nickel film presents minimum restrictions in these samples. The higher electrical conductivity of the metallic vs. the oxide and oxyhydroxide phases might be invoked to account for this difference [49]. This also agrees with the fact that the outer active nickel oxide/hydroxide catalytic layer involved in the electrochemical process is the thinness in sample *Ni-540o/CP* where the calculations above have predicted a thickness of approximately 1 nm against 1.8 and 3.2 nm calculated for the oxide and oxyhydroxide compositions. In this regard it is also noteworthy that R_2 is much higher for the bilayer electrodes which likely respond to the existence of a minimum of three different interfaces in these layer systems (i.e., C-Ni, Ni-NiO (NiO_xOH_y), NiO-active catalytic layer). The higher values for the R_3 parameter found in samples *NiO-540o/CP* and *NiOOH-540o/CP* (sample *Ni-540o/CP* presents a zero value for this parameter) also supports the higher activity of the nickel metal electrode and suggests a more effective formation of active catalytic intermediate species for the OER.

At this point, it is also noteworthy that applying the aforementioned procedure of Watzele et al. [31], the calculation of the ESCAs of electrodes *NiO-540o/CP* and *NiOOH-540o/CP* was carried out. The C_a values determined were 1.69 and 1.59 mF for *NiO-540o/CP* and *NiOOH-540o/CP* samples obtaining ECSAs values of 5.63 and 5.30 cm², slightly smaller

than that of *Ni-540o/CP* electrode (i.e., 6.13 cm²). This means that the
intrinsic surface parameter of electrodes contributes in the same manner
that the electrical conductivity in favouring that metallic nickel electrodes
prepared in an OAD configuration presents the highest reactivity for the
OER.

6.3.3. <u>Electrode performance in full anion exchange membrane water
        electrolysis cells. Influence of the active phase load in the anode</u>

Once identified that the most reliable and efficient anode for the OER
consists of a nanocolumnar Ni film prepared by MS-OAD, we address in
this section the influence of the thickness of this electrode on the
electrocatalytic performance of an electrolyzer (i.e., including both anode
and cathode of an AEMWE). The aim of this study is to optimise the
electrodes load to achieve the most efficient and reliable performance of
the cell [50].

Figure 6.11 a) shows the linear sweep voltammetries (LSVs) obtained
for different nanostructured metallic nickel anodes with *equivalent
thicknesses* ranging between 140 and 2000 nm (i.e., between 0.09 mg cm⁻²
for *Ni-140o/CP* sample to 1.45 mg cm⁻² for *Ni-2000o/CP* sample). The
cathode in these experiments was a *Ni-280o/CP* electrode. The
experiments were carried out in 1.0 M KOH solution at 40 °C, conditions
that correspond to an optimal electrolyte concentration and working
temperature of previous Chapters 4 and 5. For a fixed cell potential, the
LSV plots in Figure 6.11 a) show that the current density run parallel to
the electrode thickness until a maximum value of approximately 1080 nm.
Meanwhile, cell voltage in **Figure 6.11 b)** at a constant current of 32 mA
cm⁻² remains almost constant all along the experiment (only a slight

increase of 2-5% was found after 14 hours) and confirms that cell voltage is minimum for anodes with an *equivalent thickness* of 1080 nm. We attribute this behaviour to the nanocolumnar character of the OAD nickel layers and the fact that the available surface area and electrocatalytic sites of the anode will increase with its *equivalent thickness* of the nanocolumnar nickel films [23,51]. The breakdown of this tendency above 1080 nm must be linked with the particle agglomeration and degradation of nanocolumnar microstructure (see **Figure 6.12**), [23,52], commonly found in thick OAD thin films [12]. The thickness dependence found for the MEAs is consistent with the OER measurements performed with the half-cells where a broadening of the redox peaks sustains a higher electrical resistance through the electrode (see **Figure 6.13 a)**).
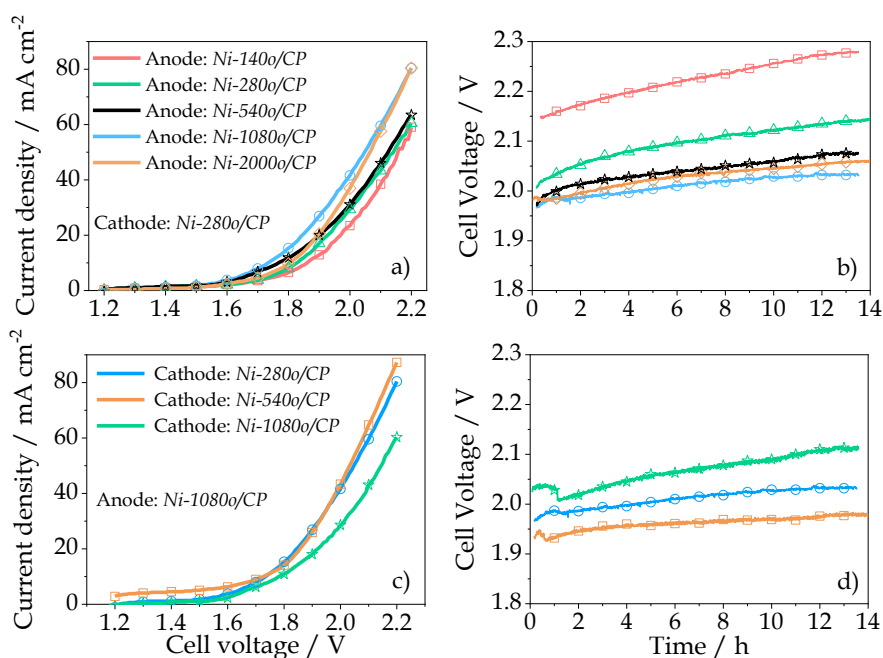
Figure 6.11. *a) LSVs and b) constant-current (32 mA cm⁻²) chronopotentiometries measured for MEA integrating Ni-YYo/CP anodic electrodes. c) LSVs and d) constant-current (32 mA cm⁻²) chronopotentiometries measured for MEA assemblies with Ni-YYo/CP cathodes and the optimum Ni-1080o/CP anode. All measurements were carried out in a 1.0 M KOH electrolyte solution at 40 º.*
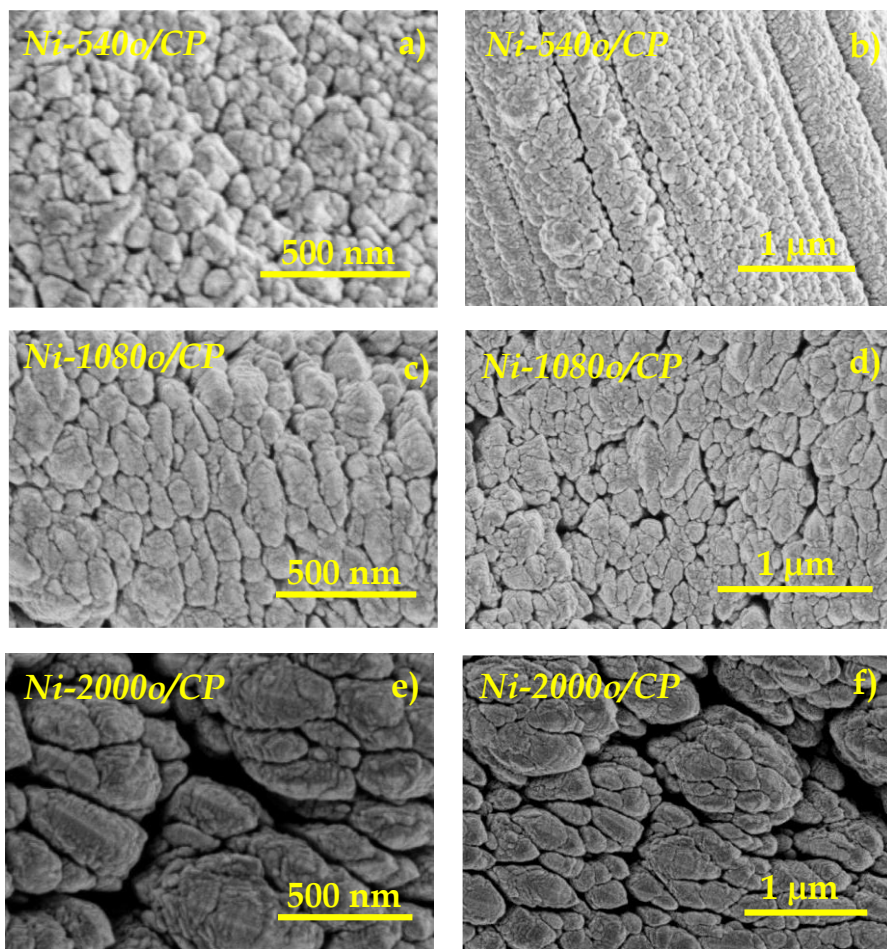
Figure 6.12. *SEM images of a), b) Ni-540o/CP, c), d) Ni-1080o/CP and e), f) Ni-2000o/CP samples at high and low magnification.*
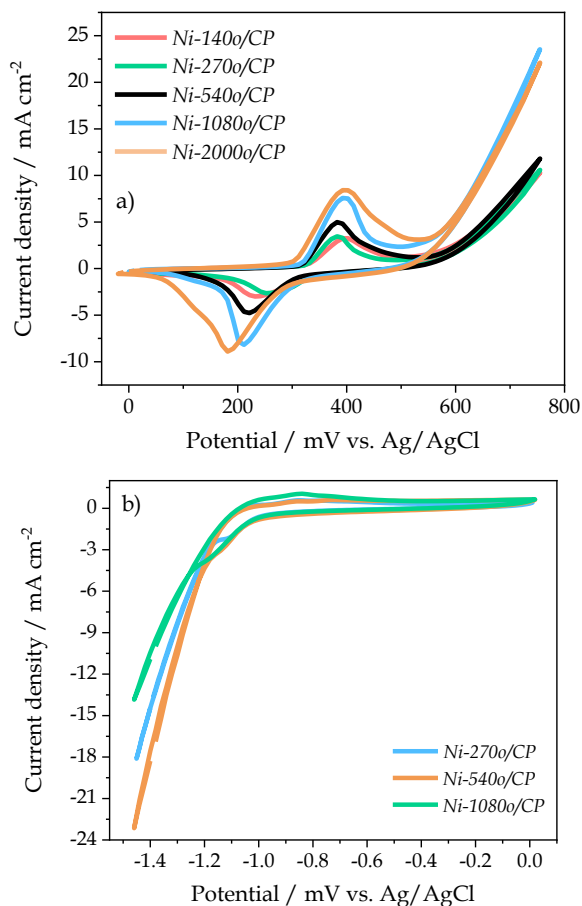
Figure 6.13. a) CV electrochemical measurements (1.0 M KOH, room temperature, scan rate of 20 mV s⁻¹) in a half-cell configuration used to monitor the OER with nanostructured Ni metallic electrodes prepared by MS-OAD. b) CVs for various Ni-YYo/CP cathodes used to monitor the HER in a half-cell configuration (1.0 M KOH solution, room temperature and scan rate of 10 mV s⁻¹).

In the quest for an optimization of cell performance, additional experiments were carried out as a function of operation temperature for the optimal anode thickness of 1080 nm. Results (summarised in **Figure 6.14)** indicate that the OER current density increases with temperature, a fact commonly attributed to an increase in the hydroxyl ion conductivity

through the membrane and a positive effect on the kinetics of the
electrochemical [25,53].
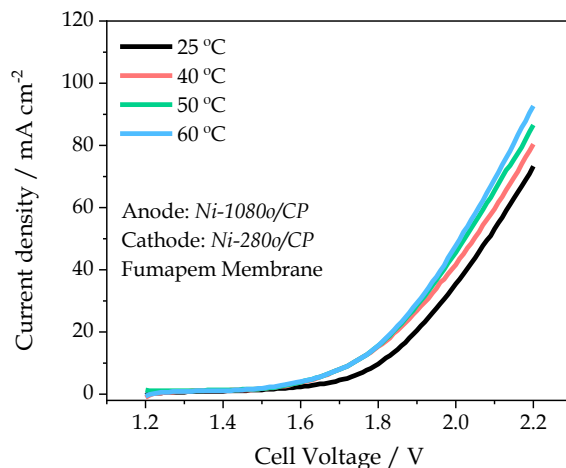
*Figure 6.14. Influence of the temperature on the performance of a MEA prepared with a
Ni-1080o/CP electrode as anode and Ni-280o/CP electrode as cathode (1.0 M KOH
solution and scan rate of 5 mV s⁻¹.)*

6.3.4. Electrode performance in full anion exchange membrane water electrolysis cells. Influence of the active phase load in the cathode

Cathode thickness is another parameter controlling the performance
of the cell. **Figure 6.11 c)** shows a series of LSV curves obtained at 40 °C
with the optimized *Ni-1080o/CP* anode and cathodes of different
equivalent thicknesses. Results show that cell performance increases with
the cathode thickness until a saturation value of 540 nm (*Ni-540o/CP*
sample). Moreover, the constant-current (32 mA cm^{-2})
chronopotentiometries in **Figure 6.11 d)** show a minimum voltage value
for the 540 nm thick cathode and that, as usually observed in this kind of
experiments [54,55], cell stabilization occurs after one hour of operation.
The optimum cathode thickness determined with the MEA assembly was

confirmed in experiments with the three-electrode cell (see **Figure 6.13 b)**) where it was also found an onset HER voltage of approximately -1050 mV vs. Ag/AgCl, in good agreement with other studies with similar electrodes [23,56]. It is noteworthy that the stability study carried out with the different electrodes (see results in Figures 11 b) and d) and **Table 6.1**) only showed a little decrease in performance with time for the different MEA assemblies (i.e., including anodes, cathodes, and membranes). The obtained data showed a change of 2.68 % for the optimum thickness and 5.66 % for thinner electrodes after 13 hours continuous operation. This performance decrease is low compared to other previous studies reported in literature [57–59].

Table 6.1. *Percentage of voltage raise per hour of operation during chronopotentiometry measurements (at 32 mA cm^{-2}) for each anode, cathode and membrane considered in this work.*

Anode	Cathode	Membrane	Voltage rise / % V h^{-1}
Ni-140$_o$/CP	*Ni-280$_o$/CP*	Fumapem	0.43
Ni-280$_o$/CP	*Ni-280$_o$/CP*	Fumapem	0.43
Ni-540$_o$/CP	*Ni-280$_o$/CP*	Fumapem	0.34
Ni-1080$_o$/CP	*Ni-280$_o$/CP*	Fumapem	0.21
	Ni-540$_o$/CP	Fumapem	0.21
		Sustainion	0.25
	Ni-1080$_o$/CP	Fumapem	0.39
Ni-2000$_o$/CP	*Ni-280$_o$/CP*	Fumapem	0.27

6.3.5. Operation, stability tests and yield of full cells

Since the performance of MEA electrolysers may be also affected by the characteristics of the anion exchange membranes, comparative experiments were carried out with Fumapem and Sustainion membranes.

Although a slightly better performance was obtained with the latter type of membranes (see **Figure 6.15**), the rather complex conditioning procedure required for its implementation in the MEA precluded its systematic use and, therefore, most results reported here have been taken for MEAs incorporating the Fumapem membrane. This choice was further supported by the fact that the time performance decrease of the complete cell was lower for the Fumapem membrane (2.68 vs. 3.3. % after 13 hours, see Table 6.1). Cycling stability of the complete cell incorporating this membrane was tested for MEAs incorporating Ni anodes and cathodes of different thickness (see **Figure 6.16).** Independently on electrode thicknesses, no distinctive differences were found after 200 CVs, thus demonstrating the high stability of the metallic Ni cathodes and anodes prepared by MS-OAD. The optimized MEA prepared with the Fumapem membrane (i.e., *Ni-1080o/CP* as anode and *Ni-540o/CP* as cathode) rendered maximum current density values of 87 mA cm^{-2} at 2.2 V operating voltage. Despite the smaller absolute value of current density per geometrical area of these electrodes than other reported in literature for similar electrode compositions [59–61], this yield is equivalent to an electrocatalytic activity per anodic catalyst load of 38 mA mg^{-1} (at 1.9 V), higher than that reported in these previous studies using nickel based systems prepared by chemical and similar techniques, such as $NiCo_2O_4$ (i.e., 10 mA mg^{-1} [1]) or Ni-Fe alloy electrodes (8 and 15 mA mg^{-1} [58,62]).
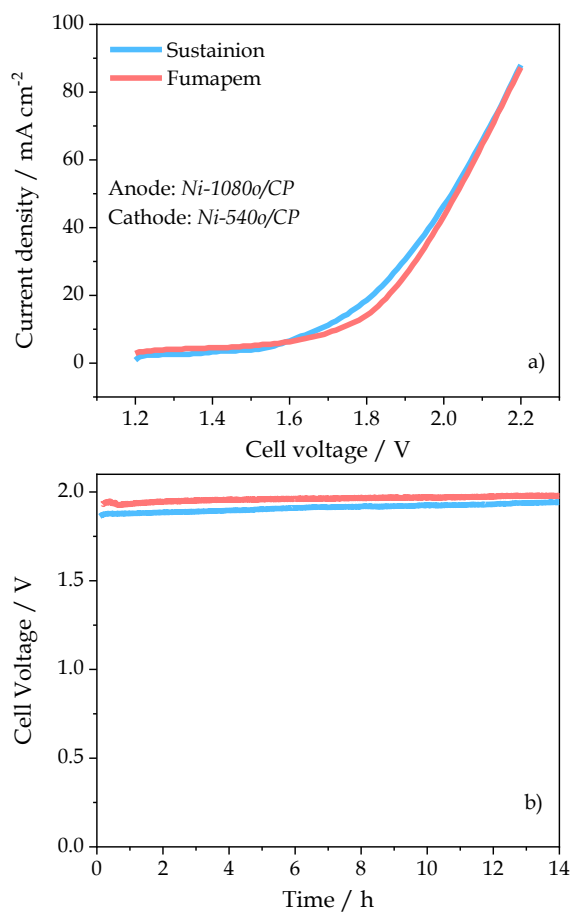
Figure 6.15. *a) LSV obtained for MEA assemblies with Sustainion® and Fumapem® anion exchange membranes and b) constant-current (32 mA cm⁻²) chronopotentiometry response obtained for these two membranes. Both sets of measurements were carried out in a 1.0 M KOH electrolyte solution at 40 °C, using a Ni-1080o/CP anode and a Ni-540o/CP cathode.*
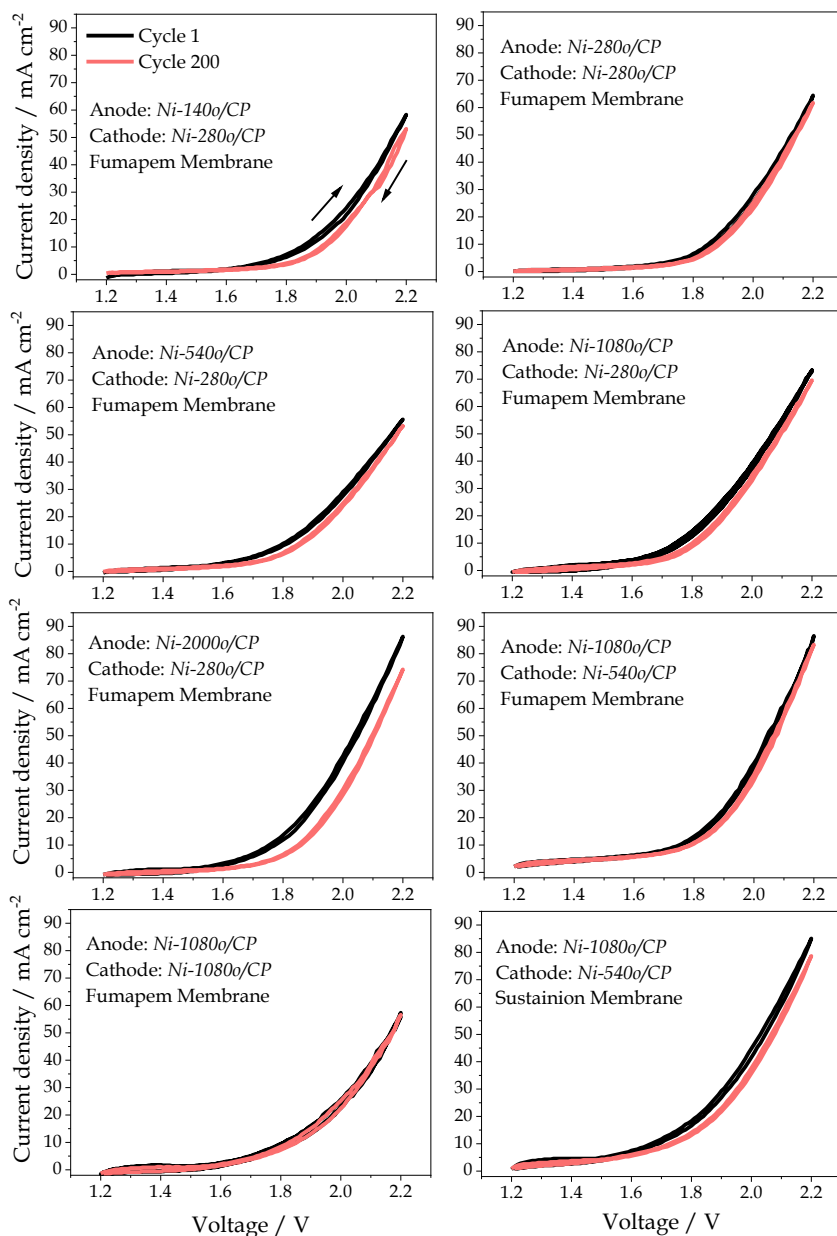
*Figure 6.16. Cyclic voltammetry experiments of Ni metallic electrodes with different
equivalent thickness used as anode and cathode electrodes and different membranes (1.0
M KOH solution at 40 ºC and scan rate 50 mV s⁻¹).*

6.4.   Conclusions

In this chapter, we have shown that the MS-OAD technique is a suitable methodology for the fabrication of nickel nanostructured electrodes for water electrolyzers. Both anodes and cathodes can be prepared at room temperature with this technique, a feature representing a significant advantage for the point of view of the processing of complete electrochemical cell devices. The possibility offered by the MS-OAD technique to prepare electrodes with a similar nanostructure but different chemical formulations (in particular metallic nickel, nickel oxide and nickel oxide/hydroxide) or a bilayer profile has served to prove that the best anode configuration corresponds to a nanostructured metallic Ni anode activated electrochemically before its use to catalyse the OER. It is found that in this metallic nickel electrode the active catalytic phase is a kind of nickel oxide/hydroxide surface layer of some nanometers of thickness covering the metallic nickel nanocolumns obtained by oblique angle deposition.

Analysis of the activated electrodes and the evaluation of the impedance curves obtained for the different types of anodes under OER conditions support that the enhanced performance of the metallic nickel anode with respect to the nickel oxide and nickel oxide/hydroxide compositions resides in the easier electron transfer and movement through the electrodes and the various interlayers built up during their fabrication and activation (i.e., basically because a lower electrical resistivity). Meanwhile the spectroscopic analysis of the different electrodes support that the active catalytic layer involved in the OER is similar for the three anode compositions and consists basically of a kind of Ni oxide-hydroxide.

The activity assessment based on the results obtained with the half-cell array was confirmed with a full electrochemical cell where both anode and cathode consisted of metallic nickel fabricated by MS-OAD. Optimum operating thicknesses for the two electrodes were determined in a full cell where their high stability was proved by electrochemically cycling the system for more than 200 times. When refereeing the maximum cell performance obtained for the optimum operating conditions to the weight of active phase incorporated in the electrodes, the obtained values were higher than those reported for electrodes made of complex bimetallic compounds and alloys prepared by alternative chemical or electrochemical routes.

6.5.   References

[1]   J. Hnát, M. Plevova, R.A. Tufa, J. Zitka, M. Paidar, K. Bouzek, Development and testing of a novel catalyst-coated membrane with platinum-free catalysts for alkaline water electrolysis, Int. J. Hydrogen Energy. 44 (2019) 17493–17504. https://doi.org/10.1016/j.ijhydene.2019.05.054.

[2]   A. Lim, H. Kim, D. Henkensmeier, S. Jong Yoo, J. Young Kim, S. Young Lee, Y.-E. Sung, J.H. Jang, H.S. Park, A study on electrode fabrication and operation variables affecting the performance of anion exchange membrane water electrolysis, J. Ind. Eng. Chem. 76 (2019) 410–418. https://doi.org/10.1016/j.jiec.2019.04.007.

[3]   S. Ghobrial, D. Kirk, S. Thorpe, Amorphous Ni-Nb-Y alloys as hydrogen evolution electrocatalysts, Electrocatalysis. 10 (2019). https://doi.org/10.1007/s12678-019-00519-4.

[4]   C. Yu, F. Xu, L. Luo, H.S. Abbo, S.J.J. Titinchi, P.K. Shen, P. Tsiakaras, S. Yin, Bimetallic Ni–Co phosphide nanosheets self-supported on nickel foam as high-performance electrocatalyst for hydrogen evolution reaction, Electrochim. Acta. 317 (2019) 191–198. https://doi.org/10.1016/j.electacta.2019.05.150.

[5] K. Nejati, S. Davari, A. Akbari, K. Asadpour-Zeynali, Z. Rezvani, A highly active oxygen evolution electrocatalyst: Ni-Fe-layered double hydroxide intercalated with the Molybdate and Vanadate anions, Int. J. Hydrogen Energy. 44 (2019) 14842–14852. https://doi.org/10.1016/j.ijhydene.2019.04.045.

[6] D.A. Corrigan, The catalysis of the oxygen evolution reaction by iron impurities in thin film nickel oxide electrodes, J. Electrochem. Soc. 134 (1987) 377–384. https://doi.org/10.1149/1.2100463.

[7] D.D. Rodene, E.H. Eladgham, R.B. Gupta, I.U. Arachchige, V. Tallapally, Crystal structure and composition-dependent electrocatalytic activity of Ni–Mo nanoalloys for water splitting to produce hydrogen, ACS Appl. Energy Mater. 2 (2019) 7112–7120. https://doi.org/10.1021/acsaem.9b01043.

[8] F. Zheng, Z. Zhang, D. Xiang, P. Li, C. Du, Z. Zhuang, X. Li, W. Chen, Fe/Ni bimetal organic framework as efficient oxygen evolution catalyst with low overpotential, J. Colloid Interface Sci. 555 (2019) 541–547. https://doi.org/10.1016/j.jcis.2019.08.005.

[9] A. Tahira, Z.H. Ibupoto, M. Vagin, U. Aftab, M.I. Abro, M. Willander, O. Nur, An efficient bifunctional electrocatalyst based on a nickel iron layered double hydroxide functionalized Co_3O_4 core shell structure in alkaline media, Catal. Sci. Technol. 9 (2019) 2879–2887. https://doi.org/10.1039/C9CY00351G.

[10] A.C. Garcia, T. Touzalin, C. Nieuwland, N. Perini, M.T.M. Koper, Enhancement of oxygen evolution activity of nickel oxyhydroxide by electrolyte alkali cations, Angew. Chemie Int. Ed. 58 (2019) 12999–13003. https://doi.org/10.1002/anie.201905501.

[11] I. Spanos, M.F. Tesch, M. Yu, H. Tüysüz, J. Zhang, X. Feng, K. Müllen, R. Schlögl, A.K. Mechler, Facile protocol for alkaline electrolyte purification and its influence on a Ni–Co oxide catalyst for the oxygen evolution reaction, ACS Catal. 9 (2019) 8165–8170. https://doi.org/10.1021/acscatal.9b01940.

[12] A. Garcia-Valenzuela, S. Muñoz-Piña, G. Alcala, R. Alvarez, B. Lacroix, A.J. Santos, J. Cuevas-Maraver, V. Rico, R. Gago, L. Vazquez, J. Cotrino, A.R. Gonzalez-Elipe, A. Palmero, Growth of nanocolumnar thin films on patterned substrates at oblique angles, Plasma Process. Polym. 16 (2019). https://doi.org/10.1002/ppap.201800135.

[13]   W. Phae-ngam, M. Horprathum, C. Chananonnawathorn, T. Lertvanithphol, B. Samransuksamer, P. Songsiriritthigul, H. Nakajima, S. Chaiyakun, Oblique angle deposition of nanocolumnar TiZrN films via reactive magnetron co-sputtering technique: The influence of the Zr target powers, Curr. Appl. Phys. 19 (2019) 894–901. https://doi.org/10.1016/j.cap.2019.05.002.

[14]   A. Garcia-Valenzuela, R. Alvarez, C. Lopez-Santos, F.J. Ferrer, V. Rico, E. Guillen, M. Alcon-Camas, R. Escobar-Galindo, A.R. Gonzalez-Elipe, A. Palmero, Stoichiometric control of SiO_x thin films grown by reactive magnetron sputtering at oblique angles, Plasma Process. Polym. 13 (2016) 1242–1248. https://doi.org/10.1002/ppap.201600077.

[15]   S. V Green, M. Watanabe, N. Oka, G.A. Niklasson, C.G. Granqvist, Y. Shigesato, Electrochromic properties of nickel oxide based thin films sputter deposited in the presence of water vapor, Thin Solid Films. 520 (2012) 3839–3842. https://doi.org/10.1016/j.tsf.2011.08.030.

[16]   J. Gil-Rostra, M. Cano, J.M. Pedrosa, F.J. Ferrer, F. García-García, F. Yubero, A.R. González-Elipe, Electrochromic behavior of $W_xSi_yO_z$ thin films prepared by reactive magnetron sputtering at normal and glancing angles, ACS Appl. Mater. Interfaces. 4 (2012) 628–638. https://doi.org/10.1021/am2014629.

[17]   J. Wang, S. Li, Y. Zhao, J. Shi, L. Lv, H. Wang, Z. Zhang, W. Feng, The influence of different Si : C ratios on the electrochemical performance of silicon/carbon layered film anodes for lithium-ion batteries, RSC Adv. 8 (2018) 6660–6666. https://doi.org/10.1039/C7RA12027C.

[18]   A. Mukanova, A. Nurpeissova, A. Urazbayev, S.-S. Kim, M. Myronov, Z. Bakenov, Silicon thin film on graphene coated nickel foam as an anode for Li-ion batteries, Electrochim. Acta. 258 (2017) 800–806. https://doi.org/10.1016/j.electacta.2017.11.129.

[19]   X.H. Huang, P. Zhang, J.B. Wu, Y. Lin, R.Q. Guo, Nickel/silicon core/shell nanosheet arrays as electrode materials for lithium ion batteries, Mater. Res. Bull. 80 (2016) 30–35. https://doi.org/10.1016/j.materresbull.2016.03.021.

[20]   X. Mei, Q. Wei, H. Long, Z. Yu, Z. Deng, L. Meng, J. Wang, J. Luo, C.-T. Lin, L. Ma, K. Zheng, N. Hu, Long-term stability of Au nanoparticle-anchored porous boron-doped diamond hybrid electrode for enhanced dopamine detection, Electrochim. Acta. 271 (2018) 84–91. https://doi.org/10.1016/j.electacta.2018.03.133.

[21]   O. Sánchez, M. Hernández-Vélez, D. Navas, M. Auger, J. Baldonedo, R. Sanz, K.R. Pirota, M. Vázquez, Functional nanostructured titanium nitride films obtained by sputtering magnetron, Thin Solid Films. 495 (2006) 149–153. https://doi.org/10.1016/j.tsf.2005.08.203.

[22]   Y. Lim, S. Hong, J. Bae, H. Yang, Y.-B. Kim, Influence of deposition temperature on the microstructure of thin-film electrolyte for SOFCs with a nanoporous AAO support structure, Int. J. Hydrogen Energy. 42 (2017). https://doi.org/10.1016/j.ijhydene.2017.03.148.

[23]   S. Ahn, B.-S. Lee, I. Choi, S. Yoo, H.-J. Kim, E. Cho, D. Henkensmeier, S. Nam, J. Jang, Development of a membrane electrode assembly for alkaline water electrolysis by direct electrodeposition of nickel on carbon papers, Appl. Catal. B Environ. 154–155 (2014) 197–205. https://doi.org/10.1016/j.apcatb.2014.02.021.

[24]   A.K. Taylor, I. Andreu, B.D. Gates, Regular dimpled nickel surfaces for improved efficiency of the oxygen evolution reaction, ACS Appl. Energy Mater. 1 (2018) 1771–1782. https://doi.org/10.1021/acsaem.8b00338.

[25]   E. López-Fernández, J. Gil-Rostra, J.P. Espinós, A.R. González-Elipe, F. Yubero, A. de Lucas-Consuegra, $Cu_xCo_{3-x}O_4$ ultra-thin film as efficient anodic catalysts for anion exchange membrane water electrolysers, J. Power Sources. 415 (2019) 136–144. https://doi.org/10.1016/j.jpowsour.2019.01.056.

[26]   R. Farhat, J. Dhainy, L.I. Halaoui, OER catalysis at activated and codeposited NiFe-Oxo/Hydroxide thin films is due to postdeposition surface-Fe and is not sustainable without Fe in solution, ACS Catal. 10 (2020) 20–35. https://doi.org/10.1021/acscatal.9b02580.

[27]   G.B. Shombe, M.D. Khan, C. Zequine, C. Zhao, R.K. Gupta, N. Revaprasadu, Direct solvent free synthesis of bare α-NiS, β-NiS and α-β-NiS composite as excellent electrocatalysts: Effect of self-capping on supercapacitance and overall water splitting activity, Sci. Rep. 10 (2020) 3260. https://doi.org/10.1038/s41598-020-59714-9.

[28]   L. Mais, S. Palmas, M. Mascia, E. Sechi, M.F. Casula, J. Rodriguez, A. Vacca, Porous Ni photocathodes obtained by selective corrosion of Ni-Cu films: synthesis and photoelectrochemical characterization, Catal. . 9 (2019). https://doi.org/10.3390/catal9050453.

[29]   M. Yu, G. Moon, E. Bill, H. Tüysüz, Optimizing Ni–Fe oxide electrocatalysts for oxygen evolution reaction by using hard templating as a toolbox, ACS Appl. Energy Mater. 2 (2019) 1199–1209.

https://doi.org/10.1021/acsaem.8b01769.

[30] I. Zaharieva, D. González-Flores, B. Asfari, C. Pasquini, M.R. Mohammadi, K. Klingan, I. Zizak, S. Loos, P. Chernev, H. Dau, Water oxidation catalysis – role of redox and structural dynamics in biological photosynthesis and inorganic manganese oxides, Energy Environ. Sci. 9 (2016) 2433–2443. https://doi.org/10.1039/C6EE01222A.

[31] S. Watzele, P. Hauenstein, Y. Liang, S. Xue, J. Fichtner, B. Garlyyev, D. Scieszka, F. Claudel, F. Maillard, A.S. Bandarenka, Determination of electroactive surface area of Ni-, Co-, Fe-, and Ir-based oxide electrocatalysts, ACS Catal. 9 (2019) 9222–9230. https://doi.org/10.1021/acscatal.9b02006.

[32] J.D. Hanawalt, H.W. Rinn, L.K. Frevel, Chemical analysis by X-ray diffraction, Ind. Eng. Chem. Anal. Ed. 10 (1938) 457–512. https://doi.org/10.1021/ac50125a001.

[33] J.D. Hanawalt, H.W. Rinn, L.K. Frevel, Chemical analysis by X-ray diffraction, Ind. Eng. Chem. Anal. Ed. 10 (1938) 457–512. https://doi.org/10.1021/ac50125a001.

[34] H.E.T.E. Swanson, Standard X-ray diffraction powder patterns, Natl. Bur. Stand. Circ. 539 (1953) 47. https://doi.org/10.1038/176147a0.

[35] M. Marezio, P.D. Dernier, J. Chenavas, J.C. Joubert, High pressure synthesis and crystal structure of $NaMn_7O_{12}$, J. Solid State Chem. 6 (1973) 16–20. https://doi.org/10.1016/0022-4596(73)90200-4.

[36] G. Natta, L. Passerini, Aluminum Arsenide, Gazz. Chim. Ital. 58 (1928) 458–460.

[37] I.G. Casella, M. Contursi, Pulsed electrodeposition of nickel/palladium globular particles from an alkaline gluconate bath. An electrochemical, XPS and SEM investigation, J. Electroanal. Chem. 692 (2013) 80–86. https://doi.org/10.1016/j.jelechem.2013.01.015.

[38] H.-X. Li, W. Hao, J. Hu, H. Wu, A photoelectrochemical sensor based on nickel hydroxyl-oxide modified n-silicon electrode for hydrogen peroxide detection in an alkaline solution, Biosens. Bioelectron. 47C (2013) 225–230. https://doi.org/10.1016/j.bios.2013.03.028.

[39] F. Muench, M. Oezaslan, M. Rauber, S. Kaserer, A. Fuchs, E. Mankel, J. Brötz, P. Strasser, C. Roth, W. Ensinger, Electroless synthesis of nanostructured nickel and nickel–boron tubes and their performance as unsupported ethanol electrooxidation catalysts, J. Power Sources. 222
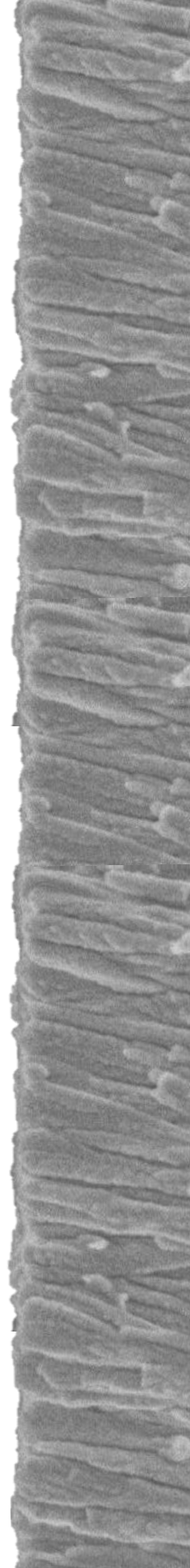
(2013) 243–252. https://doi.org/10.1016/j.jpowsour.2012.08.067.

[40] A. Shanmugavani, R.K. Selvan, Improved electrochemical performances of $CuCo_2O_4/CuO$ nanocomposites for asymmetric supercapacitors, Electrochim. Acta. 188 (2016) 852–862. https://doi.org/10.1016/j.electacta.2015.12.077.

[41] D. Drevon, M. Görlin, P. Chernev, L. Xi, H. Dau, K.M. Lange, Uncovering The role of oxygen in $Ni-Fe(O_xH_y)$ electrocatalysts using in situ soft X-ray absorption spectroscopy during the oxygen evolution reaction, Sci. Rep. 9 (2019) 1532. https://doi.org/10.1038/s41598-018-37307-x.

[42] A. Mandziak, J. de la Figuera, S. Ruiz-Gómez, G.D. Soria, L. Pérez, P. Prieto, A. Quesada, M. Foerster, L. Aballe, Structure and magnetism of ultrathin nickel-iron oxides grown on Ru(0001) by high-temperature oxygen-assisted molecular beam epitaxy, Sci. Rep. 8 (2018) 17980. https://doi.org/10.1038/s41598-018-36356-6.

[43] C. Klewe, M. Meinert, A. Boehnke, K. Kuepper, E. Arenholz, A. Gupta, J.-M. Schmalhorst, T. Kuschel, G. Reiss, Physical characteristics and cation distribution of $NiFe_2O_4$ thin films with high resistivity prepared by reactive co-sputtering, J. Appl. Phys. 115 (2014) 123903. https://doi.org/10.1063/1.4869400.

[44] D. Alders, L.H. Tjeng, F.C. Voogt, T. Hibma, G.A. Sawatzky, C.T. Chen, J. Vogel, M. Sacchi, S. Iacobucci, Temperature and thickness dependence of magnetic moments in NiO epitaxial films, Phys. Rev. B. 57 (1998) 11623–11631. https://doi.org/10.1103/PhysRevB.57.11623.

[45] M. Sharma, R.N. Aljawfi, K. Kumari, K.H. Chae, S. Gautam, S. Dalela, P.A. Alvi, S. Kumar, Investigation of local atomic structure of Ni doped SnO_2 thin films via X-ray absorption spectroscopy and their magnetic properties, J. Mater. Sci. Mater. Electron. 30 (2019) 760–770. https://doi.org/10.1007/s10854-018-0345-x.

[46] G. Jayalakshmi, K. Saravanan, B.K. Panigrahi, P. Magudapathy, High efficient electron field emission from rGO conformally coated NiO nanoflakes architecture, J. Mater. Sci. Mater. Electron. 29 (2018) 14689–14696. https://doi.org/10.1007/s10854-018-9605-z.

[47] M. Al Samarai, A.W. Hahn, A. Beheshti Askari, Y.-T. Cui, K. Yamazoe, J. Miyawaki, Y. Harada, O. Rüdiger, S. DeBeer, Elucidation of structure–activity correlations in a nickel manganese oxide oxygen evolution reaction catalyst by operando Ni L-edge X-ray absorption spectroscopy and 2p3d resonant inelastic X-ray scattering, ACS Appl. Mater. Interfaces.

11 (2019) 38595–38605. https://doi.org/10.1021/acsami.9b06752.

[48]   A. Barranco, A. Borras, A.R. Gonzalez-Elipe, A. Palmero, Perspectives on oblique angle deposition of thin films: From fundamentals to devices, Prog. Mater. Sci. 76 (2016) 59–153. https://doi.org/10.1016/j.pmatsci.2015.06.003.

[49]   S. Naghdi, K.Y. Rhee, D. Hui, S.J. Park, A review of conductive metal nanomaterials as conductive, transparent, and flexible coatings, thin films, and conductive fillers: different deposition methods and Applications, Coatings. 8 (2018). https://doi.org/10.3390/coatings8080278.

[50]   A. de Lucas-Consuegra, A.B. Calcerrada, A.R. de la Osa, J.L. Valverde, Electrochemical reforming of ethylene glycol. Influence of the operation parameters, simulation and its optimization, Fuel Process. Technol. 127 (2014) 13–19. https://doi.org/10.1016/j.fuproc.2014.06.010.

[51]   A.H. Ghanim, J.G. Koonce, B. Hasa, A.M. Rassoolkhani, W. Cheng, D.W. Peate, J. Lee, S. Mubeen, Low-loading of Pt nanoparticles on 3D carbon foam support for highly active and stable hydrogen production, Front. Chem. 6 (2018) 523.

[52]   Y.T. Lee, R.P. Gautam, S.M. Islam, C.J. Barile, Cuprous oxide electrodeposited with nickel for the oxygen evolution reaction in 1 M NaOH, J. Phys. Chem. C. 123 (2019) 1287–1292. https://doi.org/10.1021/acs.jpcc.8b10413.

[53]   A.B. Calcerrada, A.R. de la Osa, E. Lopez-Fernandez, F. Dorado, A. de Lucas-Consuegra, Influence of the carbon support on the Pt–Sn anodic catalyst for the electrochemical reforming of ethanol, Int. J. Hydrogen Energy. 44 (2019) 10616–10626. https://doi.org/10.1016/j.ijhydene.2019.03.011.

[54]   A. Konovalova, H. Kim, S. Kim, A. Lim, H.S. Park, M.R. Kraglund, D. Aili, J.H. Jang, H.-J. Kim, D. Henkensmeier, Blend membranes of polybenzimidazole and an anion exchange ionomer (FAA3) for alkaline water electrolysis: Improved alkaline stability and conductivity, J. Memb. Sci. 564 (2018) 653–662. https://doi.org/10.1016/j.memsci.2018.07.074.

[55]   M.K. Cho, A. Lim, S.Y. Lee, H.-J. Kim, S.J. Yoo, Y.-E. Sung, H.S. Park, J.H. Jang, A review on membranes and catalysts for anion exchange membrane water electrolysis single cells, J. Electrochem. Sci. Technol. 8 (2017) 183–196. https://doi.org/10.5229/JECST.2017.8.3.183.

[56]   G. Borisov, H. Penchev, K. Maksimova-Dimitrova, F. Ublekov, E. Lefterova, V. Sinigersky, E. Slavcheva, Alkaline water electrolysis facilitated via non-precious monometallic catalysts combined with highly KOH doped polybenzimidazole membrane, Mater. Lett. 240 (2019) 144–146. https://doi.org/10.1016/j.matlet.2018.12.141.

[57]   P. Ganesan, A. Sivanantham, S. Shanmugam, Nanostructured nickel–cobalt–titanium alloy grown on titanium substrate as efficient electrocatalyst for alkaline water electrolysis, ACS Appl. Mater. Interfaces.   9   (2017)   12416–12426. https://doi.org/10.1021/acsami.7b00353.

[58]   L. Xiao, S. Zhang, J. Pan, C. Yang, M. He, L. Zhuang, J. Lu, First implementation of alkaline polymer electrolyte water electrolysis working only with pure water, Energy Environ. Sci. 5 (2012) 7869–7871. https://doi.org/10.1039/C2EE22146B.

[59]   Z. Liu, S.D. Sajjad, Y. Gao, H. Yang, J.J. Kaczur, R.I. Masel, The effect of membrane on an alkaline water electrolyzer, Int. J. Hydrogen Energy. 42 (2017) 29661–29665. https://doi.org/10.1016/j.ijhydene.2017.10.050.

[60]   J.E. Park, S.Y. Kang, S.-H. Oh, J.K. Kim, M.S. Lim, C.-Y. Ahn, Y.-H. Cho, Y.-E. Sung, High-performance anion-exchange membrane water electrolysis,   Electrochim.   Acta.   295   (2019)   99–106. https://doi.org/10.1016/j.electacta.2018.10.143.

[61]   T. Pandiarajan, L. John Berchmans, S. Ravichandran, Fabrication of spinel ferrite based alkaline anion exchange membrane water electrolysers for hydrogen   production,   RSC   Adv.   5   (2015)   34100–34108. https://doi.org/10.1039/C5RA01123J.

[62]   P. Salvi, P. Nelli, M. Villa, Y. Kiros, G. Zangari, G. Bruni, A. Marini, C. Milanese, Hydrogen evolution reaction in PTFE bonded Raney-Ni electrodes,   Int.   J.   Hydrogen   Energy.   36   (2011)   7816–7821. https://doi.org/10.1016/j.ijhydene.2011.01.173.

Chapter 7

Nickel-iron bimetallic electrodes for anion exchange membrane water electrolysis
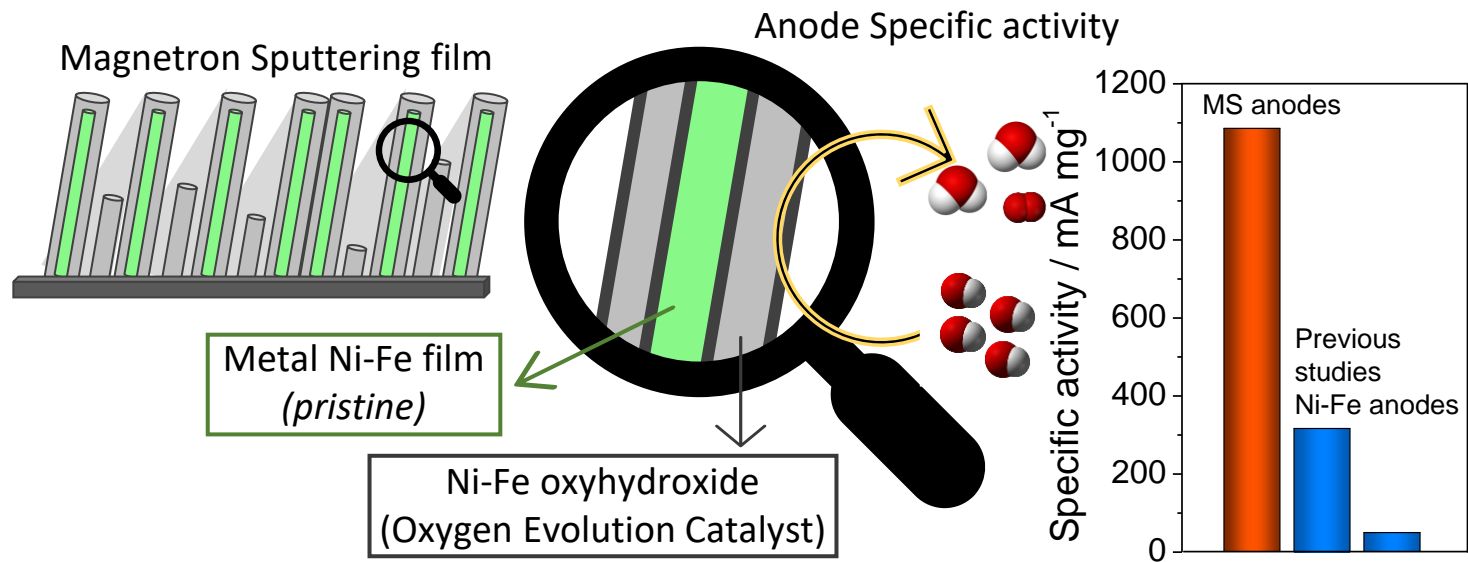
The content of this chapter is in press as:

7.1. Introduction

In the previous chapter, we have demonstrated the viability and good performance of nanostructured nickel electrode catalysts prepared by MS-OAD as anodes for AEMWE cells. To progress in the search of improved performance of this type of electrolyzers, several nickel alloy-based catalyst formulations have been proposed in the literature [1–3]. In particular it is reported that adding Fe to structure of nickel catalysts decreases the OER overpotential [4], resulting in a highly active and low cost AEMWE electrocatalytic system compared with other non-platinum catalysts [5]. Thus, in this chapter we report on the performance of bimetallic Ni-Fe catalysts electrodes prepared by MS-OAD. Among the new results of the present study, we also demonstrate the compatibility of this procedure with an efficient synthesis of nanostructure bimetallic electrodes providing high hydrogen production.

Traditional preparation methods of AEMWE electrodes often involve the addition of polymeric organic ionomer binder molecules to the catalytic inks to increase the cell performance [6,7]. The ionomer function is to increase the number of ion transport pathways at the reaction sites between the catalyst layer and the anion exchange membrane. It improves the gas permeability and, thanks to its charged functional groups, it facilities the exchange of water and OH^- anions at the catalyst surface [6,8]. However, ionomers may also be disadvantageous if, through electrostatic/covalent interactions, their charged groups occupy some catalyst active sites, leading to an increase in the HER and OER potentials [6]. Over time, ionomers may also undergo chemical degradation, resulting in a deterioration of the effective catalyst-ionomer interface and, therefore, the electrochemically active electrode surface [9].

In this chapter, we report the OER performance of several ionomer-free Ni-Fe nanostructured anodes in a three-electrode cell. A thorough structural, microstructural, chemical, and electrochemical characterization of electrodes with several Ni/Fe atomic ratios is carried out by XPS, SEM, XRD, Raman Spectroscopy, EDX and EIS. As a result of these studies, it is realized that the bimetallic character of the electrodes, their mixed oxide/hydroxide surface oxidation state and high surface area are key points accounting for their outstanding performance towards OER.

The most performance Ni-Fe anodes towards OER in half-cell electrochemical measurements have been selected and scaled up for its integration in a MEA configuration to study the influence of assembly conditions, operation temperature, electrolyte concentration and ionomer addition. The obtained results have demonstrated the outstanding properties of the fabricated bimetallic films in terms of activity, stability, and operation under ionomer-free conditions. Current density values around 400 mA cm^{-2} and 600 mA cm^{-2} at 40 $^{\circ}$C and 60 $^{\circ}$C (2.0 V) were obtained respectively, much higher than those obtained with pure Ni electrodes. The high yield obtained with these electrodes gains further relevance when considering that the current yield per unit mass of the anodic catalyst (i.e., 1086 mA mg^{-1} at 2.0 V and 40 $^{\circ}$C) is the highest among equivalent values reported in literature. The possibilities and prospects of the use of bimetallic catalyst films prepared by MS-OAD for AEMWE are also discussed in this chapter.

7.2.   Experimental

Bimetallic Ni/Fe catalyst electrodes were prepared by MS-OAD at room temperature previously explained in Chapter 3. Carbon paper substrates were used as conductive gas diffusion layer (GDL) supports to carry out the electrochemical experiments. Morphological characterization by SEM was carried out for films deposited on polished silicon wafer substrates. An *equivalent thickness* for the electrodes (540 nm for most films in this study) was obtained by cross-sectional SEM analysis of the films deposited onto the silicon substrates. Argon was used as plasma gas to obtain Ni/Fe metallic alloy electrodes.

In this chapter, samples will be identified in the paper as follows: *XX-NiFe-thickness/ZZ,* where *XX* refers the Ni/Fe at. ratio determined by EDX Spectroscopy and *ZZ* is the support used in each electrode. Ni electrodes are designated by *Ni-thickness/ZZ*. Thus, *10.1-NiFe-540/CP* and *Ni-540/CP* refer to electrodes with 10.1 Ni/Fe at. ratio and pure nickel, respectively, deposited on carbon paper with an *equivalent thickness* of 540 nm. Note that XX is just a way to label the manufactured samples according to their Ni/Fe stoichiometry determined by EDX. We denoted as *as prepared* electrodes those pristine samples that have not been used in any electrochemical test and *used* samples those used in electrochemical experiments.

All the physico-chemical characterization techniques used in this study have been briefly described in Chapter 3.

To assess the influence of the Ni/Fe at. ratio on the OER performance of anodes, a series of electrochemical experiments were carried out in a three-electrode cell (i.e., half-cell configuration, previously explained in Chapter 3).

Electrodes prepared with the Ni/Fe stoichiometry depicting the highest OER yield with the three-electrode cell were scaled-up to a MEA configuration to study the influence of additional parameters (incorporation of ionomer, cell temperature, electrolyte concentration) in the performance of an AEMWE electrolyzer cell. Thus, a *10.1-NiFe-540/CP* electrode (catalyst load of 0.35 mg cm^{-2}, *equivalent thickness* 540 nm) was used as anode and a *Ni-540/CP* electrode (load of 0.38 mg cm^{-2}, *equivalent thickness* 540 nm) as cathode. The electrodes were separated by an anion exchange membrane (Fumapem® FAA-3-50).

Typically, ionomers are mixed with the catalyst inks before their impregnation onto the corresponding gas diffusion layer [6,14,15], often with an optimized 20 % ionomer/catalyst ratio [7,8,16]. Herein, to study the influence of ionomer addition, we have incorporated the ionomer on the anode surface after the catalyst deposition on the carbon paper GDL. A 10 % Fumion FAA-3 solution in N-Methyl-2-pyrrolidone (NMP) from Fuel Cell Store was selected as ionomer. Three situations have been explored: i) ionomer-free anodes; ii) anodes impregnated with previously mentioned optimised ionomer/catalyst load (in our case dripping 4.4 mg of ionomer with a micropipette onto de catalyst deposit), labelled as *I/C=0.2* in the text); iii) anodes fully covered with ionomer solution (labelled *Ionom. Surf.* in the text). In all cases, the ionomer solvent was removed from the electrodes surface by drying in a muffle furnace at 210 °C for two hours.

In these cases, experiments consisted of linear sweep voltammetries at various fixed temperatures between 30 and 60 °C. Several electrolyte concentrations, 0.10, 0.15 and 1.0 M KOH, were used in both anode and cathode compartments. The torque applied to close the cell was varied between 1.0 and 3.0 Nm. In addition, the stability of the cell was

investigated by constant-current chronopotentiometric experiments at 400 mA cm^{-2} for 2 days and 200 cyclic voltammetry experiments, both at 40 °C.

EIS measurements were also performed for the MEA configuration (1.0 M KOH, 40 °C) at 2000 mV for a potential perturbation amplitude of 10 mV, varying the AC frequency from 100 kHz to 10 mHz.

7.3.   Results and discussion

7.3.1.   Composition and microstructure of Ni/Fe bimetallic electrodes

The surface microstructure of the Ni/Fe electrodes is exemplified with the SEM analysis of sample *10.1-NiFe-540/CP* before (**Figure 7.1 a)**) and after their use (**Figure 7.1 b)**) in a series of 25 cyclic voltammetries experiments. In both cases, a similar porous and rather homogeneous microstructure can be observed, without any appreciable degradation or delamination after use, clearly evidencing the great stability of the electrodes. Furthermore, this stability can be confirmed because no traces of Fe and Ni have been observed after performing an ICP analysis of the solution after experiments. **Figure 7.1 c)** shows a cross-sectional image of the same catalyst film deposited onto a polished silicon substrate to measure its *equivalent thickness*. This image confirms that the film is composed of nanocolumns that, separated by large voids, provide a high porosity and straightforward liquid electrolyte accessibility to the whole electrode [17]. **Figures 7.1 d-f)** show SEM images for three Ni/Fe at. ratio films deposited onto polished silicon substrates. It is apparent in these images that the addition of increasing amounts of Fe to the Ni based electrodes do not significantly modify the microstructure of the films.
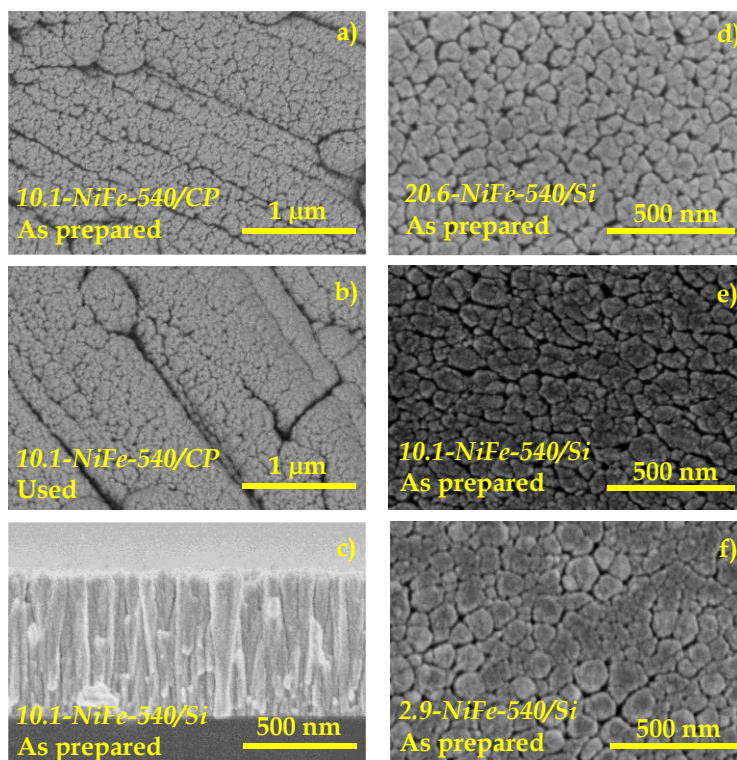
Figure 7.1. *SEM images in normal view of a) 10.1-NiFe-540/CP sample as prepared and b) after its usage in the three-electrode cell. c) Cross-sectional view SEM image of 10.1-NiFe-540/Si sample. Front view SEM images of d) 20.6-NiFe-540/Si, e) 10.1-NiFe-540/Si and f) 2.9-NiFe/Si catalyst thin films.*

Table 7.1 gathers the values of *equivalent thickness* determined from the cross-sectional SEM images of the samples deposited on flat silicon substrates, as well as the Ni/Fe at. ratio of as prepared and used electrodes, determined by EDX and XPS analysis. The differences in atomic ratios obtained for the same sample by XPS can be attributed to the different probing depth of these techniques (~3 nm depth for XPS and whole film thickness for EDX). XPS data will be discussed later. It is noteworthy that the *equivalent thickness* was similar for all electrodes (i.e., they had similar metal loadings), supporting that the electrochemical

performances of electrodes with different Ni/Fe ratios can be properly compared.

It is also remarkable that the procedure utilized to control the Ni/Fe content in the electrodes (see Chapter 3) is quite versatile and permits a straightforward control of composition. Meanwhile, the elemental mappings in **Figure 7.2** obtained for sample *10.1-NiFe-540/CP* confirm a homogeneous distribution of Ni and Fe across the whole deposited area of the electrode, supporting the existence of an atomic mixture of elements in the electrodes. The observation of oxygen in these maps, even if not homogeneously distributed, suggests that the surface of the bimetallic electrode nanostructures is oxidized because of its exposure to the air. This surface oxidation was confirmed by XPS as discussed below.

Table 7.1. *Table of the physico-chemical characterization of the Ni/Fe anode electrodes.*

Sample	Equivalent Thickness / nm	Ni/Fe at. ratio		
		EDX	XPS	
			As prepared	Used
20.6-NiFe	520	20.6	13.9	20.2
10.1-NiFe	540	10.1	8.3	11.5
7.1-NiFe	530	7.1	5.9	8.1
4.5-NiFe	550	4.5	4.6	6.4
2.9-NiFe	520	2.9	2.4	5.0
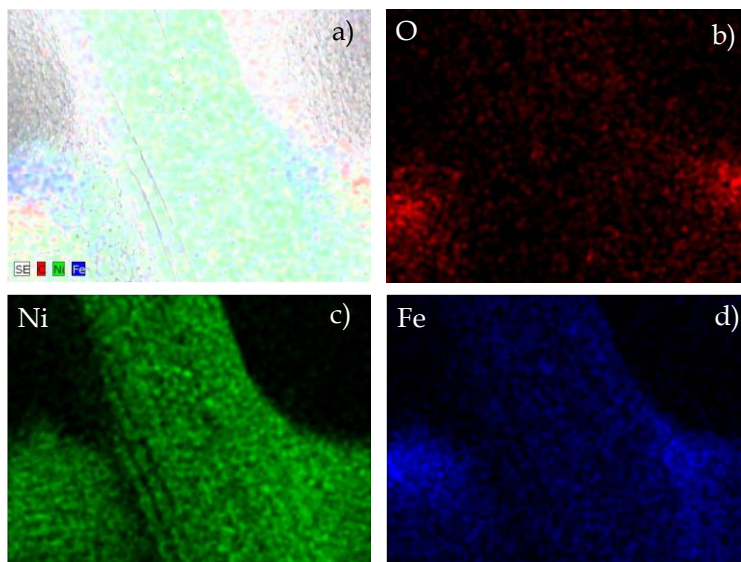
*Figure 7.2. a) General and b) O, c) Ni and d) Fe elemental EDX mapping images of
10.1-NiFe-540/CP sample.*

7.3.2. Ni/Fe atomic ratio and oxygen evolution reaction activity in a three-electrode cell configuration

To study the influence of the Ni/Fe atomic ratio in the OER, electrochemical experiments were carried out in the three-electrode cell. **Figure 7.3 a)** shows a series of cyclic voltammetries recorded for electrodes with several Ni/Fe at. ratios. These curves are compared to that of a pure Ni anode with a similar thickness, taken as reference. Two well-defined peaks can be observed in the curves. One of them is an anodic peak (around 400 mV vs. Ag/AgCl), which is generally attributed to the electrochemical oxidation of $Ni(OH)_2$ to NiOOH and the other one, the corresponding cathodic peak attributed to the reversible reaction of NiOOH to $Ni(OH)_2$ (previously detailed in Chapter 6) [18,19]. Some modifications in these redox peaks are induced by the incorporation of iron to the electrodes. Changes consisting of a shift in the Ni^{+2}/Ni^{+3}

oxidation potential to higher potentials values [20,21] are typically attributed to the formation of a Ni/Fe mixed oxyhydroxide [22,23]. In addition, the incorporation of iron has a positive effect in the OER activity, leading to a significant increase in current density values with respect to those obtained for a pure Ni anodic catalyst. This effect has been accounted by the higher OER catalytic activity of the Ni/Fe mixed oxyhydroxides with respect to that of NiOOH [23]. This enhancement has been related to the substitution of Fe^{+3} for Ni^{+2} sites in $Ni(OH)_2$ and NiOOH [24,25], leading to new Ni-O local environments with a superior activity for the OER [26]. Our results in Figure 7.3 a) show that the addition of increasing amounts of Fe to the Ni catalyst favours the OER activity until a plateau is reached for a Ni/Fe at. ratio around 10. It is likely that this value corresponds for the solubility limit of iron in the mixed oxide-hydroxide and, once this limit is exceeded, a separated FeO_xH_y phase may segregate onto the surface [27]. In the course of these cyclic voltammetry experiments with the three-electrode cell, Tafel slopes were also calculated using the Butler-Volmer equation (see **Figure 7.3 b)**). According to this equation, smaller Tafel slope values can be related to a higher electrocatalytic activity or a faster kinetics of the electron exchange process [28]. Figure 7.3 b) shows that a minimum value of 112 mV dec^{-1} is obtained for electrodes *10.1-NiFe-540/CP*. The slope value for this at. ratio is much smaller than that obtained for the pure Ni reference sample (161 mV dec^{-1}) and agrees with other published Tafel slope values reported in the literature for Ni/Fe anodes [29–31]. The improvement in the electrocatalytic activity due to the incorporation of iron also affects the onset potential values, which decrease from 530 mV vs. Ag/AgCl for pure Ni to 480 mV vs. Ag/AgCl for the *10.1-NiFe-540/CP* anodic catalyst (see **Figure 7.3 c)** (note that these values are approximate since the onset

partially overlaps with the anodic peak). In the same line, the
overpotential value required to reach 10 mA cm^{-2} (see **Figure 7.3 d)**) was
the lowest (i.e., 307 mV) for the *10.1-NiFe-540/CP* anode, in good
agreement with literature [5,32,33] (since overpotential values in our
experiment are obtained in mV vs. Ag/AgCl, they had to be converted to
mV vs. RHE, according to $E_{RHE} = E_{Ag/AgCl} + 0.059$ pH $+ E^0_{Ag/AgCl}$, where
$E^0_{Ag/AgCl} = 0.1979$ V [34] taken a pH of 13.9 for the 1.0 M KOH solution).
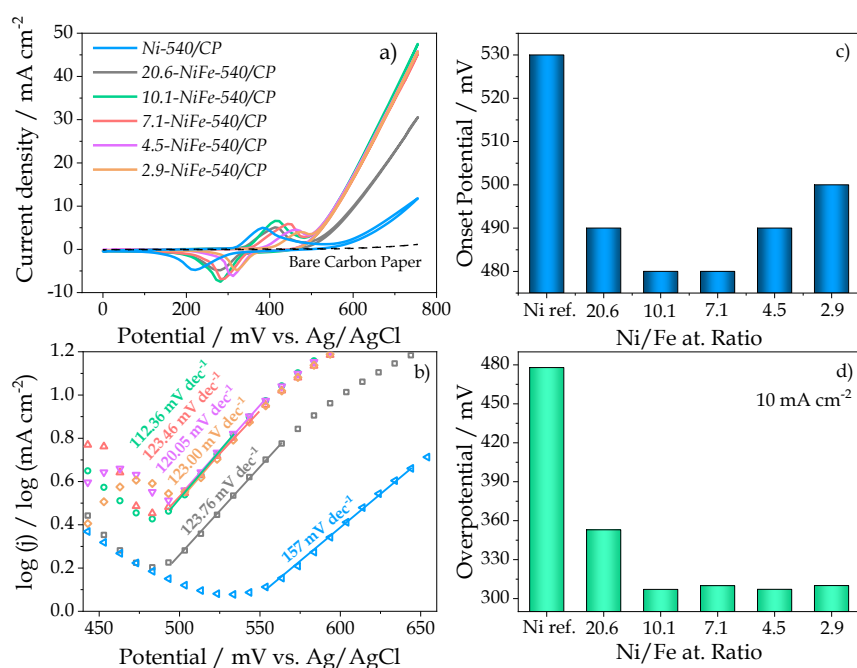
*Figure 7.3. a) Cyclic voltammetry experiments carried out for electrodes with different
Ni/Fe at. ratios in a three-electrode cell (room temperature, 1.0 M KOH electrolyte and
20 mV s^{-1} of scan rate). b) Corresponding Tafel plots (Tafel slopes obtained by linear
regression of the initial rise of the OER are included). c) Onset potential values for
OER and d) overpotential values evaluated at 10 mA cm^{-2} as a function of the Ni/Fe at.
ratio in the samples.*

The results above clearly demonstrate that, from the whole series of
prepared electrodes, the *10.1-NiFe-540/CP* anode presents the maximum

OER activity. To further investigate the causes of the high electrocatalytic activity of this electrode, a comparative EIS analysis was carried in the three-electrode cell at 700 mV vs. Ag/AgCl. **Figure 7.4** shows the Nyquist plots obtained for *Ni-540/CP* and *10.1-NiFe-540/CP* electrodes, as well as the equivalent $R_1(R_2C_1)$ electrical circuit that, according to literature, accounts well for the impedance behaviour of this type of anodes [35–37]. The table inserted in the figure shows the values of the electrical elements parameters obtained from the fitting of the experimental Z'' vs Z' curves. In this equivalent circuit, R_1 is usually related to an ohmic resistance between the surface of the working electrode and the reference electrode and it is associated with the sum of contributions due to the resistance of the electrolyte, the electrode catalyst surface and the contacts [36]. Values of this resistance parameter are rather similar for the *Ni-540/CP* and *10.1-NiFe-540/CP* electrodes, though its slightly higher value for the former electrode points to a small increase of the resistance at the electrolyte-catalyst interface in that case. On the other hand, R_2 is commonly associated with the charge transfer resistance through the electrode during the OER [36]. The observed decrease of R_2 by a factor of more than two for the *10.1-NiFe-540/CP* electrode with respect to pure nickel can be related to the highest electrocatalytic activity of the bimetallic electrodes [38], agreeing with similar tendencies found in other studies [35].

The EIS analysis can be also utilized to deduce other activity-related parameters for the electrode catalysts. Watzele et al. [39] have recently proposed a procedure to determine the ECSA using an alternative interpretation of *Nyquist* plots (more details in previous chapter). Using the same model, we have calculated the ECSA values for the *Ni-540/CP* and for *10.1-NiFe-540/CP* electrodes and got values of 6.13 and 10.13 cm^2, respectively. These values suggest that the surface available for the OER

reaction will be higher for the *10.1-NiFe-540/CP* electrode. Remarkably, it is also higher than others values reported in the literature for Ni-Fe electrode catalysts prepared by other methods [40].
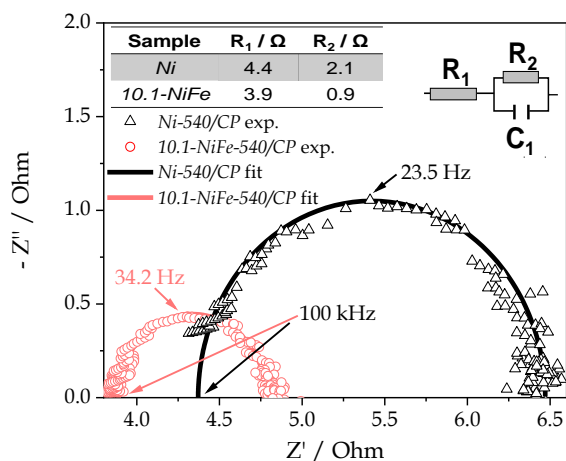
Figure 7.4. Nyquist plots of Ni-540/CP and 10.1-NiFe-540/CP samples obtained in the three-electrode cell (frequency from 100 kHz to 10 mHz). Equivalent electrical circuit and fitting values are included as insets.

7.3.3. Chemical and structural characterization of Ni/Fe electrodes before and after cyclic voltammetry analysis

Chemical compositions and oxidation states at the surface of electrode samples were investigated by XPS analysis. **Figures 7.5 a-c)** show the Ni 2p, Fe 2p and O 1s spectra obtained for as prepared samples with different Ni/Fe at. ratios. **Figures 7.5 d-f)** show a comparison of Ni 2p, Fe 2p and O 1s spectra for the *10.1-NiFe-540/CP* electrode in its as prepared state and after electrochemical cycling in the three-electrode cell. Since electrodes were deposited by MS from metallic targets using pure Ar as plasma gas, the observation of oxygen by XPS must be attributed to the surface oxidation upon exposure to ambient air [41]. In this regard, the

observation in all samples of Ni 2p shoulders at 869.8 and 853.0 eV in Figure 7.5 a) due to Ni^0 [42] confirms that surface oxidation has not progressed to the interior of the films, which must have preserved a metallic character. Ni 2p spectra are dominated by two satellite peaks at 880.5 and 861.7 eV and two main peaks at 873.5 and 855.9 eV corresponding to Ni $2p_{1/2}$ and Ni $2p_{3/2}$ levels, respectively, that must be attributed to Ni^{+2} species [43]. It has been previously also observed in Chapter 6. In the Ni/Fe bimetallic electrodes, the Fe 2p spectra depict two peaks at 725.0 and 711.4 eV corresponding to Fe $2p_{1/2}$ and Fe $2p_{3/2}$ core levels of Fe^{+3} [44]. Meanwhile the O 1s spectra depict a contribution at 531.5 eV binding energy, attributed to the OH^- groups, and another at 530.2 eV attributed to O^{2-} groups [37]. Although differences depending on sample are observed in the relative intensity of these two contributions (c.f., Figure 7.5 c)), no clear conclusions can be derived from this observation for samples exposed to air.

However, the comparison in Figures 7.5 d)-f) of the spectra of the as prepared and used *10.1-NiFe-540/CP* sample provides a valuable information regarding the electrochemically cycling effect on the surface state of samples. For example, the spectra of the used sample lack any Ni^0 contributions, indicating that surface oxidation has progressed beyond the probing depth of XPS (3-4 nm). A similar effect was observed in the previous chapter with pure Ni [37]. Thus, by XPS analysis, Ni^{+2} and Fe^{3+} seem to be the sole cationic species present at the surface of the used samples exposed to air, being likely that these cationic species were involved in the OER. Meanwhile, the O 1s spectrum in the used sample appears dominated by a single band due to OH^- groups (i.e. BE 531.5 eV). This agrees with the use of potassium hydroxide solution as electrolyte and strongly supports the involvement of a hydroxide and/or

oxyhydroxide of Ni and Fe in the OER [37,45]. Spectra from the other samples after their use in the three-electrode cell depict a similar evolution of chemical states (see **Figure 7.6**) as those reported in Figure 7.5 for sample *10.1-NiFe-540/CP*. However, it is interesting that the Ni/Fe at. ratio the surface of all samples, as determined by XPS, increases after electrochemically cycling in the basic electrolyte (c.f., Table 7.1). This feature suggests that the surface of electrode experiences a partial enrichment of Ni at the outmost surface layers during cycling. Similar surface enrichment phenomena have already been observed in previous Chapters 4 and 5 on the OER with Co/Cu oxide electrodes prepared by MS-OAD [45]. For sample *10.1-NiFe-540/CP*, the Ni/Fe determined after cycling is 11.5, relatively close to the nominal composition determined by EDX for the whole electrode. The possibility that during cycling there can be segregations and mobilization of elements at the surface will be further discussed below when presenting the XRD characterization of the investigated samples.
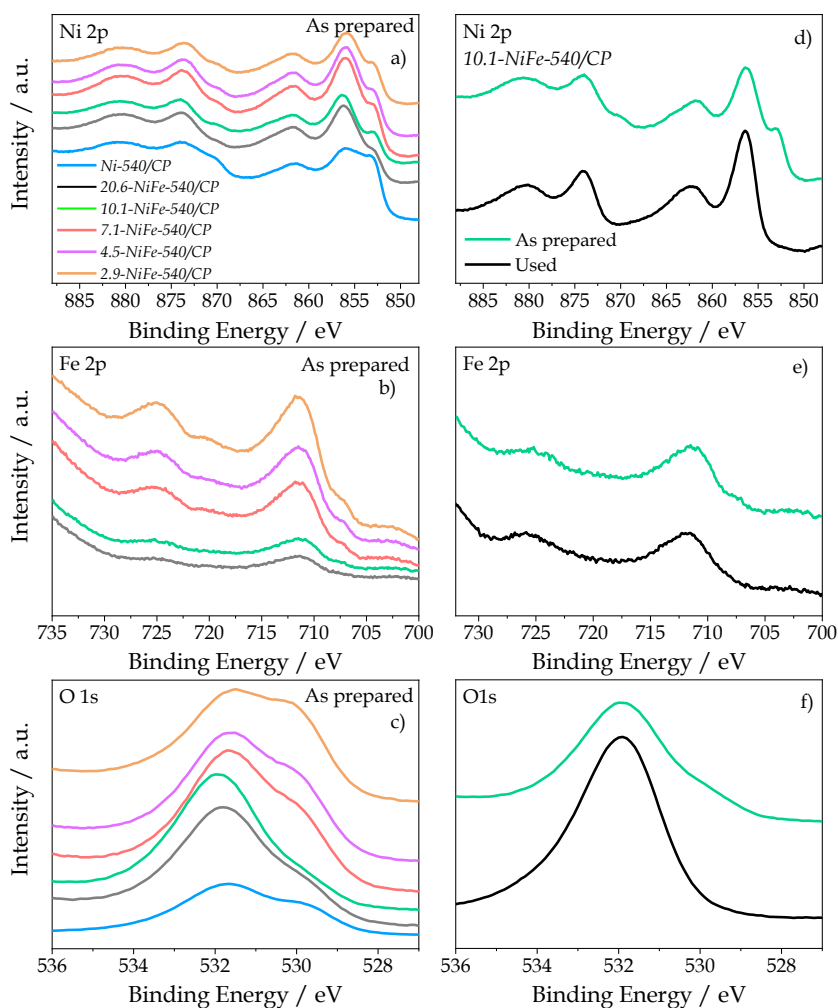
Figure 7.5. *a) Ni 2p, b) Fe 2p and c) O 1s XPS spectra of several Ni/Fe at. ratio as
prepared electrodes; d) Comparison of the Ni 2p, e) Fe 2p and f) O 1s spectra of 10.1-
NiFe-540/CP sample before and after electrochemical cycling in the three-electrode cell.*
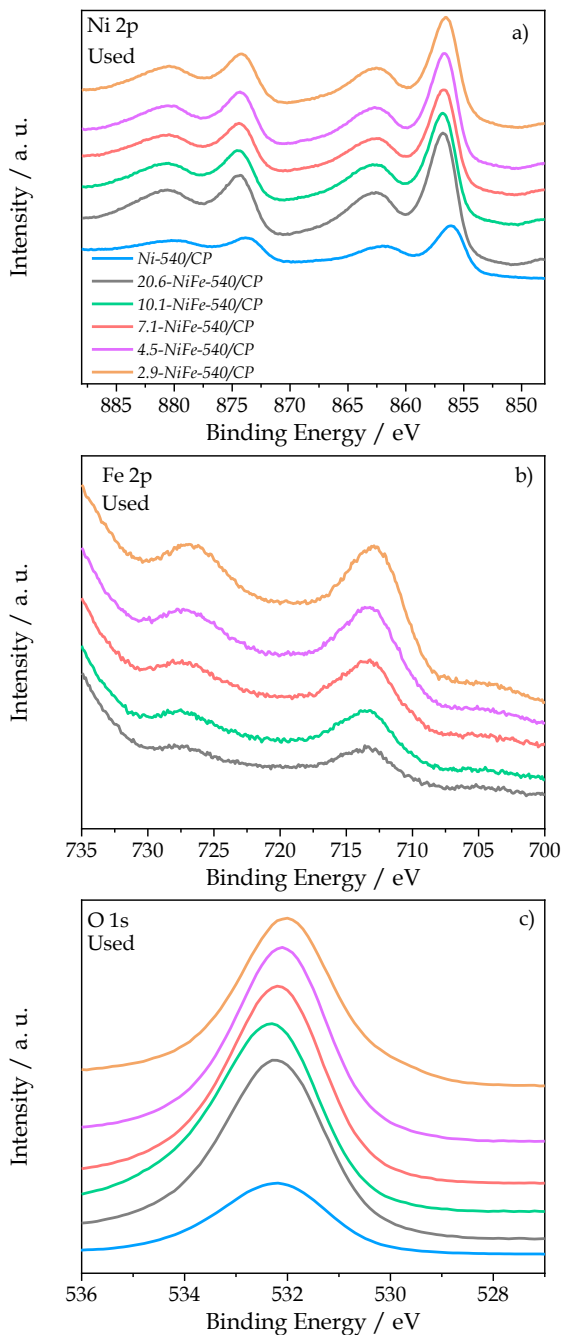
Figure 7.6. a) Ni 2p, b) Fe 2p and c) O 1s spectra of used samples as indicated.

A XRD analysis (see **Figure 7.7**) of the as prepared Ni/Fe bimetallic anodes has been performed just a fingerprint analysis of the different prepared catalysts, to illustrate that the deposited catalysts are mostly amorphous (very weak diffraction peaks are detected and note that the deposition process is at room temperature), and also to illustrate the incorporation of the iron atoms within the nickel network. In general, only a clear feature can be associated to a given phase, although in some cases two peaks or shoulders can be appreciated as for Ni, FeOOH or KOH. In addition, a comparative analysis has been carried out for sample *10.1-NiFe-540/CP* before and after its use as OER electrode. The series of diffractograms in **Figure 7.7 a)** depict a characteristic very intense diffraction peak at ~54.6 $^{\circ}$ attributed to the carbon paper used as substrate [46] that is labelled as *[a]* in the figure. In addition, two smaller diffraction peaks at approximately ~44.5 $^{\circ}$ and ~51.9 $^{\circ}$, labelled as *[b]* in the figure, can be attributed to metallic nickel or a Ni containing alloy [47]. An enlarged view of these peaks is included in **Figure 7.7 c)** to clearly show the evolution of the intensity and width of this peak depending on sample. Thus, it is apparent that the intensity of these peaks decreases and their width increases for lower Ni/Fe ratios, as expected if Fe has become incorporated within the fcc structure of Ni, forming a kind of alloy (a certain displacement of the peak at 44.5 $^{\circ}$ further supports this assumption) [48–50]. Meanwhile, quite small, but still observable peaks appear at ~42.6 $^{\circ}$ and ~43.1 $^{\circ}$ (labelled as *[c]* and *[d]*) that can be attributed to NiO and NiOOH [51]. It is noteworthy in this regard the observation of a small diffraction peak at ~37.2 $^{\circ}$ (labelled as *[h]*) both in the as prepared and used samples, that can be attributed to $NiFe_2O_4$ [52]. Peaks corresponding to the oxyhydroxides of Fe, ~36.0 $^{\circ}$, ~36.5 $^{\circ}$, ~31.7 $^{\circ}$ and ~41.4 $^{\circ}$ [53,54], labelled as *[f]* and *[g]*), appear rather intense in the *10.1-*

NiFe-540/CP used sample (**Figure 7.7 b)**) and must be linked to the effect of the KOH electrolyte in the chemical state of elements at the surface of samples. Interestingly, the diffraction peaks at ~34.9 º and ~40.5 º, likely due to Fe_2O_3 [55] (labelled as *[e]*), only appear in the *10.1-NiFe-540/CP* used electrode. In this case, two new peaks attributed to residual KOH were observed at ~32.4 º and ~39.4 º [56] (labelled as *[i]*). The lack of XRD peaks attributable to metallic Fe confirms the incorporation of Fe into the Ni structure in the form of a kind of metal alloy. Overall, this XRD analysis shows that bimetallic electrodes consist of a metallic alloy, which can be partially oxidized in agreement with the surface oxidation observed by XPS, particularly in the used samples. The observation of XRD peaks due to segregated iron oxides and hydroxides confirms the evolution of the surface of samples with the formation under certain conditions of a mixture of separated Ni and Fe oxidized phases. In agreement with the electrochemical analysis in Figure 7.3 this effect, though, should be lower in sample *10.1-NiFe-540/CP*.

The Raman analysis of samples confirms the previous view and support the existence of a mixed oxide/hydroxide phase in the Ni/Fe electrodes. The spectrum of the *Ni-540/CP* sample in **Figure 7.8** shows a characteristic peak at 521 cm^{-1} attributed to Ni^{III}-O lattice vibrations in NiOOH [57]. In comparison, the spectra of *4.5-NiFe-540/CP* and *10.1-NiFe-540/CP* electrodes show a new characteristic peak shifted positively with respect to the peak due to Ni^{III}-O vibrations. This additional band confirms the incorporation of Fe atoms in the structure through the formation of $Ni(Fe)O_xH_y$ [57,58]. We assume that this phase formed at the surface is responsible for the higher performance of Ni/Fe in comparison with that of Ni electrodes. For the metallic Ni/Fe electrodes prepared by MS-OAD in this chapter, this enhancement of surface reactivity combines

with the metallic character of the bulk of the catalyst film, a feature that
diminishes the electrical resistance of the electrode, further contributing
to the observed enhancement in reactivity.
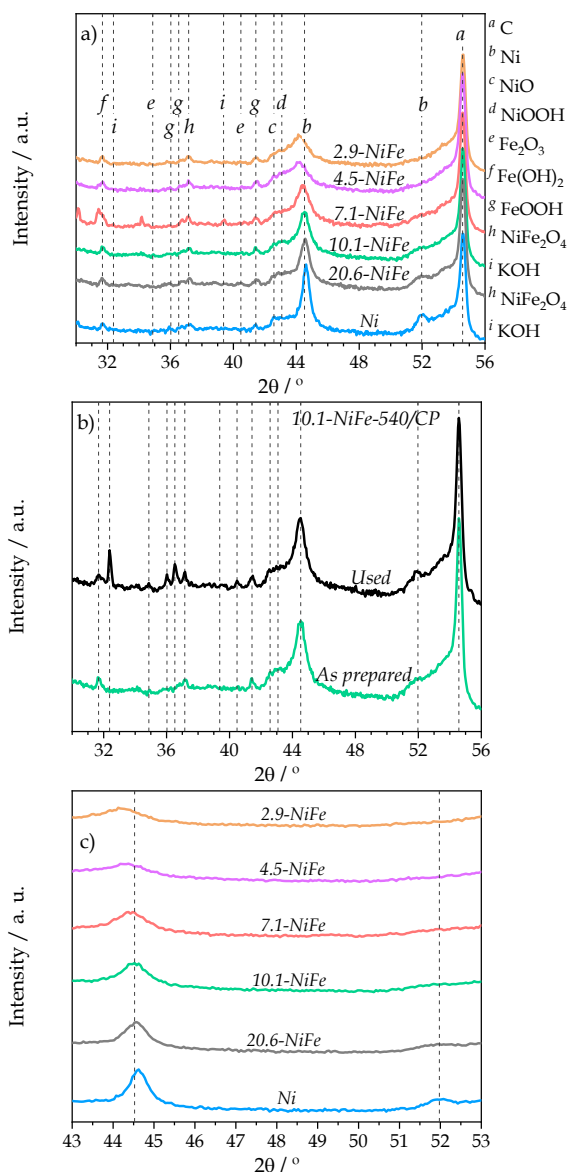
Figure 7.7*. X-Ray diffractograms of a) several as prepared Ni/Fe electrodes and b) as
prepared and used 10.1-NiFe-540/CP sample. c) Zoom of the XRD of the peaks around
44.5 and 51.9 º characteristic of metallic Ni in the different Ni/Fe catalyst thin films.*

221
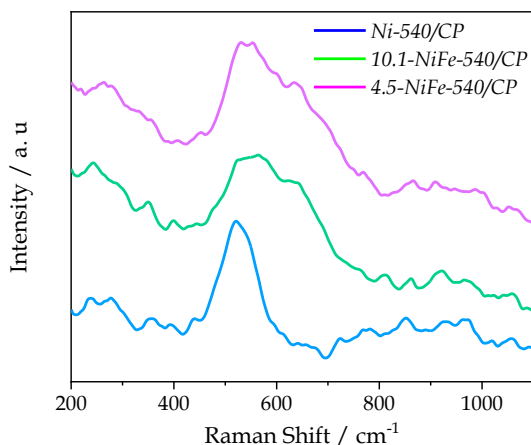
Figure 7.8. *RAMAN spectra of Ni-540/CP and XX-NiFe-540/CP anodic electrodes.*

7.3.4. Electrode performance in the anion exchange membrane water electrolysis cell configuration

The enhanced electrochemical activity of the bimetallic catalyst films, particularly that of sample *10.1-NiFe-540/CP,* determined in the three-electrode cell justifies their integration in a full AEMWE cell to determine whether this high activity remains under close to real conditions of operation. From the point of view of electrode manufacturing, this integration possesses some challenges related to the increase in the electrode area, the need to keep the microstructure and chemical behaviour described in the previous sections and the preservation of their high performance at temperatures and working conditions different than in the three-electrode cell.

222

Influence of working parameters in the performance of the AEMWE cell

The *10.1-NiFe-540/CP* electrode type was incorporated in a full
AEMWE cell to prove its reliability under close to real operation
conditions. For this purpose, a MEA composed by sample *10.1-NiFe-
540/CP* as anode, *Ni-540/CP* as cathode (in previous chapter, we showed
that these MS-OAD nickel electrodes act as optimum cathodes for the
production of hydrogen [37]) and a Fumapem® membrane were
sandwiched as explained in Chapter 3. In the resulting AEMWE cell we
studied the influence of several operation parameters, namely the torque
applied for cell assembly, the working temperature, and the KOH
concentration. **Figure 7.9 a)** shows that for low assembly torque values
(<2 Nm), current density increases with assembly pressure likely due to
contact improvement between membrane and catalysts. For assembly
pressures resulting from torques higher than 2.5 Nm, the observed
decrease in current density was attributed to a decrease in gas transport
through the carbon paper and the partial coverage of electrode surface by
gas bubbles [59]. A torque of 2.5 Nm was therefore taken as the optimum
value for cell assembly and this value was applied for the characterization
studies as a function of temperature and KOH concentration.

Figure 7.9 b) shows that global performance improves with
temperature. This is a well-known effect in AEMWE usually attributed to
an increase in the kinetics of the electrochemical reactions and in the
mobility of hydroxyl ions [60]. Assuming an Arrhenius behaviour for the
electrochemical reaction [61], the activation energy (E_a) of the process can
be calculated from the slope of the plot of the logarithm of current density
vs. the inverse of the temperature. This slope corresponds to E_a/R, with R
the gas constant value of 8.314 J (mol K)$^{-1}$, and renders E_a values of 19.1,
20.3 and 20.9 kJ mol^{-1} for operating potentials of 1.9, 2.0 and 2.1 V,

respectively. These activation energies are similar to other values reported in the literature for the same process [61,62].

Figure 7.9 c) accounts for the influence of the KOH electrolyte concentration in the polarization curves. At low KOH concentration (i.e., 0.1 M), when the process is kinetically controlled [63], the electrolyte concentration does not significantly affect the polarization curves. However, at high KOH concentrations the current density increases for V>1.9 volt, pointing to that an increase in the ion conductivity through the membrane contributes to diminish the ohmic overpotential required for the OER [64].

Stability of the AEMWE cell was also analysed monitoring its response along a chronopotentiometry experiment. For a constant current of 400 mA cm^{-2} and 40 °C of operating temperature, the curve reported in **Figure 7.9 d)** evidences a slight decrease in the cell potential over time (0.3 % V h^{-1}). This slight decrease in performance is similar to that reported in other studies with anodes prepared by MS [37,65], but lower than results corresponding to cells incorporating anodes prepared using other methods [66–68].
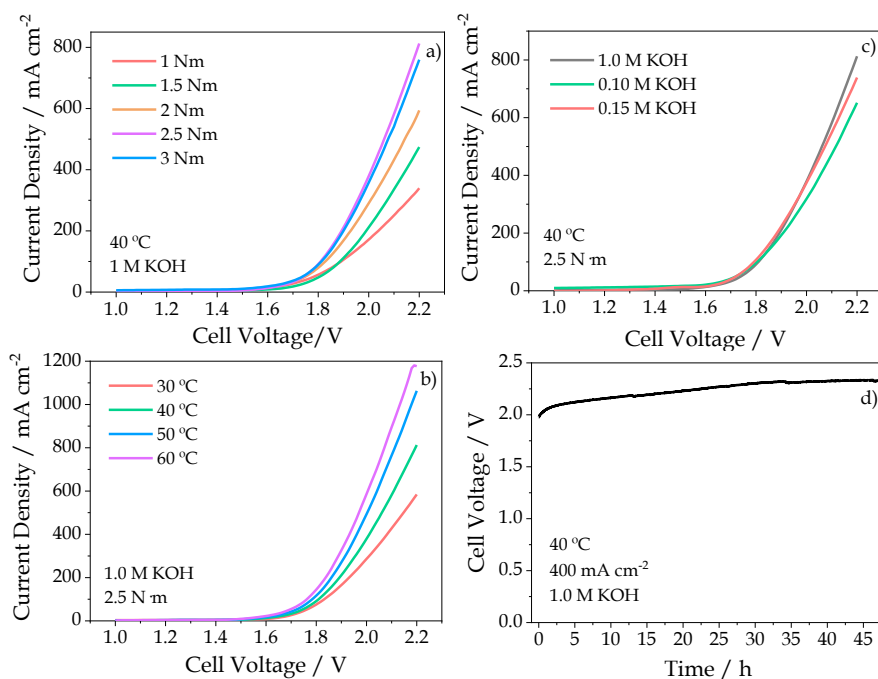
Figure 7.9*. LSVs obtained for a MEA integrated by 10.1-NiFe-540/CP and Ni-540/CP
as anodic and cathodic electrodes, respectively, a) for various cell assembly torques at 40
ºC and 1.0 M KOH, b) for various operation temperatures at an assembly torque of 2.5
Nm, 1.0 KOH, and c) for different electrolyte concentrations at 40 ºC and 2.5 Nm. d)
Constant-current chronopotentiometry curve at a fixed current of 400 mA cm^{-2}, 40 ºC,
1.0 M KOH, and an assembly torque of 2.5 Nm.*

Influence of ionomer addition to the electrodes in the performance of AEMWE cell

As previously mentioned, the addition of an ionomer is commonly
used to increase the performance of AEMWE electrolyzers [6]. When
applying traditional electrode preparation methods, the ionomer is
added to the catalyst ink and as binder and to favour the ion transfer
transport up to the reaction sites. Conversely, the ionomer can be added
after the electrode manufacturing, in most cases also resulting in an
increase in performance [1,69]. Considering that no delamination of the

active catalyst layer has been detected after long-term operation, it appears that MS electrodes do not require any binding agent to fix the catalyst layer to the GDL support. Therefore, we hypothesize that the addition of ionomer to the electrodes might principally contribute to favour the ion diffusion. To check possible improvements in performance due to ionomer addition, three different cell configurations have been tested as previously explained in the experimental section of this chapter. In general, the amount of added ionomer is optimized to maximize the electrochemical yield of the cells, with an Ionomer/Catalyst (I/C) ratio of 0.2 being an optimum value in various studies on the subject [7,8,16]. However, the AEMWE cells incorporating MS-OAD electrodes seem to behave differently. Linear sweep voltammetries in **Figure 7.10 a)** show a maximum performance for sample *10.1-NiFe-540/CP* without ionomer, and that the electrochemical response is not affected by the addition of ionomer for a I/C ratio of 0.2 (i.e., 4.4 mg of ionomer). Moreover, the performance drastically decreased adding more ionomer to cover the entire surface of the catalyst. A similar effect can be deduced from **Figure 7.10 b)**, where chronopotentiometry stability tests show that, for a constant current density of 400 mA cm^{-2} and 40 °C, a lower potential is required for the electrodes without ionomer. Moreover, for long operation times, the cell voltage increase was 0.3 % V h^{-1} for the electrode without ionomer and 0.6 % V h^{-1} and 0.9 % V h^{-1} for the electrode with I/C=0.2 and its full surface covered with ionomer, respectively. We believe that the inefficiency of ionomers with the MS-OAD electrodes is related to a morphology where diffusion constrains towards OH$^-$ seem to be unimportant and the fact that the ionomer is added once the electrode has been prepared and will likely cover part of the catalyst active sites [8].
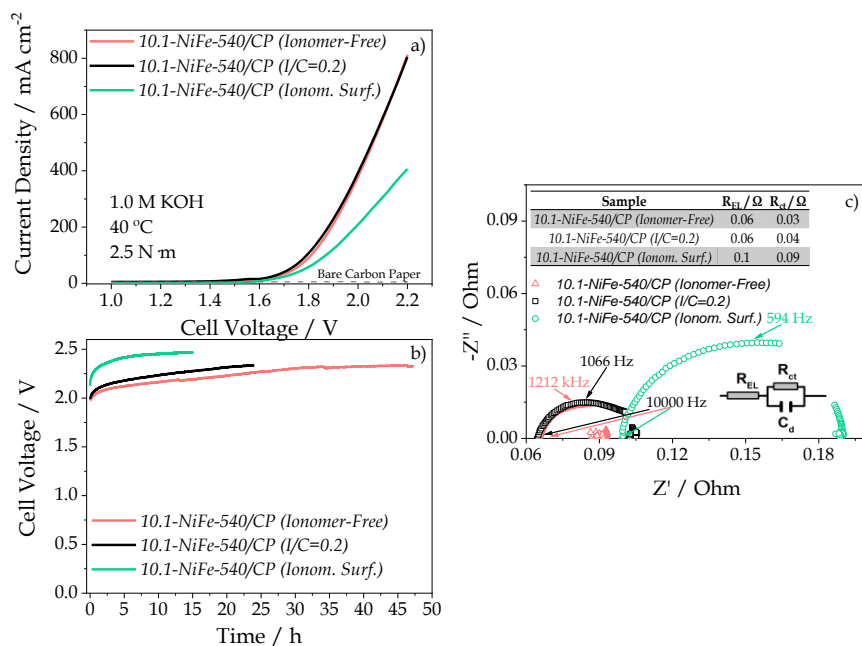
Figure 7.10. *Effect of the addition of ionomer to a 10.1-NiFe-540/CP electrode in a MEA (1.0 M KOH electrolyte solution, 40 ºC operation temperature) on a) LSV polarization curves, b) constant-current chronopotentiometry measurements (@400 mA cm⁻²), and c) impedance spectra of the cell evaluated at 2.0 V.*

This hypothesis was confirmed through various electrochemical tests as, for example, the fact that while the cyclic voltammetry curves did not change after 200 cycles with the *10.1-NiFe-540/CP* cell electrode, slight and high increases in density current were found, respectively, for the electrodes covered with ionomer at I/C=0.2 or total coverage, respectively (see **Figure 7.11**). This behaviour is consistent with a progressive dragging out of ionomer molecules from the electrode surface after the successive cycles. The detrimental role of the ionomer also agrees with the SEM observations (see **Figure 7.12**) showing that ionomer agglomerates form onto the Ni/Fe nanocolumnar structure and likely block some of the catalyst active sites. Electrochemical evidence of

this blocking effect was provided by the EIS analysis of the complete MEAs. **Figure 7.10 c)** shows the measured Nyquist plots for the three MEAs and the equivalent circuit (inset in the figure, similar to ref [22]) utilized to retrieve resistance parameters. In this representation, the intersection to the X axis at high frequencies is related to the ohmic resistance of the membrane (R_{EL}) or with the electrolyte resistance associated to the availability of OH$^-$ ions [22]. The charge transfer resistance (R_{ct}) is obtained by the difference between the two intersection at a high and low frequencies (diameter of the semicircle) and is related to the polarization resistance or to the kinetics of the electrochemical reactions [22,37]. Fitting values are included in the table inserted in the figure. The obtained values are similar to values reported for other systems including ionomers [22] and can be easily interpreted assuming that the relatively higher R_{EL} values found for the ionomer containing electrodes respond to an increase of thickness of the catalyst-ionomer layer. Similarly, the lowest R_{ct} value found for the *10.1-NiFe-540/CP* ionomer-free electrode, agrees with the little restrictions to the transfer of charge through the catalyst film in this case.
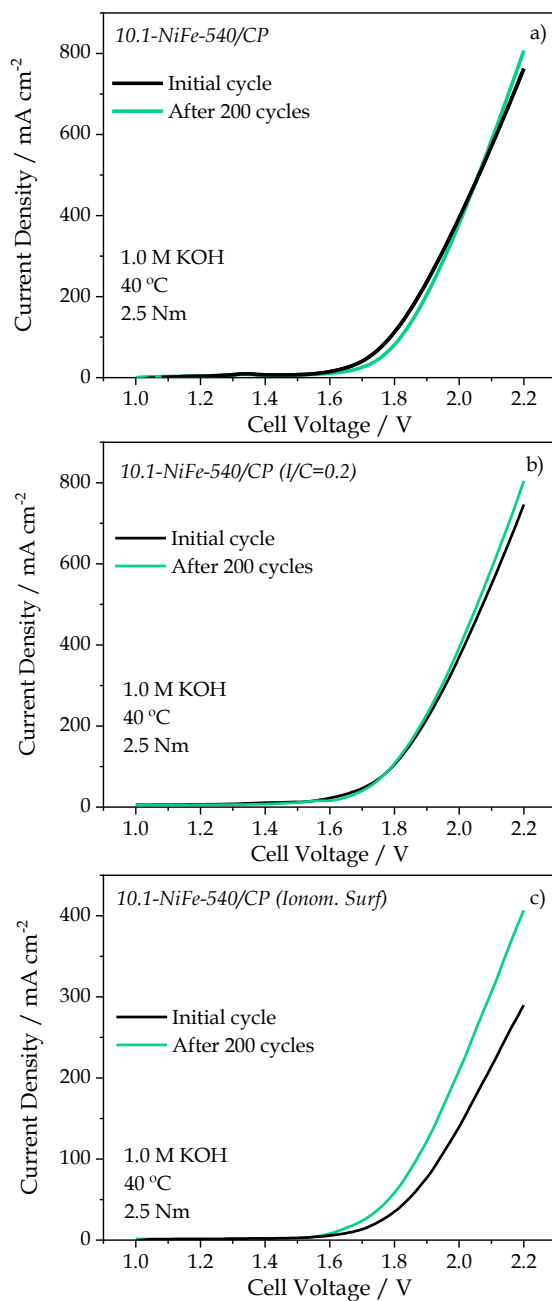
Figure 7.11. *Influence of the ionomer in MEA stability tests consisting of iterative LSV cycles. Experiments were carried out at 40 ºC with a 1.0 M KOH solution. The figures compare the 1st and the 200th LSV cycle acquired in a) ionomer-free electrodes, b) I/C=0.2, and c) Ionomer Surf.*
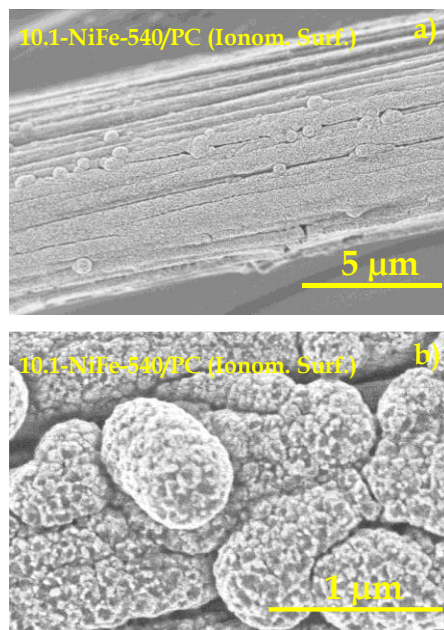
Figure 7.12. SEM images of the 10.1-NiFe-540/CP sample after adding ionomer.

7.3.5. Comparison with other anion exchange membrane water electrolysis cells

To put in context the AEMWE cell performance with Ni-Fe MS-OAD electrodes, we compare the obtained results with others recently reported in the literature. A first remark is that, although the current density value obtained here (i.e., 400 mA cm^{-2} at 2.0 V and 40 °C, increasing to about 600 mA cm^{-2} at 60 °C) is somehow smaller than reported values for electrodes prepared with an ink spraying coating process, e.g. 1900 [22], 720 [3] or 1400 mA cm^{-2} [7], it is higher than most published data in the literature, where values ranging between 140 and 250 mA cm^{-2} [1,70,71] are rather common (all current density values at between 40-50 °C).

However, the performance of the Ni-Fe anodes developed here gains a particular relevance when expressing their activity in terms of current

density per amount of catalyst (specific activity). **Figure 7.13** summarizes some of the results mentioned above formulated in these units. It is noteworthy that the current yield per amount of *10.1-NiFe-540/CP* catalyst (1086 mA mg^{-1}) is superior to any other of the values reported in the literature for Ni/Fe [1,22], Ni [3,37,70,71], cobalt-based oxides [8,45,72,73] or those obtained with a novel IrO$_2$ anodes [1,7,74]. Moreover, this result is especially outstanding considering that the AEMWE electrodes in this thesis are ionomer-free and therefore simpler from the point of view of their manufacturing and processing.
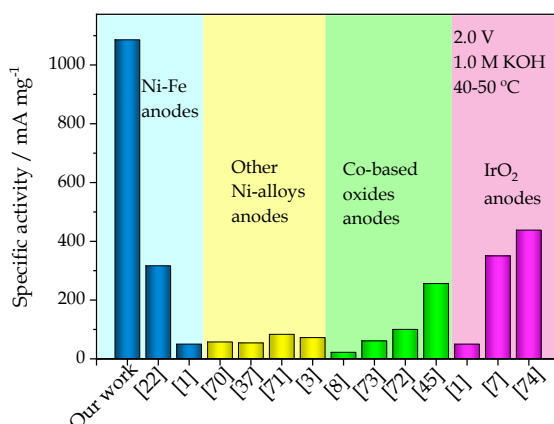
Figure 7.13. *Electrochemical performance of our 10.1-NiFe-540/CP anode based AEMWE, characterised by its specific activity, compared to other reported results from literature.*

7.4. Conclusions

The previous results and discussion have pointed out that the MS-OAD technique is a suitable method of fabrication of Ni/Fe anodes for water electrolysis cells. Incorporation of Fe within Ni based anodes improves the OER performance and we have demonstrated that a

maximum performance is reached for a Ni/Fe at. ratio of around ten (400 mA cm^{-2} at 2.0 V at 40 °C and around 600 mA cm^{-2} at 60 °C). The modifications introduced in this physical vapour deposition procedure, in terms of deposition geometry and other operating conditions render nanocolumnar thin films with a high porosity and good conformality onto the carbon paper used as GDL support. This has been demonstrated through an outstanding electrochemical response, particularly for the electrodes with the optimum composition. These electrodes presented a high reaction yield, good repetitively upon cycling and high stability, features that have been accounted for by the particular microstructure and high surface area of these electrodes and the mixing at atomic scale of their constituent elements both before and after their activation to generate a catalytically active oxide/hydroxide surface layer.

The good properties of the electrodes when tested in a three-electrode laboratory cell, have been confirmed upon their integration in a MEA for their testing in a complete AEMWE cell. In particular, it has been demonstrated that the addition of ionomers, a critical issue for most conventional AEMWE cells, does not improve the performance of MS-OAD Ni/Fe electrodes, thus simplifying the manufacture and integration of cells and reducing the costs and other problems (stability, reproducibility) associated with the incorporation of this kind of additives.

The high stability and specific activity (1086 mA mg^{-1} at 2.0 V and 40 °C) depicted by the MEA integrated *10.1-NiFe-540/CP* anode in comparison with other results recently reported in the literature, confirm the MS-OAD technique as an appropriate method to fabricate ionomer-free nanostructured electrodes for AEMWE.

7.5.   References

[1]   D. Xu, M.B. Stevens, M.R. Cosby, S.Z. Oener, A.M. Smith, L.J. Enman, K.E. Ayers, C.B. Capuano, J.N. Renner, N. Danilovic, Y. Li, H. Wang, Q. Zhang, S.W. Boettcher, Earth-abundant oxygen electrocatalysts for alkaline anion-exchange-membrane water electrolysis: effects of catalyst conductivity and comparison with performance in three-electrode cells, ACS Catal. 9 (2019) 7–15. https://doi.org/10.1021/acscatal.8b04001.

[2]   J. Xu, I. Amorim, Y. Li, J. Li, Z. Yu, B. Zhang, A. Araujo, N. Zhang, L. Liu, Stable overall water splitting in an asymmetric acid/alkaline electrolyzer comprising a bipolar membrane sandwiched by bifunctional cobalt-nickel phosphide nanowire electrodes, Carbon Energy. 2 (2020) 646–655. https://doi.org/10.1002/cey2.56.

[3]   G. Gupta, K. Scott, M. Mamlouk, Performance of polyethylene based radiation grafted anion exchange membrane with polystyrene-b-poly (ethylene/butylene)-b-polystyrene based ionomer using $NiCo_2O_4$ catalyst for water electrolysis, J. Power Sources. 375 (2018) 387–396. https://doi.org/10.1016/j.jpowsour.2017.07.026.

[4]   Y. Cheng, S.P. Jiang, Advances in electrocatalysts for oxygen evolution reaction of water electrolysis-from metal oxides to carbon nanotubes, Prog. Nat. Sci. Mater. Int. 25 (2015) 545–553. https://doi.org/10.1016/j.pnsc.2015.11.008.

[5]   D. Lim, E. Oh, C. Lim, S.E. Shim, S.-H. Baeck, Bimetallic NiFe alloys as highly efficient electrocatalysts for the oxygen evolution reaction, Catal. Today. 352 (2020) 27–33. https://doi.org/10.1016/j.cattod.2019.09.046.

[6]   A.Y. Faid, L. Xie, A.O. Barnett, F. Seland, D. Kirk, S. Sunde, Effect of anion exchange ionomer content on electrode performance in AEM water electrolysis, Int. J. Hydrogen Energy. 45 (2020) 28272–28284. https://doi.org/10.1016/j.ijhydene.2020.07.202.

[7]   J.E. Park, S.Y. Kang, S.-H. Oh, J.K. Kim, M.S. Lim, C.-Y. Ahn, Y.-H. Cho, Y.-E. Sung, High-performance anion-exchange membrane water electrolysis, Electrochim. Acta. 295 (2019) 99–106. https://doi.org/10.1016/j.electacta.2018.10.143.

[8]   I. Vincent, A. Kruger, D. Bessarabov, Development of efficient membrane electrode assembly for low cost hydrogen production by anion exchange membrane electrolysis, Int. J. Hydrogen Energy. 42 (2017) 10752–10761. https://doi.org/10.1016/j.ijhydene.2017.03.069.

[9]   B.G. Pollet, A.A. Franco, H. Su, H. Liang, S. Pasupathi, 1 - Proton
       exchange membrane fuel cells, in: F. Barbir, A. Basile, T.N.B.T.-C. of H.E.
       Veziroğlu (Eds.), Woodhead Publ. Ser. Energy, Woodhead Publishing,
       Oxford, 2016: pp. 3–56. https://doi.org/10.1016/B978-1-78242-363-
       8.00001-3.

[10]   A. Lim, H. Kim, D. Henkensmeier, S. Jong Yoo, J. Young Kim, S. Young
       Lee, Y.-E. Sung, J.H. Jang, H.S. Park, A study on electrode fabrication and
       operation variables affecting the performance of anion exchange
       membrane water electrolysis, J. Ind. Eng. Chem. 76 (2019) 410–418.
       https://doi.org/10.1016/j.jiec.2019.04.007.

[11]   K. Nejati, S. Davari, A. Akbari, K. Asadpour-Zeynali, Z. Rezvani, A
       highly active oxygen evolution electrocatalyst: Ni-Fe-layered double
       hydroxide intercalated with the Molybdate and Vanadate anions, Int. J.
       Hydrogen   Energy.   44   (2019)   14842–14852.
       https://doi.org/10.1016/j.ijhydene.2019.04.045.

[12]   D.A. Corrigan, The catalysis of the oxygen evolution reaction by iron
       impurities in thin film nickel oxide electrodes, J. Electrochem. Soc. 134
       (1987) 377–384. https://doi.org/10.1149/1.2100463.

[13]   C. Niether, S. Faure, A. Bordet, J. Deseure, M. Chatenet, J. Carrey, B.
       Chaudret, A. Rouet, Improved water electrolysis using magnetic heating
       of FeC–Ni core–shell nanoparticles, Nat. Energy. 3 (2018) 476–483.
       https://doi.org/10.1038/s41560-018-0132-1.

[14]   R. Jervis, N. Mansor, A.J. Sobrido, S. Jones, C. Gibbs, T.P. Neville, J.
       Millichamp, P.R. Shearing, D.J.L. Brett, The importance of using alkaline
       ionomer binders for screening electrocatalysts in alkaline electrolyte, J.
       Electrochem.   Soc.   164   (2017)   F1551–F1555.
       https://doi.org/10.1149/2.0441714jes.

[15]   P. Fortin, T. Khoza, X. Cao, S.Y. Martinsen, A. Oyarce Barnett, S.
       Holdcroft, High-performance alkaline water electrolysis using Aemion™
       anion exchange membranes, J. Power Sources. 451 (2020) 227814.
       https://doi.org/10.1016/j.jpowsour.2020.227814.

[16]   M. Carmo, G. Doubek, R.C. Sekol, M. Linardi, A.D. Taylor, Development
       and electrochemical studies of membrane electrode assemblies for
       polymer electrolyte alkaline fuel cells using FAA membrane and
       ionomer,   J.   Power   Sources.   230   (2013)   169–175.
       https://doi.org/10.1016/j.jpowsour.2012.12.015.

[17]   X. Zhang, J. Hampshire, K. Cooke, X. Li, D. Pletcher, S. Wright, K. Hyde, High surface area coatings for hydrogen evolution cathodes prepared by magnetron sputtering, Int. J. Hydrogen Energy. 40 (2015) 2452–2459. https://doi.org/10.1016/j.ijhydene.2014.12.107.

[18]   A.K. Taylor, I. Andreu, B.D. Gates, Regular dimpled nickel surfaces for improved efficiency of the oxygen evolution reaction, ACS Appl. Energy Mater. 1 (2018) 1771–1782. https://doi.org/10.1021/acsaem.8b00338.

[19]   M. Alsabet, M. Grdeń, G. Jerkiewicz, Electrochemical growth of surface oxides on nickel. Part 3: formation of β-NiOOH in relation to the polarization potential, Polarization Time, and Temperature, Electrocatalysis. 6 (2015) 60–71. https://doi.org/10.1007/s12678-014-0214-1.

[20]   L. Trotochaud, S.L. Young, J.K. Ranney, S.W. Boettcher, Nickel–Iron Oxyhydroxide Oxygen-Evolution Electrocatalysts: The Role of Intentional and Incidental Iron Incorporation, J. Am. Chem. Soc. 136 (2014) 6744–6753. https://doi.org/10.1021/ja502379c.

[21]   P. Thangavel, M. Ha, S. Kumaraguru, A. Meena, A.N. Singh, A.M. Harzandi, K.S. Kim, Graphene-nanoplatelets-supported NiFe-MOF: high-efficiency and ultra-stable oxygen electrodes for sustained alkaline anion exchange membrane water electrolysis, Energy Environ. Sci. 13 (2020) 3447–3458. https://doi.org/10.1039/D0EE00877J.

[22]   E. Cossar, A.O. Barnett, F. Seland, E.A. Baranova, The performance of nickel and nickel-iron catalysts evaluated as anodes in anion exchange membrane water electrolysis, Catalysts. 9 (2019). https://doi.org/10.3390/catal9100814.

[23]   O. Diaz-Morales, D. Ferrus-Suspedra, M.T.M. Koper, The importance of nickel oxyhydroxide deprotonation on its activity towards electrochemical water oxidation, Chem. Sci. 7 (2016) 2639–2645. https://doi.org/10.1039/c5sc04486c.

[24]   M. Balasubramanian, C.A. Melendres, S. Mini, X-ray Absorption Spectroscopy Studies of the Local Atomic and Electronic Structure of Iron Incorporated into Electrodeposited Hydrous Nickel Oxide Films, J. Phys. Chem. B. 104 (2000) 4300–4306. https://doi.org/10.1021/jp9921710.

[25]   P. Axmann, O. Glemser, Nickel hydroxide as a matrix for unusual valencies: the electrochemical behaviour of metal(III)-ion-substituted nickel hydroxides of the pyroaurite type, J. Alloys Compd. 246 (1997)

232–241. https://doi.org/10.1016/S0925-8388(96)02479-6.

[26]   M. Louie, A. Bell, An investigation of thin-film Ni-Fe oxide catalysts for
        the electrochemical evolution of oxygen, J. Am. Chem. Soc. 135 (2013).
        https://doi.org/10.1021/ja405351s.

[27]   D. Friebel, M.W. Louie, M. Bajdich, K.E. Sanwald, Y. Cai, A.M. Wise, M.-
        J. Cheng, D. Sokaras, T.-C. Weng, R. Alonso-Mori, R.C. Davis, J.R. Bargar,
        J.K. Nørskov, A. Nilsson, A.T. Bell, Identification of highly active Fe sites
        in (Ni,Fe)OOH for electrocatalytic water splitting, J. Am. Chem. Soc. 137
        (2015) 1305–1313. https://doi.org/10.1021/ja511559d.

[28]   G.B. Shombe, M.D. Khan, C. Zequine, C. Zhao, R.K. Gupta, N.
        Revaprasadu, Direct solvent free synthesis of bare α-NiS, β-NiS and α-β-
        NiS composite as excellent electrocatalysts: Effect of self-capping on
        supercapacitance and overall water splitting activity, Sci. Rep. 10 (2020)
        3260. https://doi.org/10.1038/s41598-020-59714-9.

[29]   A. Faid, F. Seland, S. Sunde, Optimized nickel-cobalt and nickel-iron
        oxide catalysts for the hydrogen evolution reaction in alkaline water
        electrolysis, J. Electrochem. Soc. 166 (2019) F519–F533.
        https://doi.org/10.1149/2.0821908jes.

[30]   K. . K, A. Sengeni, S. Ede, S. Kundu, Nanosheets of nickel iron hydroxy
        carbonate hydrate with pronounced OER activity under alkaline and
        near-neutral conditions, Inorg. Chem. 58 (2019).
        https://doi.org/10.1021/acs.inorgchem.8b02680.

[31]   A.M.P. Sakita, E. Vallés, R. Della Noce, A. V Benedetti, Novel NiFe/NiFe-
        LDH composites as competitive catalysts for clean energy purposes,
        Appl. Surf. Sci. 447 (2018) 107–116.
        https://doi.org/10.1016/j.apsusc.2018.03.235.

[32]   M.L. Lindstrom, R. Gakhar, K. Raja, D. Chidambaram, Facile synthesis of
        an efficient Ni-Fe-Co based oxygen evolution reaction electrocatalyst, J.
        Electrochem. Soc. 167 (2020). https://doi.org/10.1149/1945-
        7111/ab6b08.

[33]   M. Sun, Z. Wang, B. Gao, S. Wang, C. Wang, X. Song, D. Lin,
        Electrocatalytic hydrogen evolution properties of anionic NiS_2-$Ni(OH)_2$
        nanosheets produced on the surface of nickel foam, Int. J. Energy Res. 44
        (2020) 4827–4836. https://doi.org/10.1002/er.5275.

[34] L. Wang, C.-Y. Lee, P. Schmuki, Solar water splitting: preserving the beneficial small feature size in porous α-Fe_2O_3 photoelectrodes during annealing, J. Mater. Chem. A. 1 (2013) 212–215. https://doi.org/10.1039/C2TA00431C.

[35] R. Solmaz, G. Kardaş, Electrochemical deposition and characterization of NiFe coatings as electrocatalytic materials for alkaline water electrolysis, Electrochim. Acta. 54 (2009) 3726–3734. https://doi.org/10.1016/j.electacta.2009.01.064.

[36] H. Zhang, X. Li, A. Hähnel, V. Naumann, C. Lin, S. Azimi, S.L. Schweizer, A.W. Maijenburg, R.B. Wehrspohn, Bifunctional heterostructure assembly of NiFe LDH nanosheets on NiCoP nanowires for highly efficient and stable overall water splitting, Adv. Funct. Mater. 28 (2018) 1706847. https://doi.org/10.1002/adfm.201706847.

[37] E. López-Fernández, J. Gil-Rostra, J.P. Espinós, A.R. González-Elipe, A. de Lucas Consuegra, F. Yubero, Chemistry and electrocatalytic activity of nanostructured nickel electrodes for water electrolysis, ACS Catal. 10 (2020) 6159–6170. https://doi.org/10.1021/acscatal.0c00856.

[38] M. Yu, G. Moon, E. Bill, H. Tüysüz, Optimizing Ni–Fe oxide electrocatalysts for oxygen evolution reaction by using hard templating as a Toolbox, ACS Appl. Energy Mater. 2 (2019) 1199–1209. https://doi.org/10.1021/acsaem.8b01769.

[39] S. Watzele, P. Hauenstein, Y. Liang, S. Xue, J. Fichtner, B. Garlyyev, D. Scieszka, F. Claudel, F. Maillard, A.S. Bandarenka, Determination of electroactive surface area of Ni-, Co-, Fe-, and Ir-based oxide electrocatalysts, ACS Catal. 9 (2019) 9222–9230. https://doi.org/10.1021/acscatal.9b02006.

[40] P. Shinde, C.S. Rout, D. Late, P.K. Tyagi, M.K. Singh, Optimized performance of nickel in crystal-layered arrangement of $NiFe_2O_4$/rGO hybrid for high-performance oxygen evolution reaction, Int. J. Hydrogen Energy. 46 (2021) 2617–2629. https://doi.org/10.1016/j.ijhydene.2020.10.144.

[41] H.A. Bandal, A.R. Jadhav, H. Kim, Facile synthesis of bicontinuous Ni_3Fe alloy for efficient electrocatalytic oxygen evolution reaction, J. Alloys Compd. 726 (2017) 875–884. https://doi.org/10.1016/j.jallcom.2017.07.290.

[42]   J. Wang, W. Zhang, Z. Zheng, J. Liu, C. Yu, Y. Chen, K. Ma, Dendritic
        core-shell Ni@Ni(Fe)OOH metal/metal oxyhydroxide electrode for
        efficient oxygen evolution reaction, Appl. Surf. Sci. 469 (2019) 731–738.
        https://doi.org/10.1016/j.apsusc.2018.10.232.

[43]   L. Xu, L. Cao, W. Xu, Z. Pei, One-step electrosynthesis of NiFe-NF
        electrodes for highly efficient overall water splitting, Appl. Surf. Sci. 503
        (2020). https://doi.org/10.1016/j.apsusc.2019.144122.

[44]   D.H. Youn, Y.B. Park, J.Y. Kim, G. Magesh, Y.J. Jang, J.S. Lee, One-pot
        synthesis of NiFe layered double hydroxide/reduced graphene oxide
        composite as an efficient electrocatalyst for electrochemical and
        photoelectrochemical water oxidation, J. Power Sources. 294 (2015) 437–
        443. https://doi.org/10.1016/j.jpowsour.2015.06.098.

[45]   E. López-Fernández, J. Gil-Rostra, J.P. Espinós, A.R. González-Elipe, F.
        Yubero, A. de Lucas-Consuegra, $Cu_xCo_{3-x}O_4$ ultra-thin film as efficient
        anodic catalysts for anion exchange membrane water electrolysers, J.
        Power   Sources.   415   (2019)   136–144.
        https://doi.org/10.1016/j.jpowsour.2019.01.056.

[46]   A.W. Hull., A New Method of X-Ray Crystal Analysis, Phys. Rev. 10
        (1917) 661–696. https://doi.org/10.1103/PhysRev.10.661.

[47]   J.D. Hanawalt, H.W. Rinn, L.K. Frevel, Chemical analysis by X-ray
        diffraction, Ind. Eng. Chem. Anal. Ed. 10 (1938) 457–512.
        https://doi.org/10.1021/ac50125a001.

[48]   C.-C. Hu, Y.-R. Wu, Bipolar performance of the electroplated iron–nickel
        deposits for water electrolysis, Mater. Chem. Phys. 82 (2003) 588–596.
        https://doi.org/10.1016/S0254-0584(03)00316-X.

[49]   L. Luo, X. Han, Q. Zeng, Hydrogenative cyclization of levulinic acid to γ-
        valerolactone with methanol and Ni-Fe bimetallic catalysts, Catal. . 10
        (2020). https://doi.org/10.3390/catal10091096.

[50]   E. Navarro-Flores, Z. Chong, S. Omanovic, Characterization of Ni, NiMo,
        NiW and NiFe electroactive coatings as electrocatalysts for hydrogen
        evolution in an acidic medium, J. Mol. Catal. A Chem. 226 (2005) 179–197.
        https://doi.org/10.1016/j.molcata.2004.10.029.

[51]   H.E.T.E. Swanson, Standard X-ray diffraction powder patterns, Natl. Bur.
   Stand. Circ. 539 (1953) 47. https://doi.org/10.1038/176147a0.

[52] Z. Hajizadeh, F. Radinekiyan, R. Eivazzadeh-keihan, A. Maleki, Development of novel and green $NiFe_2O_4$/geopolymer nanocatalyst based on bentonite for synthesis of imidazole heterocycles by ultrasonic irradiations, Sci. Rep. 10 (2020) 11671. https://doi.org/10.1038/s41598-020-68426-z.

[53] N. Iranpour Anaraki, R. Poursalehi, Shielding effectiveness of polymeric nanocomposites filled with iron/wüstite nanoparticles, Procedia Mater. Sci. 11 (2015) 700–705. https://doi.org/10.1016/j.mspro.2015.11.041.

[54] O. Butenko, V. Boychuk, B. Savchenko, V. Kotsyubynsky, V. Khomenko, V. Barsukov, Pure ultrafine magnetite from carbon steel wastes, Mater. Today Proc. 6 (2019) 270–278. https://doi.org/10.1016/j.matpr.2018.10.104.

[55] E. Tronc, C. Chanéac, J.P. Jolivet, Structural and magnetic characterization of ε-Fe_2O_3, J. Solid State Chem. 139 (1998) 93–104. https://doi.org/10.1006/jssc.1998.7817.

[56] T. Blomberg, T. Tripathi, M. Karppinen, New chemical mechanism explaining the breakdown of protective oxides on high temperature steels in biomass combustion and gasification plants, RSC Adv. 9 (2019) 10034–10048. https://doi.org/10.1039/C9RA00582J.

[57] Q. Xu, H. Jiang, X. Duan, Z. Jiang, Y. Hu, S.W. Boettcher, W. Zhang, S. Guo, C. Li, Fluorination-enabled reconstruction of NiFe electrocatalysts for efficient water oxidation, Nano Lett. 21 (2021) 492–499. https://doi.org/10.1021/acs.nanolett.0c03950.

[58] C. Andronescu, S. Seisel, P. Wilde, S. Barwe, J. Masa, Y.-T. Chen, E. Ventosa, W. Schuhmann, Influence of temperature and electrolyte concentration on the structure and catalytic oxygen evolution activity of nickel–iron layered double hydroxide, Chem. – A Eur. J. 24 (2018) 13773–13777. https://doi.org/10.1002/chem.201803165.

[59] S. Ahn, B.-S. Lee, I. Choi, S. Yoo, H.-J. Kim, E. Cho, D. Henkensmeier, S. Nam, J. Jang, Development of a membrane electrode assembly for alkaline water electrolysis by direct electrodeposition of nickel on carbon papers, Appl. Catal. B Environ. s 154–155 (2014) 197–205. https://doi.org/10.1016/j.apcatb.2014.02.021.

[60] A. Caravaca, A. De Lucas-Consuegra, A.B. Calcerrada, J. Lobato, J.L. Valverde, F. Dorado, From biomass to pure hydrogen: Electrochemical reforming of bio-ethanol in a PEM electrolyser, Appl. Catal. B Environ.

134–135 (2013) 302–309. https://doi.org/10.1016/j.apcatb.2013.01.033.

[61]   W. Wu, J. Liu, N. Johannes, Electrodeposition of Ir–Co thin films on copper foam as high-performance electrocatalysts for efficient water splitting in alkaline medium, Int. J. Hydrogen Energy. 46 (2021) 609–621. https://doi.org/10.1016/j.ijhydene.2020.09.268.

[62]   V.M. Nikolic, S.L. Maslovara, G.S. Tasic, T.P. Brdaric, P.Z. Lausevic, B.B. Radak, M.P. Marceta Kaninski, Kinetics of hydrogen evolution reaction in alkaline electrolysis on a Ni cathode in the presence of Ni–Co–Mo based ionic activators, Appl. Catal. B Environ. 179 (2015) 88–94. https://doi.org/10.1016/j.apcatb.2015.05.012.

[63]   A. Rodríguez-Gómez, F. Dorado, A. de Lucas-Consuegra, A.R. de la Osa, Influence of the GDL and assembly mode of a PEM cell on the ethanol revalorization into chemicals, Chem. Eng. J. 402 (2020) 125298. https://doi.org/10.1016/j.cej.2020.125298.

[64]   E. Amores, J. Rodríguez, J. Oviedo, A. Lucas-Consuegra, Development of an operation strategy for hydrogen production using solar PV energy based on fluid dynamic aspects, Open Eng. 7 (2017). https://doi.org/10.1515/eng-2017-0020.

[65]   E. López-Fernández, J. Gil-Rostra, C. Escudero, I.J. Villar-García, F. Yubero, A. de Lucas Consuegra, A.R. González-Elipe, Active sites and optimization of mixed copper-cobalt oxide anodes for anion exchange membrane water electrolysis, J. Power Sources. (2020). https://doi.org/10.1016/j.jpowsour.2020.229217.

[66]   J. Parrondo, C.G. Arges, M. Niedzwiecki, E.B. Anderson, K.E. Ayers, V. Ramani, Degradation of anion exchange membranes used for hydrogen production by ultrapure water electrolysis, RSC Adv. 4 (2014) 9875–9879. https://doi.org/10.1039/C3RA46630B.

[67]   P. Ganesan, A. Sivanantham, S. Shanmugam, Nanostructured nickel–cobalt–titanium alloy grown on titanium substrate as efficient electrocatalyst for alkaline water electrolysis, ACS Appl. Mater. Interfaces. 9 (2017) 12416–12426. https://doi.org/10.1021/acsami.7b00353.

[68]   L. Xiao, S. Zhang, J. Pan, C. Yang, M. He, L. Zhuang, J. Lu, First implementation of alkaline polymer electrolyte water electrolysis working only with pure water, Energy Environ. Sci. 5 (2012) 7869–7871. https://doi.org/10.1039/C2EE22146B.

[69] A.S. Aricò, M. Girolamo, S. Siracusano, D. Sebastian, V. Baglio, M. Schuster, Polymer electrolyte membranes for water photo-electrolysis, Membranes (Basel). 7 (2017) 25. https://doi.org/10.3390/membranes7020025.

[70] J. Hnát, M. Plevova, R.A. Tufa, J. Zitka, M. Paidar, K. Bouzek, Development and testing of a novel catalyst-coated membrane with platinum-free catalysts for alkaline water electrolysis, Int. J. Hydrogen Energy. 44 (2019) 17493–17504. https://doi.org/10.1016/j.ijhydene.2019.05.054.

[71] A. Carbone, S.C. Zignani, I. Gatto, S. Trocino, A.S. Aricò, Assessment of the FAA3-50 polymer electrolyte in combination with a $NiMn_2O_4$ anode catalyst for anion exchange membrane water electrolysis, Int. J. Hydrogen Energy. 45 (2020) 9285–9292. https://doi.org/10.1016/j.ijhydene.2020.01.150.

[72] S.M. Park, M.J. Jang, Y.S. Park, J. Lee, J.-Y. Jeong, J. Jung, M.-K. Choi, Y.-S. Noh, M.-H. Seo, H.J. Kim, J. Yang, Y.D. Kim, S.M. Choi, Synthesis and characterization of the $Cu_{0.72}CO_{2.28}O_4$ catalyst for oxygen evolution reaction in an anion exchange membrane water electrolyzer, J. Korean Inst. Met. Mater. 58 (2020) 49–58. https://doi.org/10.3365/KJMM.2020.58.1.49.

[73] Y.S. Park, M.J. Jang, J. Jeong, S.M. Park, X. Wang, M.H. Seo, S.M. Choi, J. Yang, Hierarchical Chestnut-Burr like structure of copper cobalt oxide electrocatalyst directly grown on Ni foam for anion exchange membrane water electrolysis, ACS Sustain. Chem. Eng. (2020). https://doi.org/10.1021/acssuschemeng.9b06767.

[74] W. Guo, J. Kim, H. Kim, S.H. Ahn, Cu–Co–P electrodeposited on carbon paper as an efficient electrocatalyst for hydrogen evolution reaction in anion exchange membrane water electrolyzers, Int. J. Hydrogen Energy. (2021). https://doi.org/10.1016/j.ijhydene.2021.03.120.

Chapter 8

Toward an overall optimization
of the anion exchange
membrane water electrolysis cell
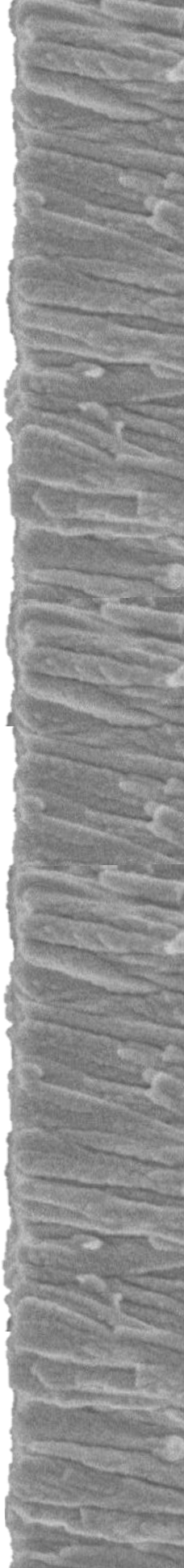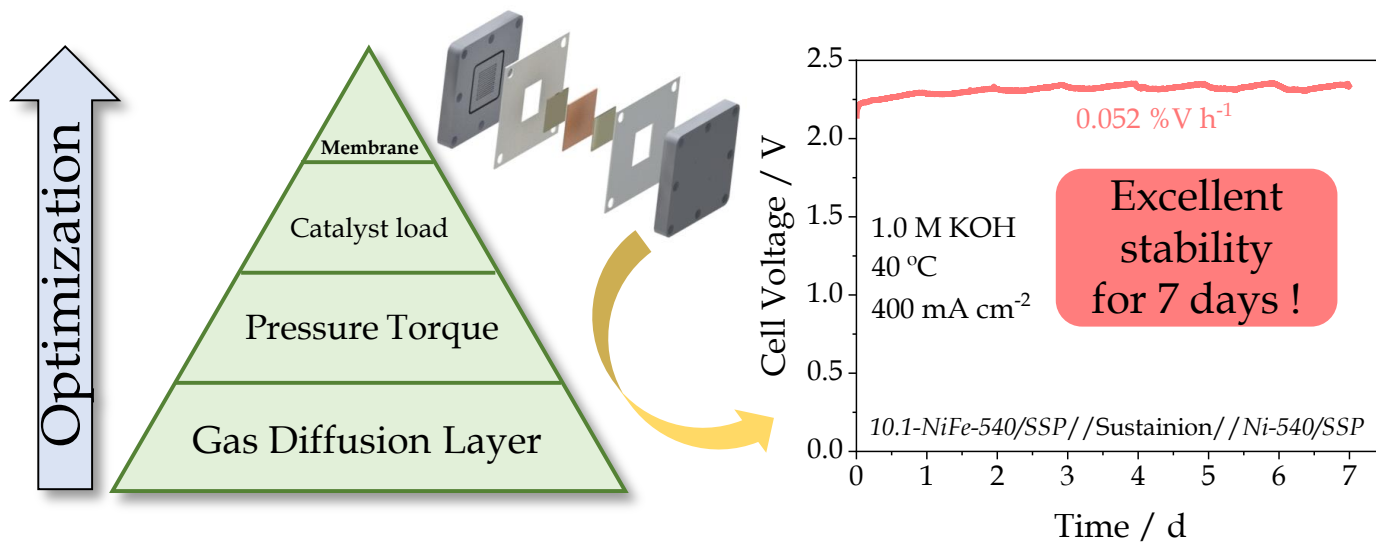
The content of this chapter is in preparation to be published as:

8.1. Introduction

In the previous results chapters of this thesis, different Co-Cu, Ni and Ni-Fe electrodes have been tested as anodes for AEMWE cells. Thus, comparing the performance towards the OER in the three-electrode cell of the different optimized electrodes of each chapter, an optimal performance was obtained for the Ni/Fe electrodes with an atomic ratio of 10.1 (see **Figure 8.1**). To progress in the search of improved performance of our AEMWE cell, in this chapter we have compared the performance of several membranes, gas diffusion layers (GDLs) and catalyst loads or *equivalent thicknesses* to determine how each isolated component affects in the global activity.
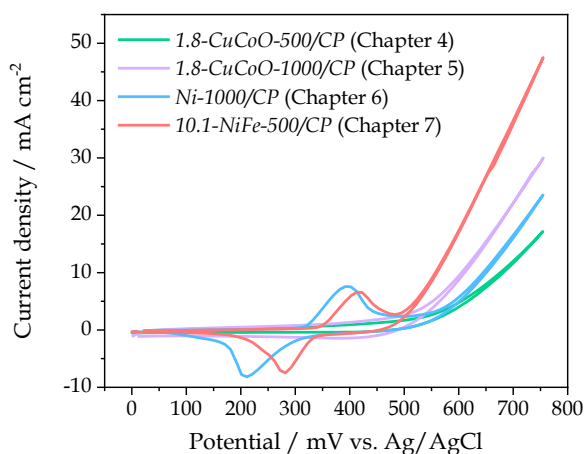

Figure 8.1. *Comparison between the optimized electrodes of the previous chapters of this thesis toward the OER in the three-electrode cell.*

The optimization of the GDL support used in the AEMWE cell is an essential parameter that requires understanding their porosity, surface morphology, gas permeability, etc. [1]. One of the main problems associated with the commercially available GDLs is the use of carbons as

carbon paper or carbon cloths as anodic GDL support. These supports provide an excellent electrical conductivity and a high available surface area. Nevertheless, although we have demonstrated some stability under mild-term operation conditions (hours), carbon is not stable in high anodic potentials for long-term use (days/weeks) due to the OH⁻ ions are excellent nucleophilic intermediate and accelerate the carbon degradation [2], providing a decrease in the electrical conductivity and in the active surface area. In addition, the gradual decomposition of the anode produces a degradation of the membrane electrode assembly decreasing the stability of the system [3]. For this reason, some gas diffusion layer as stainless-steel paper (SSP), titanium paper or nickel foam as emerged to solve these problems [4–7].

First, carbon paper and stainless-steel paper gas diffusion layers have been tested with the same catalyst layer deposited and using the same membrane and compared. The catalyst thickness of the catalyst layer deposited by magnetron sputtering on the optimum gas diffusion layer has been also optimized. Finally, with the optimum anodic and cathodic electrodes (GDL and catalyst thickness), some commercially membranes as Sustainion® X37-50, Fumapem® FAA-3-50 and Fumasep FAA-3-PK-75® have been used for the preparation of the membrane electrode assembly (MEA) and compared between them. In addition, other parameters as the torque pressure to close the cell have been studied with the objective of increasing the performance of the AEMWE cell. A detailed characterization of the electrodes has been also carried out by SEM, XPS and EIS. Using the optimal cell configuration, an excellent performance with current density values around 670 mA cm^{-2} at 2.2 V and 40 °C was obtained. A long-term chronopotentiometry experiment for 7 days with a very weak degradation of 0.05 % V h^{-1} (at fixed 400 mA cm^{-2}) has

demonstrated the high stability of the cell based on the use of an ionomer-free no noble metal catalyst-based Ni-Fe and Ni as anode and cathode prepared by MS-OAD.

8.2.   Experimental

Bimetallic Ni/Fe and Ni catalyst electrodes were prepared by MS-OAD at room temperature as has been previously explained in Chapters 3 and 7. Carbon paper (CP) and stainless-steel paper (SSP) substrates were used as conductive GDL supports to carry out the electrochemical experiments. Polished silicon wafer substrates were used to measure the *equivalent thickness* by cross-sectional SEM analysis.

In this chapter, samples will be identified in the paper as follows: *XX-NiFe-thickness/ZZ,* where *XX* refers the Ni/Fe at. ratio determined by EDX Spectroscopy and *ZZ* is the support used in each electrode. Ni electrodes are designated by *Ni-thickness/ZZ.*

All the physico-chemical characterization techniques used in this study have been briefly described in Chapter 3.

The influence of anodic and cathodic GDL support and the amount of catalyst in the electrode (catalyst *equivalent thickness*) were studied in the three-electrode cell described in Chapter 3.

To demonstrate the integration of the electrodes in a complete system, the performance of AEMWE cells were studied. Linear sweep voltammetries (LSVs) were performed between 1.0 to 2.2 V with a scan rate of 5 mV s^{-1}. All experiments were carried out in a 1.0 M KOH solution at 40 °C. The torque pressure applied to close the cell was optimized for each individual cell. The stability of the complete system was studied by

constant-current chronopotentiometry experiments at fixed 400 mA cm^{-2}
for 32 hours and cyclic voltammetry experiments (200 cycles, scan rate of
50 mV s^{-1}) in all cells. For the final optimum system, a stability constant-
current chronopotentiometry test was carried out at fixed 400 mA cm^{-2}
for 7 days.

8.3. Results and discussion

8.3.1. Influence of the gas diffusion layer support

Influence of the anodic GDL support in the OER

Due to the problem associated with the carbon degradation of
traditional carbon papers and cloths gas diffusion layers detailed in the
introduction section, the first aim of this chapter was to study the
influence of a new gas diffusion layer of stainless-steel and to compare its
performance with the traditional carbon paper support.

The surface microstructure of the SSP and CP GDLs without catalyst
are exemplified by SEM analysis in the **Figure 8.2**. It can be observed the
large porosity of both supports, providing higher pore sizes and diameter
fibers in the SSP. **Figures 8.3 a)** and **b)** show the surface microstructure of
as prepared nickel-iron catalyst deposited on SSP and CP supports,
respectively. A great porous and homogeneous microstructure can be
observed, without degradation or delamination after the use in the three-
electrode cell (see **Figures 8.3 c)** and **d)** for SEM images after use),
evidencing the high stability of the electrodes. A smaller particle size can
be observed in the Ni-Fe film deposits on SSP GDL vs. the same film
deposits in the CP GDL (Figures 8.3 a) and b)), leading to a higher
electrochemical surface area (ECSA) for the *10.1-NiFe-540/SSP* electrode
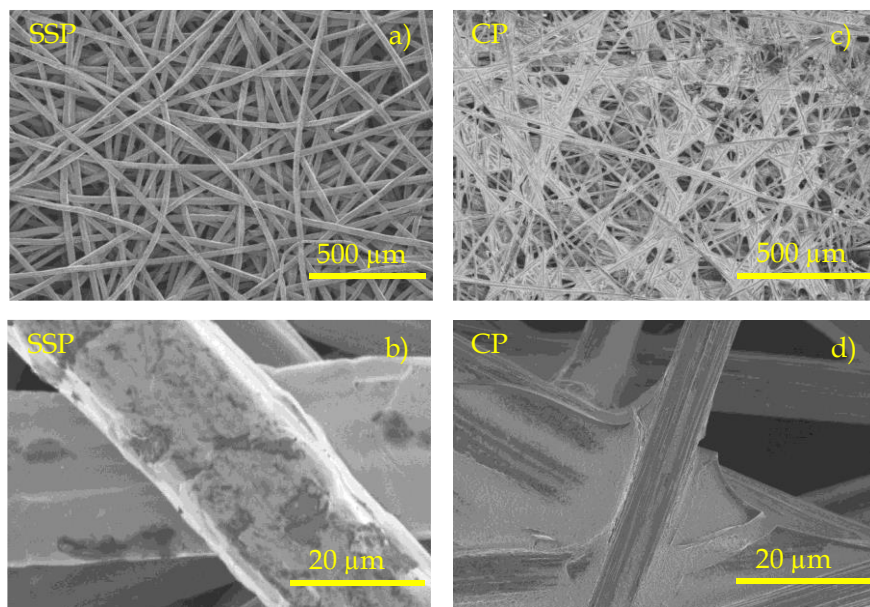as will be confirmed below.

Figure 8.2. *Front view SEM images of a) and b) SSP and c) and d) CP GDL supports.*
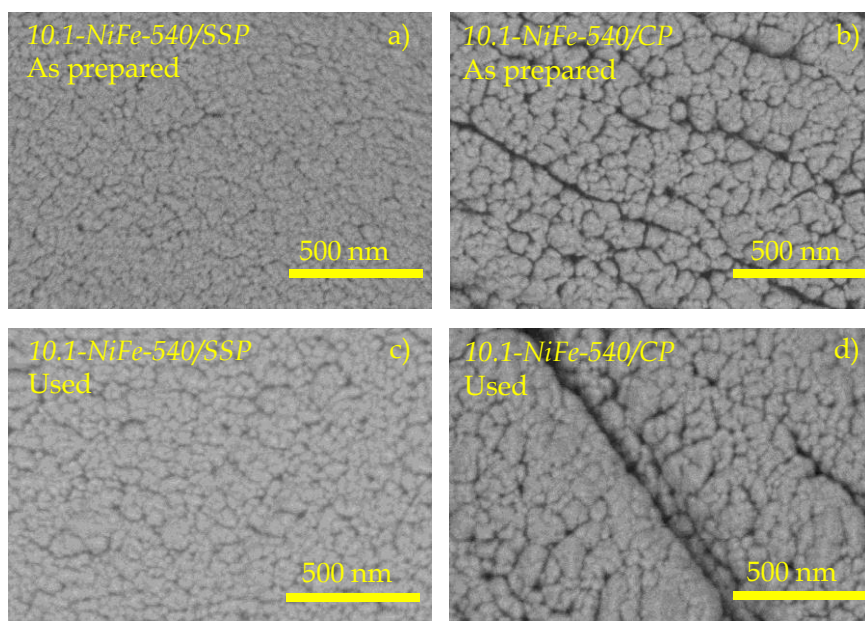

Figure 8.3. *SEM images of a) and b) as prepared and c) and d) after use in the three-electrode cell of 10.1-NiFe-540/SSP and 10.1-NiFe-540/CP anodic electrodes, respectively.*

Chemical compositions and oxidation states of the electrode surfaces were studied by XPS analysis. **Figures 8.4 a-c)** show the comparison of Ni 2p, Fe 2p and O 1s spectra for the *10.1-NiFe-540/SSP* and *10.1-NiFe-540/CP* before and after using in the three-electrode cell. The spectra of Ni-Fe catalysts supported on carbon paper have been previously described in Chapter 7. All samples show surface oxidation by XPS due to the exposition to ambient air [8]. The as prepared samples, due to the preparation of the film was carried out using pure Ar as plasma gas, revealed shoulders in Ni 2p spectra (see **Figure 8.4 a)** at 870.2 and 853.0 eV due to Ni^0 contribution [9,10] that confirmed the oxidation was only in the surface of the electrode. The two peaks at 874.0 and 856.4 eV with their two satellites at 880.7 and 861.9 eV are attributed to Ni $2p_{1/2}$ and Ni $2p_{3/2}$ for Ni^{+2} species [10,11]. In the used samples, the Ni^0 contribution disappears due to the oxidation of the catalyst surface by the KOH solution. **Figure 8.4 b)** shows no variations between the Fe 2p spectra before and after the use of the electrode in the three-electrode cell. In all cases, two peaks at 725.1 and 711.4 eV correspond to Fe $2p_{1/2}$ and Fe $2p_{3/2}$ of Fe^{+3} [11]. In **Figure 8.4 c)** two peaks at 531.8 and 530.0 eV corresponded to OH^- and O^{2-} groups [12] can be observed in the as prepared samples, maintaining a single band for OH^- groups for the used samples. This is in agreement with previous chapters and with the involvement of the hydroxide/oxyhydroxide of Ni or Ni-Fe in the oxygen evolution reaction [13] and confirms that the type of GDL support does not affect the chemical state of the Ni-Fe electrodes, neither before nor after carrying out electrochemical experiments.
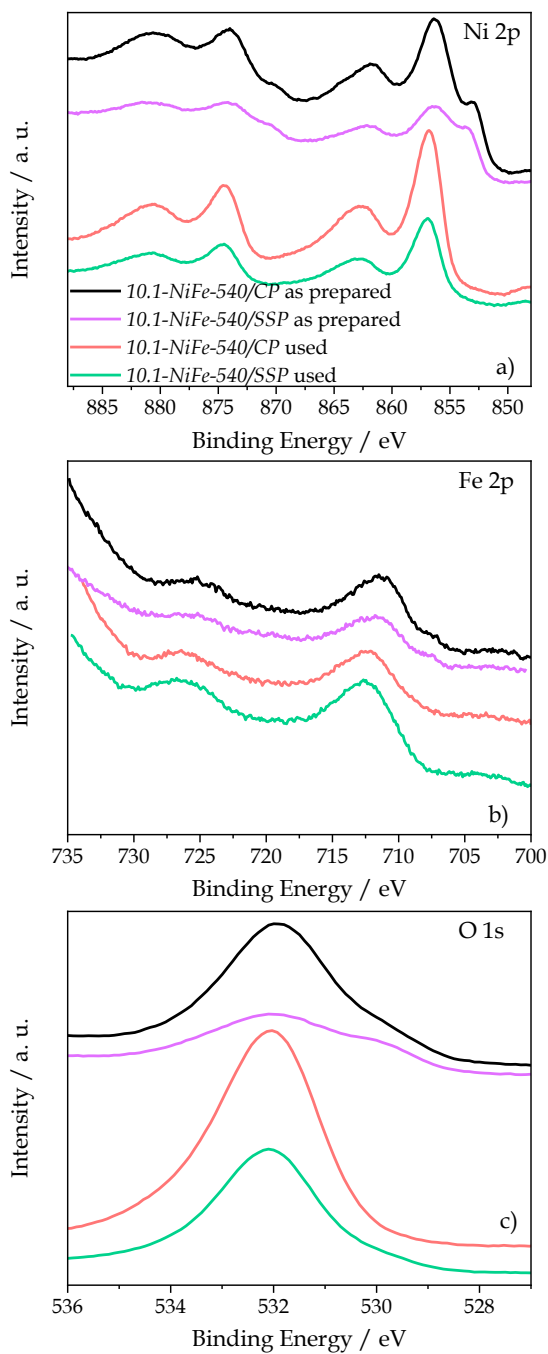
*Figure 8.4. a) Ni 2p, b) Fe 2p, and c) O 1s XPS spectra of 10.1-NiFe.540/SSP and
10.1-NiFe-540/CP as prepared and used electrodes for OER in the three-electrode cell.*

Figure 8.5 a) shows the cyclic voltammetry curves recorded for *10.1-NiFe-540/CP* and *10.1-NiFe-540/SSP* in the three-electrode cell under 1.0 M KOH solution at room temperature. As already explained in Chapter 7, two well-defined peaks were observed, an anodic peak related to the oxidation of $Ni(OH)_2$ to $NiOOH$ (at approximately 450 mV vs. Ag/AgCl), and other cathodic peak attributed to the reversible reaction of $NiOOH$ to $Ni(OH)_2$ (at approximately 320 mV vs. Ag/AgCl) [14–16]. It is observed that *10.1-NiFe-540/CP* sample is oxidized before than *10.1-NiFe-540/SSP* sample, where a shift in the redox peak to higher potential values is detected. This shift could be related to the presence of iron in the SSP substrate itself (SSP without catalyst contains 55.98 at. % of iron in their structure determined by EDX, see Table 3.1 in Chapter 3), since it has been observed in previous studies that the presence of Fe shifts the oxidation peak to $NiOOH$ towards higher potential values [17]. The onset potential is observed at approximately 500 mV vs. Ag/AgCl for both electrodes, similar value to others reported in the literature [13,18,19]. Concerning the overpotential value required to reach 10 mA cm^{-2}, *10.1-NiFe-540/SSP* anode provides a required overpotential value of 326.7 mV vs. RHE compared to 345.1 mV vs. RHE required for *10.1-NiFe-540/CP* anodic electrode. These values are in good agreement with literature for similar electrodes [20,21]. The overpotentials have been converted to mV vs. RHE to use in calculations, according to $E_{RHE} = E_{Ag/AgCl} + 0.059\ pH + E^0_{Ag/AgCl}$, where $E^0_{Ag/AgCl} = 0.1979$ V [22,23] taken a pH of 13.9 for the 1.0 M KOH solution. In addition, a higher catalytic activity for OER for *10.1-NiFe-540/SSP* was found. This superior activity could be related to the higher electrochemically active area found in the *10.1-NiFe-540/SSP* electrode calculated below. Bare carbon paper and stainless-steel supports used do

not provide any activity, associating the totality of the activity to the deposited catalyst.

To confirm the higher performance of *10.1-NiFe-540/SSP*, EIS analysis was carried out. **Figure 8.5 b)** shows the Nyquist plots obtained for *10.1-NiFe-540/CP* and *10.1-NiFe-540/SSP* anodic samples and the fit to the equivalent electrical circuit $R_1(R_2C_1)$, typical equivalent circuit for these types of anodes [24,25]. Values of the electrical fitted parameters are collected in the inset table. R_1 is usually related to an ohmic resistance between the surface of the working electrode and the reference electrode. It is related to the sum of resistances associated to the electrolyte, the electrode catalyst surface, and the contacts [15,24]. R_2 is commonly associated with the charge transfer resistance through the electrode during the oxygen evolution reaction [15,24]. It can be observed that R_1 is similar for both electrodes. This supports that the ohmic loss is the same in both electrodes, being able to associate the change in activity with morphological variations. Nevertheless, R_2 was lower for the *10.1-NiFe-540/SSP* electrode, that could be related to the highest electrocatalytic activity of this electrode leading to an improve kinetics of OER.
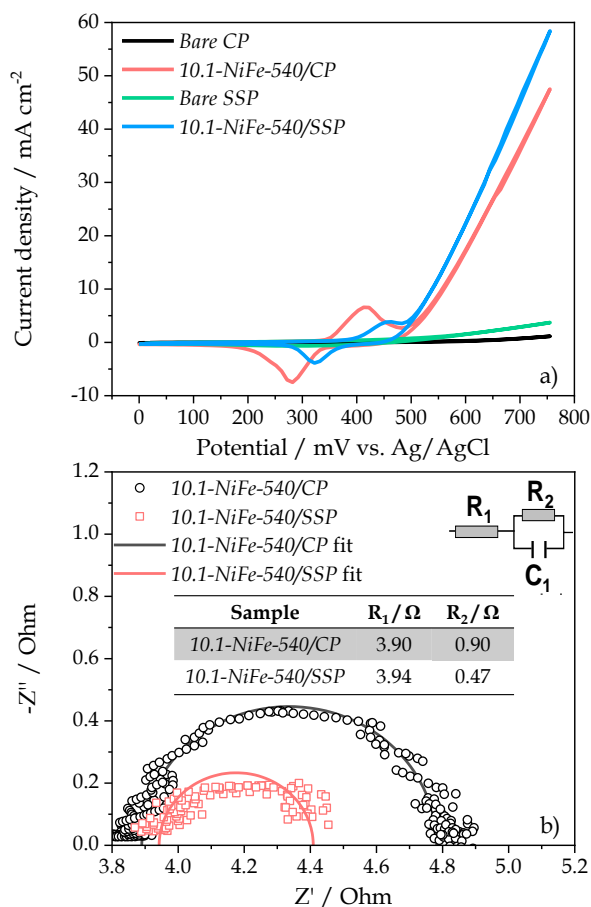
Figure 8.5. *a) Cyclic voltammetry curves of 10.1-NiFe-540/SSP and 10.1-NiFe-540/CP in a three-electrode cell at room temperature under 1.0 M KOH electrolyte and 20 mV s^{-1} of scan rate. b) Nyquist plots of 10.1-NiFe-540/SSP and 10.1-NiFe-540/CP samples obtained at 700 mV vs. Ag/AgCl. Equivalent circuit and table with fitting values are included as inset in the figure.*

EIS experiments can be also used to determine the ECSA using the alternative interpretation of Nyquist plots proposed by Watzele et al. [26] (see details in Chapter 3). By the use of the same model, we have determined an ECSA value for *10.1-NiFe-540/CP* of 10.13 cm^2 and of 27.4 cm^2 for *10.1-NiFe-540/SSP* anodic electrode. These values suggest that the

surface available for the OER reaction will be higher for the *10.1-NiFe-540/SSP* electrode and can justify the best OER activity shown in Figure 8.5 a).

Influence of the cathodic GDL support

Similarly to Figure 8.3, **Figure 8.6** shows the surface microstructure of Ni catalyst deposited on SSP (**Figure 8.6 a)** and **c)**) and CP (**Figure 8.6 b)** and **d)**) GDL support. A great porous and homogeneous microstructure can be also observed, with a high stability of the electrodes after the use in the half-cell configuration (see Figures 8.6 c) and d)) due to the lack of visible degradation or delamination in the electrodes after their use in the three-electrode cell.
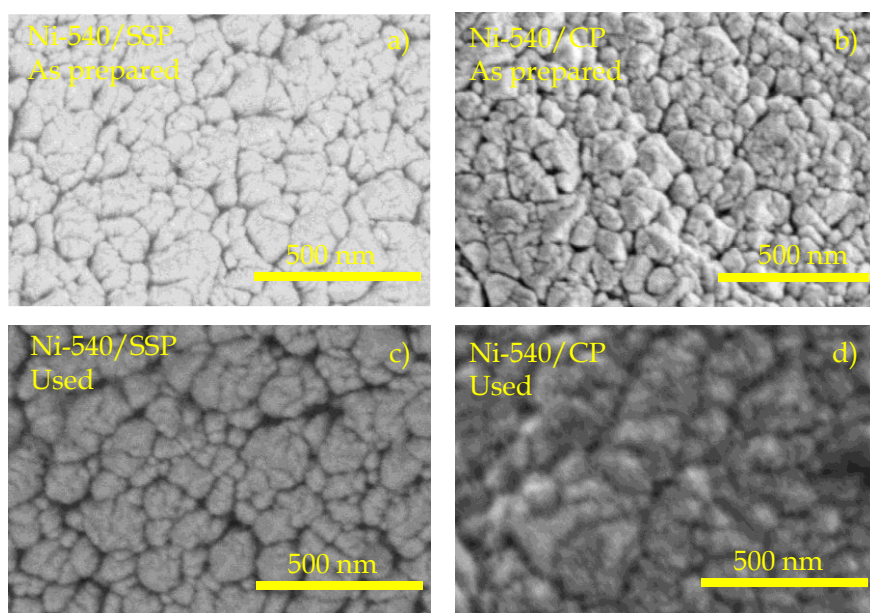

Figure 8.6. *SEM images of a) and b) as prepared and c) and d) after use in the three-electrode cell of Ni-540/SSP and Ni-540/CP cathodic electrodes, respectively.*

Figure 8.7 a) and **b)** shows the comparison of Ni 2p and O 1s spectra for the *Ni-540/SSP* and *Ni-540/CP* as prepared and used in the three-electrode cell. The spectra of Ni catalysts supported on carbon paper have been previously described in Chapter 6. In the as prepared samples can be observed the contribution of Ni^0 at 870.2 and 853.0 eV (Figure 8.7 a)) due to the catalyst layer preparation using argon as plasma gas (see similar contribution in Figure 8.4 a)) [9,10]. Other two peaks at 874.0 and 856.4 eV with their two satellites at 880.7 and 861.9 eV were attributed to Ni $2p_{1/2}$ and Ni $2p_{3/2}$ for Ni^{2+} species [10,11]. Compared to the used samples, no Ni^0 contribution was observed, attributed to the surface oxidation effect of the potassium hydroxide solution. Two peaks at 531.8 and 530.0 eV in Figure 8.7 b) corresponded to OH^- and O^{2-} groups [12] can be observed in the as prepared samples, maintaining a single band for OH^- groups for the used samples related to the KOH effect.
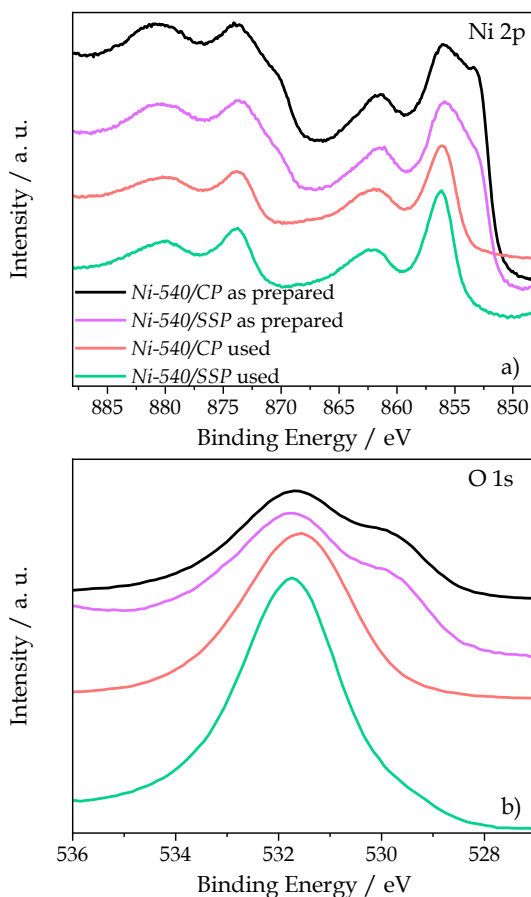
*Figure 8.7. a) Ni 2p, b) O 1s XPS spectra of Ni-540/SSP and Ni-540/CP as prepared
and used cathodic electrodes.*

Figure 8.8 shows the electrocatalytic activity of these characterized
electrodes for HER evaluated by CVs in the three-electrode cell under 1.0
M KOH solution at room temperature. For comparison, bare SSP and CP
GDL were measured under the same conditions. CP support does not
show an increase in the current density in the potential range studied,
indicating a low activity towards HER and associating the total of current
density to the catalyst film. However, some activity can be observed for
the SSP GDL, associated with the nickel and iron contain in its

257

composition. The best HER activity and the lower onset potential (at about -1100 mV vs. Ag/AgCl) were observed for the *Ni-540/SSP* sample, chosen this cathodic electrode for subsequently experiments. Comparing both electrodes, an overpotential of 1290 mV vs. Ag/AgCl (272 mV vs. RHE) to reach -10 mA cm^{-2} was obtained for the *Ni-540/CP* cathodic electrode vs. 1180 mV vs. Ag/AgCl (162 mV vs. RHE) obtained for the *Ni-540/SSP* at the current density of 10 mA cm^{-2}. To compare to the literature, the overpotentials have been converted to mV vs. RHE, according to the conversion equation previous defined. These overpotential values are consistent with other reported in the literature [27,28].
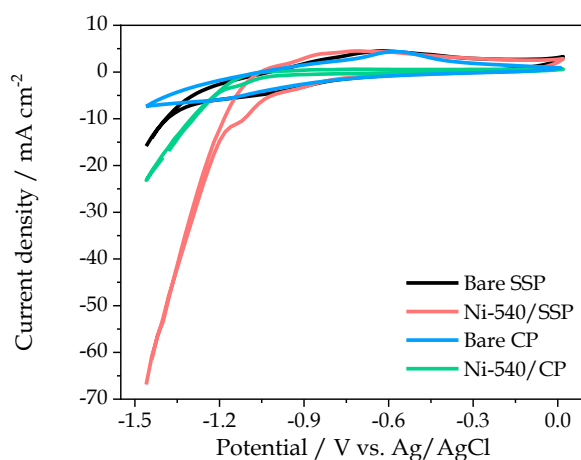
Figure 8.8. *Cyclic voltammetry curves for Ni-540/SSP and Ni-540/CP cathodes used to monitor the HER in the three-electrode cell configuration. Working conditions were fixed at 1.0 M KOH solution at room temperature with a scan rate of 10 mV s^{-1}.*

Influence of the anodic and cathodic GDL in the AEMWE performance

To test the influence of the gas diffusion layer in a membrane electrode assembly, full AEMWE cells were prepared. For this purpose, a MEA

composed by *10.1-NiFe-540/CP* as anode, *Ni-540/CP* as cathode and a
Sustainion anion exchange membrane between the anodic and cathodic
electrodes was prepared as previously explained in Chapter 3. A similar
MEA using SSP as GDL support was also prepared. All the experiments
were carried out using a 1.0 M KOH solution at 40 °C. First, an
optimization of the torque applied to close the cell was carried out. This
torque pressure depends on the gas diffusion layer, membranes or kind
of bipolar plates. For this reason, this optimization has been carried out
for each specific cell used in this work. **Figures 8.9 a)** and **c)** show that for
low assembly torque values, current densities increase with the increase
of pressure due to an improvement in the contact between the catalyst
surface and the membrane. Nevertheless, there is a breakdown in the
tendency from which current densities decrease with increasing torque
pressure. This fact can be attributed to the decrease in gas transport
through the pores of the gas diffusion layers and the partial covering of
the electrode surface by bubbles [29]. Therefore, optimum values of 4.0
Nm and 4.5 Nm were found for the CP GDL cell and SSP GDL cell,
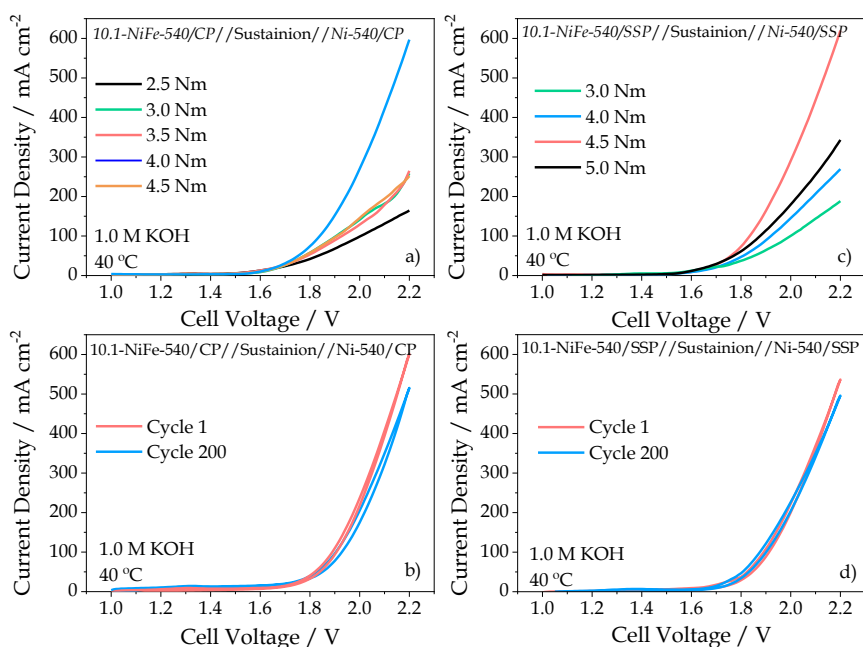respectively.

*Figure 8.9. Polarization curves obtained for MEA with electrodes deposited on a) CP
and c) SSP GDL support for various cell assembly torques at 40 °C and 1.0 M KOH. b)
and d) 200 cycles voltammetry curves for MEA with electrodes deposited on c) CP and
d) SSP GDL support at 40 °C and 1.0 M KOH.*

Concerning the AEMWE cell performance, a slight increase in the
electrocatalytic activity was observed for the stainless-steel gas diffusion
layer MEA accroding to the obtain LSV experiments (see **Figure 8.10 a)**).
The higher electrocatalytic activity was not very pronounced despite
observing a great improvement in the behavior of the cathode towards
HER in the three-electrode cell. This could be explained considering that
the OER is the higher overpotential reaction, being the results obtained
for the different anodes in the OER experiments in the three-electrode cell
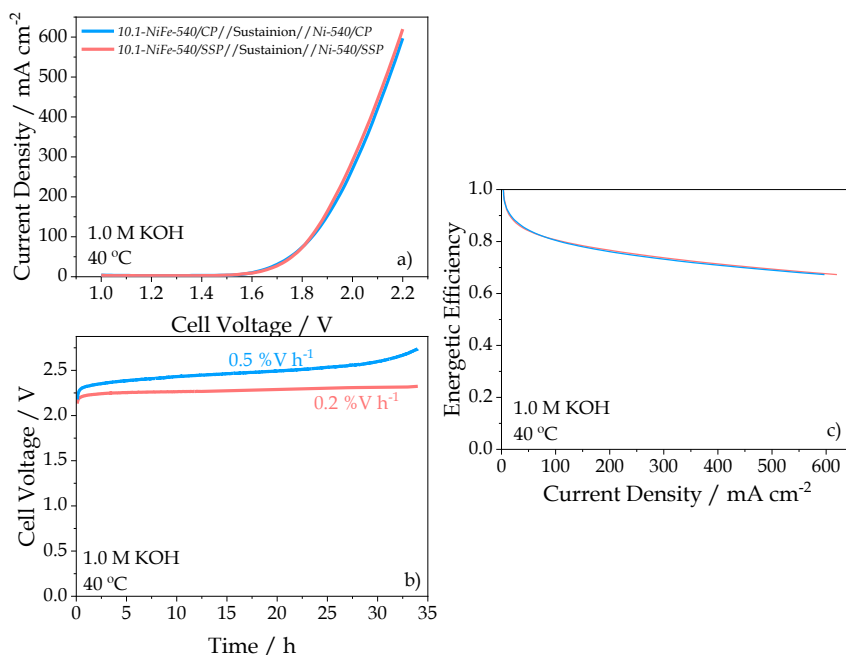not very differents [30,31].

Figure 8.10. *a) Linear sweep voltammetry curves obtained for 10.1-NiFe-540/ZZ and Ni-540/ZZ used as anodic and cathodic electrodes, respectively, and Sustainion membrane sandwiched between both electrodes. b) Constant-current (400 mA cm⁻²) chronopotentiometry measurement for the different MEAs. c) Energetic efficiency for several cell potential and current density values. All experiments were carried out at 40 °C in 1.0 M KOH electrolyte.*

However, despite not observing a great improvement in LSV curves, a great improvement in stability test (half voltage degradation compared to carbon paper) was observed using stainless-steel as gas diffusion layers (see **Figure 8.10 b)**). It is remarkable that although the initial cell potential values are similar for both cells, after 34 hours of operation, the cell with a carbon paper GDL needs 2.74 V of potential vs. 2.32 V required for the cell with a stainless steel GDL. This confirms the theory that carbon is not stable in high anodic potentials for long-term use [2], and it can be observed that it is better to work with the MEA composed of *10.1-NiFe-*

540/SSP as anode and *Ni-540/SSP* as cathode instead of the same catalyst film deposited on carbon paper substrate. The great stability of our systems has been also demonstrated by 200 cycles during cyclic voltammetry experiments (see **Figure 8.9 b)** and **d)**), obtaining similar current densities for the first and last cycle, especially for the system of SSP as GDL. In addition, SEM images of the anodic electrodes after their use in the AEMWE cell shows a color change that could suggest degradation or corrosion by OH⁻ ions on carbon paper compared to the catalysts deposited in SSP (see **Figure 8.11**).
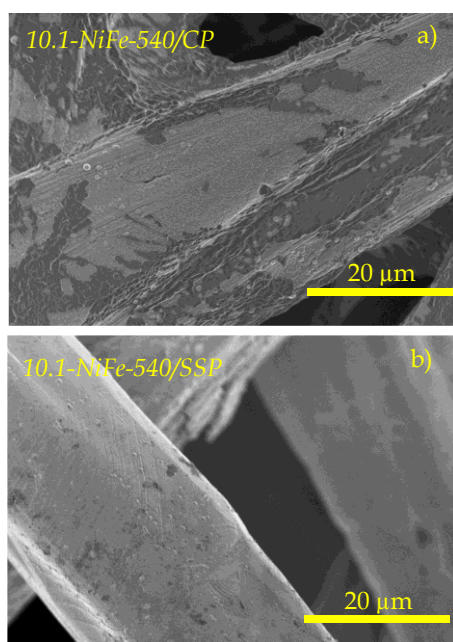

Figure 8.11. *SEM images of a) 10.1-NiFe-540/CP and b) 10.1-NiFe-540/SSP anodic electrodes after use in the AEMWE cells.*

The theorical cell voltage required for water electrolysis is 1.23 V under 1 atm and 25 °C. However, to overcome the kinetic barrier for the reaction,

water splitting requires higher potentials than 1.23 V. Energy efficiency of an electrolyzer could be defined as follows [32]:

$$\eta = \frac{\eta_F \left(\frac{n_C\,I}{2\,F}\right) HHV_{H2}}{n_C\,V_{cell}\,I} = \frac{1.48}{V_{cell}} \eta_F \qquad (8.1)$$

where η_F is the Faradaic efficiency (we have demonstrated that this efficiency is 100% in other previous studies in our group as [33]), n_c is the number of electrolysis cell connected in serie, I is the current intensity, F is the Faraday constant (F = 96485 C), HHV_{H2} is the higher heating value of hydrogen (HHV = ΔH^o = 285.8 kJ mol^{-1} = 3.24 kWh (Nm^3)$^{-1}$), and V_{cell} is the cell voltage.

Figure 8.10 c) shows the energetic efficiency of the cell to reach the different current density values. It is observed that the energy conversion efficiency decreases with the increase of the cell voltage required to obtain a determined current density value. However, as the LSV curves are similar for both cell configurations, the evolution of energy efficiency is also similar. The obtained efficiency at 2.0 V at arount 74 % is superior than others efficiencies at similar potential values reported in the literature as 66 % [32].

8.3.2. Influence of the amount of catalyst in the oxygen evolution reaction

Taking into account the previous chapters in which the optimum *equivalent thickness* for metallic nickel and copper-cobalt oxides electrodes was fixed at approximately 1000 nm [13,34], we have tested the influence of use this amount of catalyst (*equivalent thickness*) in the new electrodes used in this chapter. First, **Figure 8.12** shows the SEM cross-sectional

images of the *10.1-NiFe-540/Si* (**Figure 8.12 a)**) and *10-1-NiFe-1000/Si*
(**Figure 8.12 b)**). It can be confirmed the nanocolumnar structure typical
from the OAD-MS fabrication technique observed in previous chapters in
this thesis.
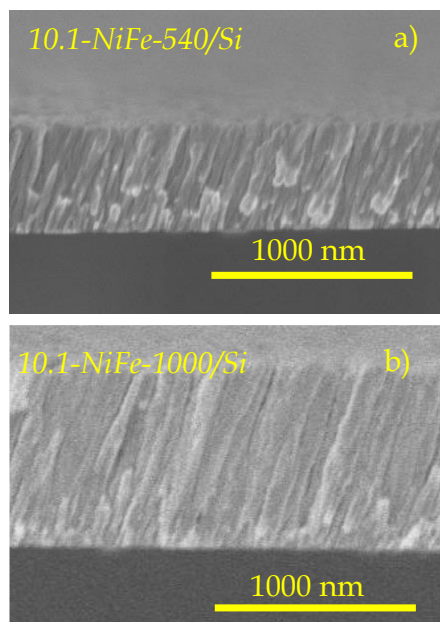
*Figure 8.12. Cross-sectional view SEM image of NiFe samples with different
equivalent thickness deposited on flat silicon substrate.*

Figure 8.13 a) shows the cyclic voltammetry curves recorded for *10.1-
NiFe-540/SSP* and *10.1-NiFe-1000/SSP* in the three-electrode cell under 1.0
M KOH solution at room temperature. The oxidation and reduction
observed peaks have been explained before for Figure 8.5. In both cases,
the onset potential for the OER appears at approximately 500 mV vs.
Ag/AgCl, in line with values reported in the literature [13,18,19]. Finally,
comparing the OER voltage range, the yield is similar for both electrodes.
For this reason, we have chosen the anodic electrode with the lowest
catalyst load (*10.1-NiFe-540/SSP*) for subsequent experiments. This

similar behavior is attributed to a balance between two effects: an increase in the electrocatalytic active sites with the increase in the amount of catalyst, and an increase in the particle agglomerations of the nanocolumnar structure of the film, that reduce the number of active sites in line with the increase in the amount of catalyst (see **Figure 8.14**) [29,35]. Furthermore, it can be observed that the bare stainless-steel support used does not provide activity, associating the totality of the activity to the deposited catalyst.
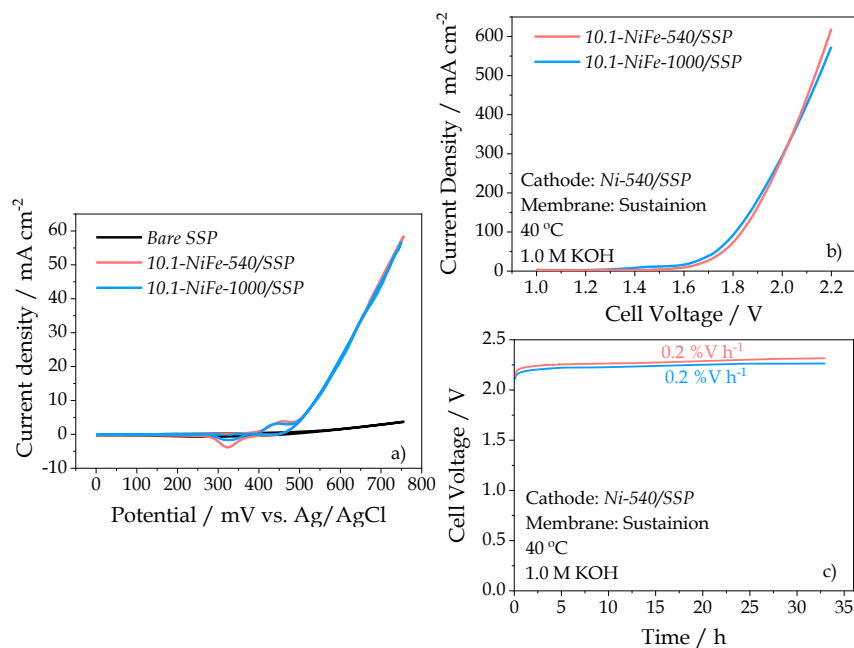
Figure 8.13. *a) Cyclic voltammetry experiments of 10.1-NiFe-thickness/SSP samples tested as anodic electrodes in the three-electrode cell for OER at room temperature under 1.0 M KOH solution. b) Linear sweep voltammetry curves obtained for 10.1-NiFe-thickness/SSP anodic electrodes, Ni-540/SSP cathodic electrode, and Sustainion membrane sandwiched between both electrodes. b) Constant-current (400 mA cm⁻²) chronopotentiometry measurement for the different MEAs. All experiments in AEMWE cell were carried out at 40 °C in 1.0 M KOH electrolyte.*
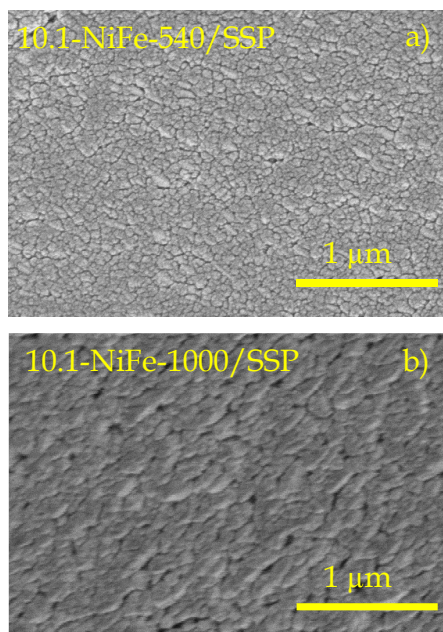
*Figure 8.14. SEM images of a) 10.1-NiFe-540/SSP and b) 10.1-NiFe-1000/SSP as
prepared anodic electrodes.*

To test the behavior of these electrodes in a membrane electrode
assembly, full AEMWE cells were tested. For this purpose, two MEAs
composed by *10.1-NiFe-540/SSP* and *10.1-NiFe-1000/SSP* as anode, *Ni-
540/SSP* as cathode and a Sustainion anion exchange membrane between
both electrodes were prepared. **Figure 8.13 b)** shows LSVs obtained for
the two different amounts of catalyst cells carried out at 40 °C under 1.0
M KOH solution. It can be observed similar current density values for
both electrodes confirming the results observed in the half-cell and
selecting, therefore, the electrode with less amount of catalyst for next
experiments.

Figure 8.13 c) shows the long-term stability test of the cells. For a
constant current density of 400 mA cm^{-2}, the potential response was
monitored for 32 hours and data evidence a slight decrease in the cell

potential over time (0.2 % V h^{-1} for *10.1-NiFe-540/SSP* and *10.1-NiFe-1000/SSP* cells) similar than other previous studies with electrodes prepared by magnetron sputtering [13,34]. Figure 8.9 d) (previously explained) and **Figure 8.15** show the cycling stability test of the complete cells, demonstrating the high stability of the system in these degradation conditions due to no distinctive differences were found between first and 200th cycle.
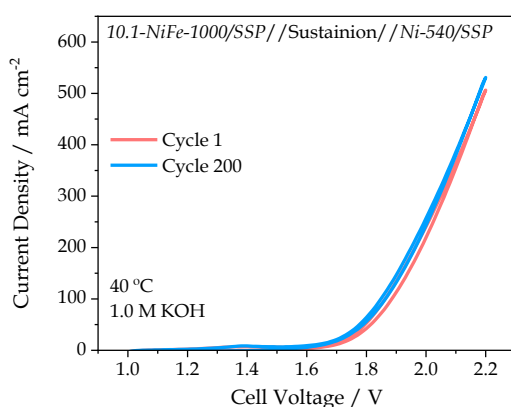
Figure 8.15. 200 cycles voltammetry curves for a MEA with 10.1-NiFe-1000/SSP as anodic electrode, Ni-540/SSP as cathodic electrode, and Sustainion membrane sandwiched between both of them at 40 °C and 1.0 M KOH.

8.3.3.   Influence of the membrane in the anion exchange membrane water electrolysis performance

To study the influence of the membrane in the global AEMWE performance, three commercial membranes were tested, Fumapem® FAA-3-50, Fumasep FAA-3-PK-75®, and Sustainion® X37-50. First, similar to the previous cells, the torque pressure to close the cell has been optimized for each cell (see **Figure 8.16** and previous optimization for Sustainion membrane in Figure 8.9 c)). Optimum values of 3.0 Nm for

both, Fumapem and Fumasep membranes cells, were found vs. 4.5 Nm
for Sustainion membrane system.
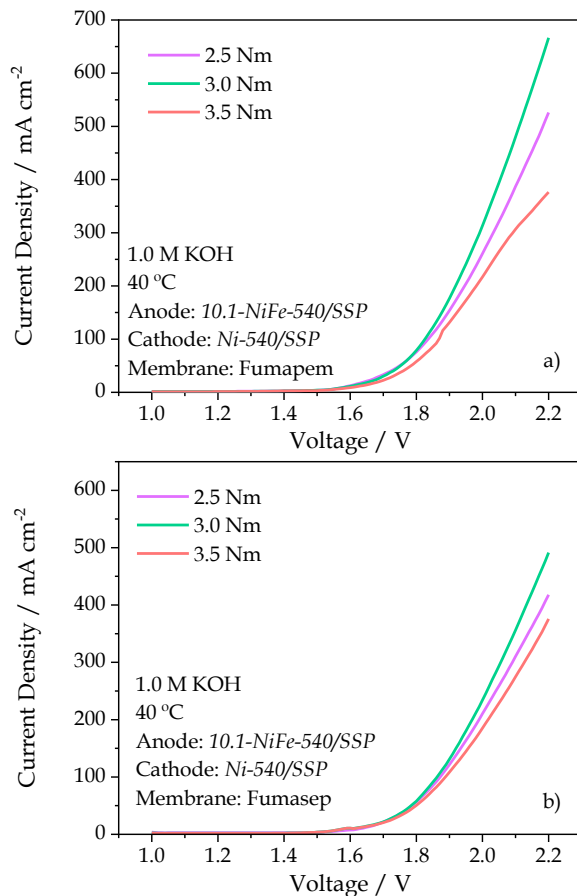
*Figure 8.16. Polarization curves obtained for a MEA with 10.1-NiFe-540/SSP as
anodic electrode, Ni-540/SSP as cathodic electrode and a) Fumapem and b) Fumasep
membrane for various cell assembly torques at 40 ºC and 1.0 M KOH.*

LSVs observed in **Figure 8.17 a)** demonstrated that, under the same
operation conditions and electrodes, Sustainion membrane presented the
higher performance. The same tendency was found for the energetic
efficiency (see **Figure 8.17 b)**), where the cell with *10.1-NiFe-540/SSP* as

anode, *Ni-540/SSP* as cathode and Sustainion as AEM presented the best results. Other studies reported in the literature have also demonstrated that Sustainion membrane had lower resistance than other commercial membrane tested [5] or a better performance than other tested membranes as Aemion™ or Tokuyama A201 [36].

Finally, to demonstrate the stability of the optimum water electrolysis cell in a near real conditions, a long-term stability test of 7 days was carried out (see **Figure 8.17 c)**). In the figure it can be observed the excellent stability of the system with only 0.05 % V h^{-1} (at 400 mA cm^{-2}) degradation, similar or even inferior to other values reported in the literature for similar electrodes as 0.04 % V h^{-1} (24 hours, at 300 mA cm^{-2}) [37], 0.13 % V h^{-1} (46 hours, at 500 mA cm^{-2}) [38], or 0.06 % V h^{-1} (100 hours, at 200 mA cm^{-2}) [39]. In addition, it is important to mention that most of the works reported in the literature have carried shorter stability experiments or working at lower current density values conditions. On the other hand, it is important to emphasize that we use a novel electrode preparation technique in one stage, without generating waste and without the need to use ionomer, reducing costs and problems associated with this compound.
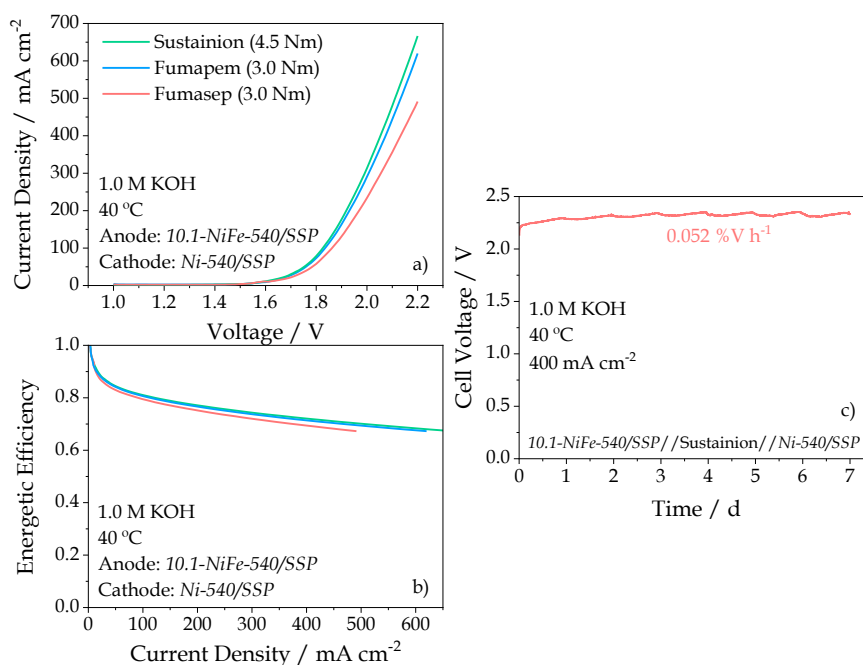
Figure 8.17. *a) Linear sweep voltammetry curves obtained for 10.1-NiFe-540/SSP and
Ni-540/SSP used as anodic and cathodic electrodes, respectively, and several kinds of
commercial membranes sandwiched between both electrodes. b) Energetic efficiency for
several cell potential and current density values. c) Constant-current (400 mA cm⁻²)
chronopotentiometry measurement for final optimum cell for 7 days. All experiments
were carried out at 40 ºC in 1.0 M KOH electrolyte.*

8.4. Conclusions

In contrast to the most used gas diffusion layer in the literature, the
carbon paper, other no carbonous supports as stainless-steel GDL
provide more stable results avoiding the problems associated with the
oxidation or degradation of the carbon paper. In this chapter, it has been
demonstrated that with MS-OAD technique it is possible to work with
different metallic GDL. In addition, it has been confirmed that the type of
support does not affect the chemical state of the Ni-Fe electrodes, neither
before nor after carrying out electrochemical experiments. Concerning

270

the catalyst thickness, it has been demonstrated that an increase of above 540 nm does not provide any improvement in the cell performance. The influence of the kind of membrane was also studied using several commercial membranes and obtaining better performance and stability with the Sustainion membrane. The low contribution of HER to whole cell activity has been also demonstrated.

As conclusion, the influence of the *equivalent thickness* of the catalyst layer, gas diffusion layer and membrane has been studied reaching an optimum AEMWE cell. The maximum performance for the optimum cell reached current density values of 670 mA cm^{-2} at 2.2 V. Finally, we have demonstrated an excellent stability for 7 days with a slight degradation of 0.05 % V h^{-1} (at 400 mA cm^{-2}), one of the lower degradations found in the literature for AEMWE cells. These results are very relevant when testing the cells in conditions close to the real ones in view for their possible practical application.

8.5.   References

[1]   K. Scott, 10 - Membrane electrode assemblies for polymer electrolyte membrane fuel cells, Functional Materials for Sustainable Energy Applications, Woodhead Publishing, (2012) 279–311. https://doi.org/10.1533/9780857096371.3.279.

[2]   X. Wu, K. Scott, F. Xie, N. Alford, A reversible water electrolyser with porous PTFE based OH− conductive membrane as energy storage cells, J. Power Sources. 246 (2014) 225–231. https://doi.org/10.1016/j.jpowsour.2013.07.081.

[3]   G. Borisov, A. Stoyanova, E. Lefterova, E. Slavcheva, A novel non-carbon gas diffusion layer for PEM water electrolysis anodes, Izv. Po Khimiya Bulg. Akad. Na Nauk. 45 (2015).

[4]   Q. Xu, S.Z. Oener, G. Lindquist, H. Jiang, C. Li, S.W. Boettcher, Integrated reference electrodes in anion-exchange-membrane electrolyzers: impact

of stainless-steel gas-diffusion layers and internal mechanical pressure, ACS Energy Lett. 6 (2021) 305–312. https://doi.org/10.1021/acsenergylett.0c02338.

[5] Z. Liu, S.D. Sajjad, Y. Gao, H. Yang, J.J. Kaczur, R.I. Masel, The effect of membrane on an alkaline water electrolyzer, Int. J. Hydrogen Energy. 42 (2017) 29661–29665. https://doi.org/10.1016/j.ijhydene.2017.10.050.

[6] D. Xu, M.B. Stevens, M.R. Cosby, S.Z. Oener, A.M. Smith, L.J. Enman, K.E. Ayers, C.B. Capuano, J.N. Renner, N. Danilovic, Y. Li, H. Wang, Q. Zhang, S.W. Boettcher, Earth-abundant oxygen electrocatalysts for alkaline anion-exchange-membrane water electrolysis: effects of catalyst conductivity and comparison with performance in three-electrode cells, ACS Catal. 9 (2019) 7–15. https://doi.org/10.1021/acscatal.8b04001.

[7] I. Vincent, Hydrogen production by water electrolysis with an ultrathin anion-exchange membrane (AEM), Int. J. Electrochem. Sci. 13 (2018) 11347–11358. https://doi.org/10.20964/2018.12.84.

[8] H.A. Bandal, A.R. Jadhav, H. Kim, Facile synthesis of bicontinuous Ni3Fe alloy for efficient electrocatalytic oxygen evolution reaction, J. Alloys Compd. 726 (2017) 875–884. https://doi.org/10.1016/j.jallcom.2017.07.290.

[9] A.M. Hengne, A.K. Samal, L.R. Enakonda, M. Harb, L.E. Gevers, D.H. Anjum, M.N. Hedhili, Y. Saih, K.-W. Huang, J.-M. Basset, Ni–Sn-supported ZrO_2 catalysts modified by indium for selective CO_2 hydrogenation to methanol, ACS Omega. 3 (2018) 3688–3701. https://doi.org/10.1021/acsomega.8b00211.

[10] Y.S. Chen, J.F. Kang, B. Chen, B. Gao, L.F. Liu, X.Y. Liu, Y.Y. Wang, L. Wu, H.Y. Yu, J.Y. Wang, Q. Chen, E.G. Wang, Microscopic mechanism for unipolar resistive switching behaviour of nickel oxides, J. Phys. D. Appl. Phys. 45 (2012) 65303. https://doi.org/10.1088/0022-3727/45/6/065303.

[11] L. Xu, L. Cao, W. Xu, Z. Pei, One-step electrosynthesis of NiFe-NF electrodes for highly efficient overall water splitting, Appl. Surf. Sci. 503 (2020). https://doi.org/10.1016/j.apsusc.2019.144122.

[12] K. Zhang, X. Xia, S. Deng, Y. Zhong, D. Xie, G. Pan, J. Wu, Q. Liu, X. Wang, J. Tu, Nitrogen-doped sponge Ni fibers as highly efficient electrocatalysts for oxygen evolution reaction, Nano-Micro Lett. 11 (2019) 21. https://doi.org/10.1007/s40820-019-0253-5.

[13]   E. López-Fernández, J. Gil-Rostra, J.P. Espinós, A.R. González-Elipe, A.
de Lucas Consuegra, F. Yubero, Chemistry and electrocatalytic activity of
nanostructured nickel electrodes for water electrolysis, ACS Catal. 10
(2020) 6159–6170. https://doi.org/10.1021/acscatal.0c00856.

[14]   Š. Trafela, J. Zavašnik, S. Šturm, K.Ž. Rožman, Formation of a
Ni(OH)2/NiOOH active redox couple on nickel nanowires for
formaldehyde detection in alkaline media, Electrochim. Acta. 309 (2019)
346–353. https://doi.org/10.1016/j.electacta.2019.04.060.

[15]   J. Yan, L. Kong, Y. Ji, J. White, Y. Li, J. Zhang, P. An, S. Liu, S.-T. Lee, T.
Ma, Single atom tungsten doped ultrathin α-Ni(OH)$_2$ for enhanced
electrocatalytic water oxidation, Nat. Commun. 10 (2019) 2149.
https://doi.org/10.1038/s41467-019-09845-z.

[16]   A.K. Taylor, I. Andreu, B.D. Gates, Regular Dimpled Nickel Surfaces for
Improved Efficiency of the Oxygen Evolution Reaction, ACS Appl.
Energy   Mater.   1   (2018)   1771–1782.
https://doi.org/10.1021/acsaem.8b00338.

[17]   S. Anantharaj, S. Kundu, S. Noda, "The Fe Effect": A review unveiling the
critical roles of Fe in enhancing OER activity of Ni and Co based catalysts,
Nano   Energy.   80   (2021)   105514.
https://doi.org/10.1016/j.nanoen.2020.105514.

[18]   T. Liu, CC#17-Single-crystalline NiFe-hydroxide nanosheets for
catalyzing oxygen evolution, (2018).

[19]   R. Farhat, J. Dhainy, L.I. Halaoui, OER catalysis at activated and
codeposited NiFe-oxo/hydroxide thin films is due to postdeposition
surface-Fe and is not sustainable without Fe in solution, ACS Catal. 10
(2020) 20–35. https://doi.org/10.1021/acscatal.9b02580.

[20]   M.L. Lindstrom, R. Gakhar, K. Raja, D. Chidambaram, Facile synthesis of
an efficient Ni-Fe-Co based oxygen evolution reaction electrocatalyst, J.
Electrochem.   Soc.   167   (2020).   https://doi.org/10.1149/1945-
7111/ab6b08.

[21]   D. Lim, E. Oh, C. Lim, S.E. Shim, S.-H. Baeck, Bimetallic NiFe alloys as
highly efficient electrocatalysts for the oxygen evolution reaction, Catal.
Today. 352 (2020) 27–33. https://doi.org/10.1016/j.cattod.2019.09.046.

[22]   S. Hoang, S. Guo, N.T. Hahn, A.J. Bard, C.B. Mullins, Visible light driven
photoelectrochemical   water   oxidation   on   nitrogen-modified   TiO$_2$

nanowires, Nano Lett. 12 (2012) 26–32. https://doi.org/10.1021/nl2028188.

[23] L. Wang, C.-Y. Lee, P. Schmuki, Solar water splitting: preserving the beneficial small feature size in porous α-Fe_2O_3 photoelectrodes during annealing, J. Mater. Chem. A. 1 (2013) 212–215. https://doi.org/10.1039/C2TA00431C.

[24] H. Zhang, X. Li, A. Hähnel, V. Naumann, C. Lin, S. Azimi, S.L. Schweizer, A.W. Maijenburg, R.B. Wehrspohn, Bifunctional heterostructure assembly of NiFe LDH nanosheets on NiCoP nanowires for highly efficient and stable overall water splitting, Adv. Funct. Mater. 28 (2018) 1706847. https://doi.org/10.1002/adfm.201706847.

[25] R. Solmaz, G. Kardaş, Electrochemical deposition and characterization of NiFe coatings as electrocatalytic materials for alkaline water electrolysis, Electrochim. Acta. 54 (2009) 3726–3734. https://doi.org/10.1016/j.electacta.2009.01.064.

[26] S. Watzele, P. Hauenstein, Y. Liang, S. Xue, J. Fichtner, B. Garlyyev, D. Scieszka, F. Claudel, F. Maillard, A.S. Bandarenka, Determination of electroactive surface area of Ni-, Co-, Fe-, and Ir-based oxide electrocatalysts, ACS Catal. 9 (2019) 9222–9230. https://doi.org/10.1021/acscatal.9b02006.

[27] F. Jing, Q. Lv, J. Xiao, Q. Wang, S. Wang, Highly active and dual-function self-supported multiphase NiS–NiS_2–Ni_3S_2/NF electrodes for overall water splitting, J. Mater. Chem. A. 6 (2018) 14207–14214. https://doi.org/10.1039/C8TA03862G.

[28] G. Yan, X. Zhang, L. Xiao, Prussian blue analogues-derived bimetallic phosphide hollow nanocubes grown on Ni foam as water splitting electrocatalyst, J. Mater. Sci. 54 (2019) 7087–7095. https://doi.org/10.1007/s10853-019-03362-6.

[29] S. Ahn, B.-S. Lee, I. Choi, S. Yoo, H.-J. Kim, E. Cho, D. Henkensmeier, S. Nam, J. Jang, Development of a membrane electrode assembly for alkaline water electrolysis by direct electrodeposition of nickel on carbon papers, Appl. Catal. B Environ. s 154–155 (2014) 197–205. https://doi.org/10.1016/j.apcatb.2014.02.021.

[30] M. Carmo, D.L. Fritz, J. Mergel, D. Stolten, A comprehensive review on PEM water electrolysis, Int. J. Hydrogen Energy. 38 (2013) 4901–4934. https://doi.org/10.1016/j.ijhydene.2013.01.151.

[31] L. Tao, P. Guo, W. Zhu, T. Li, X. Zhou, Y. Fu, C. Yu, H. Ji, Highly efficient mixed-metal spinel cobaltite electrocatalysts for the oxygen evolution reaction, Chinese J. Catal. 41 (2020) 1855–1863. https://doi.org/10.1016/S1872-2067(20)63638-5.

[32] C. Lamy, P. Millet, A critical review on the definitions used to calculate the energy efficiency coefficients of water electrolysis cells working under near ambient temperature conditions, J. Power Sources. 447 (2020) 227350. https://doi.org/10.1016/j.jpowsour.2019.227350.

[33] E. López-Fernández, J. Gil-Rostra, J.P. Espinós, A.R. González-Elipe, F. Yubero, A. de Lucas-Consuegra, $Cu_xCo_{3-x}O_4$ ultra-thin film as efficient anodic catalysts for anion exchange membrane water electrolysers, J. Power Sources. 415 (2019) 136–144. https://doi.org/10.1016/j.jpowsour.2019.01.056.

[34] E. López-Fernández, J. Gil-Rostra, C. Escudero, I.J. Villar-García, F. Yubero, A. de Lucas Consuegra, A.R. González-Elipe, Active sites and optimization of mixed copper-cobalt oxide anodes for anion exchange membrane water electrolysis, J. Power Sources. (2020). https://doi.org/10.1016/j.jpowsour.2020.229217.

[35] Y.T. Lee, R.P. Gautam, S.M. Islam, C.J. Barile, Cuprous oxide electrodeposited with nickel for the oxygen evolution reaction in 1 M NaOH, J. Phys. Chem. C. 123 (2019) 1287–1292. https://doi.org/10.1021/acs.jpcc.8b10413.

[36] I. V Pushkareva, A.S. Pushkarev, S.A. Grigoriev, P. Modisha, D.G. Bessarabov, Comparative study of anion exchange membranes for low-cost water electrolysis, Int. J. Hydrogen Energy. 45 (2020) 26070–26079. https://doi.org/10.1016/j.ijhydene.2019.11.011.

[37] J. Chang, G. Wang, A. Belharsa, J. Ge, W. Xing, Y. Yang, Stable $Fe_2P_2S_6$ nanocrystal catalyst for high-efficiency water electrolysis, Small Methods. 4 (2020) 1900632. https://doi.org/10.1002/smtd.201900632.

[38] H. Li, M.R. Kraglund, A.K. Reumert, X. Ren, D. Aili, J. Yang, Poly(vinyl benzyl methylpyrrolidinium) hydroxide derived anion exchange membranes for water electrolysis, J. Mater. Chem. A. 7 (2019) 17914–17922. https://doi.org/10.1039/C9TA04868E.

[39] A. Konovalova, H. Kim, S. Kim, A. Lim, H.S. Park, M.R. Kraglund, D. Aili, J.H. Jang, H.-J. Kim, D. Henkensmeier, Blend membranes of polybenzimidazole and an anion exchange ionomer (FAA3) for alkaline

water electrolysis: Improved alkaline stability and conductivity, J. Memb. Sci. 564 (2018) 653–662. https://doi.org/10.1016/j.memsci.2018.07.074.

Chapter 9

Nanostructured nickel-based electrodes for hybrid ethanol-water electrolysis
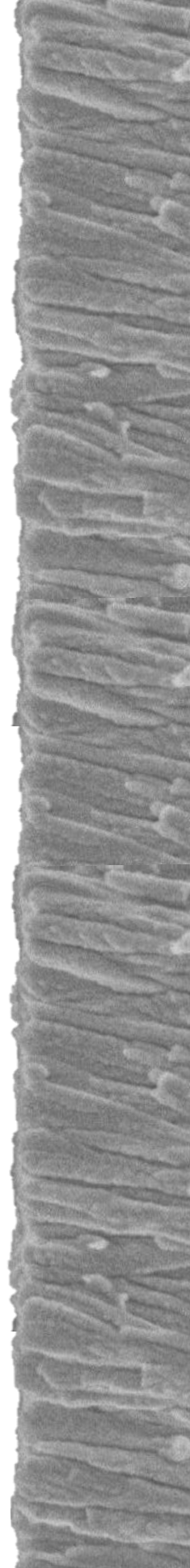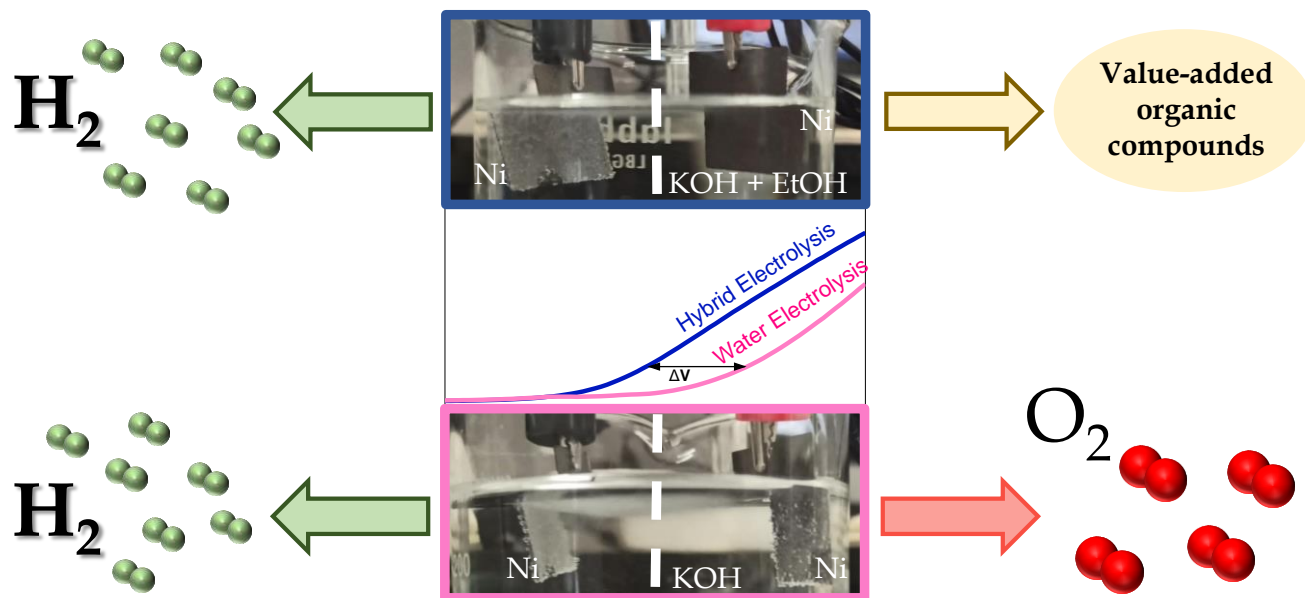
The content of this chapter is under review as:

9.1.   Introduction

In Chapters 6-8 we have studied and optimized the behaviour of different nickel-based electrodes under water electrolysis conditions. In addition, it has been observed that the OER is the bottleneck of the whole electrolysis process due to its sluggish kinetic involving a four proton-coupled electron transfer ($4OH^-{\rightarrow}2H_2O+O_2+4e^-$) [1,2]. This process requires a high redox potential that impairs the entire H_2 production effectiveness. To overcome this limitation, hybrid water electrolysis has emerged in recent years as a suitable technology encompassing the advantages associated to the more favourable thermodynamics and kinetics of the oxidation reactions of organic substances [1].

The main advantages associated to the addition of organic substances to the electrolyte solutions are the reduction of the operation voltage required for the electrolysis process and the possibility to obtain valuable products in the anode, completely separated from the pure hydrogen stream produced at the cathode [1]. In this context, ethanol electrolysis has been proposed as a promising method to produce hydrogen at low power consumption, a feature linked to the fact that the organic molecules provide part of the potential energy required for electrolysis [3]. Ethanol is easy to produce [1], has low toxicity and high availability [4]. It can be produced by fermentation of biomass, without changes in the natural balance of carbon dioxide in the atmosphere [5]. In addition, the possibility to produce value-added organic compounds (e.g., acetic acid or acetaldehydes) at the anode and H_2, the sole gas product of this electrochemical reaction, at the cathode makes this process extremely attractive.

Conventionally, precious metals such as Au, Pt, Pd or their alloys have been used to act as ethanol oxidation reaction (EOR) electrocatalysts [6–8]. However, their high cost and scarcity limit their use for practical applications. Unlike most studies utilizing precious metals for the EOR electrode, in this chapter we propose the use of cheaper and more abundant metals as electrocatalyst. In concrete, we have used the nickel and nickel-iron catalyst electrodes prepared by MS-OAD for the previous chapters of this thesis for the hybrid ethanol-water electrolysis.

The influence of the nickel loading, the amount of ethanol in the electrolyte solution or the addition of Fe to the Ni electrode on the EOR performance have been studied in a three-electrode cell configuration. A complete characterization of electrodes has been carried out by XPS, SEM and XRD. The anode type and operating conditions optimized in the three-electrode cell were then transferred to a complete and scaled-up anion exchange membrane (AEM) cell using a similar nickel electrode as cathode. The obtained results have evidenced the high performance and stability (for 3 days) of the electrodes prepared by MS-OAD for this kind of hybrid ethanol-water electrolysis. It has been also proved that no O_2 is produced in the anode (i.e., discarding any contribution from OER) and that there is a clear enhancement of current density with respect to that for pure water electrolysis at the same voltage (242 mA cm^{-2} at 2.0 V with 1.0 M KOH vs. 343 mA cm^{-2} in a 1.5 M EtOH and 1.0 M KOH solution).

9.2.   Experimental

Nanostructured nickel and nickel-iron electrocatalysts (Ni/Fe at. ratio =10) were deposited by MS-OAD as described in Chapters 3 and 6 to 8.

Electrocatalysts were simultaneously deposited on carbon paper GDL substrates (used in the electrochemical experiments) and on polished silicon wafers (to determine its *equivalent thickness* of the deposited films).

Along this chapter, the different electrodes (i.e., the catalyst loads deposited on the carbon paper GDL support) will be identified as *XX-thickness/YY,* where XX refers to the catalyst (either Ni or 10.1-NiFe), *thickness* refers to its *equivalent thickness* (in nanometers) and *YY* refers the support used in each electrode. Thus, a *Ni-1080/CP* refers to a Ni electrode with an *equivalent thickness* of 1080 nm and *10.1-NiFe-540/CP* refers to a NiFe electrode with a Ni/Fe at. ratio about 10 (as determined by EDX analysis) with an *equivalent thickness* of 540 nm both deposited on carbon paper.

All the physico-chemical techniques used in this chapter have been described in Chapter 3.

The performance towards the EOR as a function of the ethanol content in the electrolyte, the catalyst nature and load in the electrodes were assessed by means of electrochemical experiments carried out in the three-electrode cell described in Chapter 3. All measurements were carried out at room temperature applying a scan rate of 20 mV s^{-1} and a voltage range from 0 to 750 mV vs. Ag/AgCl. Aqueous 1.0 M KOH electrolyte solutions with ethanol contents ranging from 0.0 to 2.0 M EtOH were investigated to optimize the EtOH content.

The optimal anodic electrode and ethanol content in the electrolyte required for the EOR in the half-cell configuration were transferred to a MEA configuration. The influence of the KOH content in the electrolyte

solution on the electrochemical performance was also studied in this
configuration.

Ni and Ni-Fe deposits (*equivalent thickness* of 540 nm, equivalent to 0.38
mg cm^{-2} and 0.35 mg cm^{-2} of catalyst load) supported on carbon paper
were used as electrodes. In the MEA, electrodes were separated by a
Fumapem FAA-3-50 AEM. The same nickel catalyst film, already
optimized in previous Chapter 6 [9], has been used as cathode to simplify
the manufacturing process. The cell was tightly closed with screws
applying a torque pressure of 2.5 Nm.

Linear sweep voltammetry (LSV) experiments were done varying the
potential from 1.0 to 2.0 V (40 °C, scan rate of 5.0 mV s^{-1}). In these
experiments, 1.5 M EtOH solution was used with several KOH electrolyte
concentrations (from 0.1 to 4.0 M KOH) to optimize the KOH content for
the hybrid electrolysis process. In addition, CV experiments (voltage
range from 0.0 to 2.2 V, scan rate of 50 mV s^{-1}, 200 cycles) and constant-
current chronopotentiometric measurements (current density fixed at 300
mA cm^{-2} for 72 hours, electrolyte solution replaced every 24 hours) were
carried out with a 2.0 M KOH and 1.5 M EtOH electrolyte solution to
investigate the stability of the cell.

To visually check in an unseparated electrochemical cell the
production or lack of oxygen production, both electrodes (anode and
cathode) were immersed in a vessel to simulate a membrane-less cell,
where the production or lack of bubbles of oxygen were observed. For
these experiments, a 1.0 M KOH or 1.0 M KOH + 1.5 M EtOH solutions
(at 1.8 V) were used.

9.3. Results and discussion

9.3.1. Physico-chemical characterization of the electrodes

The surface microstructure of nickel and nickel-iron electrocatalysts layers have been previously studied in Chapters 6 and 7 of this thesis. It had been showed that the films present a nanocolumnar structures with a high porosity.

The chemical state at the surface of the electrodes was studied by XPS analysis of the Ni and Ni-Fe electrocatalysts as prepared (already studied in previous chapters) and after a series of electrochemical CV experiments (i.e., used electrocatalyst) in the three-electrode cell in KOH-EtOH electrolyte solutions. Regarding the Ni and O signals, both *Ni-540/CP* and *10.1-NiFe-540/CP* electrocatalysts presented a quite similar behaviour. The spectra in **Figure 9.1 a)** and **c)** correspond to the Ni $2p_{3/2}$ signal of the as prepared and used *Ni-540/CP* and *10.1-NiFe-540/CP* electrodes, respectively. The Ni $2p_{3/2}$ spectrum of the used samples are characterized by a main peak at 856.5 eV of binding energy, and their corresponding satellite, at ~6 eV higher binding energy, which are characteristic features of oxide and hydroxide nickel phases [12]. Meanwhile, the spectrum of the as prepared samples shows an additional contribution at 853.4 eV due to metallic Ni^0 [13]. The metallic contribution disappears in the used sample because of the partial oxidation produced by immersion in the KOH electrolyte solution and the electrochemical cycling. **Figure 9.1 b)** and **e)** show the O 1s spectra of the same samples. Peak at 531.7 is attributed to OH^- groups [14] and peak at 529.9 to O^{2-} anions [15]. In the O 1s of the used sample, the contribution of this O^{2-} ions disappear, and the spectrum depicts a single band at 531.7 eV, resulting from a surface enrichment in OH^- groups. This behaviour is attributed to the formation

of a hydroxide layer during the EOR electrochemical cycles in an alkaline medium and has been previously observed by us under OER conditions in previous chapters [9,16]. This effect also suggests that the active catalytic phase for the EOR is a nickel oxide/hydroxide formed at the surface of the electrodes. We will show later that this attribution agrees with the development of redox oxidation peaks in the CV diagrams. In **Figure 9.1 d)**, the Fe 2p spectra before and after electrochemical testing depict two peaks at 725.0 and 711.4 eV corresponding to Fe $2p_{1/2}$ and Fe $2p_{3/2}$ core levels of Fe^{+3} as it could be observed in Chapter 7 [17]. This finding is in line with the detection of a Ni-Fe oxide phase by XRD also observed in Chapter 7 and indicates that an oxidized external layer is the active phase in the EOR.
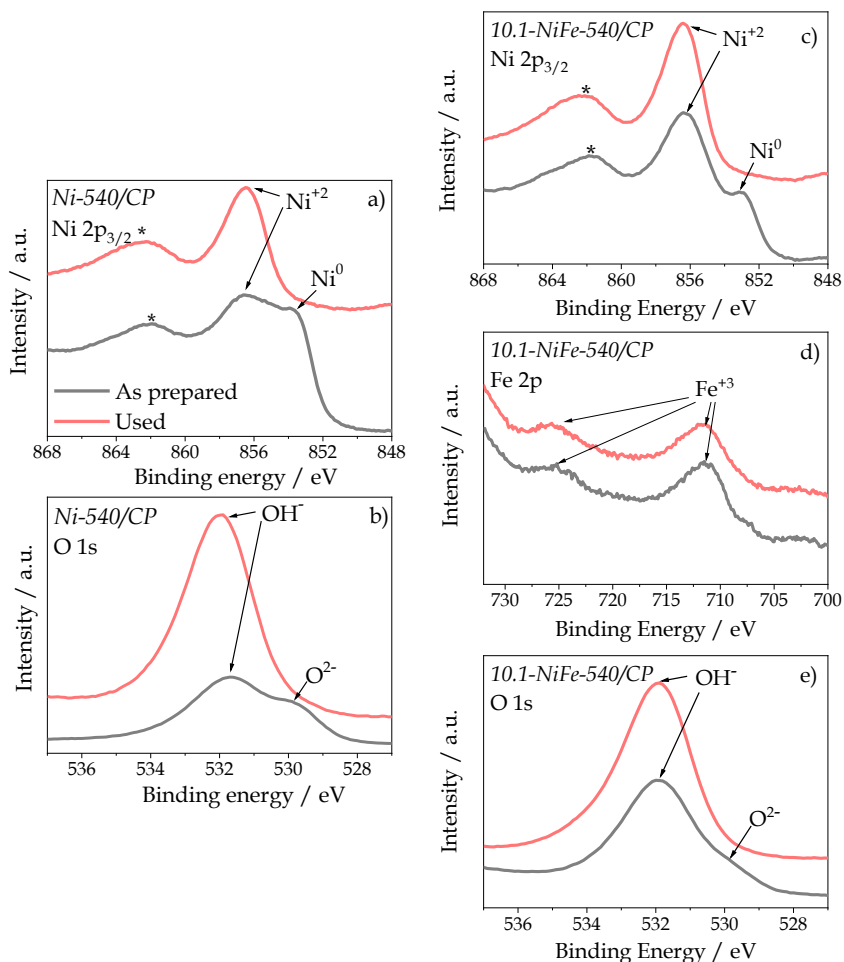
***Figure 9.1**. a) Ni 2p$_{3/2}$ and b) O 1s spectra of Ni-540/CP and c) Ni 2p$_{3/2}$, d) Fe 2p and e) O 1s spectra of 10.1-NiFe-540/CP catalyst samples as prepared and used after the experiments in the three-electrode cell.*

9.3.2. Oxygen evolution reaction vs. ethanol oxidation reaction

Figure 9.2 a) and **b)** show the electrochemical cyclic voltammetry curves of *Ni-540/CP* and *10.1-NiFe-540/CP* electrodes, respectively, for several feeding solutions (1.0 M KOH without ethanol, 1.5 M EtOH without KOH and 1.0 M KOH + 1.5 M EtOH). These concentrations of reactants have been taken for a preliminary proof of concept example and will be optimized as explained later.

A first point deserving a comment in the diagrams for the *Ni-540/CP* electrocatalyst in Figure 9.2 a) is that an ethanol solution without KOH is completely inactive, a feature supporting that a basic pH is needed for the ethanol/water electrolysis. In the experiments with a 1.0 M KOH electrolyte solution without ethanol, a well-defined peak at approximately 380 mV vs. Ag/AgCl develops during the positive scan. This peak is attributed to a redox oxidation process of $Ni(OH)_2$ to NiOOH previously explained in other chapters [9,18,19]. The corresponding redox reduction peak obtained during the negative scan appears at approximately 180 mV vs. Ag/AgCl, and it is attributed to the reversible reaction from NiOOH to $Ni(OH)_2$ [9,18,19]. Meanwhile, the onset potential for the oxygen evolution reaction (OER) appears between 500-600 mV, in agreement with previously reported values [9,20,21].

When EtOH is added to the feeding electrolyte solution containing 1.0 M KOH, ethanol electro-oxidation to intermediate species such as acetaldehydes and/or acetic acid are expected to occur associated to the NiOOH formation in the positive voltage sweep. It is also interesting here that the onset potential for the EOR appears at about the same value than the potential for the nickel redox oxidation peak, thus suggesting that the formed NiOOH is involved in the EOR, probably acting as electron transfer mediator of the oxidation process [22]. It is likely that the ethanol oxidation by chemical reaction with NiOOH may induce a decrease in the amount of nickel oxyhydroxide species at the surface of the electrode. A decrease in the formation of this kind of species can be visualized by the observed decrease in the intensity of the negative peak at ~250 mV (attributed to the electro-reduction reaction of the NiOOH to $Ni(OH)_2$ [23]), measured in the reverse scan, in comparison with the equivalent peak in the curve for the pure KOH electrolyte.

In agreement with these experimental findings, the oxidation of ethanol and other simple alcohols has been proposed to occur through the following mechanism [24–26]:

$$Ni(OH)_2 + OH^- \rightleftharpoons NiOOH + H_2O + e^- \qquad (9.1)$$

$$NiOOH + CH_3CH_2OH \rightarrow Ni(OH)_2 + \text{Intermediate species} \qquad (9.2)$$
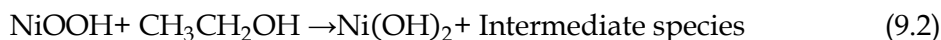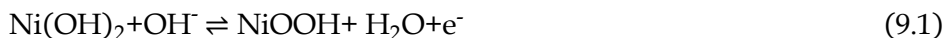
According to these reactions, the Ni surface becomes immediately hydroxidized when it is immersed in a KOH solution [27]. Then, in a first redox step (**Eq. (9.1)**), Ni(OH)$_2$ species react with OH$^-$ and become electrochemically oxidized to NiOOH. In a second reaction (**Eq. (9.2)**), these NiOOH species promote the oxidation of ethanol to compounds such as acetaldehydes and/or acetic acid. It is noteworthy that these two processes, the formation of nickel oxyhydroxides and the oxidation of ethanol, seem to occur at the same potential values.

Most significant evidence in Figure 9.2 a) is the higher current density obtained for the hybrid ethanol/water electrolysis in comparison with the values obtained by the standard water electrolysis at polarization voltages above 600 mV vs. Ag/AgCl (i.e., when the OER occurs in standard water electrolysis in basic media). The more favourable thermodynamics and kinetics for the oxidation reaction of organic substances (ethanol in this case, EOR) have been previously claimed to account for similar differences between EOR and OER [1,28].
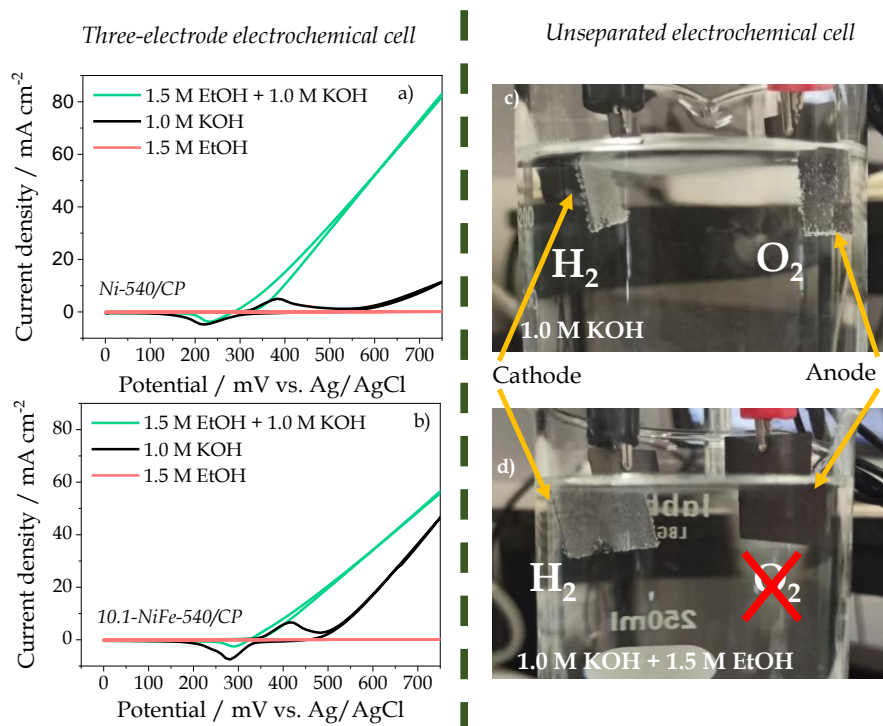
Figure 9.2. Cyclic voltammetry curves obtained for a) Ni-540/CP and b) 10.1-NiFe-540/CP electrodes, respectively, in the absence and presence of ethanol, KOH and mixtures in a three-electrode cell. c) Pure water electrolysis and d) hybrid ethanol-water electrolysis tests, with O_2 and lack of O_2 production at the anode, respectively. Both experiments at 1.8 V in an unseparated electrochemical cell.

An equivalent analysis for the water and hybrid ethanol/water electrolysis with a *10.1-NiFe-540/CP* electrocatalyst is presented in Figure 9.2 b). A well-known effect of the addition of iron to a nickel structure is an increase in the OER activity [29,30] for standard AEM water electrolysis. Herein, we have tested the *10.1-NiFe-540/CP* electrocatalysts for both OER and EOR reactions to determine whether the incorporation of iron is also beneficial for the latter process. Figure 9.2 a) and b) show that the incorporation of iron in the structure of the catalyst electrode produces some changes in the CVs: a shift in the Ni^{+2}/Ni^{+3} oxidation peak

to higher voltage values and an enhancement of performance for the OER (previously observed in Chapter 7). In relation with the XPS analysis in Figure 9.1, this supports a higher catalytic activity for OER of nickel-iron mixed oxyhydroxides than pure nickel oxyhydroxide [31]. The substitution of Fe^{+3} for Ni^{+3} sites at the edges of NiOOH particles has been claimed to account for the observed enhancement of OER activity [32]. Unlike this behaviour for OER, the electrode containing Fe presents a lower electrocatalytic activity for EOR. This smaller activity can be related with the shift of the NiOOH formation peak to a higher potential value and the fact that NiOOH seems to play an essential role as electron transfer mediator in EOR processes. A decrease in catalytic activity has been previously associated to the higher onset potentials for EOR in Ni-Fe in comparison with Ni pure films [33]. Herein, we have confirmed this difference determining the Tafel slopes from the plots in Figure 9.2 a) and b) applying the Butler-Volmer equation (see **Figure 9.3**). Smaller Tafel slope values indicate either a higher electrocatalytic activity or a faster kinetics for the electron exchange process [34]. Comparing both electrodes, the trend observed in the CV experiments in Figure 9.2 a) and b) agrees with the calculated values of the Tafel slopes determined for water or hybrid ethanol/water electrolysis conditions. Thus, when the electrolyte is a KOH aqueous solution, the Tafel slope was lower for the Ni-Fe electrode (113.0 mV dec^{-1}) than for Ni electrode (152.3 mV dec^{-1}) (**Figure 9.3 b)**). This behaviour was the opposite when ethanol was added to the electrolyte, when a Tafel slope of 48.4 mV dec^{-1} was obtained for the Ni-Fe electrode and 45.5 mV dec^{-1} for the Ni electrode (**Figure 9.3 c)**). It is also noteworthy, that for the *Ni-540/CP* electrocatalyst, a great decrease in the Tafel slope was found when EtOH was added to the electrolyte, (i.e., 45.5 mV dec^{-1} vs. 152.3 mV dec^{-1} with only KOH) (**Figure**

9.3 a)), supporting the increase in activity already evidenced by the diagrams in Figure 9.2 a). As a result of this comparative analysis of electrodes behaviour and due to the decrease in reactivity for the Ni-Fe electrocatalyst, pure nickel was selected for subsequent ethanol-water electrolysis experiments.
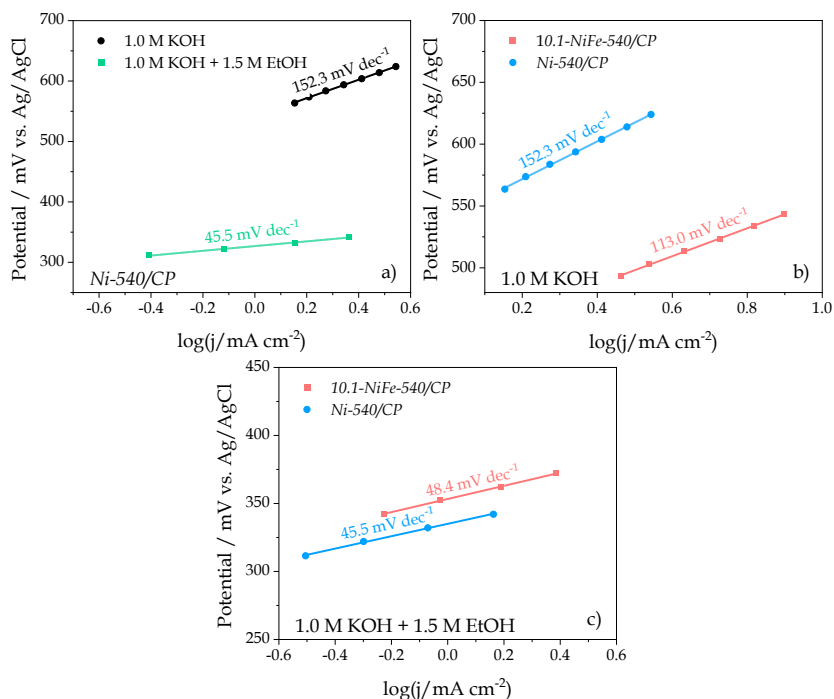
Figure 9.3. *Tafel plots of a) Ni-540/CP in a 1.0 M KOH and 1.0 M KOH + 1.5 M EtOH solution and comparative between Ni-540/CP and 10.1-NiFe-540/CP electrodes b) in a 1.0 M KOH solution and c) in a 1.0 M KOH + 1.5 M EtOH solution. The Tafel slopes were obtained from the linear fits to the initial rise of the OER and EOR curves.*

A key point for the optimization of EOR is that no OER takes place simultaneously during hybrid ethanol/water electrolysis. In the experiments carried out in this work, this is actually suggested by the common slope of the curve for the up and down cycles in Figure 9.2 a).

This common trend supports that the involved electrochemical process is similar or, in other words, there is no OER but EOR under the used operating conditions. Additional evidences proving this fact were obtained directly observing the behaviour of an unseparated electrolysis cell as shown in **Figure 9.2 c)** and **d)**. The experiments were carried out with two *Ni-540/CP* electrodes used as anode and cathode under conditions of 1.0 M KOH (Figure 9.2 c)) and 1.0 M KOH + 1.5 M EtOH (Figure 9.2 d)). According to Figure 9.2 c) abundant O_2 bubbles are produced at the anode when only KOH is present in the electrolyte solution. Unlike this behaviour, when EtOH is added to the electrolyte (Figure 9.2 d)) no bubbles can be seen at the electrode, what confirms that thermodynamical and/or kinetic conditions are more favorable for EOR that for OER [35].

To optimize the operating conditions of the hybrid ethanol/water electrolysis with the Ni electrocatalyst, additional experiments were carried out. **Figure 9.4 a)** shows the influence of nickel electrocatalyst load (expressed in terms of *equivalent thickness*) in the cyclic voltammetry experiments. First evidence is that the bare carbon paper substrate does not induce any electrochemical reaction, proving that the current density produced with the other electrodes is the result of the deposited electrocatalyst. The curves in this figure show that the electrocatalytic activity increases with the catalyst load up to an *equivalent thickness* of 540 nm. For larger loads, the electrochemical activity stabilises. We attribute this stabilization to that the number of electrocatalytic active sites accessible to reactants does not increase continuously with the amount of catalyst [9,36,37]. For this reason, in this study, an anodic electrode with this optimal *equivalent thickness* of 540 nm was selected for further experiments. **Figure 9.4 b)** shows the effect of the ethanol content in the

electrolyte solution on the catalyst electrochemical performance. When the ethanol concentration in the electrolyte increases from 0.5 to 1.5 M, the current density slightly increases because more molecules are available for the electro-oxidation reaction. When the ethanol concentration increases up to 2.0 M a significative decrease in the current density takes place. A similar behaviour has been observed in previous studies in the literature and it can be associated with various experimental factors. First, to a decrease in the ionic conductivity of the electrolyte solution due to an increase in the less polarizable alcohol concentration. Second, that an excess of unreacted ethanol can reduce the availability of the hydroxide ions at the catalyst sites [38,39].

Maximum EOR efficiency for the *Ni-540/CP* electrocatalysts was obtained for 1.0 M KOH aqueous electrolyte solution and 1.5 M EtOH added as fuel. Under these conditions, when applying a voltage of 1.5 V vs. RHE (482 mV vs. Ag/AgCl) a current density of about 27 mA cm^{-2} was obtained in the three-electrode cell (note that the conversion of the process is faradaic and that the totality of current gives rise to H_2). This value is similar than that obtained with nickel-cobalt electrodes (i.e., 34 mA cm^{-2} for 3.0 M EtOH and 1.0 M KOH) [40], but higher than values obtained with other nickel or nickel-cobalt electrodes providing about 6.5 mA cm^{-2} [33] (1.0 M EtOH and 0.1 M NaOH), 12.5 mA cm^{-2} [23] (0.5 M EtOH and 1.0 M NaOH), or 6 mA cm^{-2} [5] (0.5 M EtOH and 1.0 M NaOH).
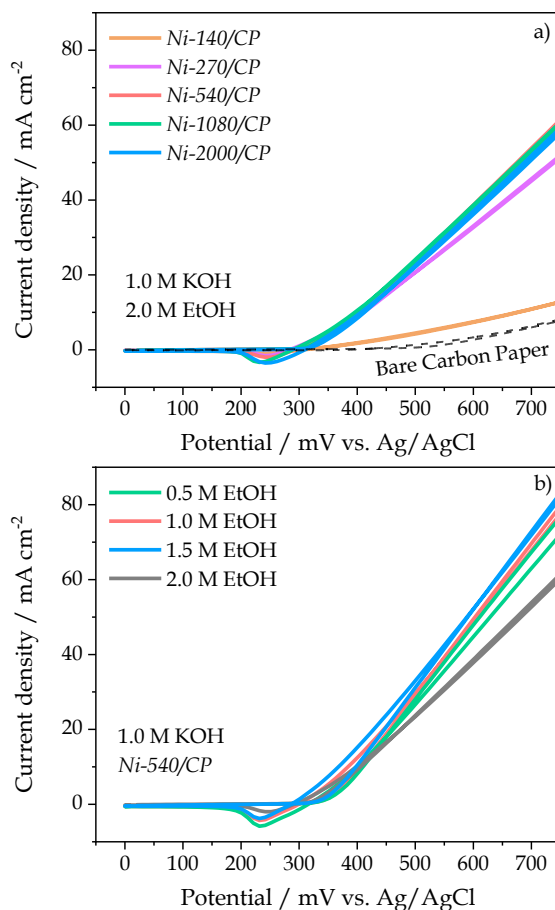
Figure 9.4. a) Cyclic voltammetry curves recorded for Ni anode sample with increasing equivalent thickness (1.0 M KOH and 2.0 M EtOH solution, scan rate 20 mV s^{-1}, room temperature). b) Influence of EtOH concentration vs. current density at different potential values at room temperature fixed 1.0 M KOH solution by means of a Ni-540/CP electrode.

9.3.3. Electrode performance in an anion exchange membrane electrolysis cell

To test the applicability of the nickel electrocatalyst electrodes prepared by magnetron sputtering for coupled hydrogen evolution and ethanol oxidation in a complete electrolysis cell, a MEA was fabricated

using two *Ni-540/CP* electrodes as anode and cathode and a Fumapem FAA-3-50 AEM membrane sandwiched between them. The cathode was optimized in the previous Chapter 6 of this thesis [9]. The use of the same electrocatalyst for both anode and cathode simplifies the manufacturing procedure and reduces the costs of the electrolyzer. As shown in **Figure 9.5 a)**, the cell voltage required for hybrid ethanol/water electrolysis is lower than that needed for standard water electrolysis. This must be due to the more favourable thermodynamics and/or kinetics encountered for the oxidation reaction of organic substances (ethanol in this case) [1,28] than for water oxidation. For example, the required potential for the hybrid ethanol/water electrolysis to provide a current density of 50 mA cm^{-2} is about 160 mV less than for the water electrolysis. This voltage reduction (and therefore power reduction) is similar to that reported in the literature where, for example, 200 mV were quoted by Wang, W. et al [4], or 110 mV by Sheng, S. et al [1], under similar working conditions than in our work.

The effect of the KOH electrolyte concentration on the electrochemical performance was assessed by linear sweep voltammetries in experiments carried out for the optimized 1.5 M EtOH fuel concentration (see **Figure 9.5 b)**). The overall current density of the cell experienced an increase when the KOH concentration was risen from 0.1 to 2.0 M. This is probably due to an improvement in the ionic conductivity of the electrolyte solution and to a higher availability of hydroxide species for the electrochemical process. The observed change of tendency above 2.0 M KOH is probably due to that a too high KOH concentration can produce a large surface coverage of the electrocatalyst by hydroxide ions, thus restricting the accessibility of ethanol molecules to the catalyst active sites [38,41]. Hence, in this study, a 1.5 M EtOH concentration and a KOH

concentration of 2.0 M were selected as optimum operation conditions. A current density value of 232 mA cm^{-2} was obtained at 1.8 V. This value of current density is much higher than that obtained by other authors as Sheng, S. et al [1] (80 mA cm^{-2}) or Wang, W. et al [4] (55 mA cm^{-2}) under similar voltage and temperature operating conditions. The higher efficiency obtained here supports the high potential of the MS-OAD technology for the manufacture of catalyst electrodes for hybrid water electrolyzers. In addition to the already mentioned advantages of this method in terms of a low metal load or the clean character of the manufacturing method, it must be highlighted that MS-OAD electrodes do not require the addition of any type of ionomer or binder. Ionomer may cause chemical electrode degradation and deterioration and produce a progressive decrease in current density [42,43].
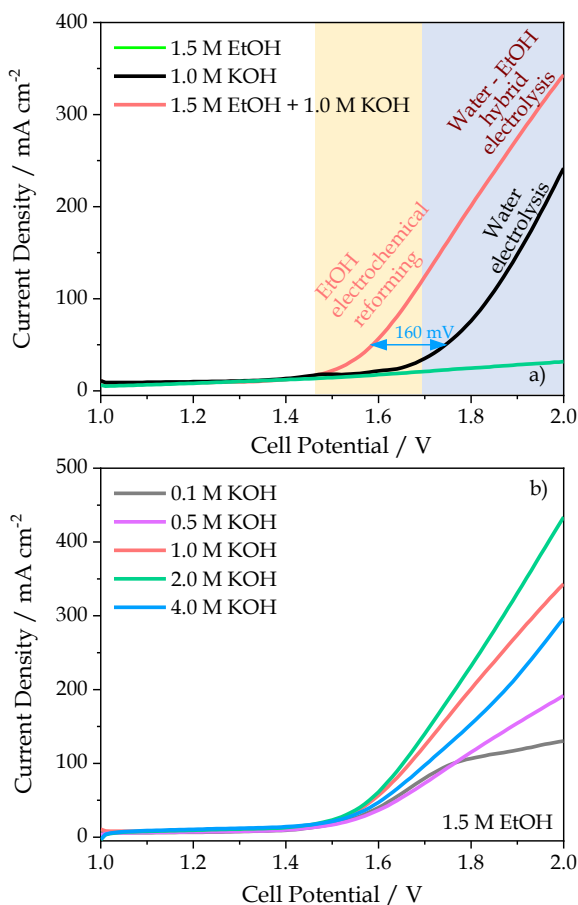
*Figure 9.5. a) LSV curves for Ni-540/CP electrodes used as anode and cathode in a
complete cell with and without 1.5 M EtOH and 1.0 M KOH. b) Influence of the KOH
concentration vs. current density at several cell potential under 1.5 M EtOH (both at
room temperature, and 5.0 mV s⁻¹ of scan rate).*

To further prove the reliability of MS-OAD electrodes, two stability
tests were carried with MEA cell electrolyzer incorporating the *Ni-540/CP*
electrocatalysts (used both as anode and cathode). **Figure 9.6 a)** shows 200
cyclic voltammetry measurements taken for the optimal EtOH and KOH
electrolyte concentrations, at 40 °C. The figure proves a great

reproducibility in the cell response under these conditions. In addition, the plot in **Figure 9.6 b)** demonstrates a high operational stability after 72 hours continuous operation at 300 mA cm^{-2}. By this latter test, it is noteworthy that we replaced the fuel/electrolyte solution every 24 hours to remove the secondary intermediate products resulting from the ethanol electro-oxidation (e.g., acetates molecules among others). Thus, although a slight increase with time was observed in the cell potential (about 0.2 % V h^{-1}), the replacement of the used ethanol-electrolyte solution with a new one permitted to recover the initial cell potential and proved that the slight degradation observed can be linked to the progressive oxidation of ethanol (for example, after five hours of cell operation a fourth of the ethanol present in the solution should have been oxidized assuming a faradaic behaviour), to the development of an overpotential for the EOR [44] or the stabilization and/or accommodation on the nickel electrode of impurities present in the medium [45].
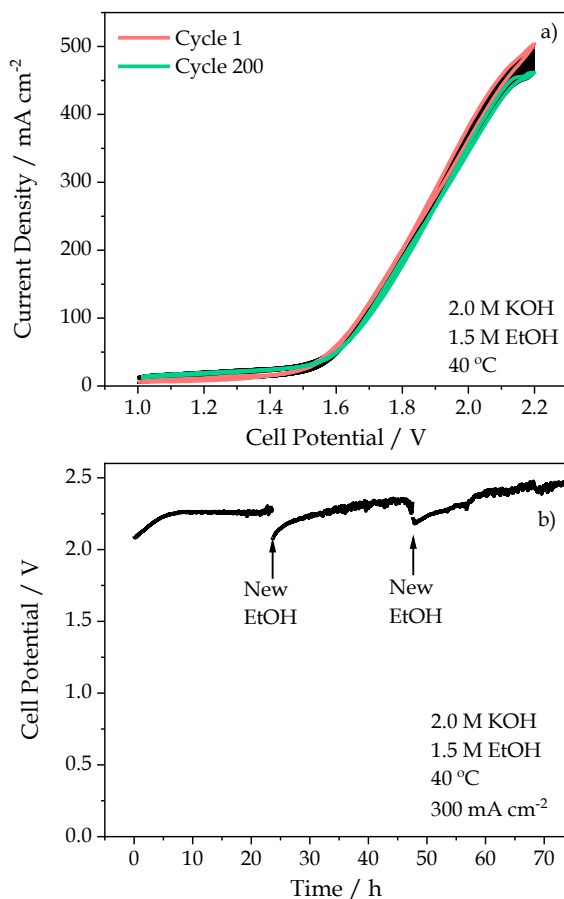
Figure 9.6. *Stability tests of MEA cell electrolyzer fabricated with Ni-540/CP catalyst electrodes (used as anode and cathode). All measurements performed at 40 °C, 1.5 M EtOH fuel and 2.0 M KOH electrolyte solution. a) 200 cycles voltammetries acquired with scan rate of 50 mV s^{-1} (1st and 200th cycles are highlighted, respectively). b) Constant current chronopotenciometry recorded at 300 mA cm^{-2}. Electrolyte/fuel solution was replaced every 24 hours.*

It has been highlighted above that, for similar currents, the cell voltage is lower for the ethanol/water electrolysis than for the water electrolysis. This indicates that less energy is needed to produce the same amount of hydrogen in the former case. Comparing the energy consumption in kWh

kgH_2^{-1} at two fixed current density values (100 and 200 mA cm^{-2}), the energy decrease amounted to 9.3 % and 8.1 % (**Figure 9.7**), respectively. This figure confirms that, from the viewpoint of energy consumption, the hybrid electrolysis is more competitive than a pure water electrolysis to produce hydrogen.
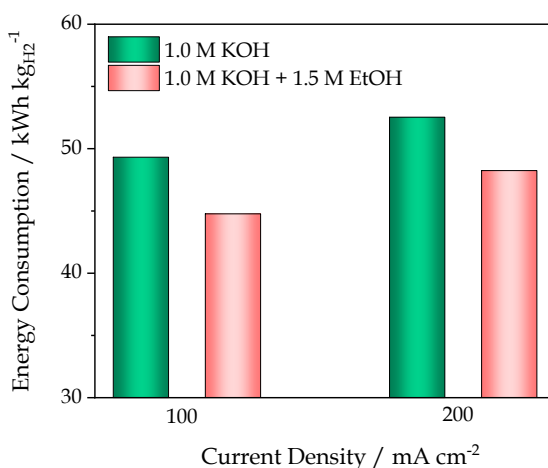
Figure 9.7. Energy consumption in kWh kgH_2^{-1} at different current density for the hybrid ethanol/water electrolysis and sole water electrolysis.

9.4.   Conclusions

In this chapter, Ni and Ni-Fe catalysts based anodes prepared by MS-OAD and several operation conditions have been optimized towards hybrid ethanol/water electrolysis. The following main conclusions are obtained:

- Ni-Fe based anodes present lower electrocatalytic activity towards EOR than *Ni-540/CP* anodes, despite their higher performance towards OER in standard AEM water electrolysis.

299

- The cell operation voltage for hybrid ethanol/water electrolysis is lower than that for standard water electrolysis for the same hydrogen production, thus decreasing the overall energy consumption of the process.

- During ethanol/water hybrid electrolysis and H_2 production conditions, OER does not take place on the anode side of the electrolyzer, providing the possibility to get other value-added organic compounds (acetic acid or acetaldehydes) at the anode side of the cell. Since H_2 produced at the cathode side of the cell is the only gas product of the EOR, security issues of the electrolysis process can be released since no explosive mixtures O_2/H_2 may form.

- The Ni based catalysts electrodes prepared by MS-OAD are highly efficient towards hydrogen production (relative low amount of catalyst is required for high H_2 production) and present an excellent stability (after 3 days test), both featured demonstrating the high potentiality of this preparation method for the manufacturing of electrodes.

Finally, regarding the potential use of this technology for real industrial application, experiments should be carried out replacing pure ethanol as fuel/reactant of this hybrid electrolysis process by a real bioethanol stream or other biomass molecules. These conditions would take advantage of these wastes and reduce the costs for the hydrogen production.

9.5. References

[1] S. Sheng, Y. Song, L. Sha, K. Ye, K. Zhu, Y. Gao, J. Yan, G. Wang, D. Cao, Simultaneous hydrogen evolution and ethanol oxidation in alkaline medium via a self-supported bifunctional electrocatalyst of Ni-Fe phosphide/Ni foam, Appl. Surf. Sci. 561 (2021) 150080. https://doi.org/10.1016/j.apsusc.2021.150080.

[2] W. Zhu, T. Zhang, Y. Zhang, Z. Yue, Y. Li, R. Wang, Y. Ji, X. Sun, J. Wang, A practical-oriented NiFe-based water-oxidation catalyst enabled by ambient redox and hydrolysis co-precipitation strategy, Appl. Catal. B Environ. 244 (2018). https://doi.org/10.1016/j.apcatb.2018.12.021.

[3] A. Caravaca, F.M. Sapountzi, A. de Lucas-Consuegra, C. Molina-Mora, F. Dorado, J.L. Valverde, Electrochemical reforming of ethanol–water solutions for pure H2 production in a PEM electrolysis cell, Int. J. Hydrogen Energy. 37 (2012) 9504–9513. https://doi.org/10.1016/j.ijhydene.2012.03.062.

[4] W. Wang, Y.-B. Zhu, Q. Wen, Y. Wang, J. Xia, C. Li, M.-W. Chen, Y. Liu, H. Li, H.-A. Wu, T. Zhai, Modulation of molecular spatial distribution and chemisorption with perforated nanosheets for ethanol electro-oxidation, Adv. Mater. 31 (2019) 1900528. https://doi.org/10.1002/adma.201900528.

[5] J. Zhan, M. Cai, C. Zhang, C. Wang, Synthesis of mesoporous NiCo2O4 fibers and their electrocatalytic activity on direct oxidation of ethanol in alkaline media, Electrochim. Acta. 154 (2015) 70–76. https://doi.org/10.1016/j.electacta.2014.12.078.

[6] G. Yang, Q. Zhang, H. Yu, F. Peng, Platinum-based ternary catalysts for the electrooxidation of ethanol, Particuology. 58 (2021) 169–186. https://doi.org/10.1016/j.partic.2021.01.007.

[7] R. Rizo, S. Pérez-Rodríguez, G. García, Well-defined platinum surfaces for the ethanol oxidation reaction, ChemElectroChem. 6 (2019) 4725–4738. https://doi.org/10.1002/celc.201900600.

[8] Z.X. Liang, T.S. Zhao, J.B. Xu, L.D. Zhu, Mechanism study of the ethanol oxidation reaction on palladium in alkaline media, Electrochim. Acta. 54 (2009) 2203–2208. https://doi.org/10.1016/j.electacta.2008.10.034.

[9] E. López-Fernández, J. Gil-Rostra, J.P. Espinós, A.R. González-Elipe, A. de Lucas Consuegra, F. Yubero, Chemistry and electrocatalytic activity of

nanostructured nickel electrodes for water electrolysis, ACS Catal. 10 (2020) 6159–6170. https://doi.org/10.1021/acscatal.0c00856.

[10]   M. Cano, F.J. Garcia-Garcia, D. Rodríguez-Padrón, A.R. González-Elipe, J.J. Giner-Casares, R. Luque, Ultrastable $Co_xSi_yO_z$ nanowires by glancing angle deposition with magnetron sputtering as novel electrocatalyst for water oxidation, ChemCatChem. 11 (2019) 6111–6115. https://doi.org/10.1002/cctc.201901730.

[11]   J. Dervaux, P.-A. Cormier, P. Moskovkin, O. Douheret, S. Konstantinidis, R. Lazzaroni, S. Lucas, R. Snyders, Synthesis of nanostructured Ti thin films by combining glancing angle deposition and magnetron sputtering: A joint experimental and modeling study, Thin Solid Films. 636 (2017) 644–657. https://doi.org/10.1016/j.tsf.2017.06.006.

[12]   A.M. Hengne, A.K. Samal, L.R. Enakonda, M. Harb, L.E. Gevers, D.H. Anjum, M.N. Hedhili, Y. Saih, K.-W. Huang, J.-M. Basset, Ni–Sn-supported ZrO_2 catalysts modified by indium for selective CO_2 hydrogenation to methanol, ACS Omega. 3 (2018) 3688–3701. https://doi.org/10.1021/acsomega.8b00211.

[13]   Y.S. Chen, J.F. Kang, B. Chen, B. Gao, L.F. Liu, X.Y. Liu, Y.Y. Wang, L. Wu, H.Y. Yu, J.Y. Wang, Q. Chen, E.G. Wang, Microscopic mechanism for unipolar resistive switching behaviour of nickel oxides, J. Phys. D. Appl. Phys. 45 (2012) 65303. https://doi.org/10.1088/0022-3727/45/6/065303.

[14]   S.-Q. Liu, H.-R. Wen, Ying-Guo, Y.-W. Zhu, X.-Z. Fu, R. Sun, C.-P. Wong, Amorphous Ni(OH)2 encounter with crystalline CuS in hollow spheres: A mesoporous nano-shelled heterostructure for hydrogen evolution electrocatalysis, Nano Energy. 44 (2018) 7–14. https://doi.org/10.1016/j.nanoen.2017.11.063.

[15]   D. Xiong, W. Li, L. Liu, Vertically aligned porous nickel(II) hydroxide nanosheets supported on carbon paper with long-term oxygen evolution performance, Chem. – An Asian J. 12 (2017) 543–551. https://doi.org/10.1002/asia.201601590.

[16]   E. López-Fernández, J. Gil-Rostra, J.P. Espinós, A.R. González-Elipe, F. Yubero, A. de Lucas-Consuegra, $Cu_xCo_{3-x}O_4$ ultra-thin film as efficient anodic catalysts for anion exchange membrane water electrolysers, J. Power Sources. 415 (2019) 136–144. https://doi.org/10.1016/j.jpowsour.2019.01.056.

[17]   D.H. Youn, Y.B. Park, J.Y. Kim, G. Magesh, Y.J. Jang, J.S. Lee, One-pot
synthesis of NiFe layered double hydroxide/reduced graphene oxide
composite as an efficient electrocatalyst for electrochemical and
photoelectrochemical water oxidation, J. Power Sources. 294 (2015) 437–
443. https://doi.org/10.1016/j.jpowsour.2015.06.098.

[18]   M. Urso, G. Torrisi, S. Boninelli, C. Bongiorno, F. Priolo, S. Mirabella,
$Ni(OH)_2$@Ni core-shell nanochains as low-cost high-rate performance
electrode for energy storage applications, Sci. Rep. 9 (2019) 7736.
https://doi.org/10.1038/s41598-019-44285-1.

[19]   S.P. E, D. Liu, R.A. Lazenby, J. Sloan, M. Vidotti, P.R. Unwin, J. V
Macpherson, Electrodeposition of nickel hydroxide nanoparticles on
carbon nanotube electrodes: correlation of particle crystallography with
electrocatalytic properties, J. Phys. Chem. C. 120 (2016) 16059–16068.
https://doi.org/10.1021/acs.jpcc.5b12741.

[20]   S. Ahn, B.-S. Lee, I. Choi, S. Yoo, H.-J. Kim, E. Cho, D. Henkensmeier, S.
Nam, J. Jang, Development of a membrane electrode assembly for
alkaline water electrolysis by direct electrodeposition of nickel on carbon
papers, Appl. Catal. B Environ. 154–155 (2014) 197–205.
https://doi.org/10.1016/j.apcatb.2014.02.021.

[21]   A.K. Taylor, I. Andreu, B.D. Gates, Regular dimpled nickel surfaces for
improved efficiency of the oxygen evolution reaction, ACS Appl. Energy
Mater. 1 (2018) 1771–1782. https://doi.org/10.1021/acsaem.8b00338.

[22]   H.B. Hassan, Z.A. Hamid, Electrodeposited Ni–Cr2O3 nanocomposite
anodes for ethanol electrooxidation, Int. J. Hydrogen Energy. 36 (2011)
5117–5127. https://doi.org/10.1016/j.ijhydene.2011.01.024.

[23]   A.F.B. Barbosa, V.L. Oliveira, J. van Drunen, G. Tremiliosi-Filho, Ethanol
electro-oxidation reaction using a polycrystalline nickel electrode in
alkaline media: Temperature influence and reaction mechanism, J.
Electroanal.   Chem.   746   (2015)   31–38.
https://doi.org/10.1016/j.jelechem.2015.03.024.

[24]   A. Hatamie, E. Rezvani, A.S. Rasouli, A. Simchi, Electrocatalytic
oxidation of ethanol on flexible three-dimensional interconnected
nickel/gold composite foams in alkaline media, Electroanalysis. 31 (2019)
504–511. https://doi.org/10.1002/elan.201800490.

[25]   J.-J. Huang, W.-S. Hwang, Y.-C. Weng, T.-C. Chou, Electrochemistry of
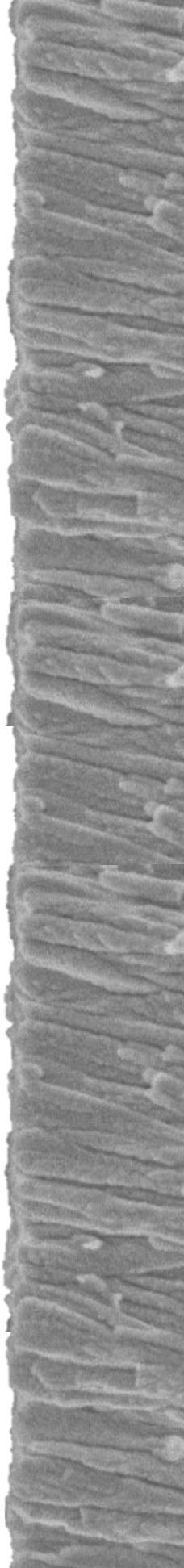ethanol oxidation on Ni-Pt alloy electrodes in KOH solutions, Mater.

Trans. 50 (2009) 1139–1147.
https://doi.org/10.2320/matertrans.MRA2008418.

[26]   I. Danaee, M. Jafarian, M. Sharafi, F. Gobal, A kinetic investigation of
        ethanol oxidation on a nickel oxyhydroxide electrode, J. Electrochem. Sci.
        Technol. 3 (2012) 50–56. https://doi.org/10.33961/JECST.2012.3.1.50.

[27]   S.L. Medway, C.A. Lucas, A. Kowal, R.J. Nichols, D. Johnson, In situ
        studies of the oxidation of nickel electrodes in alkaline solution, J.
        Electroanal. Chem. 587 (2006) 172–181.
        https://doi.org/10.1016/j.jelechem.2005.11.013.

[28]   A. Caravaca, A. De Lucas-Consuegra, A.B. Calcerrada, J. Lobato, J.L.
        Valverde, F. Dorado, From biomass to pure hydrogen: electrochemical
        reforming of bio-ethanol in a PEM electrolyser, Appl. Catal. B Environ.
        134–135 (2013) 302–309. https://doi.org/10.1016/j.apcatb.2013.01.033.

[29]   F. Dionigi, Z. Zeng, I. Sinev, T. Merzdorf, S. Deshpande, M.B. Lopez, S.
        Kunze, I. Zegkinoglou, H. Sarodnik, D. Fan, A. Bergmann, J. Drnec, J.F.
        de Araujo, M. Gliech, D. Teschner, J. Zhu, W.-X. Li, J. Greeley, B.R.
        Cuenya, P. Strasser, In-situ structure and catalytic mechanism of NiFe
        and CoFe layered double hydroxides during oxygen evolution, Nat.
        Commun. 11 (2020) 2522. https://doi.org/10.1038/s41467-020-16237-1.

[30]   Q. Xu, H. Jiang, X. Duan, Z. Jiang, Y. Hu, S.W. Boettcher, W. Zhang, S.
        Guo, C. Li, Fluorination-enabled reconstruction of NiFe electrocatalysts
        for efficient water oxidation, Nano Lett. 21 (2021) 492–499.
        https://doi.org/10.1021/acs.nanolett.0c03950.

[31]   O. Diaz-Morales, D. Ferrus-Suspedra, M.T.M. Koper, The importance of
        nickel oxyhydroxide deprotonation on its activity towards
        electrochemical water oxidation, Chem. Sci. 7 (2016) 2639–2645.
        https://doi.org/10.1039/c5sc04486c.

[32]   M.B. Stevens, C.D.M. Trang, L.J. Enman, J. Deng, S.W. Boettcher, Reactive
        Fe-sites in Ni/Fe (oxy)hydroxide are responsible for exceptional oxygen
        electrocatalysis activity, J. Am. Chem. Soc. 139 (2017) 11361–11364.
        https://doi.org/10.1021/jacs.7b07117.

[33]   D. Martín-Yerga, G. Henriksson, A. Cornell, Effects of incorporated iron
        or cobalt on the ethanol oxidation activity of nickel (oxy)hydroxides in
        alkaline media, Electrocatalysis. 10 (2019) 489–498.
        https://doi.org/10.1007/s12678-019-00531-8.

[34] G.B. Shombe, M.D. Khan, C. Zequine, C. Zhao, R.K. Gupta, N. Revaprasadu, Direct solvent free synthesis of bare α-NiS, β-NiS and α-β-NiS composite as excellent electrocatalysts: Effect of self-capping on supercapacitance and overall water splitting activity, Sci. Rep. 10 (2020) 3260. https://doi.org/10.1038/s41598-020-59714-9.

[35] X. Cui, M. Chen, R. Xiong, J. Sun, X. Liu, B. Geng, Ultrastable and efficient H2 production via membrane-free hybrid water electrolysis over a bifunctional catalyst of hierarchical Mo–Ni alloy nanoparticles, J. Mater. Chem. A. 7 (2019) 16501–16507. https://doi.org/10.1039/C9TA03924D.

[36] S. Cui, X. Liu, Z. Sun, P. Du, Noble metal-free copper hydroxide as an active and robust electrocatalyst for water oxidation at weakly basic pH, ACS Sustain. Chem. Eng. 4 (2016) 2593–2600. https://doi.org/10.1021/acssuschemeng.6b00067.

[37] E. López-Fernández, J. Gil-Rostra, C. Escudero, I.J. Villar-García, F. Yubero, A. de Lucas Consuegra, A.R. González-Elipe, Active sites and optimization of mixed copper-cobalt oxide anodes for anion exchange membrane water electrolysis, J. Power Sources. (2020). https://doi.org/10.1016/j.jpowsour.2020.229217.

[38] E. Ruiz-López, E. Amores, A. Raquel de la Osa, F. Dorado, A. de Lucas-Consuegra, Electrochemical reforming of ethanol in a membrane-less reactor configuration, Chem. Eng. J. 379 (2020) 122289. https://doi.org/10.1016/j.cej.2019.122289.

[39] U.K. Gupta, H. Pramanik, Electrooxidation study of pure ethanol/methanol and their mixture for the application in direct alcohol alkaline fuel cells (DAAFCs), Int. J. Hydrogen Energy. 44 (2019) 421–435. https://doi.org/10.1016/j.ijhydene.2018.03.008.

[40] N.A.M. Barakat, M. Motlak, A.A. Elzatahry, K.A. Kahlil, E.A.M. Abdelghani, Ni_xCo_{1-x} alloy nanoparticle-doped carbon nanofibers as effective non-precious catalyst for ethanol oxidation, Int. J. Hydrogen Energy. 39 (2014) 305–316. https://doi.org/10.1016/j.ijhydene.2013.10.061.

[41] J. Paula, D. Nascimento, J. Linares Leon, Influence of the anolyte feed conditions on the performance of an alkaline glycerol electroreforming reactor, J. Appl. Electrochem. 45 (2015). https://doi.org/10.1007/s10800-015-0848-6.

[42] G. Papakonstantinou, G. Algara-Siller, D. Teschner, T. Vidaković-Koch,

R. Schlögl, K. Sundmacher, Degradation study of a proton exchange membrane water electrolyzer under dynamic operation conditions, Appl. Energy. 280 (2020) 115911. https://doi.org/10.1016/j.apenergy.2020.115911.

[43]   B. Mayerhöfer, K. Ehelebe, F.D. Speck, M. Bierling, J. Bender, J.A. Kerres, K.J.J. Mayrhofer, S. Cherevko, R. Peach, S. Thiele, On the effect of anion exchange ionomer binders in bipolar electrode membrane interface water electrolysis, J. Mater. Chem. A. 9 (2021) 14285–14295. https://doi.org/10.1039/D1TA00747E.

[44]   H. Ju, S. Giddey, S.P.S. Badwal, R.J. Mulder, T.R. Gengenbach, Methanol-water co-electrolysis for sustainable hydrogen production with PtRu/C-SnO2 electro-catalyst, Ionics (Kiel). 24 (2018) 2367–2378. https://doi.org/10.1007/s11581-017-2371-8.

[45]   A. Konovalova, H. Kim, S. Kim, A. Lim, H.S. Park, M.R. Kraglund, D. Aili, J.H. Jang, H.-J. Kim, D. Henkensmeier, Blend membranes of polybenzimidazole and an anion exchange ionomer (FAA3) for alkaline water electrolysis: Improved alkaline stability and conductivity, J. Memb. Sci. 564 (2018) 653–662. https://doi.org/10.1016/j.memsci.2018.07.074.

Chapter 10

Concluding remarks and
future prospects

The main objective of this thesis was the fabrication of efficient and low-cost electrodes to be used in anion exchange membrane water electrolyzers and their validation in cell operation conditions. For this purpose, an unconventional technology for the preparation of catalysts, magnetron sputtering at oblique angle deposition (MS-OAD), was used. As it is described before, comparing to the other traditional electrode fabrication methods, MS-OAD is an environmentally friendly one-step method highly reproducible and scalable, that operates at room temperature. In this thesis work, we have demonstrated that it provides highly efficient nanostructured electrodes to be considered in AEMWE.

10.1. Conclusions

Partial conclusions of this thesis have been included at the end of each chapter section of this manuscript. In order to give an overall idea of the accomplished achievements, they are summarised below:

❖ It is demonstrated that MS-OAD technology is suitable to produce high performance nanostructured catalyst electrodes prepared directly on suitable backing electrode supports. Thus, it allows fabrication of catalyst electrodes of different elemental and chemical compositions (oxides, hydroxides, metallic), loads, or even layered structures.

❖ Co/Cu mixed oxides, Ni and Ni-Fe metallic catalyst electrodes prepared by MS-OAD demonstrated to be, by first time in the literature, active and stable in form of ultrathin electrodes for their use in AEMWE cells. In addition, it has been confirmed the best

behavior as anodic catalyst of Ni-Fe electrodes compared to other Co/Cu or pure Ni electrodes towards OER reaction.

❖ It is obtained better electrochemical performance in amorphous solid solution of the Co/Cu oxides than in corresponding well crystallize phases of these mixed oxides.

❖ Nanostructured Ni and Ni-Fe based electrodes prepared by MS-OAD, can be incorporated in AEMWE cells with an ionomer-free approach, simplifying the manufacture and integration of cells and reducing the cost and other associated problems with the addition of this kind of additives. Besides, these catalyst electrodes present high electrochemical performance for low catalyst loads due to their intrinsic nanostructure that bestows high specific electrochemical active surface area.

❖ The addition of iron atoms within the nickel metallic structure of nanostructured electrodes improves the electrochemical performance of the AEMWE cells where they are incorporated.

❖ For the best Ni-Fe anode catalysts, the replacement of carbon paper by stainless steel GDL supports contributes to improve long-term electrochemical stability of the AEMWE cell where they are incorporated. Thus, it is demonstrated the current densities per amount of catalyst load in this optimized cells are about the highest found in the literature for similar operation conditions with weak aging effects.

❖ Nanostructured nickel catalyst electrodes present superior performance than Ni-Fe electrodes for hybrid ethanol-water electrolysis process. The AEMWE cell incorporating these Ni

310

based electrodes presents a reduction in the electrical energy consumption and excellent stability to produce hydrogen comparing to water electrolysis.

10.2. Future work

The following future points in order to complete the current state of the investigation of this thesis can be carried out:

❖ To prepare trimetallic electrodes by MS-OAD by combining of Ni, Fe, Co, Cu, Cr, Zn, Mo or Mn in single layers or in multilayers configurations.

❖ To optimize the rest of the components and conditions (GDL, membrane, pressure torques…) of the electrolyzer in the hybrid-water electrolysis conditions. To replace ethanol by a real bioethanol stream or other biomass molecules in order to take advantage of these wastes and reduce the costs of the hydrogen production.

❖ To scale to a more real system to achieve a higher hydrogen production rate by increasing the electrode area and the number of cells (stacks).

❖ To test the stability of the cell for some months coupling to a solar panels system to demonstrate the viability to use this system for self-sufficiency in a real house.

❖ To use the same electrodes in another electrochemical application as the already proven good performance as glucose sensors in order to demonstrate the feasibility of using these electrodes

prepared by MS-OAD in a wide variety of applications (CO_2 electroreduction, …).

❖ To combine the N_2 plasma-activated process to improve the water splitting performance.

Chapter 11

Scientific production and patents
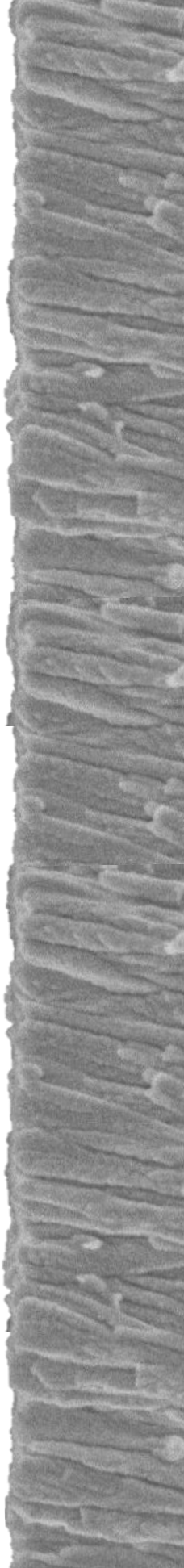
Publications

This doctoral thesis has resulted in the following publications:

1. **E. López-Fernández**, J. Gil-Rostra, J. P. Espinós, A. R. González-Elipe, F. Yubero, A. de Lucas Consuegra. *$Cu_xCo_{3-x}O_4$ ultra-thin film as efficient anodic catalysts for anion exchange membrane water electrolyzers*, Journal of Power Sources, 415 (2019) 136-144. https://doi.org/10.1016/j.jpowsour.2019.01.056

2. **E. López-Fernández**, J. Gil-Rostra, J. P. Espinós, A. R. Gonzalez-Elipe, A. de Lucas Consuegra, F. Yubero. *Chemistry and electrocatalytic activity of nanostructured nickel electrodes for water electrolysis*, ACS Catalysis, 10 (2020) 6159-6170. https://doi.org/10.1021/acscatal.0c00856

3. **E. López-Fernández**, J. Gil-Rostra, C. Escudero, I. J. Villar-García, F. Yubero, A. de Lucas Consuegra, A. R. González-Elipe. *Active sites and optimization of mixed copper-cobalt oxide anodes for anion exchange membrane water electrolysis*, Journal of Power Sources, 485 (2021) 229217. https://doi.org/10.1016/j.jpowsour.2020.229217

4. **E. López-Fernández**, C. G. Sacedón, J. Gil-Rostra, F. Yubero, A. R. González-Elipe, A. de Lucas-Consuegra. *Recent advances in alkaline exchange membrane water electrolysis and electrode manufacturing*, Molecules, 26(21) (2021) 6326.

5. **E. López-Fernández**, C. G. Sacedón, J. Gil-Rostra, J. P. Espinós, A. R. González-Elipe, F. Yubero, A. de Lucas-Consuegra. *Ionomer-Free Nickel-Iron bimetallic electrodes for efficient anion exchange membrane water electrolysis*, Chemical Engineering Journal. In press.

6. **E. López-Fernández**, C. G. Sacedón, J. Gil-Rostra, J. P. Espinós, A. R. González-Elipe, F. Yubero, A. de Lucas-Consuegra. *Nanostructured nickel electrocatalysts for hybrid ethanol-water AEM electrolysis*, Journal of Environmental Chemical Engineering. Under review.

7. **E. López-Fernández**, C. G. Sacedón, J. Gil-Rostra, J. P. Espinós, A. R. González-Elipe, F. Yubero, A. de Lucas-Consuegra. *Towards an overall optimization of an anion exchange membrane water electrolysis cell*. In preparation.

In addition, other related works have been published throughout the thesis:

1. N. Gutiérrez-Guerra, J.A. González, J.C. Serrano-Ruiz, **E. López-Fernández**, J.L. Valverde, A. de Lucas-Consuegra. *Gas-phase electrocatalytic conversion of CO_2 to chemicals on sputtered Cu and Cu-C catalysts electrodes*, Journal of Energy Chemistry, 31 (2019) 46-53. https://doi.org/10.1016/j.jechem.2018.05.005

2. A.B. Calcerrada, A R. de la Osa, **E. Lopez-Fernandez**, F. Dorado, A. de Lucas-Consuegra. *Influence of the carbon support on the Pt-Sn anodic catalyst for the electrochemical reforming of ethanol*, International Journal of Hydrogen Energy, 44 (2019) 10616-10626. https://doi.org/10.1016/j.ijhydene.2019.03.011

3. **E. López-Fernández**, J. Gil-Rostra, J. P. Espinós, R. González, F. Yubero, A. de Lucas Consuegra, A. R. González-Elipe. *Robust label-free $Cu_xCo_yO_z$ electrochemical sensors for hexose detection during fermentation process monitoring*, Sensors and Actuators B: Chemical 304 (2020) 127360. https://doi.org/10.1016/j.snb.2019.127360

4. C. G. Sacedón, **E. López-Fernández**, A. R. de la Osa, F. Dorado, E. Amores, A. de Lucas-Consuegra. *Preliminary design of a self-sufficient electrical storage system based on electrolytic hydrogen for power supply in a residential application*, Energies, 11(20) (2021) 9582. https://doi.org/10.3390/app11209582

5. C. G. Sacedón, **E. López-Fernández**, J. P. Espinós, A.R. González-Elipe, F. Yubero, J. Gil-Rostra, A. de Lucas-Consuegra. *Non-noble metals nanostructured electrodes for energy-saving hydrogen production from alkaline water via urea electrocatalysis*. In preparation.

Conference contributions

During the development of the thesis, the following presentations related with this thesis have been carried out at national and international conferences:

Oral presentations

1. <u>**E. López-Fernández**</u>, J. Gil-Rostra, J.P. Espinós, A. de Lucas-Consuegra, F. Yubero, A. R. González-Elipe. *Water electrolysis with nanostructured CoO_x-CuO_x electrodes prepared by magnetron sputtering at oblique angles*. XV Congreso Nacional de Materiales / I Iberian Meeting on Materials Science (CNMAT 2018), Salamanca (Spain), July 2018.

2. <u>**E. López-Fernández**</u>, *Catalizadores anódicos preparados por magnetron sputtering para la electrólisis de agua*. CicCartuja Phd Talks, Sevilla (Spain), April 2019.

3. **E. López-Fernández**, J. Gil-Rostra, J.P. Espinós, A.R. González-Élipe, F. Yubero, A. de Lucas-Consuegra. *Nickel nanostructured electrodes prepared by magnetron sputtering for anion exchange membrane water electrolysis*. X Iberian Conference on Tribology / XI Iberian Vacuum Conference (IBERTRIVA 2019), Sevilla (Spain), June 2019.

4. **E. López-Fernández**, J. Gil-Rostra, J.P. Espinós, A.R. González-Élipe, F. Yubero, A. de Lucas-Consuegra. *Nanostructured electrodes prepared by magnetron sputtering for water electrolysis*. XIV Young Science Symposium, Ciudad Real (Spain), July 2020.

5. **E. López-Fernández**, J. Gil-Rostra, J.P. Espinós, A.R. González-Élipe, F. Yubero, A. de Lucas-Consuegra. *Química y actividad electrocatalítica de electrodos de níquel nanoestructurados para electrólisis de agua*. IV Encuentro de Jóvenes Investigadores de la SECAT (IV JJII SECAT 2020), Bilbao (Spain), September 2020.

6. **E. López-Fernández**, C. G. Sacedón, J. Gil-Rostra, A. R. González-Elipe F. Yubero, A. de Lucas-Consuegra. *Nickel electrodes prepared by magnetron sputtering for water and ethanol-water hybrid electrolysis*. XV Young Science Symposium, Ciudad Real (Spain), July 2021.

7. A. de Lucas-Consuegra, **E. López-Fernández**, A.R. González-Élipe, C. G. Sacedón, J.P. Espinós, F. Yubero, J. Gil-Rostra. *"Universal" Nickel based electrodes prepared by magnetron sputtering for alkaline Exchange membrane water and ethanol-water hybrid electrolysis*. 51st IUPAC General Assembly and 48th World Chemistry Congress / 104th Canadian Chemistry Conference and Exhibition (IUPAC- CCCE 2021), Canadá, Online, August 2021.

8. **E. López-Fernández**, C. G. Sacedón, J. Gil-Rostra, J. P. Espinós, A. R. González-Elipe, A. de Lucas-Consuegra, F. Yubero. *Mixed copper-cobalt oxide anodes for efficient anion exchange membrane water electrolysis*. 2021 Iberian Vacuum Meeting (RIVA 2021), Online, October 2021.

Poster presentations

1. <u>A. de Lucas-Consuegra</u>, **E. López-Fernández**, J. Gil-Rostra, J. P. Espinós, F. Yubero, A. R. González-Elipe. *Preparation of nanostructured $Cu_xCo_yO_z$ anodes by magnetron sputtering for anion exchange membrane water electrolysis*. 69th Annual Meeting of the International Society of Electrochemistry (ISE 2018), Bologna (Italy), September 2018.

2. **E. López-Fernández**, J. Gil-Rostra, J.P. Espinós, A.R. González-Élipe, F. Yubero, A. de Lucas-Consuegra. *Electrodos nanoestructurados de $Cu_xCo_yO_z$ para electrólisis de agua con membranas de intercambio aniónico*. VIII Jornadas doctorales de la UCLM, Cuenca (Spain), October 2018.

3. **E. López-Fernández**, <u>A. de Lucas-Consuegra</u>, J.P. Espinós, J. Gil-Rostra, A.R. González-Élipe, F. Yubero. *Anion exchange membrane water electrolysis with ultra-thin film electrodes prepared by magnetron sputtering*. 25th Topical Meeting of the International Society of Electrochemistry (ISE 2019), Toledo (Spain), May 2019.

4. **E. López-Fernández**, J. Gil-Rostra, J.P. Espinós, A.R. González-Élipe, F. Yubero, <u>A. de Lucas-Consuegra</u>. *Catalizadores anódicos nanoestructurados preparados por magnetron sputtering para la*

electrólisis de agua con membranas de intercambio aniónico. Reunión de la Sociedad Española de Catálisis (SECAT 2019), Córdoba (Spain), June 2019.

5. **E. López-Fernández**, J. Gil-Rostra, J.P. Espinós, A.R. González-Élipe, F. Yubero, A. de Lucas-Consuegra. *Electrodos nanoestructurados de Ni preparados por magnetron sputtering para electrólisis de agua con membranas de intercambio aniónico*. IX Jornadas doctorales de la UCLM, Ciudad Real (Spain), October 2019.

6. **E. López-Fernández**, <u>C. G. Sacedón</u>, J. Gil-Rostra, A. R. González-Elipe, F. Yubero, A. de Lucas-Consuegra. *Magnetron Sputtering y la electrólisis híbrida, una solución competitiva para la producción de hidrógeno verde*. Reunión de la Sociedad Española de Catálisis (SECAT 2021), Valencia (Spain), October 2021.

Patents

During the development of the thesis, the following process has been submitted to be patented:

1. Patent application submitted: *Porous ionomer free layered metal alloy electrocatalysts electrode*. Submission number: 300429558. Priority number: EP21383006. Priority date: 05 November 2021. Applicant(s): CSIC, UCLM. Inventors: F. Yubero, A.R. González-Élipe, J. Gil-Rostra, J. P. Espinós, E. López-Fernández, A. de Lucas-Consuegra, C. G. Sacedón.

EDUCATION:

- PhD student in the Chemical and Environmental Engineering program. University of Castilla-La Mancha.

  2017-Present

- MSC in Chemical Engineering. University of Castilla-La Mancha. Rating: 8.90.

  2015-2017

- BSC in Chemical Engineering. University of Castilla-La Mancha. Rating: 8.19.

  2011-2015

PROFESSIONAL EXPERIENCE:

- Predoctoral researcher scientific (FPU/00344). University of Castilla-La Mancha.

  2018-Present

- Contract for Research Project. Institute of Materials Science of Sevilla (ICMSE).

  2017-2018

- Research Initiation Grant. University of Castilla-La Mancha.

  2017

- Internship. CT Ingenieros. Puertollano.

  2016

- Internship. CT Ingenieros. Puertollano.

  2015

- Collaboration grant with Electrochemical and Environmental Engineering Laboratory. University of Castilla-La Mancha.

  2014-2015

AWARDS:

- Article of the month cicCartuja May 2019, April 2020 and June 2020.

- 2º award of the 2020 cicCartuja EBRO FOODs Research prize for the scientific article "Chemistry and Electrocatalytic Activity of Nanostructured Nickel Electrodes for Water Electrolysis".

Ester
López Fernández

Chemical Engineer

About me:

I am chemical engineer from the University of Castilla-La Mancha (Spain). This doctoral thesis in Chemical and Environmental Engineering summarizes my research activity at the University of Castilla-La Mancha and the Institute of Materials Science of Seville between 2017 and 2021. During this period, I have been co-author of 9 scientific publications and a patent application. I have participated in 4 research projects and 16 scientific congresses.

Languages:

English: Medium-High

Spanish: native

Contact:

+34660690446

eslofer93@gmail.com

linkedin.com/in/ester-lópez-fernández-38483719a

Date 10/11/2021